Volume 3 Issue 3 | July 2023

MICROSTRUCTURES

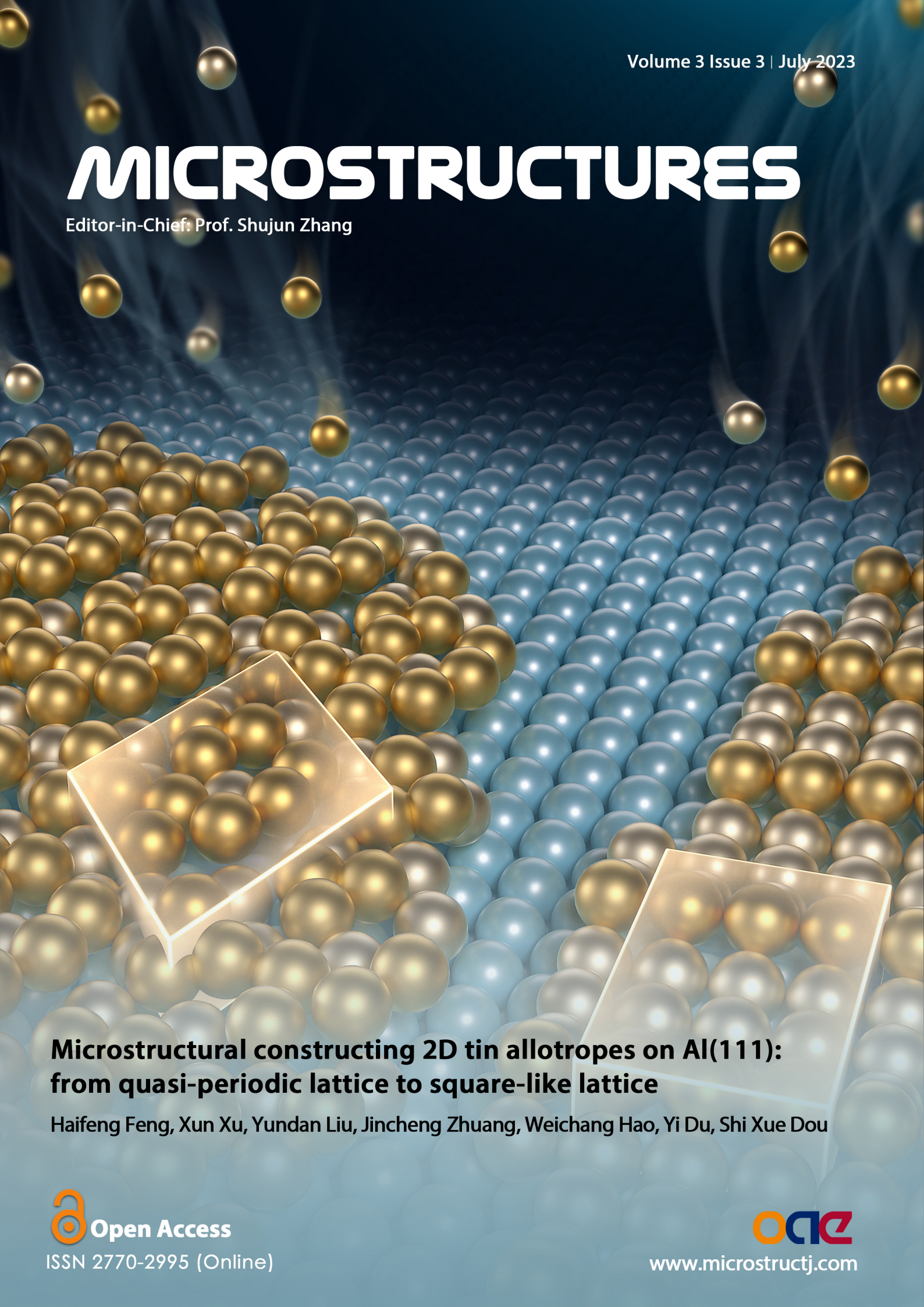

Microstructural constructing 2D tin allotropes on Al(111): from quasi-periodic lattice to square-like lattice

Haifeng Feng, Xun Xu, Yundan Liu, Jincheng Zhuang, Weichang Hao, Yi Du, Shi Xue Dou

Open Access
ISSN 2770-2995 (Online)
www.microstructj.com

EDITORIAL BOARD

GENERAL INFORMATION

About the Journal

Microstructures, ISSN 2770-2995 (Online), is a peer-reviewed and continuously published online journal with print on demand compilation of articles published. The journal's full text is available online at www.jcmtjournal.com. The journal allows free access (Open Access) to its contents and permits authors to self-archive final accepted version of Microstructure, which is the nature, quantity and distribution of structural elements or phases that make up materials, determines the properties of materials. Understanding microstructure-properties relationships is critical for the design of materials. With the increase of demand and investment in new materials around the globe, there has been a great deal of interest in the exploration and manipulation of microstructure in materials science and engineering.

Information for Authors

Manuscripts should be prepared in accordance with Author Instructions.
Please check www.microstructj.com/pages/view/author_instructions for details.
All manuscripts should be submitted online at https://oaemesas.com/login?JournalId=microstructures.

Copyright

Permissions

For information on how to request permissions to reproduce articles/information from this journal, please visit www.microstructj.com.

Disclaimer

The information and opinions presented in the journal reflect the views of the authors and not of the journal or its Editorial Board or the Publisher. Publication does not constitute endorsement by the journal. Neither the *Microstructures* nor its publishers nor anyone else involved in creating, producing or delivering the *Microstructures* or the materials contained therein, assumes any liability or responsibility for the accuracy, completeness, or usefulness of any information provided in the *Microstructures*, nor shall they be liable for any direct, indirect, incidental, special, consequential or punitive damages arising out of the use of the *Microstructures*. The *Microstructures*, nor its publishers, nor any other party involved in the preparation of material contained in the *Microstructures* represents or warrants that the information contained herein is in every respect accurate or complete, and they are not responsible for any errors or omissions or for the results obtained from the use of such material. Readers are encouraged to confirm the information contained herein with other sources.

Publisher

OAE Publishing Inc.
245 E Main Street st112, Alhambra, CA 91801, USA
Website: www.oaepublish.com

Contacts

E-mail: editorialoffice@microstructj.com
Website: www.microstructj.com

Microstructures

CONTENTS

Volume 3 / Issue 3 / July 2023 /

Xu *et al. Microstructures* 2023;3:2023015
DOI: 10.20517/microstructures.2022.40

Microstructures

Research Article

Open Access

Check for updates

Novel casting CoCrNiAl eutectic high entropy alloys with high strength and good ductility

Ning Xu, Yubo Huang, Yuxian Cao, Shilei Li, Yan-dong Wang

Beijing Advanced Innovation Center for Materials Genome Engineering, State Key Laboratory for Advanced Metals and Materials, University of Science and Technology Beijing, Beijing 100083, China.

Correspondence to: Prof. Shilei Li, Beijing Advanced Innovation Center for Materials Genome Engineering, State Key Laboratory for Advanced Metals and Materials, University of Science and Technology Beijing, Beijing 100083, China. E-mail: lishilei@ustb.edu.cn; Prof. Yan-dong Wang, Beijing Advanced Innovation Center for Materials Genome Engineering, State Key Laboratory for Advanced Metals and Materials, University of Science and Technology Beijing, Beijing 100083, China. E-mail: ydwang@ustb.edu.cn

How to cite this article: Xu N, Huang Y, Cao Y, Li S, Wang Yd. Novel casting CoCrNiAl eutectic high entropy alloys with high strength and good ductility. *Microstructures* 2023;3:2023015. https://dx.doi.org/10.20517/microstructures.2022.40

Received: 2 Nov 2022 **First Decision:** 7 Dec 2022 **Revised:** 10 Feb 2023 **Accepted:** 14 Feb 2023 **Published:** 27 Feb 2023

Academic Editor: Huijun Li **Copy Editor:** Fangling Lan **Production Editor:** Fangling Lan

Abstract

Eutectic high-entropy alloys (EHEAs) have drawn increasing interest due to their fine castability as well as appealing properties in recent years. In this work, two bulk-casting $Co_{20-x/3}Cr_{20-x/3}Ni_{50-x/3}Al_{10+x}$ (x = 8 and 9) EHEAs with regular $L1_2$/B2 lamellar morphologies were successfully fabricated and studied. Both EHEAs show high ultimate strength of ~1200 MPa combined with good uniform ductility (> 9%). Post-deformation transmission electron microscopy results indicated a high density of dislocations and stacking faults in the $L1_2$ lamellae, while no obvious dislocation in the B2 phases. This work can broaden the optimization of composition design in EHEAs and provide useful guidance for further development of CoCrNiAl EHEAs.

Keywords: Eutectic high-entropy alloys, lamellar morphology, stacking faults, dislocations

INTRODUCTION

High entropy alloys (HEAs), which were proposed in 2004, have drawn increasing interest due to their appealing properties relative to conventional alloys consisting of one or two principal elements[1-4]. Despite alloying various principal elements, HEAs, frequently solidify into simple crystal structures, such as face-centered-cubic (FCC), body-centered-cubic (BCC) and hexagonal-close-packed (HCP) crystal structures or

their ordered types (such as $L1_2$, B2 and $D0_{19}$)[5-10]. Generally, considering the as-cast mechanical properties of HEAs, FCC-structured HEAs exhibit good ductility but relatively low strength, while BCC or HCP-structured HEAs show high strength but limited ductility[11-13]. These single mechanical properties, poor castability and composition segregation can seriously deteriorate the further engineering applications of the as-cast HEAs[14,15].

Lu *et al.* first reported the concept of eutectic high entropy alloys (EHEAs) and developed a cast $AlCoCrFeNi_{2.1}$ EHEA with alternating FCC($L1_2$)/BCC(B2) lamellar morphologies and an outstanding combination of high strength and large ductility[16]. Recently, the mechanical properties of $AlCoCrFeNi_{2.1}$ EHEA were enhanced further by thermo-mechanical processing, that is, cold rolling in multi-steps to a reduction in thickness of ~90%, followed by annealing[15,17,18]. More recently, Shi *et al.* designed a directionally solidified $Al_{19}Fe_{20}Co_{20}Ni_{41}$ EHEA with ~50% uniform tensile elongation, three times that of conventional cast EHEAs and comparable strength, which provides novel guidance in developing new structured materials with large elongation and high fracture toughness[19]. Up to now, A wide range of cast EHEAs with outstanding mechanical properties and different compositions have been reported[20-26].

In the past years, Co-Cr-Ni-Al alloys have shown latent capacities to form conventional eutectic microstructures, which can be verified by Calculation of Phase Diagrams (CALPHAD) methods[27-29]. However, the microstructures for good mechanical properties and underlying deformation mechanisms of this type of EHEA still need more investigation. We initially designed $Co_{20-x/3}Cr_{20-x/3}Ni_{50-x/3}Al_{10+x}$ to investigate the Al content on the microstructures and mechanical properties of our CoCrNiAl alloys. Surprisingly, we found that a nominal composition of $Co_{20-x/3}Cr_{20-x/3}Ni_{50-x/3}Al_{10+x}$ (x = 8 and 9) (hereinafter named 18Al and 19Al, respectively.) can form eutectic microstructures with regular $L1_2$/B2 lamellar morphologies, which is similar with the lamellar structures in most studied as-cast EHEAs[12,14,27-29]. Electron probe microanalyzers, scanning and transmission electron microscopes were adopted to character the eutectic microstructures, chemical compositions and deformation mechanisms to reveal the origin of the good properties.

MATERIALS AND METHODS

CoCrNiAl alloys were prepared using arc-melting constituent elements with a purity of > 99.9 (wt.%). These two alloys were re-melted five times to improve the chemical homogeneity under a Ti-gettered argon atmosphere. The molten alloys were then drop-cast into a water-cooled copper mold with dimensions of 10 mm × 10 mm × 60 mm. Dog-bone-shaped tensile specimens with a cross-section area of 3.0 × 0.9 mm^2 and a gauge length of 10 mm were cut from the cast ingots by electrical discharge machining. Room-temperature tensile tests were conducted in a CMT4305 universal electronic tensile testing machine with a strain rate of 1×10^{-3} s^{-1}. At least three tensile experiments were repeated to improve the reproducibility. Crystal structures of these as-cast specimens were examined by X-ray diffraction (XRD) with Cu Ka radiation (Rigaku SmartLab). The 2θ scanning was performed in the range of 20°-100° at a scanning speed of 5°/min. Thermal behaviors of the as-cast HEAs were investigated by a differential scanning calorimeter (DSC) operated in an argon atmosphere at a heating/cooling rate of 10 °C /min. Nanoindentation tests were performed at least five tests for each phase using a G200 Nano Indenter system. During each indentation test, the depth was increased from 0 nm to 100 nm over a period of 20 s, and kept constant for 10 s. The tip contact did not extend beyond each phase. The microstructures were characterized by a field emission scanning electron microscope (Carl Zeiss Supra55) equipped with an electron backscatter diffraction (EBSD) detector (Oxford Instrument), electron probe microanalyzer (EPMA, SHIMADZU, 8050G) and transmission electron microscope (TEM) (FEI Tecnai G2 F20 operated at the voltage of 200 kV). The chemical characterizations of different phases were conducted using an energy dispersive spectroscopy (EDS) system attached to a transmission electron microscope (TEM). The EBSD and EPMA specimens

were polished with a 2000-grit SiC paper, followed by electropolishing in an $HClO_4$:C_2H_6O = 1:9 solution with a direct voltage of 20 V at room temperature. TEM specimens were mechanically ground to about 50 μm thickness, punched to Φ3 mm circle sheets, and then thinned by twin-jet electro-polished using a mixture of 10% perchloric acid and 90% alcohol (vol.%) with a direct voltage of 30 V at a temperature of -18 °C.

RESULTS AND DISCUSSION

The XRD patterns of the as-cast 18Al and 19Al alloys, as shown in Figure 1A. Both 18Al and 19Al alloys have the FCC + BCC duplex phase microstructure. DSC curves of the 18Al and 19Al alloys are seen in Figure 1B. Both alloys show only one exothermic peak, confirming that 18Al and 19Al EHEAs are at the eutectic position, which can be attributed to their eutectic compositions. This phenomenon was also detected in other EHEAs, such as in $AlCoCrFeNi_{2.1}$ [12], $Nb_{0.62}Fe_{1.98}Co_{1.22}Ni_{1.00}$ [30], $CoCrFeNiTa_{0.4}$ [31], and $CoCrFeNiMo_{0.8}$ alloys[32].

Figure 2A and D show the scanning electron microscope (SEM) images of as-cast 18Al and 19Al alloys, exhibiting that the as-cast 18Al and 19Al alloys both have a typical lamellar morphology of eutectic microstructure. The electron backscatter diffraction (EBSD) inverse pole figures and phase maps of as-cast 18Al and 19Al EHEAs are seen in Figure 2B and C, Figure 2E and F, respectively. Different lamellar growth directions were observed in the adjacent FCC grains of 18Al and 19Al EHEAs [Figure 2B and E], indicating that these EHEAs possess a different lamellar arrangement in the grains with different orientations. The EBSD phase maps in Figure 2C and F show that dark and light lamellae in Figure 2A and B are FCC and BCC phases, respectively. The corresponding content of FCC and BCC phases in 18Al EHEA is about 59.2 vol.% and 40.8 vol.%. Compared with the 18Al EHEA, 19Al EHEA has a higher content of the BCC phase, and the content of the BCC phase in 19Al EHEA is about 50.4 vol.%. Moreover, wider BCC lamellae in 19Al EHEA were observed in Figure 2F. In 18Al EHEA, $L1_2$ and B2 phases with nanoindentation hardness of 5.0 ± 0.6 GPa and 6.2 ± 0.7 GPa, respectively, while in 19Al EHEA, $L1_2$ and B2 phases with nanoindentation hardness of 4.6 ± 0.5 GPa and 5.7 ± 0.9 GPa, respectively. These results are consistent with the previous research that the B2 phase is harder than the $L1_2$ phase[19].

To better understand the microstructural features of as-cast 18Al and 19 Al EHEAs, we performed transmission electron microscopy (TEM) observation equipped with energy dispersive spectroscopy (EDS). Figure 3A and D exhibit the alternating lamellae microstructure of as-cast 18Al and 19Al EHEAs, respectively. According to the selected area electron diffraction patterns (SADPs) in Figure 3B and E, the dark and light lamellar in 18Al and 19Al EHEAs are $L1_2$ and B2 phases, respectively. $L1_2$ and B2 phases can be seen as ordered modes of FCC and BCC phases. EDS maps [Figure 3C and F] and SADPs reveal that the Ll_2 lamellae in 18Al and 19Al EHEAs enriched in Co and Cr while B2 phases in 18Al and 19Al EHEAs enriched in Ni and Al but depleted in Cr and Co. We noted that the B2 phases in 18Al are not well enriched in Ni and Al, mainly due to the B2 phases being eroded away during the TEM sample preparation, as seen in Figure 3A. The average widths of the BCC lamellae in 18Al and 19Al EHEAs are ~0.3 μm and ~0.5 μm, respectively. It is widely reported in Fe, Cr contained EHEAs that it is easy to precipitate in the form of spherical particles in the B2 phases owing to the Cr element showing a limited solid solubility[14,33-35]. While we failed to observe particles in the B2 lamellar of our 18Al and 19Al EHEAs, as exhibited by the STEM images of Figure 3A and D. This phenomenon may be ascribed to the removed Fe element in our EHEAs, which is similar to other EHEA[27]. In the recently-reported $Ni_{30}Co_{30}Cr_{10}Fe_{10}Al_{18}W_2$ and $Al_{19.25}Co_{18.86}Fe_{18.36}Ni_{43.53}$ EHEAs, the orientation relationship between the $L1_2$ and B2 phases is determined to be $[011]L1_2$ // $[\bar{1}11]B2$ and $(11\bar{1})L1_2$ // $(01\bar{1})B2$, meeting the classical K-S relationship[33,36]. This semi-coherent interface is usually accompanied by a great number of lattice misfit dislocations[33,36]. During the

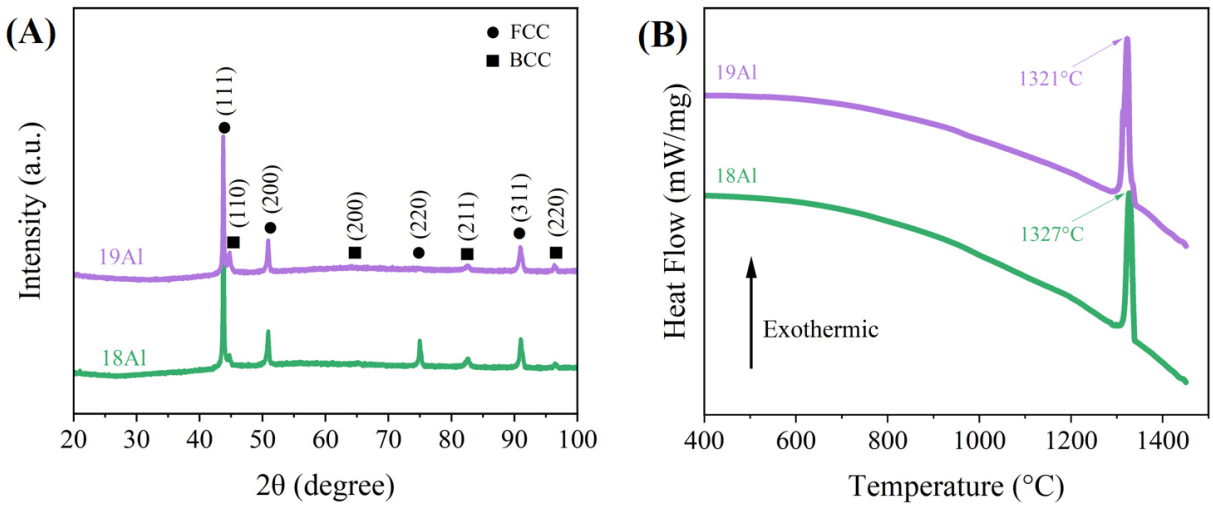

Figure 1. (A) XRD patterns of as-cast 18Al and 19Al EHEAs. (B) DSC curves of as-cast 18Al and 19Al EHEAs.

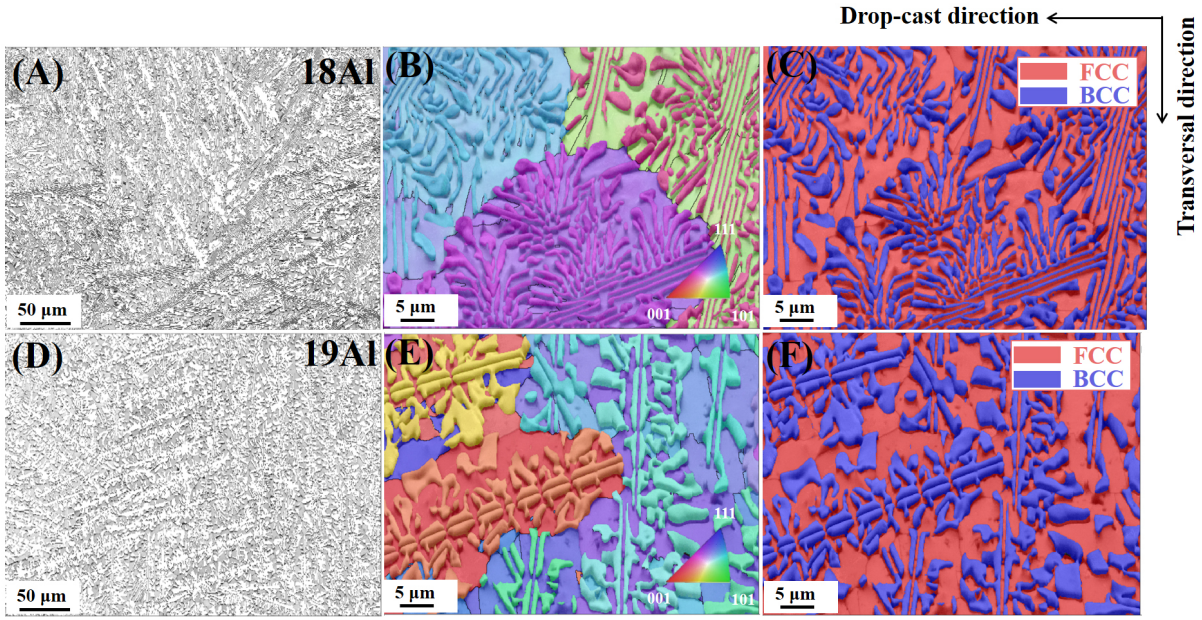

Figure 2. The microstructural features of as-cast 18Al and 19 Al EHEAs: (A-C) SEM image, inverse pole figure and phase map of 18Al EHEA; (D-F) SEM image, inverse pole figure and phase map of 19Al EHEA.

tensile deformation, this interface can block the dislocation glide further and lead to the high strength of our EHEAs.

Figure 4A displays the engineering stress-strain curves of as-cast 18Al and 19Al EHEAs tested at room temperature, exhibiting the mechanical properties including yield stress (YS), ultimate tensile strength (UTS), and total elongation (EL). The 18Al EHEA displays a yield strength of ~708 MPa, an ultimate tensile strength of ~1179 MPa, and a fracture elongation of ~0.1. The 19Al sample slightly increases the yield stress to ~734 MPa, the ultimate tensile strength to ~1219 MPa, and slightly decreases the elongation to ~0.09. 18Al and 19Al EHEAs have a high ultimate tensile strength of ~1200 MPa, which is ~ 2.3 times as strong as the as-cast $Co_{20}Cr_{20}Ni_{50}Al_{10}$ base alloy with a single-phase FCC structure. Both 18Al and 19Al EHEAs show

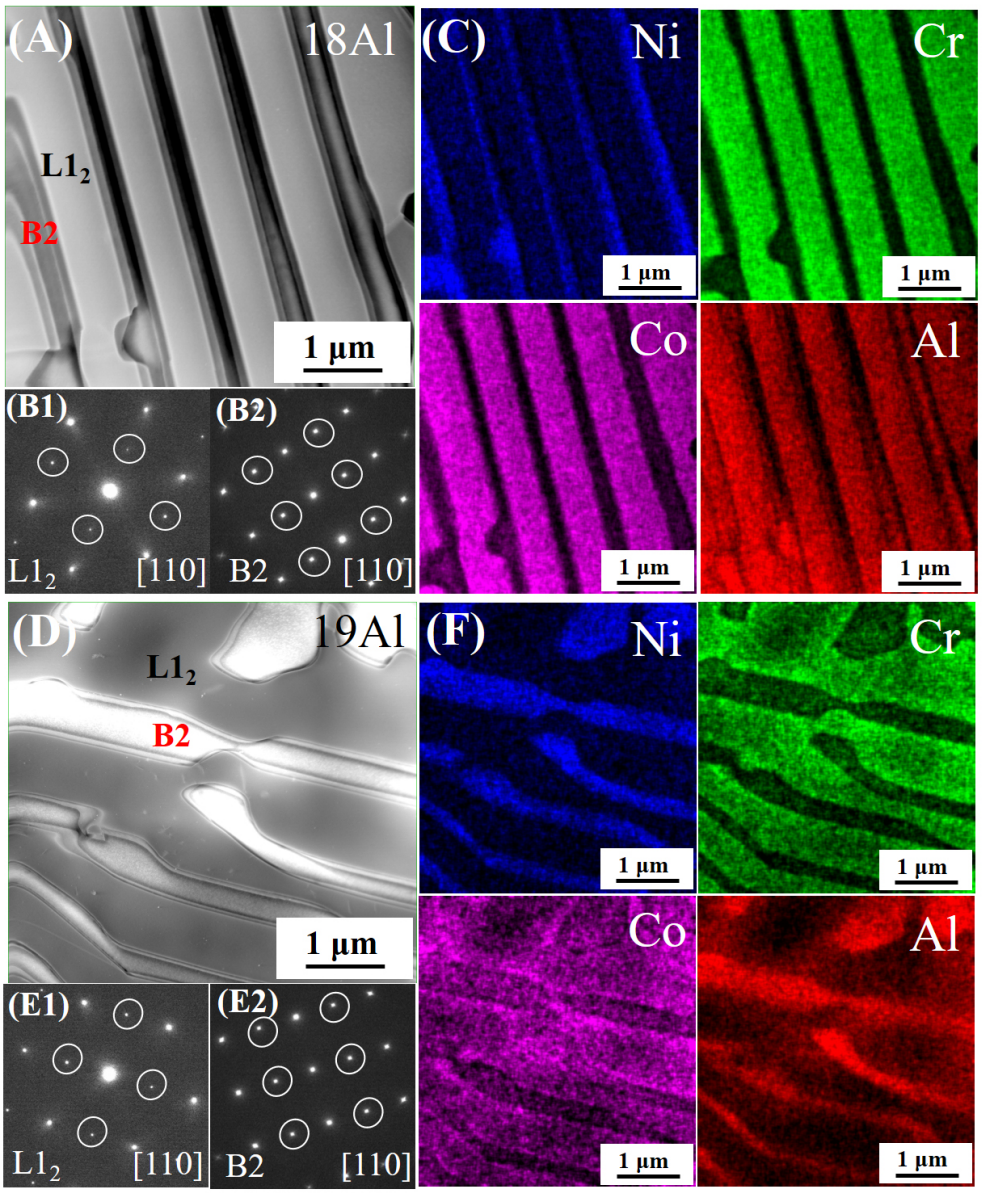

Figure 3. Scanning TEM (STEM) images showing the $L1_2$ and B2 lamellae of as-cast (A) 18Al and (D) 19Al EHEAs. Two selected-area-diffraction patterns (SADPs) of $L1_2$ and B2 lamellae in (B) 18Al and (E) 19Al EHEAs, respectively. Superlattice-diffraction spots of the $L1_2$ and B2 phases are marked by white circles. Energy-dispersive spectroscopy (EDS) maps of STEM images exhibiting the distribution of Ni, Cr, Co, Al in (C) 18Al and (F) 19Al EHEAs, respectively.

high ultimate tensile strength combined with good uniform ductility. Furthermore, little necking was detected in the stress-strain curves of two EHEAs. Figure 4B gives the strain-hardening rates of both 18Al and 19Al EHEAs. The strain-hardening rates of 18Al and 19Al EHEAs first drop quickly in region I, followed by an upturn to achieve their maximum values in region II. The strain hardening rate of 19Al EHEA is higher than that of the 18Al EHEA in this region, owing to more FCC/BCC phase boundaries that could effectively create remarkable hetero-deformation induced (HDI) hardening during the tensile deformation. The soft $L1_2$ phases will start plastic deformation first in 18Al and 19Al EHEAs, while the soft $L1_2$ phases will not be able to deform flexibly because of the deformation limit imposed by the remaining elastic B2 phases[15]. Additionally, due to the wider BCC lamellae, more geometrically necessary dislocations

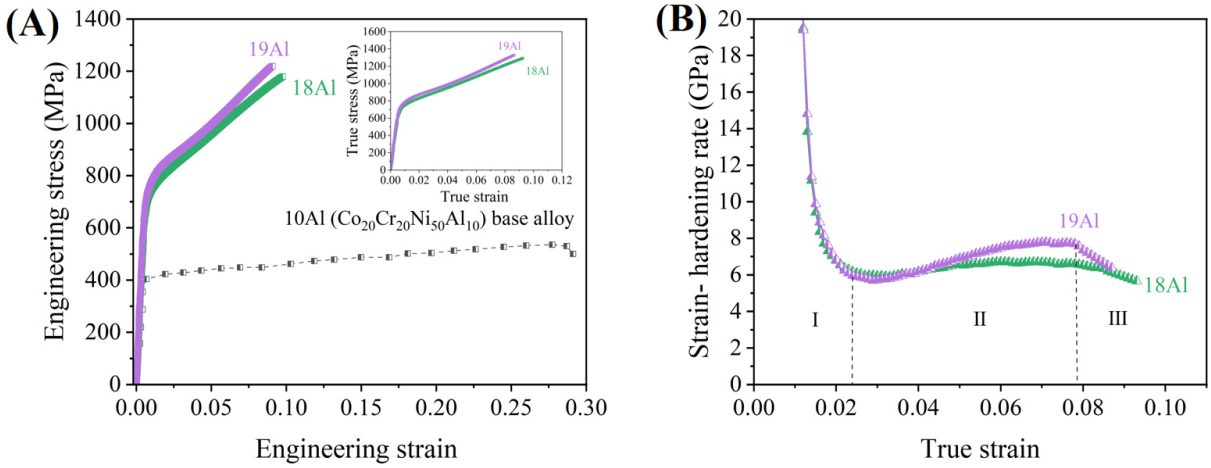

Figure 4. Mechanical responses of as-cast 18Al and 19Al EHEAs tested at room temperature. (A) The engineering stress-strain curves of 18Al and 19Al EHEAs were tested at room temperature. The inset shows the corresponding true stress-strain curve. (B) The strain hardening rate vs true strain plots of 18Al and 19Al EHEAs.

(GNDs) were prevented and piled up at FCC/BCC boundaries of 19Al in this deformation stage, resulting in larger long-range back stress in $L1_2$ phases[37-39]. The GNDs piled up at the FCC/BCC boundaries also generated forward stress in the B2 phases[37], promoting the plastic deformation of the B2 phases. When both the $L1_2$ and B2 phases were plastically deformed, the softer $L1_2$ phases would undergo larger plastic strain, leading to a heterogeneous deformation[37,38]. To accommodate the heterogeneous deformation, enough strain gradients must be present near the heterogeneous FCC/BCC surfaces, thereby producing a more remarkable HDI hardening[37] in 19Al. Finally, although the as-cast 18Al and 19Al EHEAs show an abnormal inability to sustain high strain-hardening rates over a narrow region III, they both have sufficient uniform tensile strains (> 9%).

Figure 5A and B exhibit bright-field (BF) TEM images of alternating lamellae in the ~9% strained 18Al and 19Al EHEAs. Two kinds of {111} plane traces were detected in the $L1_2$ lamellae of 18Al EHEA, as shown in Figure 5A. Figure 5B is a bright-field (BF) micrograph showing stacking faults (SFs) in the $L1_2$ lamellae of 19Al EHEA at [110] zone axis. In addition, strain-induced stacking faults were also observed in $AlCoCrFeNi_{2.1}$ EHEA[14] and additively manufactured EHEAs[40]. This scenario suggested that the stacking fault was another significant deformation type of our EHEAs besides the planar dislocation slip mentioned above in the $L1_2$ lamellae. Figure 5A and B show a high density of dislocations occurring in the $L1_2$ lamellae, while no obvious dislocations are detected in the B2 phases. In the recently-reported $AlCoCrFeNi_{2.1}$ EHEA, dislocations in the B2 lamellae can be detected in $(\bar{1}10)$ and (110) slip bands, and these dislocations could be hindered by the spherical precipitates enriched in the Cr element[14].

We investigated the fracture surfaces of 18Al and 19Al EHEAs to further reveal the damage and fracture mechanisms of the developed as-cast EHEAs at room temperature. These images of two EHEA samples in Figure 5C and D unveiled a similar fracture morphological character, namely, trench-type microstructures and several blocky phases with the cleavage character on the fracture surface[14,16,33]. More specifically, these two EHEAs both featured two types of fracture modes, i.e., brittle-type fracture in the BCC phase accompanied by a ductile fracture in the FCC phase. To better understand the blocky phases on the fracture surface of two EHEAs, we performed the EPMA analysis for the flat fracture surface of the 18Al EHEA. The EPMA images in Figure 5E reveal that the blocky phase is enriched in Ni and Al, but depleted in Co and Cr. The EPMA results indicate that blocky NiAl-rich phases are BCC precipitates. These BCC precipitates may

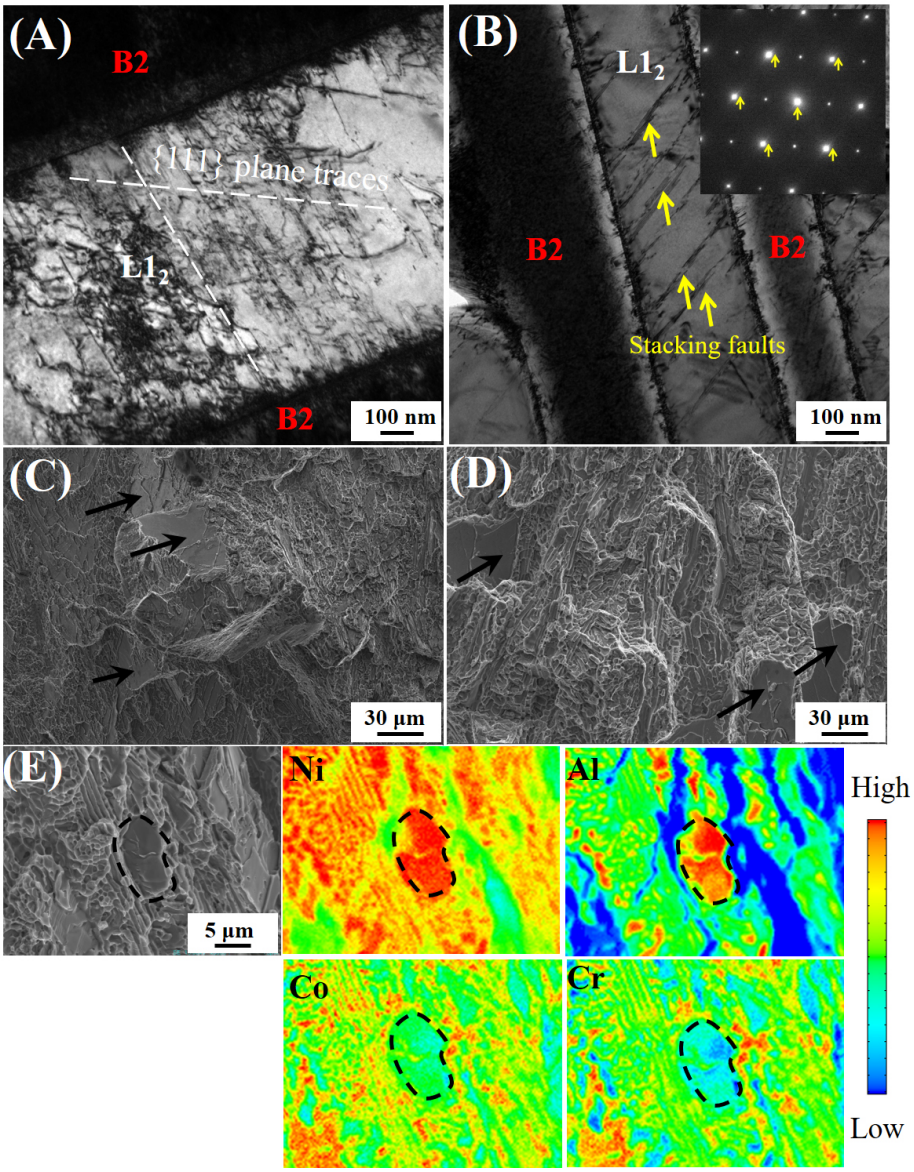

Figure 5. TEM images of alternating lamellae under the ~9% strained 18Al (A) and 19Al (B) EHEAs. The selected area electron diffraction (SAED) pattern with diffraction fringes (yellow arrows) such as trailing around diffraction spots indicates the presence of SFs. The fractography morphologies of as-cast (C) 18Al and (D) 19Al EHEAs show the mixed ductile and brittle fracture types at room temperature. Blocky phases in 18Al and 19Al EHEAs are marked by black arrows. (E) EPMA maps for the blocky phase on the fracture surface of 18Al EHEA. The blocky phase is highlighted by the black line.

be formed by a decomposition behavior, which has been detected in other EHEAs[15]. Given the blocky BCC morphology, it is reasonable to assume that the BCC particles are barely deformed while the FCC lamellae are easily stretched during the deformation. As shown in Figure 5C and D, the bright lines are stretched FCC lamellae, and the dark blocks at the bottom of the trench are BCC precipitates.

CONCLUSIONS

In summary, two novels casting CoCrNiAl EHEAs [$Co_{20-x/3}Cr_{20-x/3}Ni_{50-x/3}Al_{10+x}$ (x = 8 and 9)] composed of the $L1_2$ and B2 phases were studied. The corresponding contents of B2 phases in two EHEAs are ~40.8 vol.%

and 50.4 vol.%, respectively. The Ll_2 lamellae in two EHEAs enriched in Co and Cr, while B2 phases in two EHEAs enriched in Ni and Al but depleted in Cr and Co. Both EHEAs have a high ultimate strength of ~1200 MPa combined with good uniform ductility (> 9%). In the ~9% strained $Co_{17.33}Cr_{17.33}Ni_{47.34}Al_{18}$ and $Co_{17}Cr_{17}Ni_{47}Al_{19}$ EHEAs, a high density of dislocations as well as stacking faults in the $L1_2$ lamellar, while no obvious dislocations are detected in the B2 phases. Moreover, Trench-type microstructures and several blocky phases with the cleavage character on the fracture surface show that brittle-type fracture in the BCC phase is accompanied by a ductile fracture in the FCC phase of two EHEAs.

DECLARATIONS

Authors' contributions

Design: Xu N
Experiments: Xu N, Huang Y, Cao Y
Data analysis: Xu N, Li S
Manuscript writing: Xu N, Li S Wang Yd
Manuscript revision and supervising: Li S, Wang Yd

Availability of data and materials

Not applicable.

Financial support and sponsorship

This work was financially supported by the National Natural Science Foundation of China (NSFC) (Nos. 52171098 and 51921001), the National High-level Personnel of Special Support Program (No. ZYZZ2021001), and the Fundamental Research Funds for the Central Universities (No. FRF-BD-20-02B).

Conflicts of interest

All authors declared that there are no conflicts of interest.

Ethical approval and consent to participate

Not applicable.

Consent for publication

Not applicable.

REFERENCES

1. Cantor B, Chang ITH, Knight P, Vincent AJB. Microstructural development in equiatomic multicomponent alloys. *Mater Sci Eng A* 2004;375-7:213-8. DOI
2. Yeh JW, Chen SK, Lin SJ, et al. Nanostructured high-entropy alloys with multiple principal elements: novel alloy design concepts and outcomes. *Adv Eng Mater* 2004;6:299-303. DOI
3. Zhang Y, Zuo TT, Tang Z, et al. Microstructures and properties of high-entropy alloys. *Prog Mater Sci* 2014;61:1-93. DOI
4. George EP, Raabe D, Ritchie RO. High-entropy alloys. *Nat Rev Mater* 2019;4:515-34. DOI
5. Lei Z, Liu X, Wu Y, et al. Enhanced strength and ductility in a high-entropy alloy via ordered oxygen complexes. *Nature* 2018;563:546-50. DOI PubMed
6. Xu N, Li S, Li R, et al. In situ investigation of the deformation behaviors of $Fe_{20}Co_{30}Cr_{25}Ni_{25}$ and $Fe_{20}Co_{30}Cr_{30}Ni_{20}$ high entropy alloys by high-energy X-ray diffraction. *Mater Sci Eng A* 2020;795:139936. DOI
7. Zhou S, Liaw PK, Xue Y, Zhang Y. Temperature-dependent mechanical behavior of an $Al_{0.5}Cr_{0.9}FeNi_{2.5}V_{0.2}$ high-entropy alloy. *Appl Phys Lett* 2021;119:121902. DOI
8. Lu W, An F, Liebscher CH. Detwinning/twin growth-induced phase transformation in a metastable compositionally complex alloy. *Microstructures* 2022;2:17. DOI

9. Zhang T, Ma S, Zhao D, et al. Simultaneous enhancement of strength and ductility in a NiCoCrFe high-entropy alloy upon dynamic tension: Micromechanism and constitutive modeling. *Int J Plast* 2020;124:226-46. DOI
10. Ma Q, Yang H, Wang Z, Shi X, Liaw PK, Qiao J. High strength and ductility in partially recrystallized $Fe_{40}Mn_{20}Cr_{20}Ni_{20}$ high-entropy alloys at cryogenic temperature. *Microstructures* 2022;2:15. DOI
11. Yan X, Liaw PK, Zhang Y. Ultrastrong and ductile BCC high-entropy alloys with low-density via dislocation regulation and nanoprecipitates. *J Mater Sci Technol* 2022;110:109-16. DOI
12. Lu Y, Dong Y, Guo S, et al. A promising new class of high-temperature alloys: eutectic high-entropy alloys. *Sci Rep* 2014;4:6200. DOI PubMed PMC
13. He J, Liu W, Wang H, et al. Effects of Al addition on structural evolution and tensile properties of the FeCoNiCrMn high-entropy alloy system. *Acta Mater* 2014;62:105-13. DOI
14. Gao X, Lu Y, Zhang B, et al. Microstructural origins of high strength and high ductility in an $AlCoCrFeNi_{2.1}$ eutectic high-entropy alloy. *Acta Mater* 2017;141:59-66. DOI
15. Shi P, Ren W, Zheng T, et al. Enhanced strength-ductility synergy in ultrafine-grained eutectic high-entropy alloys by inheriting microstructural lamellae. *Nat Commun* 2019;10:489. DOI PubMed PMC
16. Lu Y, Gao X, Jiang L, et al. Directly cast bulk eutectic and near-eutectic high entropy alloys with balanced strength and ductility in a wide temperature range. *Acta Mater* 2017;124:143-50. DOI
17. Wani I, Bhattacharjee T, Sheikh S, Bhattacharjee P, Guo S, Tsuji N. Tailoring nanostructures and mechanical properties of $AlCoCrFeNi_{2.1}$ eutectic high entropy alloy using thermo-mechanical processing. *Mater Sci Eng A* 2016;675:99-109. DOI
18. Wani IS, Bhattacharjee T, Sheikh S, et al. Ultrafine-grained $AlCoCrFeNi_{2.1}$ eutectic high-entropy alloy. *Mater Res Lett* 2016;4:174-9. DOI
19. Shi P, Li R, Li Y, et al. Hierarchical crack buffering triples ductility in eutectic herringbone high-entropy alloys. *Science* 2021;373:912-8. DOI PubMed
20. Jin X, Zhou Y, Zhang L, Du X, Li B. A novel $Fe_{20}Co_{20}Ni_{41}Al_{19}$ eutectic high entropy alloy with excellent tensile properties. *Mater Lett* 2018;216:144-6. DOI
21. Huo W, Zhou H, Fang F, Xie Z, Jiang J. Microstructure and mechanical properties of $CoCrFeNiZr_x$ eutectic high-entropy alloys. *Mater Des* 2017;134:226-33. DOI
22. Jin X, Bi J, Zhang L, et al. A new $CrFeNi_2Al$ eutectic high entropy alloy system with excellent mechanical properties. *J Alloys Compd* 2019;770:655-61. DOI
23. Wang M, Lu Y, Wang T, et al. A novel bulk eutectic high-entropy alloy with outstanding as-cast specific yield strengths at elevated temperatures. *Scr Mater* 2021;204:114132. DOI
24. Jiao W, Li T, Chang X, et al. A novel Co-free $Al_{0.75}CrFeNi$ eutectic high entropy alloy with superior mechanical properties. *J Alloys Compd* 2022;902:163814. DOI
25. Lu Y, Dong Y, Jiang H, et al. Promising properties and future trend of eutectic high entropy alloys. *Scr Mater* 2020;187:202-9. DOI
26. He F, Wang Z, Cheng P, et al. Designing eutectic high entropy alloys of $CoCrFeNiNb_x$. *J Alloys Compd* 2016;656:284-9. DOI
27. Liu F, Xiao X, Huang L, Tan L, Liu Y. Design of NiCoCrAl eutectic high entropy alloys by combining machine learning with CALPHAD method. *Mater Today Commun* 2022;30:103172. DOI
28. Wu M, Wang S, Huang H, Shu D, Sun B. CALPHAD aided eutectic high-entropy alloy design. *Mater Lett* 2020;262:127175. DOI
29. Liu Q, Liu X, Fan X, et al. Designing novel AlCoCrNi eutectic high entropy alloys. *J Alloys Compd* 2022;904:163775. DOI
30. Duan D, Wu Y, Chen H, et al. A strategy to design eutectic high-entropy alloys based on binary eutectics. *J Mater Sci Technol* 2022;103:152-6. DOI
31. Jiang H, Han K, Gao X, et al. A new strategy to design eutectic high-entropy alloys using simple mixture method. *Mater Des* 2018;142:101-5. DOI
32. Yan P, Chang J, Wang W, Zhu X, Lin M, Wei B. Eutectic growth kinetics and microscopic mechanical properties of rapidly solidified $CoCrFeNiMo_{0.8}$ high entropy alloy. *Acta Mater* 2022;237:118149. DOI
33. Shi P, Li Y, Wen Y, et al. A precipitate-free AlCoFeNi eutectic high-entropy alloy with strong strain hardening. *J Mater Sci Technol* 2021;89:88-96. DOI
34. Dong Y, Yao Z, Huang X, et al. Microstructure and mechanical properties of $AlCo_xCrFeNi_{3-x}$ eutectic high-entropy-alloy system. *J Alloys Compd* 2020;823:153886. DOI
35. Shukla S, Wang T, Cotton S, Mishra RS. Hierarchical microstructure for improved fatigue properties in a eutectic high entropy alloy. *Scr Mater* 2018;156:105-9. DOI
36. Wu Q, Wang Z, Zheng T, et al. A casting eutectic high entropy alloy with superior strength-ductility combination. *Mate Lett* 2019;253:268-71. DOI
37. Zhu Y, Wu X. Perspective on hetero-deformation induced (HDI) hardening and back stress. *Mater Res Lett* 2019;7:393-8. DOI
38. Huang C, Wang Y, Ma X, et al. Interface affected zone for optimal strength and ductility in heterogeneous laminate. *Mater Today* 2018;21:713-9. DOI
39. Rizi M, Minouei H, Lee BJ, Toroghinejad MR, Hong SI. Effects of carbon and molybdenum on the nanostructural evolution and strength/ductility trade-off in $Fe_{40}Mn_{40}Co_{10}Cr_{10}$ high-entropy alloys. *J Alloys Compd* 2022;911:165108. DOI
40. Ren J, Zhang Y, Zhao D, et al. Strong yet ductile nanolamellar high-entropy alloys by additive manufacturing. *Nature* 2022;608:62-8. DOI PubMed

Feng *et al. Microstructures* 2023;3:2023017
DOI: 10.20517/microstructures.2023.01

Microstructures

Research Article

Open Access

Microstructural constructing 2D tin allotropes on Al(111): from quasi-periodic lattice to square-like lattice

Haifeng Feng[1,2], Xun Xu[3], Yundan Liu[4], Jincheng Zhuang[1,2], Weichang Hao[1,2], Yi Du[1,2], Shi Xue Dou[2,3]

[1]School of Physics, Beihang University, Beijing 100191, China.
[2]Centre of Quantum and Matter Sciences, International Research Institute for Multidisciplinary Science, Beihang University, Beijing 100191, China.
[3]Institute for Superconducting and Electronic Materials, Australian Institute for Innovative Materials, University of Wollongong, Wollongong, New South Wales 2500, Australia.
[4]School of Physics and Optoelectronics, Xiangtan University, Xiangtan 411105, Hunan, China.

Correspondence to: Prof./Dr. Yi Du, School of Physics, Beihang University, Beijing 100191, China. E-mail: yi_du@buaa.edu.cn; Dr. Haifeng Feng, School of Physics, Beihang University, Beijing 100191, China. E-mail: haifengfeng@buaa.edu.cn

How to cite this article: Feng H, Xu X, Liu Y, Zhuang J, Hao W, Du Y, Dou SX. Microstructural constructing 2D tin allotropes on Al(111): from quasi-periodic lattice to square-like lattice. *Microstructures* 2023;3:2023017. https://dx.doi.org/10.20517/microstructures.2023.01

Received: 9 Jan 2023 **Revised:** 14 Feb 2023 **Revised:** 16 Feb 2023 **Accepted:** 23 Feb 2023 **Published:** 14 Mar 2023

Academic Editor: Zibin Chen **Copy Editor:** Fangling Lan **Production Editor:** Fangling Lan

Abstract

The lattice arrangement and degree of buckling have been playing vital roles in the structure stability, bonding configuration, and electronic band structures of two-dimensional (2D) single-layer materials. Here, we fabricate two tin allotropes beyond honeycomb stanene by epitaxial growth method on Al(111). Sn-I phase with quasi-periodic lattice and Sn-II phase with square-like lattice have been identified by scanning tunneling microscopy. Combined with scanning tunneling spectroscopy, it is revealed that Sn-II phase with four-coordinate tin atoms exhibits enhanced decoupling effects due to their saturated bonds. In this study, the discovery of new lattice arrangements with well-defined atomic structures beyond honeycomb lattice provides an appealing approach to searching 2D elemental single layers and novel physical properties.

Keywords: Stanene, epitaxial growth, 2D lattice, STM

INTRODUCTION

Two-dimensional (2D) tin in honeycomb lattice, also known as stanene, has attracted enormous research attention in the field of condensed matter physics as a candidate for room temperature quantum spin Hall (QSH) insulator and recently discovered topological superconductor[1-3]. The arrangement of 2D lattice and degree of buckling have been playing vital roles in the structure stability, bonding configuration, and electronic band structures of 2D tin, as exemplified by a number of epitaxially grown stanene systems, such as planar stanene on Cu(111), strained stanene on Sb(111), and stanene Au(111)[4-12]. Aiming at either pursuing superior or new physical properties, allotropes of 2D tin beyond planar and buckled honeycomb structures have been widely predicted. 2D tin with dumbbell structure and staggered layered dumbbell structure is predicted to be a stable topological insulator and topological Dirac semimetal, respectively[13,14]. Besides, 2D tetragonal tin with repeated square and octagon rings is predicted to be a node line semimetal protected by the combination of spatial inversion and time-reversal symmetries[15]. Double-layer 2D tin with a square lattice has also been proposed to be favorable for free-standing films[16]. In contrast to the intensive theoretic exploration, experimental construction of 2D allotropes beyond honeycomb and buckled honeycomb structures, however, are rarely reported for either tin or other 2D elemental single layers[17-20], which requires subtle interaction and proper lattice-matching between the substrate and the elemental layer.

In this work, two different 2D tin allotropes with quasi-periodic lattice and square-like lattice are fabricated on Al(111) by epitaxial growth method at different tin coverages. Scanning tunneling microscopy (STM) and scanning tunneling spectroscopy (STS) studies reveal their atomic structures, electronic properties, and the degree of interaction with the substrate. We find that in the sub-monolayer region, tin overlayer prefers the quasi-periodic lattice, in which three-coordinate and four-coordinate tin atoms coexist. While at 1 monolayer (ML) and above, the quasi-periodic lattice transforms to the square-like lattice with four-coordinate tin atoms, which exhibits apparently enhanced decoupling with the substrate.

MATERIALS AND METHODS

The growth of tin on Al(111) and STM measurements were carried out in the ultra-high vacuum (>1 × 10^{-10} Torr). The Al(111) single crystal with a well-polished surface was purchased from Mateck, GmbH. The Al(111) single crystal was treated in the ultra-high vacuum condition by cycles of sputtering and annealing. The process of epitaxial growth is illustrated in Figure 1A, in which Sn atoms were evaporated from a home-made crucible onto Al(111) at 293 K. The as-grown samples were then *in-situ* transferred to STM chamber for characterization at 77 K. During the STM and STS tests, the voltage was applied to the sample. All the STM images were acquired at constant current mode. The dI/dV measurements were acquired with a lock-in technique with a sample voltage modulation of 10 mV at 937 Hz. The STM images were analyzed using WSxM software[21].

RESULTS AND DISCUSSION

Figure 1B and C show two typical surface topographies after deposition of sub-monolayer tin on Al(111) surface. The majority of islands are found on the same atomic layer of Al(111), between which an apparent boundary can be observed as indicated by the white dashed line in Figure 1B. In addition, several islands that are not adjacent to the step edges can also be found [Figure 1C]. These two types of islands turn out to show the same superstructure, as shown in Figure 1D, which exhibits hexagonal structure with a periodicity of around 1.5 nm and directions of +/- 19° with respect to Al[1$\bar{1}$0] direction. Therefore, they are assigned to be Sn-I phase. Moreover, during the scanning, the Sn-I islands can easily be scratched at extremely low sample bias, here, 5 mV, as shown in Figure 1E. The apparent height measurement along a phase I island [Figure 1C] and the scratched area [Figure 1E] are shown in Figure 1F and G, respectively, in which the same apparent height is verified for the scratched area and the lower terrace. This indicates that Sn-I islands

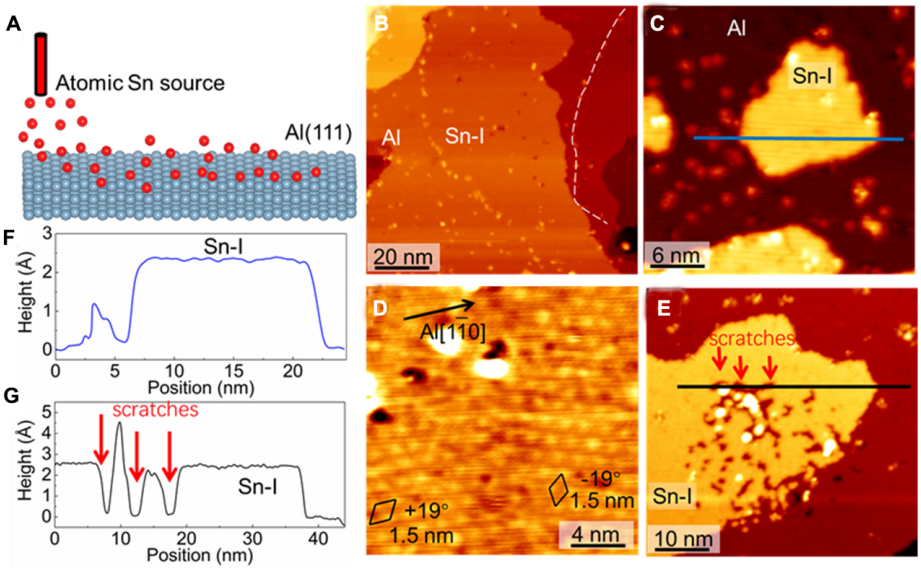

Figure 1. (A) Schematic diagram of the epitaxial growth of Sn on the surface of Al(111). (B and C) Typical scanning tunneling microscopy (STM) images of as-prepared surfaces showing the coexistence of bare substrate and sub-monolayer Sn-I phase [(2 V, 50 pA for (B) and 1 V, 50 pA for (C)]. (D) Enclosed STM image of Sn-I phase, showing two lattice directions with their unit cell marked by black rhombuses (0.5 V, 50 pA). (E) The STM image (1 V, 50 pA) of a selected area after scanning at an extremely low sample bias which induced scratches on the surface of Sn-I phase. (F and G) Height profiles along the corresponding lines in (C) (blue) and (E) (black).

are tin overlayers on the Al(111) surface and possess strong enough bond strengths between in-plane tin atoms. The formation of tin overlayer on the surface of Al(111), instead of surface alloy, is consistent with the immiscible nature between tin and Al[22].

The atomic resolution STM image of Sn-I phase is shown in Figure 2A, with the unit cell of the superstructure marked by the light blue rhombus. The superstructure and lattice direction match well with the $2\sqrt{7}a \times 2\sqrt{7}a$ $R19.1°$ of Al(111) [shortened as $2\sqrt{7}a$, a is the unit cell of Al(111)]. The superstructure is also apparent in the corresponding fast Fourier transform (FFT) image [Figure 2B and C], in which periodicities of $2\sqrt{7}a$ and $2\sqrt{7}/3a$ can be identified as marked by six light blue circles and six purple circles, respectively. These periodicities are reproduced in the inverse-FFT image of these spots [Figure 2D], indicating both translational and rotational symmetries of the lattice. The sketch of the $2\sqrt{7}a \times 2\sqrt{7}a$ structure on the Al(111) substrate is exhibited in Figure 2E. It is clear that this quasi-periodicity of $2\sqrt{7}a$ is not composed by a simple triangle or honeycomb lattice, but a complex tiling of triangle, square and pentagon lattices, as mimicked in Figure 2F. From the comparison, the $2\sqrt{7}/3a$ periodicity and their surroundings satellite spots in the inverse-FFT images can be assigned to the triangle lattices with different directions as marked in Figure 2F. In addition, a set of twelve-fold spots (green circles) can be identified in the FFT image and the corresponding inverse-FFT image [Figure 2D], which forms a dodecagon lattice. This complex superstructure of Sn-I phase can be understood as a mix of three-coordinate and four-coordinate Sn atoms in the tiling of triangle, square, and pentagon units.

The difference in the electronic properties of Sn-I and the substrate can be revealed by the bias-dependent STM images in which their height differences vary at different sample biases [Figure 3A-C]. Sn-I exhibits a decreased apparent height from 0.23 nm at 1 V to 0.21 nm at 3 V, while Al(111) shows a constant step height of 0.23 nm. In addition to the superstructure $2\sqrt{7}a$ and the Al(111) lattice, two sets of square-like lattices can be seen at the boundary area in the atomic resolution STM image [Figure 3D]. These two square-like lattices show a same lattice constant of 0.3 nm and coincident lattice directions of the

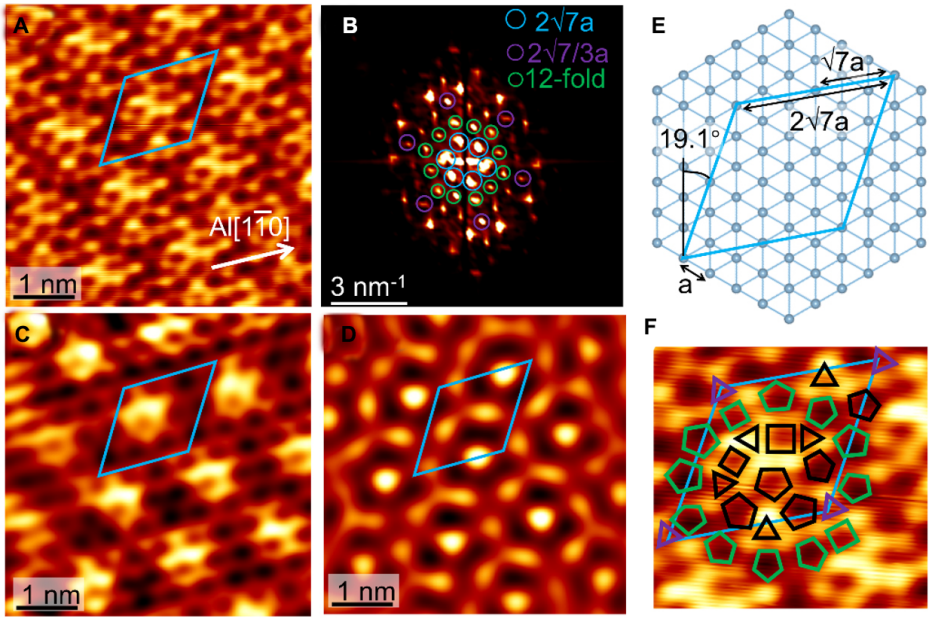

Figure 2. (A) Atomic resolution STM image of Sn-I phase with the unit cell marked by the rhombus (-50 mV, 50 pA). (B) Fast Fourier transform (FFT) image of (A) with the periodicity of 2√7*a* × 2√7*a* structure, 2√7/3*a* × 2√7/3*a* structure, and the dodecagonal periodicity (12-fold) marked by light blue, purple, and green circles. (C and D) Inverse-FFT image obtained from the 2√7*a* × 2√7*a* structure and the dodecagonal periodicity marked by light blue and green circles in (B), respectively. (E) Sketch of the 2√7*a* × 2√7*a* structure on the Al(111) substrate. (F) Sketch of the triangle-square-pentagon tiling on the surface of Sn-I phase, with the unit cell of 2√7*a* × 2√7*a* marked by the light blue rhombus and the dodecagonal periodicity marked by green shapes, respectively.

superstructure. Therefore, for these two different Sn-I phases, whether connecting with Al(111) with boundaries or not, different electronic structures are expected. However, only the variation of the spectral weight can be seen without apparent difference in the spectral features from the comparison of Sn-I and Al(111) in the dI/dV spectra [Figure 3E]. This indicates that even though Sn-Sn bonds form in Sn-I, strong orbital hybridization between tin atoms and Al atoms exists, which is very likely raised by the unsaturated electrons contributed by the large proportion of the three-coordinate tin atoms.

When the coverage of tin atoms is increased to 1 ML and above [Figure 4A], a second phase with stripe feature (Sn-II) appears on the surface covering the whole surface. With the atomic resolution STM image in Figure 4B, Sn-II phase is revealed to be square-like lattice with the lattice constant of 0.3 nm, which is the same as the atomic structure of the boundary between Sn-I phase and Al(111). Therefore, with the same lattice constant and lattice direction, Sn-II phase is thought to gradually form from Sn-I phase with increasing coverage at the boundary area. The difference is that Sn-II phase exhibits a 4 × 6 stripe structure [Figure 4B and C], whose coverage is estimated to be around 0.78 with respect to the topmost Al atomic layer. It is most likely that the stripe structure forms as a result of lattice buckling to release the lattice strain, which has been observed in other epitaxial stanene films[5-7].

Here, the square-like tin allotrope, however, is rare in the epitaxial growth elemental films on hexagonal substrates which usually exhibit hexagonal or trigonal lattice geometries. The unusual difference in geometry between the epitaxial film and substrate can be explained by the decoupling effect of increased bonding strength between tin atoms at higher tin coverage. The formation of four-coordinate bonds in the square geometry can also decrease the number of unsaturated bonds and reduce the orbital hybridization with the substrate, thereby promoting the decoupling effect. This conjecture is supported by the fact that Sn

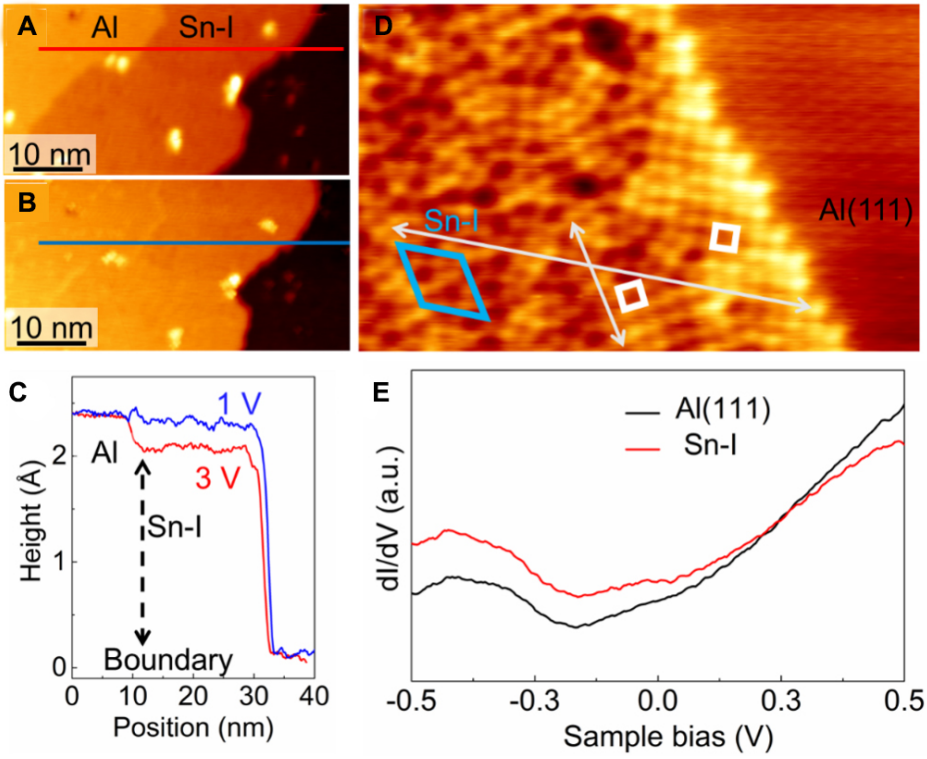

Figure 3. (A and B) STM images of a selected area with coexistence of Sn-I phase and bare substrate under different sample biases [3 V for (A) and 1 V for (B)]. (C) Height profiles along the corresponding lines in (A) (red curve) and (B) (blue curve). (D) The STM image of a boundary area between Sn-I phase and the bare substrate showing the square-like lattice at the boundary (-50 mV, 50 pA). (E) dI/dV spectra on Al(111) and Sn-I phase.

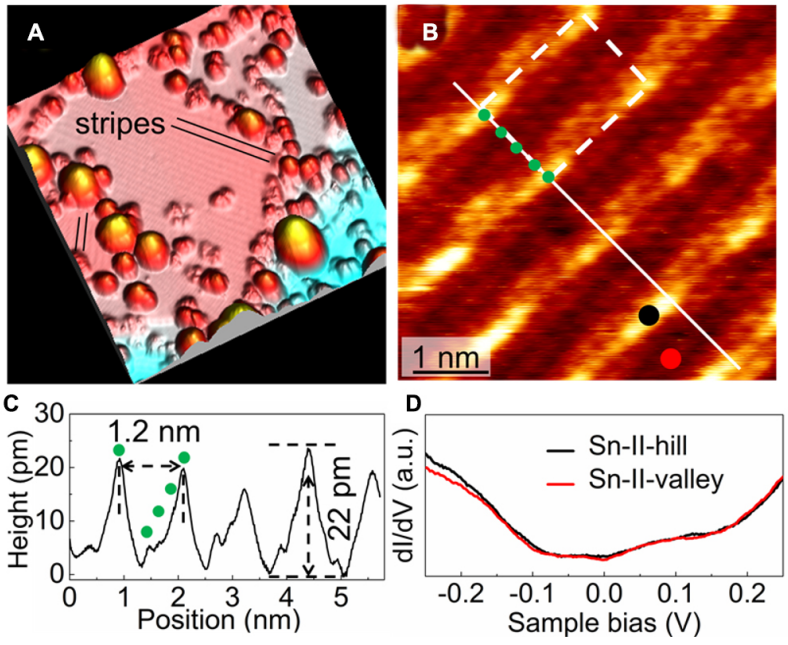

Figure 4. (A) STM image of the surface after deposition of > 1 ML Sn on Al(111) showing stripe structure (Sn-II phase) and abundant clusters on the surface (2.5 V, 50 pA, image size is 50 nm × 50 nm). (B) Atomic resolution STM image of Sn-II phase (16 mV, 900 pA). (C) Height profile along the white line in (B). (D) dI/dV spectra on the hill and valley of the stripe structure of Sn-II phase.

nanoclusters appear on the surface of Sn-II as the coverage is much higher than 1 ML [Figure 4A], which indicates that Sn-II phase is acting as a "buffer" layer that decreases the interaction between the surplus tin atoms and the substrate and enables the formation of Sn nanocluster. The dI/dV spectra on Sn-II phase [Figure 4D] show apparent depression of local density of states in the close vicinity of the Fermi level compared to Sn-I phase, which agrees with the decoupling effect.

CONCLUSIONS

In summary, two 2D tin allotropes with quasi-periodic lattice and square-like lattice are fabricated on Al(111) by epitaxial growth method at different tin coverages. Beyond sub-monolayer coverage, the enhanced decoupling effect occurs and induces a square-like lattice, which is rarely found among epitaxial elemental monolayers on metal substrates with hexagonal lattice. The presence of these two well-defined structures adds another degree of freedom to stanene and other 2D elemental monolayers beyond the honeycomb and buckled honeycomb lattices regarding the lattice symmetry design and tunning the interaction between epitaxial films and substrates.

DECLARATIONS

Authors' contributions

Made substantial contributions to conception and design of the study and performed data analysis and interpretation: Feng H, Du Y

Performed data acquisition and provided administrative, technical, and material support: Feng H, Xu X, Liu Y, Zhuang J, Hao W, Dou SX

Availability of data and materials

Not applicable.

Financial support and sponsorship

This work is supported by the National Natural Science Foundation of China (12074021, 12104033, 12004321, 12274016, 52073006), the Fundamental Research Funds for the Central Universities and Australian Research Council (LP180100722).

Conflicts of interest

All authors declared that there are no conflicts of interest.

Ethical approval and consent to participate

Not applicable.

Consent for publication

Not applicable.

REFERENCES

1. Xu Y, Yan B, Zhang HJ, et al. Large-gap quantum spin hall insulators in tin films. *Phys Rev Lett* 2013;111:136804. DOI PubMed
2. Zhu FF, Chen WJ, Xu Y, et al. Epitaxial growth of two-dimensional stanene. *Nat Mater* 2015;14:1020-5. DOI PubMed
3. Liao M, Zang Y, Guan Z, et al. Superconductivity in few-layer stanene. *Nat Phys* 2018;14:344-8. DOI
4. Deng J, Xia B, Ma X, et al. Epitaxial growth of ultraflat stanene with topological band inversion. *Nat Mater* 2018;17:1081-6. DOI PubMed
5. Gou J, Kong L, Li H, et al. Strain-induced band engineering in monolayer stanene on Sb(111). *Phys Rev Mater* 2017;1:054004. DOI

6. Liu Y, Gao N, Zhuang J, et al. Realization of strained stanene by interface engineering. *J Phys Chem Lett* 2019;10:1558-65. DOI PubMed
7. Yuhara J, Fujii Y, Nishino K, et al. Large area planar stanene epitaxially grown on Ag(111). *2D Mater* 2018;5:025002. DOI
8. Xu C, Chan Y, Chen P, et al. Gapped electronic structure of epitaxial stanene on InSb(111). *Phys Rev B* 2018;97:035122. DOI
9. Zang Y, Jiang T, Gong Y, et al. Realizing an epitaxial decorated stanene with an insulating bandgap. *Adv Funct Mater* 2018;28:1802723. DOI
10. Maniraj M, Stadtmüller B, Jungkenn D, et al. A case study for the formation of stanene on a metal surface. *Commun Phys* 2019;2:2. DOI
11. Zheng X, Zhang J, Tong B, Du R. Epitaxial growth and electronic properties of few-layer stanene on InSb(111). *2D Mater* 2020;7:011001. DOI
12. Zhao C, Li L, Zhang L, et al. Coexistence of robust edge states and superconductivity in few-layer stanene. *Phys Rev Lett* 2022;128:206802. DOI PubMed
13. Tang P, Chen P, Cao W, et al. Stable two-dimensional dumbbell stanene: a quantum spin hall insulator. *Phys Rev B* 2014;90:121408. DOI
14. Cao W, Tang P, Zhang S, Duan W, Rubio A. Stable dirac semimetal in the allotropes of group-IV elements. *Phys Rev B* 2016;93:241117. DOI
15. Xu C, Wang Y, Han R, Tu H, Yan Y. Topological node line semimetal state in two-dimensional tetragonal allotrope of Ge and Sn. *New J Phys* 2019;21:033005. DOI
16. Borlido P, Huran AW, Marques MAL, Botti S. Structural prediction of stabilized atomically thin tin layers. *NPJ 2D Mater Appl* 2019;3:1-5. DOI
17. Niu T, Zhou W, Zhou D, et al. Modulating epitaxial atomic structure of antimonene through interface design. *Adv Mater* 2019;31:e1902606. DOI PubMed
18. Zhou D, Meng Q, Si N, et al. Epitaxial growth of flat, metallic monolayer phosphorene on metal oxide. *ACS Nano* 2020;14:2385-94. DOI PubMed
19. Nevalaita J, Koskinen P. Atlas for the properties of elemental two-dimensional metals. *Phys Rev B* 2018:97. DOI
20. Zhang Z, Mannix AJ, Hu Z, et al. Substrate-induced nanoscale undulations of borophene on silver. *Nano Lett* 2016;16:6622-7. DOI PubMed
21. Horcas I, Fernández R, Gómez-Rodríguez JM, Colchero J, Gómez-Herrero J, Baro AM. WSXM: a software for scanning probe microscopy and a tool for nanotechnology. *Rev Sci Instrum* 2007;78:013705. DOI PubMed
22. Feng H, Liu C, Zhou S, et al. Experimental realization of two-dimensional buckled Lieb lattice. *Nano Lett* 2020;20:2537-43. DOI PubMed

Ying *et al. Microstructures* 2023;3:2023018
DOI: 10.20517/microstructures.2022.47

Microstructures

Research Article

Open Access

Check for updates

Formation of strong and ductile FeNiCoCrB network-structured high-entropy alloys by fluxing

Huiqiang Ying[1,#], Xiao Yang[1,#], Haiyan He[2,#], Kairui Tao[1], Zheng Guo[1], Lifeng Wang[3], Jiacheng Ge[1], Sinan Liu[1], Shu Fu[1], Yu Lou[1], Lunhua He[4,5,6], Yang Ren[7], He Zhu[1], Zhenduo Wu[8,9], Si Lan[1]

[1]Herbert Gleiter Institute of Nanoscience, School of Materials Science and Engineering, Nanjing University of Science and Technology, Nanjing 210094, Jiangsu, China.
[2]School of Physical Sciences, Great Bay University, Dongguan 523000, Guangdong, China.
[3]Nanjing Huaxing Pressure Vessel Manufacture Co., Nanjing 210000, Jiangsu, China.
[4]Beijing National Laboratory for Condensed Matter Physics, Institute of Physics, Chinese Academy of Sciences, Beijing 100190, China.
[5]Spallation Neutron Source Science Center, Dongguan 523803, Guangdong, China.
[6]Songshan Lake Materials Laboratory, Dongguan 523808, Guangdong, China.
[7]Department of Physics, City University of Hong Kong, 83 Tat Chee Avenue, Kowloon, Hong Kong, China.
[8]City University of Hong Kong (Dongguan), Dongguan 523000, Guangdong, China.
[9]Center for Neutron Scattering, City University of Hong Kong Shenzhen Research Institute, Shenzhen 518057, Guangdong, China.
[#]Authors contributed equally.

Correspondence to: Prof. Zhenduo Wu, City University of Hong Kong (Dongguan), Dongguan 523000, Guangdong, China. E-mail: zd.wu@cityu.edu.cn; Prof. Si Lan, Herbert Gleiter Institute of Nanoscience, School of Materials Science and Engineering, Nanjing University of Science and Technology, Nanjing 210094, Jiangsu, China. E-mail: lansi@njust.edu.cn

How to cite this article: Ying H, Yang X, He H, Tao K, Guo Z, Wang L, Ge J, Liu S, Fu S, Lou Y, He L, Ren Y, Zhu H, Wu Z, Lan S. Formation of strong and ductile FeNiCoCrB network-structured high-entropy alloys by fluxing. *Microstructures* 2023;3:2023018. https://dx.doi.org/10.20517/microstructures.2022.47

Received: 30 Dec 2022 **First Decision:** 31 Jan 2023 **Revised:** 22 Feb 2023 **Accepted:** 3 Mar 2023 **Published:** 24 Mar 2023

Academic Editor: Huijun Li **Copy Editor:** Fangling Lan **Production Editor:** Fangling Lan

Abstract

A series of $[(FeNiCo)_{0.85}Cr_{0.15}]_{100-x}B_x$ (x = 12, 15, 17) high-entropy alloys with network-like microstructures (N-HEAs) and a wavelength of 3-5 μm was prepared using the fluxing method. The novel N-HEAs exhibited higher strength and ductility compared with samples obtained by suction casting. Neutron diffraction and scanning electron microscopy measurements showed that the network-like structure contained soft face-centered cubic (FCC) and hard tetragonal Cr_2B-type sub-networks. The network-like structure was formed during the solidification of the molten alloy from a deeply undercooled state, achieved by removing impurities and most metallic oxides through B_2O_3 fluxing. The mechanical properties could be tuned by modifying the composition to change the volume fractions of the different sub-networks. When x decreased from 17 to 12, the compressive yield strength decreased from 1.6 to 1.1 GPa, while the compressive strain increased from ~20% to ~70%. The N-HEA samples with x = 12

and 15 also exhibited a good tensile ductility of 19% and 14%, respectively. *In situ* synchrotron X-ray diffraction results revealed an inhomogeneous deformation behavior, i.e., the soft FCC phase yielded prior to the hard Cr_2B-type phase, which bore more stress in the initial stage of the plastic deformation. In the later stage of the plastic deformation, the ductility of the sample was provided by the FCC phase, together with some contributions from the Cr_2B-type phase.

Keywords: Network-structured high-entropy alloys, neutron and X-ray diffraction, mechanical properties, fluxing method

INTRODUCTION

High-entropy alloys (HEAs) or multi-principal-element alloys are a new class of structural materials that have attracted widespread attention since their first synthesis in 2004[1-3]. The development of HEAs provided a new strategy for alloy design, leading to the discovery of new alloys with superior properties in a wide range of loading conditions[4,5]. By tuning the composition, various researchers have developed HEAs with exceptional ductility and fracture toughness at temperatures down to 20 K[6-8], as well as strong and ductile mechanical behavior from cryogenic temperatures to 1073 K[9], and excellent soft magnetic properties with high strength and ductility[10]. Moreover, the nanoscale structural design has been applied to further increase the strength and ductility of HEAs by introducing nanoscale precipitation[11], compositional modulation[12], or disordered grain boundaries[13]. However, these heterogeneous nanostructures may be unstable at elevated temperatures or difficult to fabricate in bulk sizes[14,15], which limits their industrial application. On the other hand, at a larger (i.e., sub-micron to micron) scale, the structure of the HEAs could also significantly influence their mechanical properties, as in the case of lamellar structures[16] or equiaxed grains[17]. These structures could be controlled by conventional thermal/mechanical treatments, i.e., cold/hot rolling or annealing[18-20]. Thus, developing new structures at the sub-micron to micron scale by engineering-friendly methods could be a promising way to accelerate the application of HEAs.

The fluxing technique is a widely used heat treatment method in metallurgy, in which the impurity and metallic oxide contents of the molten alloy are reduced by immersing in molten oxides[21] or salts[22] to improve its properties. This approach has been successfully applied to achieve a large undercooling of different alloy melts, in order to alter the solidification kinetics[23,24] or even form bulk metallic glasses[21]. Novel microstructures could be formed when the melt is solidified at a deeply undercooled state by fluxing, which is difficult to reach with other techniques. For example, using the B_2O_3 fluxing treatment, Fe-C and Fe-B-C alloys can be cast into an interconnected network morphology at the submicron to micron scale, showing higher strength and plasticity than white cast iron with a typical eutectic structure[25].

In this work, the B_2O_3 fluxing treatment was applied to fabricate high-entropy alloys with novel network-like microstructures (N-HEAs)[26,27]. A high degree of undercooling (385 K) was achieved for $[(FeNiCo)_{0.85}Cr_{0.15}]_{100-x}B_x$ (x = 12, 15, 17) N-HEAs with a diameter of ~13 mm. The morphology of the microstructures was inspected by scanning electron microscopy (SEM) and transmission electron microscopy (TEM), and the phase composition was studied by energy-dispersive spectroscopy (EDS) and neutron diffraction. The deformation mechanism was further investigated using *in situ* synchrotron X-ray diffraction during tension test. We also discuss the origin of the large undercooling, the relationship of the mechanical properties with the microstructures, as well as phase fractions, and the deformation mechanism.

MATERIALS AND METHODS

Sample preparation and fluxing treatment

$[(FeNiCo)_{0.85}Cr_{0.15}]_{100-x}B_x$ (x = 12, 15, 17) ingots were prepared by vacuum induction heating using pure elements (purity > 99.95 wt.%). Then, the alloy ingots were remelted at least five times under a high-purity Ti-gettered argon atmosphere in a water-cooled copper crucible; the ingots were flipped each time to improve the chemical homogeneity. After that, the alloy ingots were transferred into molten B_2O_3 and underwent fluxing treatment for 2 h at 1,473 K in a dry-cleaned fused silica tube with inner and outer diameters of 16 and 19 mm, respectively. A schematic diagram of the fluxing experiment setup is shown in Figure 1A. After the fluxing treatment, the fused silica tube was removed from the muffle furnace and cooled in air. A high-speed camera and a thermocouple[28] were used to record the cooling process of the system and the temperature history, respectively. To measure the liquidus temperature (T_L) of the samples, differential scanning calorimeter (DSC) experiments (Netzsch 404 F3) were performed under a high-purity argon atmosphere, with a cooling rate of 20 K min^{-1} from 1,500 K to 300 K.

Neutron and synchrotron X-ray diffraction experiments

Time-of-flight neutron diffraction experiments in transmission mode were carried out on the General Purpose Powder Diffractometer (GPPD) beamline at the China Spallation Neutron Source[29], with a neutron beam bandwidth and size of 4.5 Å and 40 × 20 mm, respectively. Diffraction data were collected for 2 h on each sample. The microstructure was determined by Rietveld refinement using the GSAS software[30]. *In situ* high-energy synchrotron X-ray diffraction measurements were performed at the 11-ID-C beamline of the Advanced Photon Source (APS, Argonne National Laboratory). High-energy X-rays with a wavelength of 0.01173 nm were used for data collection. The strain rate used in the *in situ* tensile test is 4×10^{-4} s^{-1}. The lattice strain ε_{hkl} was calculated as $(d_{hkl} - d^{\circ}_{hkl})/(d^{\circ}_{hkl})$, where d_{hkl} is the lattice spacing of the hkl planes, and d°_{hkl} is the corresponding value for the stress-free sample[6].

Morphology characterization and mechanical tests

The morphology and composition of the alloy were characterized using FEI Quanta 250F SEM, JSM-IT500HR SEM, and FEI Talos F200X TEM microscopes equipped with an attached X-ray EDS instrument. Cylinder-shaped compressive samples with a diameter of 3 mm and a height of 4.5 mm, as well as dog-bone-shaped tensile specimens with a gauge length of 10 mm and a thickness of 1mm were fabricated by electrical discharge machining. To obtain the tensile specimens, the spherical fluxed ingots were subjected to an additional treatment, consisting of annealing at 1,273 K for 10 h, hot rolling (with 80% thickness reduction), and annealing at 1,273 K for 10 h again. Uniaxial compressive and tensile tests were performed on a UTM4304GD testing machine with a strain rate of 1×10^{-3} s^{-1}. Hardness values were measured with a HVST-1000Z (Deka Precision Measuring Instrument) tester.

RESULTS

Measurement of degree of undercooling achieved by fluxing treatment

Figure 1B shows the solidification process of the $[(FeNiCo)_{0.85}Cr_{0.15}]_{83}B_{17}$ alloy melt immersed in molten B_2O_3. The photographs in Figure 1B display the cooling process of the molten alloy ingot. After air-cooling for 35 s 14 ms, recalescence occurred due to latent heat released during crystallization[31]. The crystallization occurred on the sample surface, and the crystal/liquid interface gradually moved across the whole sample within 5 ms. Figure 1C shows the temperature changes during the cooling process, as recorded by the thermocouple. At the beginning of the process, the sample was air-cooled with an average cooling rate of 2 K s^{-1}. The temperature increased by 135 K during recalescence, as marked by the red arrow in Figure 1C. The liquidus temperature of the $[(FeNiCo)_{0.85}Cr_{0.15}]_{83}B_{17}$ N-HEA was measured to be 1,350 K [Figure 1D]. Thus, the undercooling of the molten alloys with a diameter of approximately 13 mm could be estimated at 385 K. The DSC curves of $[(FeNiCo)_{0.85}Cr_{0.15}]_{85}B_{15}$ and $[(FeNiCo)_{0.85}Cr_{0.15}]_{88}B_{12}$ N-HEAs are also shown in

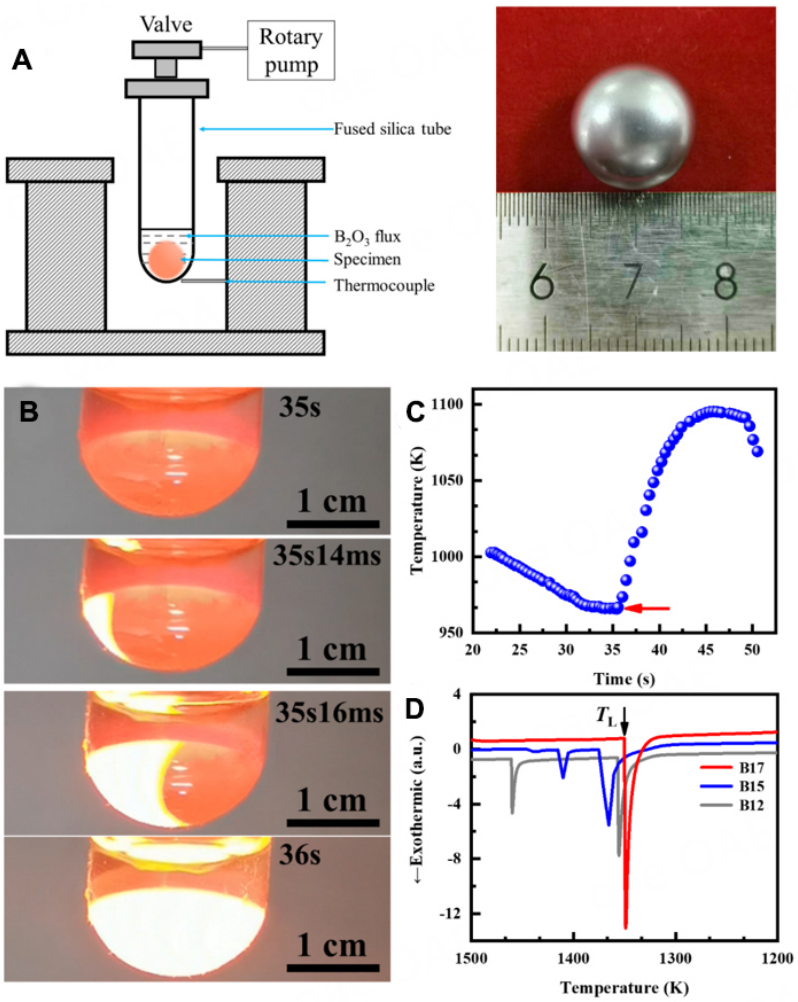

Figure 1. (A) Schematic diagram of B_2O_3 fluxing experiment setup (left). Photograph of alloy ingot showing the morphology of the specimen after fluxing (units: cm) (right). (B) Solidification process of molten alloy droplet, showing the recalescence phenomenon. (C) Cooling curve of $[(FeNiCo)_{0.85}Cr_{0.15}]_{83}B_{17}$ N-HEA melt. The red arrow indicates the occurrence of recalescence. (D) DSC curves of $[(FeNiCo)_{0.85}Cr_{0.15}]_{100-x}B_x$ (x = 12, 15, 17) N-HEAs during cooling process. The black arrow indicates the liquidus temperature of $[(FeNiCo)_{0.85}Cr_{0.15}]_{83}B_{17}$ N-HEA.

Figure 1D for comparison.

Neutron diffraction measurements and phase identification

The neutron diffraction patterns of the fluxed N-HEAs are shown in Figure 2A-C. Because of the neutron absorption of the B element, samples were polished to a thickness of ~200 μm to increase the transmittance. Vanadium boxes were used as sample holders; hence, the diffraction spectrum of the vanadium background could also be observed. Rietveld refinement of the neutron diffraction patterns revealed that the fluxed N-HEAs contained a tetragonal Cr_2B-type intermetallic phase and an FCC solid solution. The lattice parameter of the FCC solid solution was 3.5643 Å, while the parameters of the Cr_2B-type intermetallic phase were $a = b = 5.0926$ Å, $c = 4.2237$ Å, and $\alpha = \beta = \gamma = 90°$. For the sample with $x = 17$, the fraction of the Cr_2B-type phase was 61 wt.%, larger than that of the FCC phase, 39 wt.%. When the B content decreased to 12%, the fraction of Cr_2B-type phase dropped to 55 wt.%, and the FCC phase fraction increased to 45 wt.%. For the sample with $x = 15$, the phase fractions lay between the above values. Image processing based on the CAD software was employed to calculate the volume fraction of the two phases, according to the contrast

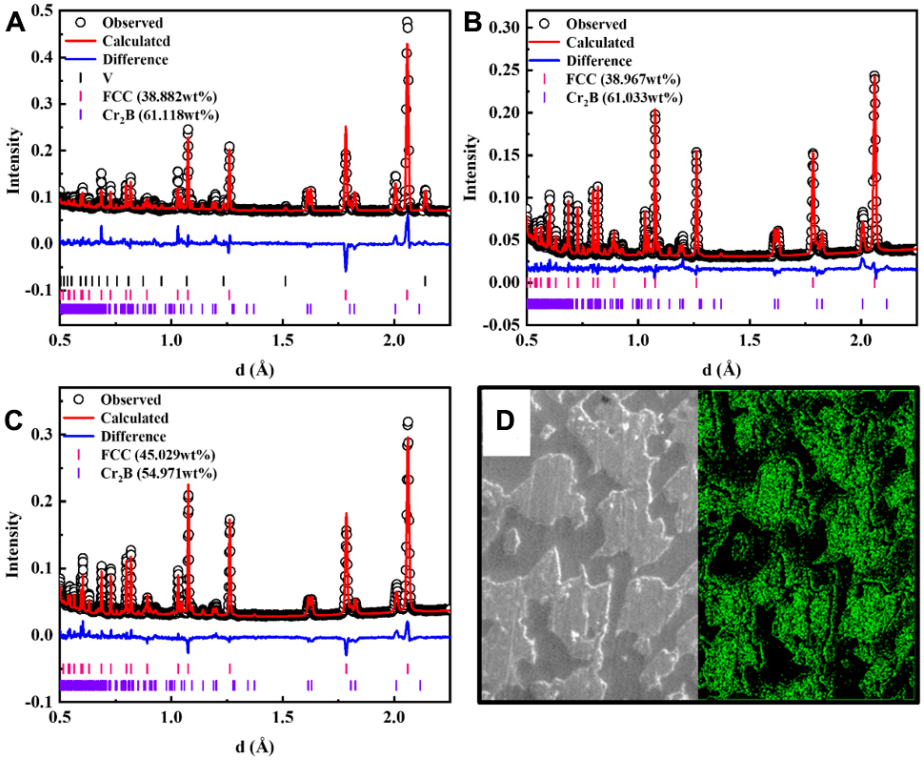

Figure 2. Neutron diffraction patterns and Rietveld refinement results of the fluxed $[(FeNiCo)_{0.85}Cr_{0.15}]_{100-x}B_x$ N-HEAs, with x = 17 (A), 15 (B), and 12 (C). (D) Illustration of image processing approach used to estimate the phase fractions; the left half shows the SEM image, and the right half displays the processed image used to calculate the phase fraction.

difference between different phases in SEM images of the samples (details of the phase identification from the SEM images are presented in Section "Network-like morphology of fluxed N-HEA samples"); the results are illustrated in Figure 2D, which is consistent with the data obtained from neutron diffraction.

Network-like morphology of fluxed N-HEA samples

Figure 3A-D show SEM images of the $[(FeNiCo)_{0.85}Cr_{0.15}]_{100-x}B_x$ (x = 12, 15, 17) N-HEAs. Figure 3A displays the SEM image of the non-fluxed suction-cast $[(FeNiCo)_{0.85}Cr_{0.15}]_{83}B_{17}$ N-HEA, showing coarse and elongated dendrites with sizes above 10 μm[32]. However, as shown in Figure 3B, the fluxed N-HEAs possessed a uniform network-like morphology, consisting of dark (zone A) and bright (zone B) sub-networks. The wavelength of the network structure was around 3-5 μm, thus smaller than the size of the dendrites in the non-fluxed sample. When the B content changed from 12% to 17%, the volume fraction of the dark phase (zone A) showed a gradual increase [Figure 3B-D]. For samples with x < 12%, the network structure may be further broken because the volume fraction of the dark phase is too small to be well interconnected.

Figure 4A and B show the elemental distributions of zones A and B determined by SEM/EDS mapping analysis of the $[(FeNiCo)_{0.85}Cr_{0.15}]_{83}B_{17}$ HEA. Zone A was found to be Cr-rich, whereas zone B was Ni-rich. Even though the non-fluxed sample had a different morphology, its elemental distribution was similar to the fluxed samples, with the brighter part containing more Ni. Because of its low atomic number, the B element is too light to be detected by EDS, and the corresponding data are not accurate in Figure 4. The results for the fluxed $[(FeNiCo)_{0.85}Cr_{0.15}]_{85}B_{15}$ and $[(FeNiCo)_{0.85}Cr_{0.15}]_{88}B_{12}$ samples were consistent with those obtained for $[(FeNiCo)_{0.85}Cr_{0.15}]_{83}B_{17}$. The TEM/EDS mapping results of the fluxed $[(FeNiCo)_{0.85}Cr_{0.15}]_{83}B_{17}$

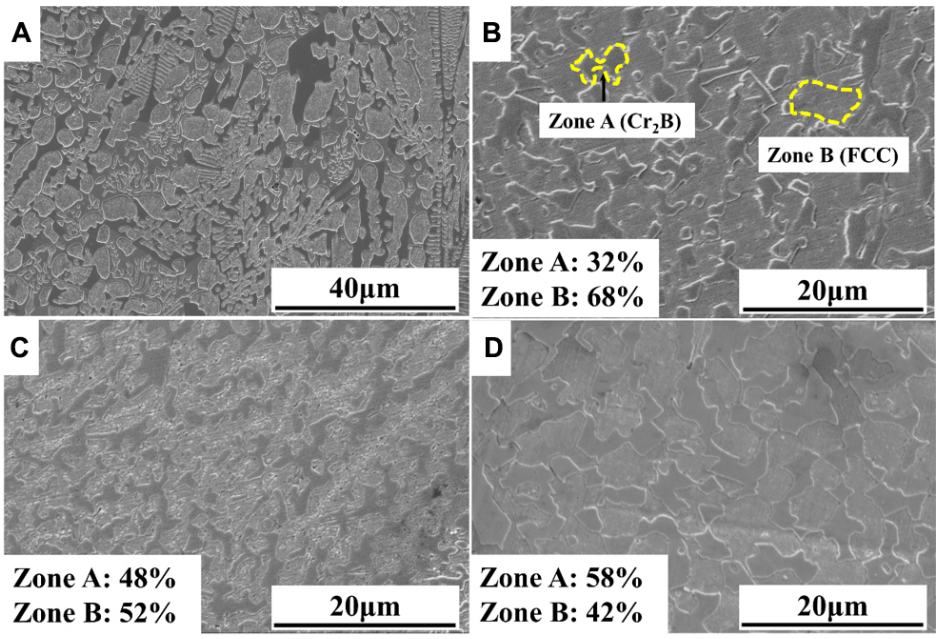

Figure 3. SEM images showing morphology of bulk $[(FeNiCo)_{0.85}Cr_{0.15}]_{100-x}B_x$ (x = 12, 15, 17) N-HEAs prepared by suction casting after arc melting for x = 17 (A), and by the fluxing method for x = 12 (B), x = 15 (C), and x = 17 (D). The phase fractions obtained by SEM image processing are superimposed in the figures for direct comparison.

sample are also shown in Figure 4C. The selected-area electron diffraction patterns displayed in the insets of the bright-field TEM image in Figure 4C show the phase information of each network. The elemental distribution of both networks was consistent with that obtained by SEM/EDS. As the TEM/EDS results may be more accurate than SEM/EDS, the compositions of zone A and zone B obtained with this approach are summarized in Table 1.

Mechanical properties of fluxed samples with different B contents

Figure 5A shows the compressive stress-strain curves of the fluxed $[(FeNiCo)_{0.85}Cr_{0.15}]_{100-x}B_x$ (x = 12, 15, 17) N-HEAs. As a reference, the figure also shows the data of the non-fluxed suction-cast $[(FeNiCo)_{0.85}Cr_{0.15}]_{83}B_{17}$ N-HEA, which exhibited a brittle fracture behavior, with an ultimate strength of 2.3 GPa. The fluxed N-HEAs, with a uniform network-like structure, showed an excellent combination of strength and plasticity. The yield strength and compressive strain of the sample with x = 17 (denoted as B17) were 1.6 GPa and 20%, respectively, whereas those of the sample with x = 12 (denoted as B12) were 1.1 GPa and > 70%, respectively. The mechanical properties of the sample with x = 15 (B15) were intermediate between those of the B17 and B12 samples. Because of its significant plasticity, the B12 sample did not break up during the compression test. In addition, the fluxed N-HEAs showed work-hardening behavior, as illustrated by the corresponding rate curves in Figure 5B. In particular, the tensile ductility of the B12 and B15 samples reached 19% and 14%, respectively [Figure 5C]. Because of the dual-phase structure and hot rolling treatment for tensile specimens, there is a tension-compression asymmetry of B12 and B15 samples. The yield strength, compressive strain, and hardness data are summarized in Figure 5D, which shows a good correlation of these parameters with the B content and volume fractions of the constituent phases.

Deformation mechanism revealed by *in situ* synchrotron X-ray diffraction

Figure 6A shows the synchrotron X-ray diffraction patterns of the $[(FeNiCo)_{0.85}Cr_{0.15}]_{88}B_{12}$ sample at different deformation stages along the loading direction. The enlarged view shows the changes in peak position and intensity, as well as the broadening of the peak profile during deformation. The lattice strains of the

Table 1. Chemical compositions of zone A and zone B estimated from TEM/EDS (at. %)

Element concentration (at. %)	Fe	Ni	Co	Cr	B
Zone A (dark region in Figure 4B)	26.47	10.33	26.87	35.08	1.25
Zone B (bright region in Figure 4B)	27.85	36.46	29.84	5.84	0.01

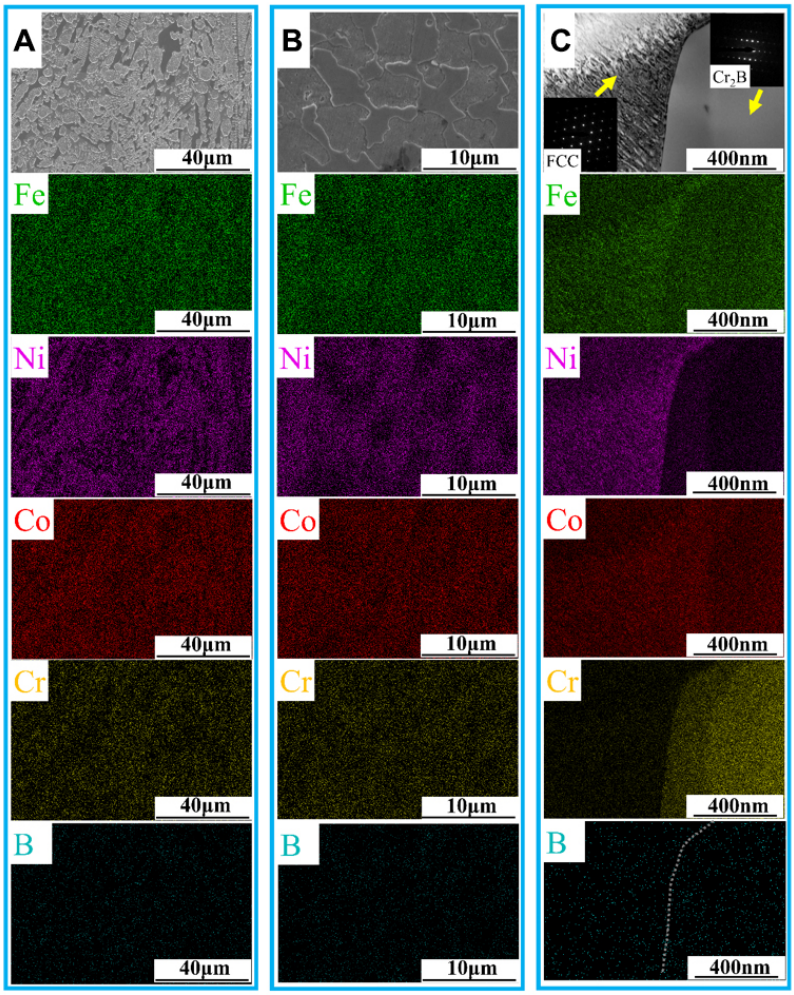

Figure 4. SEM/EDS mapping results for the non-fluxed suction-cast (A) and fluxed (B) $[(FeNiCo)_{0.85}Cr_{0.15}]_{83}B_{17}$ N-HEAs, showing Zone A (Cr_2B) is Cr-rich and Zone B (FCC) is Ni-rich. (C) TEM/EDS mapping results for the fluxed $[(FeNiCo)_{0.85}Cr_{0.15}])_{83}B_{17}$ N-HEA. The upper picture of (C) is the TEM bright field image, showing the Cr_2B grain (right part) and the FCC grain (left part with moire fringes). The insets display the selected area electron diffraction patterns of each phase. The dashed line in the B element map of (C) denotes the grain boundary.

different phases were derived from the position shifts[6] of different Bragg peaks, and the results are shown in Figure 6B. According to the yielding of the different phases, the whole deformation could be divided into three regions. In the elastic region I (below 350 MPa), the lattice strain for all orientations changes linearly with the applied stress. The different slopes are a result of elastic anisotropy[33]. For the FCC phase, the (200) grains exhibited the largest lattice strain, while the (111) and (222) ones showed the smallest values. For the Cr_2B-type phase, the (002) grains displayed the largest lattice strain, followed by the (112) and (202) planes. Table 2 summarizes the grain orientation dependence of the elastic moduli (E_{hkl}), obtained from the slope of the linear relationship of stress and strain in the elastic region. In the FCC phase, (200) and (111) were the

Table 2. Elastic moduli of different (hkl) planes in FCC and Cr_2B-type phases

FCC phase				Cr_2B-type phase		
E_{111}/GPa	E_{200}/GPa	E_{220}/GPa	E_{311}/GPa	E_{002}/GPa	E_{112}/GPa	E_{202}/GPa
244 ± 7	160 ± 4	222 ± 8	197 ± 2	168 ± 4	190 ± 4	229 ± 8

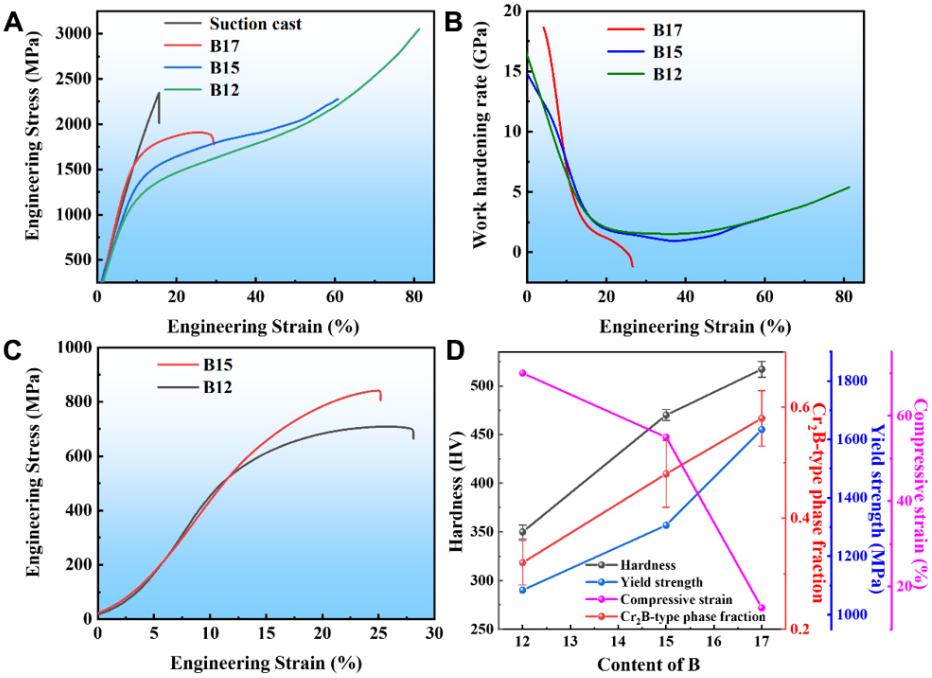

Figure 5. (A) Engineering compressive stress-strain curves of $[(FeNiCo)_{0.85}Cr_{0.15}]_{100-x}B_x$ (x = 12, 15, 17) N-HEAs. (B) Work-hardening rate curves for fluxed samples. (C) Tensile stress-strain curves of fluxed B12 and B15 samples. (D) Evolution of mechanical properties of $[(FeNiCo)_{0.85}Cr_{0.15}]_{100-x}B_x$ N-HEAs as a function of B content.

elastically softest and stiffest orientations, respectively, similar to other FCC alloys[34,35]. In the Cr_2B-type phase, the (002) orientation was more compliant compared with the (112) and (202) ones. Above 350 MPa (region II), the lattice strains for all FCC grains lost their linear relationship and stopped increasing with the applied stress, indicating that the FCC phase yielded. The plastic deformation of the soft FCC phase was constrained by the hard Cr_2B-type phase, as no macroscopic yielding could be observed. In contrast, the lattice strains of the Cr_2B-type phase increased more rapidly. When the stress increased to around 500 MPa (region III), the Cr_2B-type phase started to deform plastically, as evidenced by the deviation from the linearity of the (112) and (202) planes. Moreover, the lattice strain of the Cr_2B-type phase in regions II and III was generally larger than that of the FCC phase, showing that the Cr_2B-type phase bore more stress in the plastic regime; this indicates the existence of stress partitioning among the different phases[36,37]. Another feature worth noting is the absence of splitting between the lattice strains of the (111) and (222) planes in the FCC phase, suggesting that no stacking fault was formed during deformation[38].

The evolution of the normalized peak intensity, representing the texture development, is shown in Figure 6C for both the FCC and Cr_2B-type phases. In the case of the FCC phase, no noticeable texture was observed in region I. After yielding (regions II and III), the normalized intensity of the (111) and (222) peaks increased, while that of the (220) decreased. These intensity changes result from the characteristic texture caused by dislocation slip in FCC alloys[39-42]. Combined with the lattice strain evolution results, we

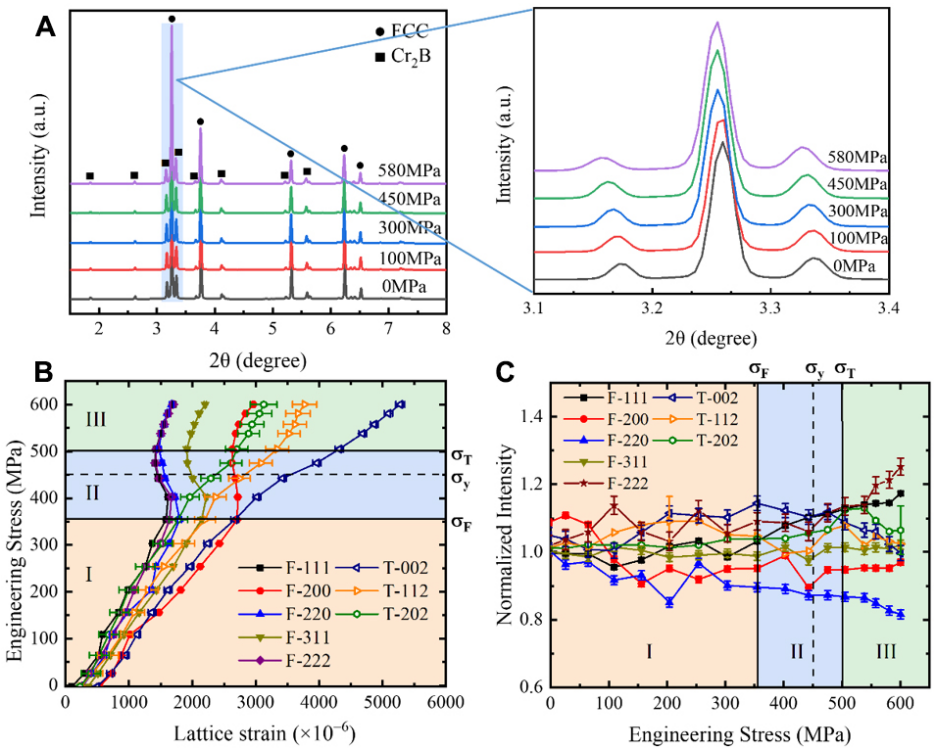

Figure 6. (A) Synchrotron X-ray diffraction patterns of $[(FeNiCo)_{0.85}Cr_{0.15}]_{88}B_{12}$ sample along the loading direction at different deformation stages. The inset shows an enlarged view of the evolution of the main peaks. (B) Relationship of lattice strain of FCC and Cr_2B-type phases with engineering stress. (C) Texture development (represented by the normalized integrated intensity of different Bragg peaks) in FCC and Cr_2B-type phases with engineering stress. For clarity, error bars are only shown for selected points on (112) and (202) reflections. F and T denote the FCC and tetragonal Cr_2B-type phases, respectively.

can conclude that dislocation slip was the main deformation mechanism for the FCC phase. However, no distinct texture was formed in the Cr_2B-type phase.

DISCUSSION

Origin of large degree of undercooling

The as-prepared fluxed N-HEAs showed high strength and ductility. One of the key requirements for forming a network-like structure at the submicron to micron scale is that the deep undercooled liquid state should be accessible before crystallization[25]. In this work, the degree of undercooling in the centimeter-sized B17 N-HEAs could reach values as high as 385 K, showing the great application potential of this alloy. The fluxing agent B_2O_3 plays an essential role in reducing the contents of impurities and surface metallic oxides in the sample, increasing the undercooling degree[21]. On the other hand, various degrees of chemical short-range order can coexist in the molten alloys, due to the complex composition of HEAs[43], which hinders crystallization during undercooling[44,45]. These two mechanisms could explain the large undercooling of the N-HEAs.

Formation of network morphology in fluxed N-HEAs

One of the possible mechanisms of network structure formation is spinodal decomposition. A liquid-state miscibility gap may exist in the undercooled liquids of metal-metalloid alloy systems (i.e., Fe-B, Fe-B-C), due to the existence of unique short-range orders in the undercooled liquids[24,28,46]. The chemical complexity of the undercooled HEA liquids studied here would facilitate the formation of short-range order[43], potentially enabling the formation of a metastable miscibility gap. Once sufficient undercooling is reached,

the HEA liquids may transform into network liquids through spinodal decomposition[47]. The solidification of the spinodal network liquids then results in the formation of a crystalline network structure. Moreover, other mechanisms may also be factors of network structure. Literature[48-50] showed that the Rayleigh instability may induce the fragmentation of dendrites during recalescence at large undercooling, resulting in a network structure. Furthermore, another factor is the entropy effect. With increasing configurational entropy, the growth morphology may transit from dendritic to faceted[51,52], leading to a structure that is different from the dendritic[32,53], lamellar[54], or equiaxed grain structures[55,56] formed through conventional casting processes. Using conventional methods, the microstructures can only be modified in the solid state by thermal/mechanical treatments to introduce precipitates, structural defects, or refinement of the as-cast grains[55,57]. The fluxing technique offers a unique route to directly develop the network structure in bulk-sized samples through the solidification of undercooled liquids, highlighting the promising potential of the fluxed N-HEAs in industrial applications.

Composition dependence of phase fractions

The present results showed that the network-like structure could be controlled by tuning the B content of the alloys. The EDS results summarized in Table 1 show little difference between the Fe and Co contents in the two phases, while the Ni and Cr contents were significantly different. The enthalpy of mixing (ΔH) between elements is summarized in Table 3[58], which shows that the absolute ΔH value between Cr and B was the largest. Thus, it is reasonable that Cr and B prefer to segregate to form intermetallic phases in one sub-network. This was also confirmed by the neutron diffraction results, which revealed the presence of Cr_2B-type intermetallic phases. As long as the Cr element is still present in the FCC solid solution, the volume fraction of Cr_2B may increase with increasing B content.

Structural origin of improved mechanical properties

As summarized in Figure 5D, the mechanical behavior is correlated with the volume fractions of the soft/ductile FCC phase and hard/brittle Cr_2B-type intermetallic phase. The samples with a lower volume fraction of hard/brittle Cr_2B intermetallic phase exhibit a lower hardness and yield strength but a higher compressive strain. *In situ* synchrotron X-ray diffraction measurements of the tensile behavior of the B12 alloy revealed a three-stage deformation process, with the ductile FCC phase yielding earlier, and the hard Cr_2B-type intermetallic phase yielding later than the macroscopic yielding in the plastic region. The whole deformation is inhomogeneous, indicating that the deformation is accommodated between the two phases, maintaining the plastic compatibility. This heterogeneous deformation has also been observed in austenite-ferrite dual-phase steels[59,60]. The Cr_2B-type intermetallic phase bears more stress after yielding, as evidenced by the larger lattice strain. Similar to multiphase steel, where the hard phases bearing more stress ensure a sufficient work-hardening capability[37], the hard Cr_2B-type phase in the B12 alloy may contribute to a strain-hardening effect and an excellent combination of strength and ductility. Moreover, the FCC phase also has high work hardening ability due to the multiple slip systems as well as other deformation mechanisms such as stacking fault, twinning and phase transformation[6,39]. In this study, dislocations could be observed, as revealed by the increasing trend of F-111 and F-222 intensity in the plastic region, and no evidence of the involving stacking faults and phase transformation could be found from the synchrotron experiments. Further investigation is needed to explain the work-hardening effect of the FCC phase at a large strain.

In addition, although our *in situ* loaded sample only deformed to several percent, a tiny increase of lattice strain in the FCC phase after 500 MPa could be observed, which means that stress was partitioned with the FCC phase[61]. A previous study of austenite-martensite dual-phase steel attributed the improved ductility to stress transfer from the hard to the soft phase, forcing the two phases to deform together[33]. The cooperative deformation, as well as stress partitioning, could inhibit the strain localization and thus delay

Table 3. ΔH values (kJ/mol) between elements calculated by Miedema's model[58]

Elements	Fe	Ni	Co	Cr	B
Fe	/	-2	-1	-1	-26
Ni	-2	/	0	-7	-24
Co	-1	0	/	-4	-24
Cr	-1	-7	-4	/	-31
B	-26	-24	-24	-31	/

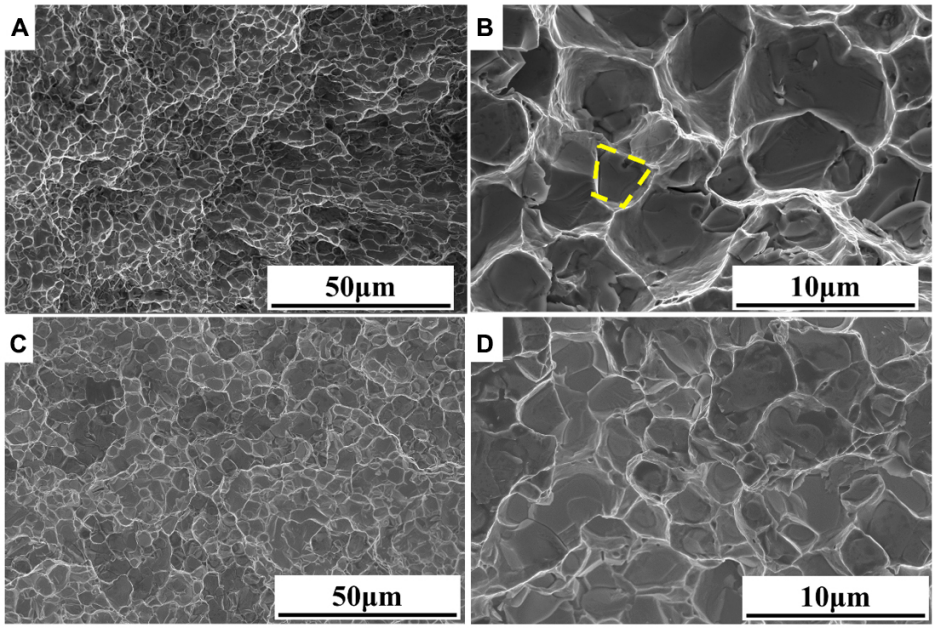

Figure 7. Fracture surface of B12 (A and B) and B15 (C and D) tensile samples, displayed at different magnifications.

the crack activation. Similar to this phenomenon, the enhanced combination of strength and ductility in the B12 alloy can be correlated to the dual-phase structure, where the hard Cr_2B-type intermetallic phase and the soft FCC phase deform synergically.

Figure 7 shows SEM images of the fracture surface of B12 obtained after the tensile test (the fracture surface of the B15 sample, i.e., Figure 7C and D, is similar). As shown in Figure 7A, the fracture surface contained uniformly distributed dimples, a typical fracture morphology for ductile samples[62]. The size of the dimples was about 3-5 μm, similar to the wavelength of a network structure. Furthermore, no large micro-voids were found on the fracture surfaces. Previous studies showed that 304 L austenitic stainless steels[63] and CrFeCoNi HEAs[62] with small-size dimples had high ductility. Our results indicate that the soft FCC phase may participate in the deformation process in stages involving large plastic deformations, contributing to improved ductility. The enlarged view of the fracture surface [Figure 7B] also displays some fracture patterns with sharp angles (marked by yellow lines), similar to the intergranular fracture surface of brittle samples[64]. This may be attributed to the deformation of the Cr_2B-type phase.

CONCLUSION

In this work, a series of $[(FeNiCo)_{0.85}Cr_{0.15}]_{100-x}B_x$ (x = 12, 15, 17) N-HEAs combining high strength and plasticity were successfully synthesized by the B_2O_3 fluxing technique. We used a set of advanced

characterization techniques to understand the structure and properties of these alloys. The conclusions are summarized below:

(1) The B_2O_3 fluxing treatment achieved a large degree of undercooling (385 K) of the centimeter-size N-HEAs alloy melts.

(2) The fluxed N-HEAs had a network-like structure with a wavelength of 3-5 μm; one sub-network consisted of a hard Cr_2B-type intermetallic phase, while the other was a soft FCC solid solution.

(3) The volume fraction of the two sub-networks could be tailored by varying the B concentration, resulting in a gradual change in the yield strength and compressive strain of the N-HEAs. When the B content decreased from 17% to 12%, the yield strength decreased from 1.6 to 1.1 GPa and the compressive strain increased from 20% to 70%.

(4) N-HEAs with B contents of 12% and 15% further exhibited a good tensile ductility of 19% and 14%, respectively. The *in situ* synchrotron X-ray diffraction analysis of the tensile behavior demonstrated that the whole deformation process could be divided into three regions based on the lattice strain evolution. This heterogeneous deformation originated from the strength difference between the two phases. Dynamic stress partitioning between the soft FCC phase and the hard Cr_2B-type intermetallic phases induced a cooperative deformation, which improved the ductility.

This work provides an industry-friendly route to fabricate N-HEAs with superior and controllable mechanical properties. Moreover, microalloying and thermal/mechanical treatment could be employed to further develop fluxed N-HEAs with excellent strength and ductility.

DECLARATIONS

Acknowledgements

We acknowledge Ms. Weixia Dong for her help in DSC measurements. This research used the resources of the Advanced Photon Source, a US Department of Energy (DOE) Office of Science User Facility operated for the DOE Office of Science by Argonne National Laboratory (No. DE-AC02-06CH11357). We acknowledge the support of the GPPD beamline of China Spallation Neutron Source (CSNS) in providing neutron diffraction research facilities.

Authors' contributions

Design: Lan S, Wu Z
Experiments and data collection: Yang X, Tao K, Guo Z, Wang L, Fu S, Lou Y, Ren Y, He L
Data analysis: Ying H, He H, Liu S, Ge J, Zhu H
Manuscript writing: Ying H, He H, Lan S, Wu Z
Manuscript revision and supervising: Lan S, Wu Z
All authors have read and agreed to the published version of the manuscript.

Availability of data and materials

The data that support the findings of this study are available from the corresponding author upon reasonable request.

Financial support and sponsorship

This work was financially supported by the National Key R&D Program of China (No. 2021YFB3802800), the National Natural Science Foundation of China (Nos. 51871120, 52222104, 52201190, and 12261160364), the Natural Science Foundation of Jiangsu Province (No. BK20200019), and Shenzhen Fundamental Research Program (No. JCYJ20200109105618137). Z.-D. Wu and S. Lan acknowledge the support of the Guangdong-Hong Kong-Macao Joint Laboratory for Neutron Scattering Science and Technology.

Conflicts of interest

All authors declared that there are no conflicts of interest.

Ethical approval and consent to participate

Not applicable.

REFERENCES

1. Zhang Y, Zuo TT, Tang Z, et al. Microstructures and properties of high-entropy alloys. *Prog Mater Sci* 2014;61:1-93. DOI
2. Yeh J, Chen S, Lin S, et al. Nanostructured high-entropy alloys with multiple principal elements: novel alloy design concepts and outcomes. *Adv Eng Mater* 2004;6:299-303. DOI
3. Cantor B, Chang I, Knight P, Vincent A. Microstructural development in equiatomic multicomponent alloys. *Mater Sci Eng A* 2004;375-377:213-8. DOI
4. Ye Y, Wang Q, Lu J, Liu C, Yang Y. High-entropy alloy: challenges and prospects. *Mater Today* 2016;19:349-62. DOI
5. George EP, Raabe D, Ritchie RO. High-entropy alloys. *Nat Rev Mater* 2019;4:515-34. DOI
6. Naeem M, He H, Zhang F, et al. Cooperative deformation in high-entropy alloys at ultralow temperatures. *Sci Adv* 2020;6:eaax4002. DOI PubMed PMC
7. Liu D, Yu Q, Kabra S, et al. Exceptional fracture toughness of CrCoNi-based medium- and high-entropy alloys at 20 kelvin. *Science* 2022;378:978-83. DOI PubMed
8. Gludovatz B, Hohenwarter A, Catoor D, Chang EH, George EP, Ritchie RO. A fracture-resistant high-entropy alloy for cryogenic applications. *Science* 2014;345:1153-8. DOI PubMed
9. Zhang C, Yu Q, Tang YT, et al. Strong and ductile FeNiCoAl-based high-entropy alloys for cryogenic to elevated temperature multifunctional applications. *Acta Mater* 2023;242:118449. DOI
10. Han L, Maccari F, Souza Filho IR, et al. A mechanically strong and ductile soft magnet with extremely low coercivity. *Nature* 2022;608:310-6. DOI PubMed PMC
11. Yang T, Zhao YL, Tong Y, et al. Multicomponent intermetallic nanoparticles and superb mechanical behaviors of complex alloys. *Science* 2018;362:933-7. DOI PubMed
12. Ding Q, Zhang Y, Chen X, et al. Tuning element distribution, structure and properties by composition in high-entropy alloys. *Nature* 2019;574:223-7. DOI PubMed
13. Yang T, Zhao YL, Li WP, et al. Ultrahigh-strength and ductile superlattice alloys with nanoscale disordered interfaces. *Science* 2020;369:427-32. DOI PubMed
14. Zhang BB, Tang YG, Mei QS, Li XY, Lu K. Inhibiting creep in nanograined alloys with stable grain boundary networks. *Science* 2022;378:659-63. DOI PubMed
15. Wang J, Kou Z, Fu S, et al. Ultrahard BCC-AlCoCrFeNi bulk nanocrystalline high-entropy alloy formed by nanoscale diffusion-induced phase transition. *J Mater Sci Technol* 2022;115:29-39. DOI
16. Han L, Xu X, Wang L, Pyczak F, Zhou R, Liu Y. A eutectic high-entropy alloy with good high-temperature strength-plasticity balance. *Mater Res Lett* 2019;7:460-6. DOI
17. Han L, Xu X, Li Z, Liu B, Liu CT, Liu Y. A novel equiaxed eutectic high-entropy alloy with excellent mechanical properties at elevated temperatures. *Mater Res Lett* 2020;8:373-82. DOI
18. Li Z, Raabe D. Influence of compositional inhomogeneity on mechanical behavior of an interstitial dual-phase high-entropy alloy. *Mater Chem Phys* 2018;210:29-36. DOI
19. Bhattacharjee P, Sathiaraj G, Zaid M, et al. Microstructure and texture evolution during annealing of equiatomic CoCrFeMnNi high-entropy alloy. *J Alloys Compd* 2014;587:544-52. DOI
20. Zhang K, Fu Z, Zhang J, et al. Annealing on the structure and properties evolution of the CoCrFeNiCuAl high-entropy alloy. *J Alloys Compd* 2010;502:295-9. DOI
21. Kui HW, Greer AL, Turnbull D. Formation of bulk metallic glass by fluxing. *Appl Phys Lett* 1984;45:615-6. DOI

22. Utigard TA. The properties and uses of fluxes in molten aluminum processing. *JOM* 1998;50:38-43. DOI
23. Lau C, Kui H. Microstructures of undercooled germanium. *Acta Metall Mater* 1991;39:323-7. DOI
24. Ho C, Leung C, Yip Y, Mok S, Kui H. Ductile $Fe_{83}C_{17}$ alloys of ultrafine networklike microstructure. *Metall Mat Trans A* 2010;41:3443-51. DOI
25. Ho CM, Kui HW. Ductile and high strength white cast iron of ultrafine interconnected network morphology. *Metall Mat Trans A* 2011;42:3826-37. DOI
26. Lu Y, Dong Y, Guo S, et al. A promising new class of high-temperature alloys: eutectic high-entropy alloys. *Sci Rep* 2014;4:6200. DOI
27. Gao X, Lu Y, Zhang B, et al. Microstructural origins of high strength and high ductility in an $AlCoCrFeNi_{2.1}$ eutectic high-entropy alloy. *Acta Mater* 2017;141:59-66. DOI
28. Wu Z, Lu X, Wu Z, Kui H. Spinodal decomposition in $Pd_{41.25}Ni_{41.25}P_{17.5}$ bulk metallic glasses. *J Non Cryst Solids* 2014;385:40-6. DOI
29. Chen J, Kang L, Lu H, Luo P, Wang F, He L. The general purpose powder diffractometer at CSNS. *Phys Rev B Condens Matter* 2018;551:370-2. DOI
30. Allen C. Larson RBVD. General structure analysis system (GSAS) report LAUR 86-748. Los Alamos national laboratory. 2004. Available from: https://11bm.xray.aps.anl.gov/documents/GSASManual.pdf [Last accessed on 22 March 2023].
31. Lan S, Blodgett M, Kelton KF, Ma JL, Fan J, Wang X. Structural crossover in a supercooled metallic liquid and the link to a liquid-to-liquid phase transition. *Appl Phys Lett* 2016;108:211907. DOI
32. Wu X, Wang B, Rehm C, et al. Ultra-small-angle neutron scattering study on temperature-dependent precipitate evolution in $CoCrFeNiMo_{0.3}$ high entropy alloy. *Acta Mater* 2022;222:117446. DOI
33. Xu S, Li J, Cui Y, et al. Mechanical properties and deformation mechanisms of a novel austenite-martensite dual phase steel. *Int J Plast* 2020;128:102677. DOI
34. Clausen B, Lorentzen T, Bourke MA, Daymond MR. Lattice strain evolution during uniaxial tensile loading of stainless steel. *Mater Sci Eng A* 1999;259:17-24. DOI
35. Pang J, Holden T, Wright J, Mason T. The generation of intergranular strains in 309H stainless steel under uniaxial loading. *Acta Mater* 2000;48:1131-40. DOI
36. Ma L, Wang L, Nie Z, et al. Reversible deformation-induced martensitic transformation in $Al_{0.6}CoCrFeNi$ high-entropy alloy investigated by *in situ* synchrotron-based high-energy X-ray diffraction. *Acta Mater* 2017;128:12-21. DOI
37. Fu B, Yang W, Wang Y, Li L, Sun Z, Ren Y. Micromechanical behavior of TRIP-assisted multiphase steels studied with *in situ* high-energy X-ray diffraction. *Acta Mater* 2014;76:342-54. DOI
38. Warren BE. X-ray diffraction. Courier Corporation; 1990. Available from: https://scholar.google.com/scholar?cluster=15231993657912304740&hl=zh-TW&as_sdt=0,5 [Last accessed on 22 March 2023].
39. He H, Naeem M, Zhang F, et al. Stacking fault driven phase transformation in CrCoNi medium entropy alloy. *Nano Lett* 2021;21:1419-26. DOI PubMed
40. Taylor GI. Plastic strain in metals. Available from: https://cir.nii.ac.jp/crid/1573105974372618880 [Last accessed on 22 March 2023].
41. Cheng S, Stoica AD, Wang XL, et al. Deformation crossover: from nano- to mesoscale. *Phys Rev Lett* 2009;103:035502. DOI PubMed
42. Wang B, He H, Naeem M, et al. Deformation of CoCrFeNi high entropy alloy at large strain. *Scr Mater* 2018;155:54-7. DOI
43. Chen X, Wang Q, Cheng Z, et al. Direct observation of chemical short-range order in a medium-entropy alloy. *Nature* 2021;592:712-6. DOI PubMed
44. Lan S, Zhu L, Wu Z, et al. A medium-range structure motif linking amorphous and crystalline states. *Nat Mater* 2021;20:1347-52. DOI
45. Lan S, Wu Z, Wei X, et al. Structure origin of a transition of classic-to-avalanche nucleation in Zr-Cu-Al bulk metallic glasses. *Acta Mater* 2018;149:108-18. DOI
46. Li Q, Kui H. Formation of bulk magnetic nanostructured $Fe_{40}Ni_{40}P_{14}B_6$ alloys by metastable liquid state phase separation. *MRS Online Proc Lib* 1999;581:277-82. DOI
47. Cahn JW. On spinodal decomposition. *Acta Metall* 1961;9:795-801. DOI
48. Nagashio K, Kuribayashi K. Growth mechanism of twin-related and twin-free facet Si dendrites. *Acta Mater* 2005;53:3021-9. DOI
49. Schwarz M, Karma A, Eckler K, Herlach DM. Physical mechanism of grain refinement in solidification of undercooled melts. *Phys Rev Lett* 1994;73:1380-3. DOI PubMed
50. Herlach DM, Simons D, Pichon PY. Crystal growth kinetics in undercooled melts of pure Ge, Si and Ge-Si alloys. *Philos Trans A Math Phys Eng Sci* 2018;376:20170205. DOI PubMed PMC
51. Jackson K. The present state of the theory of crystal growth from the melt. *J Cryst Growth* 1974;24-25:130-6. DOI
52. Cahn JW. Theory of crystal growth and interface motion in crystalline materials. *Acta Metall* 1960;8:554-62. DOI
53. Fan J, Zhang L, Yu P, et al. A novel high-entropy alloy with a dendrite-composite microstructure and remarkable compression performance. *Scr Mater* 2019;159:18-23. DOI
54. Shi P, Ren W, Zheng T, et al. Enhanced strength-ductility synergy in ultrafine-grained eutectic high-entropy alloys by inheriting microstructural lamellae. *Nat Commun* 2019;10:489. DOI PubMed PMC
55. Wu Z, Bei H, Otto F, Pharr G, George E. Recovery, recrystallization, grain growth and phase stability of a family of FCC-structured multi-component equiatomic solid solution alloys. *Intermetallics* 2014;46:131-40. DOI

56. Senkov O, Wilks G, Scott J, Miracle D. Mechanical properties of $Nb_{25}Mo_{25}Ta_{25}W_{25}$ and $V_{20}Nb_{20}Mo_{20}Ta_{20}W_{20}$ refractory high entropy alloys. *Intermetallics* 2011;19:698-706. DOI
57. Wang Z, Baker I, Guo W, Poplawsky JD. The effect of carbon on the microstructures, mechanical properties, and deformation mechanisms of thermo-mechanically treated $Fe_{40.4}Ni_{11.3}Mn_{34.8}Al_{7.5}Cr_6$ high entropy alloys. *Acta Mater* 2017;126:346-60. DOI
58. Takeuchi A, Inoue A. Classification of bulk metallic glasses by atomic size difference. *Mater Trans* 2005;46:2817-29. DOI
59. Harjo S, Tomota Y, Lukáš P, et al. *In situ* neutron diffraction study of α-γ Fe-Cr-Ni alloys under tensile deformation. *Acta Mater* 2001;49:2471-9. DOI
60. Lee S, Woo W, De Cooman BC. Analysis of the plasticity-enhancing mechanisms in 12 pctMn Austeno-ferritic steel by *in situ* neutron diffraction. *Metall Mat Trans A* 2014;45:5823-8. DOI
61. Tomota Y, Tokuda H, Adachi Y, et al. Tensile behavior of TRIP-aided multi-phase steels studied by *in situ* neutron diffraction. *Acta Mater* 2004;52:5737-45. DOI
62. Naeem M, He H, Harjo S, et al. Temperature-dependent hardening contributions in CrFeCoNi high-entropy alloy. *Acta Mater* 2021;221:117371. DOI
63. Das A, Tarafder S. Geometry of dimples and its correlation with mechanical properties in austenitic stainless steel. *Scr Mater* 2008;59:1014-7. DOI
64. Parrington RJ. Fractography of metals and plastics. *Pract Fail Anal* 2002;2:16-9. DOI

Teng *et al. Microstructures* 2023;3:2023019
DOI: 10.20517/microstructures.2023.07

Microstructures

Review

Open Access

Filled carbon-nanotube heterostructures: from synthesis to application

Yu Teng[1,2,#], Jing Li[1,#], Jian Yao[1], Lixing Kang[1], Qingwen Li[1]

[1]Advanced Materials Division, Suzhou Institute of Nano-Tech and Nano-Bionics, Chinese Academy of Sciences, Suzhou 215123, Jiangsu, China.
[2]School of Nano Science and Technology, University of Science and Technology of China, Hefei 230026, Anhui, China.
[#]Authors contributed equally.

Correspondence to: Prof. Lixing Kang, Advanced Materials Division, Suzhou Institute of Nano-Tech and Nano-Bionics, Chinese Academy of Sciences, Suzhou 215123, Jiangsu, China. E-mail: lxkang2013@sinano.ac.cn; Prof. Qingwen Li, Advanced Materials Division, Suzhou Institute of Nano-Tech and Nano-Bionics, Chinese Academy of Sciences, Suzhou 215123, Jiangsu, China. E-mail: qwli2007@sinano.ac.cn

How to cite this article: Teng Y, Li J, Yao J, Kang L, Li Q. Filled carbon-nanotube heterostructures: from synthesis to application. *Microstructures* 2023;3:2023019. https://dx.doi.org/10.20517/microstructures.2023.07

Received: 2 Feb 2023 **First Decision:** 14 Mar 2023 **Revised:** 20 Mar 2023 **Accepted:** 23 Mar 2023 **Published:** 3 Apr 2023

Academic Editor: Yang Ren **Copy Editor:** Fangling Lan **Production Editor:** Fangling Lan

Abstract

Carbon nanotubes (CNTs) have a one-dimensional (1D) hollow tubular structure formed by graphene curling with remarkable electronic, optical, mechanical, and thermal properties. Except for the applications based on their intrinsic properties, such as electronic devices, THz sensors, and conductive fiber, CNTs can also act as nano-vessels for nano-chemical reactions and hosts for encapsulating various materials to form heterostructures. In this review, we have summarized the research status on filled carbon-nanotube heterostructures from four aspects: synthesis, morphological and electronic structure analysis, potential applications, and perspective. We begin with an overview of the filling methods and mechanisms of the 1D heterostructures. Following that, we discuss their properties in terms of morphological and electronic structure. The burgeoning applications of 1D heterostructures in nano-electronic, energy, storage, catalysis, and other fields are then thoroughly overviewed. Finally, we offer a brief perspective on the possible opportunities and challenges of filled CNTs heterostructures.

Keywords: Filled carbon nanotubes heterostructures, confinement effect, morphological structure, electronic structure, applications

INTRODUCTION

CNTs have received widespread attention since they were confirmed to exist in 1991 by Japanese scientist Iijima[1] due to their one-dimensional (1D) nanostructure with remarkable electronic[2], optical[3], mechanical[4], and thermal properties[5]. Because of these characteristics, CNTs are critical for the advancement of electronics and nanoelectronics[6]. For single-walled carbon nanotubes (SWCNTs), the nanotube band structure is determined by the nanotube radius and chirality, which can be either metallic or semiconductor[7]. Using a SWCNT as the gate and molybdenum disulfide (MoS_2) as channel materials, a one-nanometer physical gate length transistor with a subthreshold swing of ~65 mV dev^{-1} at 298 K was achieved, breaking the five-nanometer-limitation of Si technology[8]. Furthermore, as separation methods for high-purity semiconductor single-walled carbon nanotube (s-SWCNT, > 99.99%)[9] have matured, high-performance high-density arrays s-SWCNT field effect transistors have been developed[10], positioning s-SWCNTs as the candidate elements for the manufacture of next-generation electronic devices.

Another intriguing feature of CNT is its unusual tubular structure with a nanometer diameter, which makes it an ideal nanoscale vessel for restricted chemical reactions[11] as well as a powerful method to control the electronic structure of CNTs by filling it with specific substances[12]. Since the feasibility of filling carbon nanotubes with guest substances was predicted in 1992, and the Pb@MWCNT was first synthesized in 1993[13], attempts to fill the CNTs with gas, liquid, and solid substances have been extensively explored. According to the aforementioned pioneering works, numerous new nanoclusters[14], nanowires[15], and nanoribbons guests[16] were observed inside CNTs, which were different from that in their bulk states[17] due to the confined space of 1D nanotube channels. To exhibit the influence of the diameter of the CNTs, SnTe nanowires, for example, were transformed from monatomic chains to curvilinear chains, hyperbolic chains, and then to 2 × 2 rock salt[18]. CNT template-assisted growth can help produce 1D materials with high aspect ratios. However, nanoscale materials are thermodynamically unstable and susceptible to degradation by air and water. Materials encapsulated within CNTs can be protected from reactions with the surrounding medium, particularly oxidation, when exposed to air. Additionally, nanoscale guest materials within CNTs can be stabilized by the strong carbon walls acting as a barrier. In a highly confined space, X@CNTs provide a new combination to strengthen and stabilize chemical elements, enabling chemically stable new crystal structures[19]. As a result, the filled carbon-nanotube heterostructures pave the way for research into confinement-stabilized nonequilibrium materials and related emergent physical phenomena.

On the other hand, the carbon nanotube's electronic band structure would be modified by the interaction between the carbon wall and the guest substance[12,20]. Synthesized SWCNT samples consist of a mixture of metallic and semiconducting nanotubes, resulting in uneven properties. Customizing the electronic properties of SWCNTs is crucial for their advanced applications. Therefore, filling CNTs to control their electronic structure is necessary. For strongly interacting heterostructure systems, allowing for electron exchange between the encapsulated electron donor or electron acceptor materials and the CNTs, which controls the electronic properties of CNTs. For instance, the electronic acceptor 1,1′-didodecyl-4,4′-bipyridinium dihexafluorophosphate (Viol) was filled into the metallic SWCNT to transit it into the semiconducting state[21]. For weakly interacting heterostructure systems, although the electron transfer is hindered, the radial vibrations of the carbon nanotubes are suppressed, causing them to deform[22]. The single CNT in discrete-filled heterostructure systems would split into a series of quantum dots[23]. Therefore, CNTs can be designed with the help of filling for particular applications, such as sensors[24], p-n junctions[25], transistors[26] and so forth.

The purpose of this manuscript is to give an overview of the state-of-the-art research on filled CNTs heterostructures, from synthesis to application. The filling methods and mechanism are covered in detail in

the Section "INTRODUCTION" of the review. The investigation of the morphological and electronic structure of filled CNTs heterostructures using transmission electron microscopy and spectroscopic techniques forms the focus of the Section "FILLING METHOD AND MECHANISM" of the review. The Section "MORPHOLOGICAL AND ELECTRONIC STRUCTURE OF FILLED CNTS HETEROSTRUCTURES" of the manuscript reviews potential applications of filled CNTs heterostructures in a different field. Finally, we put forward a view on the possible opportunities and challenges of filled CNTs heterostructures.

FILLING METHOD AND MECHANISM

Successful filling of gas, liquid, and solid materials into the hollow nanospace of the CNT is possible, and the filling methods are categorized as *in situ* (filling of CNT during their growth)[27] and *ex-situ* (filling of pre-formed CNT)[28]. The mechanism of filling materials inside CNTs is mainly due to the unique tubular structure of CNTs, which provides a sealed space for encapsulating materials inside. The diameter of CNTs can be controlled to match the size of guest molecules, thereby effectively trapping them inside. In addition, the strong van der Waals force between guest molecules and the inner wall of CNTs also helps to limit the effect and prevent molecules from diffusing outward. Depending on the properties of the filled materials, the vast majority of filled CNTs heterostructures are made using the *ex-situ* method, which primarily includes encapsulation from the gas or liquid phases, as well as sequential transformations in the cavity after pre-encapsulation. According to some studies, the adsorption effect of the lumens of carbon nanotubes is the main reason for filling the gas molecule[29]. The principle of filling liquids and solids is mainly based on capillary and wetting effects[30]. According to Young's equation and Laplace equation theory, the force between the liquid and the inner surface of the carbon tube must be large enough to allow it to infiltrate[31]. During the filling process, it is inevitable that the CNTs will have indirect contact or a surface coating with the guest material, and necessary post-processing, such as cleaning with appropriate solvents, is required to maximize the elimination of residual substances outside the tube that may affect the system.

In-situ filling

In-situ filling is filling CNTs directly with foreign material while they are being synthesized. As a result, the carbon nanotubes can be kept intact with a high fill rate, effectively isolating the encapsulation material from the surrounding environment. However, the *in situ* filling method yields a low filling yield, and some impurity elements will enter the interior of the carbon nanotubes during the filling process[32]. *In situ* filling mainly includes arc discharge[33] and molten salt electrolysis[34].

The arc discharge method is also called the graphite arc method. The vacuum reactor is filled with inert gas or hydrogen. Graphite rods of different sizes are used as electrodes. During the growth and filling process, the graphite rods at one end are gradually consumed, and the carbon nanotubes grow at the other end. This method was used by Guerret-Piécourt *et al.* to create element-filled CNTs *in situ*[33].

Molten salt electrolysis is a method in which an inorganic salt is heated to melt into a liquid electrolyte in a carbon crucible for electrolysis to fill CNTs, which was first proposed by Hsu *et al.* They used this method to fill CNTs with Li_2C_2, LiCl, Sn, Pb, Bi, and Sn-Pb alloy[34,35].

Ex-situ filling

Ex-situ filling refers to the process of filling guest substances into the pre-synthesized carbon nanotubes, which is the most widely used approach to filled nanotubes preparation. According to the physical properties of the filled materials, they are introduced into the cavity of CNTs in the form of liquid or steam, corresponding to the liquid phase method and the gas phase method[28], respectively. In order to fill the

CNTs, their ends need to be opened first. Heat treatment in an oxidizing environment, such as H_2O_2, O_2[36], O_3[37], HNO_3, H_2SO_4[38], $KMnO_4$[39], or Br_2[40] is mainly used opening approaches. To obtain a more pure CNT, combined thermal treatment and concentrated acid treatment are necessary to remove the various contaminants, such as amorphous carbon, graphite electrode particles, and catalyst[41].

Filling of CNTs from the liquid phase entails impregnating the opened tube with melts or solutions of target compounds. Although many examples of liquid-phase filling of carbon nanotubes have been reported, the mechanism has not been determined. We assume that liquid-phase filling of carbon nanotubes is a so-called capillary wetting phenomenon[30], then the Young and Laplace equations can be used to describe the mechanism[31]:

$$\Delta P_{re} = \beta \cdot \frac{R + r}{R \cdot r} \tag{1}$$

where ΔP_{re} represents the pressure change, β represents the surface tension coefficient, and R and r represent two different curvature radii of the surface, respectively. When the liquid level in the nanotube rises, it saturates the tube wall and forms a meniscus at the top [Figure 1].

The meniscus is approximately regarded as a spherical shape, and the liquid is in contact with the capillary wall at a certain angle θ, then the following formula is obtained[31]:

$$\Delta \rho = \frac{2\beta cos\theta}{r} \tag{2}$$

where $\Delta\rho$ is the density difference between two phases.

According to the equation, when the contact Angle exceeds 90°, external forces are needed to drive the rise of capillarity. When the contact angle is below 90°, spontaneous filling will occur. Surface tension β is the force of liquid surface shrinkage. Liquids with low surface tension are more likely to spread through the tube, which is manifested by the smaller contact angle and the reduced driving force required for spontaneous filling. β of some common solvents and metal halides packed into carbon nanotubes at the melting point has been tested or calculated as follows (unit: mN/m): water (72.8), methanol (22.07), acetone (23.46), tetrachloromethane (26.43)[42], AgCl (113-173), AgBr (151), AgI (171), KCl (93), KI (70), $NdCl_3$ (102), $ZnCl_4$ (1.3), PbO (132), V_2O_5 (53), *etc.*[43] The filling of salts such as metal halides and oxides is often carried out in this method, such as KI, AgI, and Sb_2O_3 filled by Sloan's group[44]. The following table[45-66] is a list of various materials that have been reported in the literature for filling CNTs in recent years.

Vacuum and high temperatures are used to fill CNTs from the gas phase. An encapsulated material is heated inside a sealed tube until it vaporizes (or sublimates), but keep the temperatures as low as possible to prevent (or reduce) de-encapsulation[35]. The vapor of the compound that is enclosed during CNTs annealing enters the nanotube via capillary condensation and crystalizes during subsequent cooling. During the gas phase filling process, no other substances are introduced; thus, there is no pollution to the environment[67]. The major defect of this approach, however, is also obvious. First, the reaction temperature should be less than 1,000 °C to avoid destroying the CNTs or reacting with carbon to close the CNT's ends[67]. Second, the filled substances are typically discrete in the hollow nanospace of CNTs, which makes it difficult to control the filling yields[68]. As a result, the gas phase filling approach is appropriate for molecule crystals containing inorganic clusters, organic molecules, and complexes with low boiling or sublimation temperatures. The filling systems for fullerenes[61] and their derivatives[69] are typical examples.

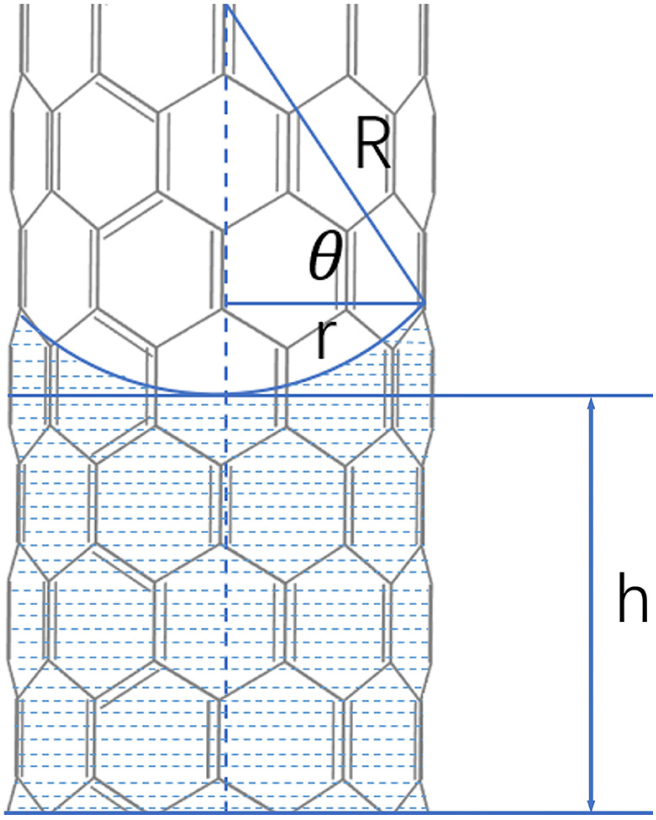

Figure 1. The liquid level rises in a capillary.

Recently, a novel method for multistep inorganic synthesis has been established, in which the pre-filled nanotube undergoes sequential chemical transformations[70]. For example, the metal precursors, such as metal halides and complexes, are first pre-filled into the CNTs and then perform thermal decomposition or Hydrogen reduction to form metal nanoparticles@CNT. After that, the second reactant, such as H_2S, Te, is introduced and reacted with the metal nanoparticles to yield chalcogenides. For example, inorganic nanoribbons $[MS_2]_n$@SWCNT (M = Mo or W) can be prepared through sequential transformations of $M(CO)_6$ (M = Mo or W) to nanoclusters and nanoclusters to nanoribbons [Figure 2A]. Various graphene nanoribbons can be obtained by high-temperature polymerization of the selected small organic molecules encapsulated in the cavities of CNTs [Figure 2B][16].

MORPHOLOGICAL AND ELECTRONIC STRUCTURE OF FILLED CNTS HETEROSTRUCTURES

The characteristics of CNTs mainly include hollow nanospace morphology[71], conductivity, chirality[72], and so on. Two critical questions must be addressed as the substance fills the carbon tube. First, how does the coaction between the inner filler and the carbon tube modify the characters of the carbon tube itself? Second, how does the confined space of the carbon tube affect the crystal phase and heterostructures of the inner filler? The former has significant implications for the application of the new heterostructures, whereas the latter can be used to study many space-confined scientific issues. Therefore, this section discusses the morphological and electronic structure of some intriguingly filled CNTs heterostructures.

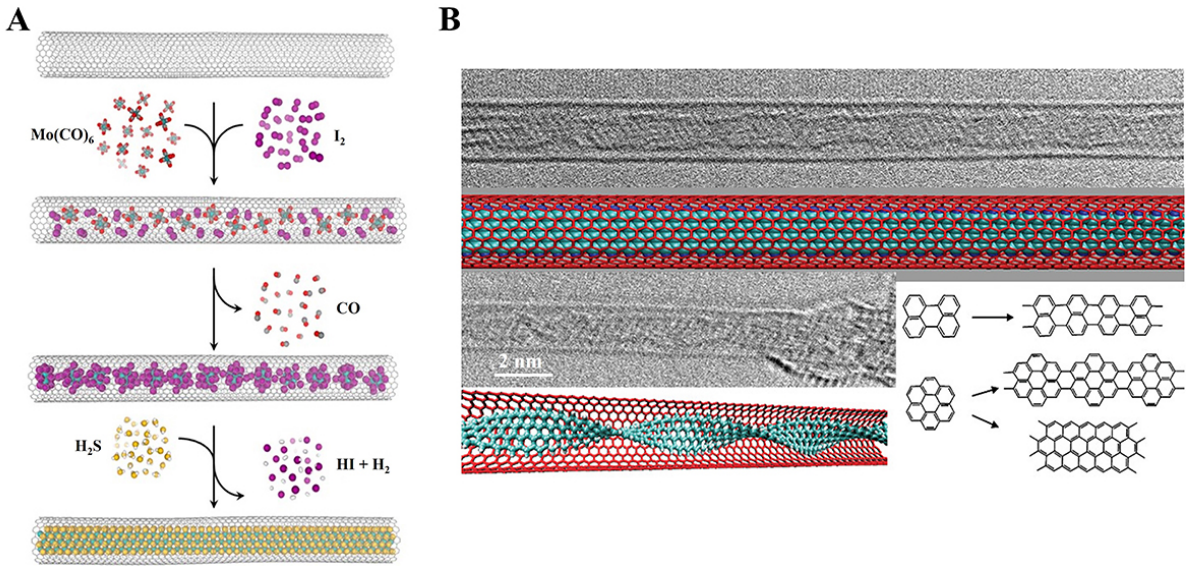

Figure 2. Multistep synthesis performed in carbon nanotubes: (A) Multistep in organic synthesis. The encapsulation and conversion of $Mo(CO)_6$ and iodine molecules into $[Mo_6I_{14}]^{2-}$ nanocluster and regenerate $[MoS_2]_n$ nanoribbons (Reproduced with permission[70]. Copyright 2016, American Chemical Society). (B) Multistep organic synthesis. The encapsulation and conversion of the organic molecule perylene or coronene into graphene nanoribbons (Reproduced with permission[16].Copyright 2011, American Chemical Society).

Morphological structure of filled CNTs heterostructures

As mentioned in Table 1, various inorganic as well as organic materials have been filled in the CNTs until today. To study the morphological structure of the heterostructures, transmission electron microscopy (TEM) is a basic research method. Studies have shown that when the accelerating voltage of TEM is less than 86 kV, the carbon nanotubes can still maintain structural integrity under the action of high-energy electron beams[73]. High-resolution transmission electron microscopy (HR-TEM) provides clearer internal structure information than TEM, such as interplanar spacing, atomic arrangement, and other information[74]. HR-TEM allows researchers to directly "observe" chemical reactions in nanoscale space. Aberration-corrected transmission electron microscopy (AC-TEM) is more powerful than HR-TEM in structure information. The biggest advantage of AC-TEM is that spherical aberration correction reduces aberration and thus improves resolution. The resolution of traditional TEM is at the nanometer scale, while the resolution of AC-TEM can reach the Å scale[75]. Improved resolution means a deeper understanding of the material, making observations of single atoms possible. Here, we attempt to provide a brief review of the previous efforts made in the compounding of X@CNTs based on the chemical composition of the filling objects.

Element materials

Element materials with low sublimation temperatures can be filled using the gas phase method by placing opened CNTs and bulk powder under a high vacuum and high temperature directly. Guan *et al.* introduced iodine to SWCNTs by heating the opened SWCNT and iodine elemental in a clean glass tube [Figure 3A][76]. The structure of the filled iodine transitions from the helical atomic chain to the crystalline phase as the diameter of the SWCNT becomes larger from Figure 3B. Phase transitions of I from chains to crystalline structures are observed inside the SWCNT around the critical diameter of 1.45 ± 0.05 nm. Furthermore, the structure of the host SWCNT is elliptically distorted by the helical I_n chains because of the repulsive interaction between I_3^- or I_5^- species and the SWCNT. In the Te@SWCNT system, the single-chain or few-chain limit Te nanowire also exhibits a helical structure, but the behavior maintains the structural

Table 1. Various materials for filling CNTs

Material	CNT	Method	Outcomes	Applications	Ref.
Sn	MWCNTs	Arc discharge	Enhance microwave absorption.	Microwave absorbent	[45]
S	SWCNTs/DWCNTs	CVT	Self-assembly of conductive sulfur chains in CNTs is realized.		[46]
Te	DWCNTs	CVT	Observe the Raman response of tellurium-filled CNTs.	Optoelectronic devices	[47]
Eu	SWCNTs	CVT	A high yield controlled synthesis method for Eu nanowires is proposed.	Electronic devices	[48]
GaTe/SnS/Bi_2Se_3	SWCNTs	CVT	GaTe, SnS, and Bi_2Se_3 are encapsulated into the SWCNTs for the first time.	Electronic devices	[49]
Nb/V/$TiTe_3$	MWCNTs	CVT	MTe_3 are synthesized in CNTs for the first time.		[50]
$NbSe_3$	MWCNTs	In-tube reaction	A single nanowire $NbSe_3$ is synthesized for the first time.		[51]
Bi_2Te_3/GaSe	SWCNTs	In-tube reaction	Bi_2Te_3 and GaSe are encapsulated into the SWCNTs for the first time.	Electronic devices	[52]
$CsPbBr_3$/$CsSnI_3$	SWCNTs	In-tube reaction	The smallest isolated halide perovskite structure is synthesized within CNTs.	Optoelectronic devices	[53]
Fe-S	CNTs	CVT	Fe-S@CNTs are prepared using CNT as a reactor.	Anode material	[54]
CdSe	SWCNTs	In-tube reaction	CdSe nanowires are prepared by self-assembly and directional assembly under the constraint of SWCNTs.	Optoelectronic devices	[55]
ReS_2	SWCNTs	In-tube reaction	Ultrathin ReS_2 nanoribbons are synthesized for the first time.	Nano-electrodes	[56]
$HfTe_2$	CNTs	In-tube reaction	$HfTe_2$ nanoribbons are synthesized by CVT in CNTs.	Metal-semiconductor Schottky heterojunctions	[57]
WS_2	SWCNTs/ DWCNTs	In-tube reaction	WS_2 nanoribbons with uniform widths are synthesized using CNTs as templates.	Spintronics	[58]
SnSe	SWCNTs	CVT	It is demonstrated that SnSe form ordered nanocrystals in narrow SWCNTs, and the band gap is significantly enlarged.	Solar cells	[59]
MoS_2	SWCNTs/DWCNTs	In-tube reaction	MoS_2 nanoribbons with uniform width are synthesized using CNTs as a template.	Synthesis method	[60]
C_{60}	SWCNTs	CVT	The relationship between electron dose and the bimolecular reaction of fullerene in CNTs is reported.		[61]
N@C_{60}	SWCNTs	CVT	N@C_{60}@SWCNTs are synthesized, and it was found that pod samples could be converted into DWCNTs.		[62]
Gd@C_{82}	MWCNTs	CVT	The transport characteristics of Gd@C_{82}@CNTs as a field effect transistor channel are introduced.	Electronic devices	[63]
Sc_3N@C_{80}	SWCNTs	CVT	Nano-pods formed by Sc_3N@C_{80} are prepared and characterized.		[64]
La@C_{82}	SWCNTs	CVT	EELS is used to measure the charge transfer between materials.		[65]
Gd_2@C_{92}	SWCNTs	CVT	The dynamic behavior of limit atoms in metallic fullerenes is observed by HRTEM		[66]

MWCNTs: Multi-walled carbon nanotubes; DWCNTs: double-walled carbon nanotubes; CVT: chemical vapor transport; EELS: electron energy loss spectroscopy; HRTEM: high-resolution transmission electron microscopy.

characteristics of Te nanowire crystal rather than the interaction between Te and CNT [Figure 3C][77]. However, the situation became more complicated for element S of the same group as Te after being filled. It was observed that the sulfur chains confined within the carbon nanotubes lacked a definite structure[78] and were markedly different from the previously proposed linear or zigzag structures[46]. Instead, they tended to assume conformations resembling the cyclo-S_8 allotrope. Density functional theory (DFT) calculations showed that a more disordered sulfur chain structure was more stable than linear and zigzag conformations when the sulfur chain was confined within the SWCNT. Various nanowires, such as Eu [Figure 3D][48] and Sn [Figure 3E][15], are filled in carbon nanotubes using this simple process.

For element materials with high melting point temperatures or strong chemical active and unstable, multistep sequential chemical transformations within the pre-filled nanotube is an effective method. Novel metal nanowires (Ag[79], Pt[80], *etc.*), 3d metal (Fe[81], Co[82], Ni[83] *etc.*), and carbon nanowires[84] filled inside CNT were synthesized with this method. For example, the nanowire Fe, Co, Ni, and their alloys@CNTs can be synthesized by the pyrolysis of related pre-filled metallocene@CNT. The Fe nanowire filled inside CNT has a diameter of 20-40 nm with a filling of 60% and exhibits strong ferromagnetic behavior at room temperature[85]. Similarly, the ferromagnetic nanowires filled CNTs with different reaction precursors were also reported in several other pieces of literature[86]. As a true 1D nanocarbon, the sp^1 hybridized carbon chain is predicted to have novel chemical and physics properties, but because of its strong chemical activity and extreme instability, it is difficult to synthesize in common conditions[87]. In 2016, the sp^1 hybridized carbon chain inside DWCNTs (LLCC@DWCNT) was first synthesized by Shi *et al.*, which provides a practical strategy for the preparation of the true 1D carbon chain [Figure 3F][84].

Organic and metal-organic molecule cluster

The vast majority of organic molecules are nanosized but less stable in the atmospheric environment[88]. Filling the molecule inside the cavity of CNT can improve molecular stability while also serving as a precursor for the preparation of other complex materials, such as graphene nanoribbons[16], polymers compounds[89], and inorganic metal compounds[14].

C_{60} was the first molecule studied inside CNTs[90]. Following that, many other larger fullerenes[91] and endohedral metallofullerenes[92] were successfully filled and were used to study the interaction, intermolecular spacing, molecular orientation, molecular motion, and reaction behavior in the confined space. According to TEM measurements of C_{60}@CNTs, the intermolecular spacing in the nanotube is shorter than in bulk crystals, which is coincident with the van der Waals forces that induce compression of fullerenes inside the nanotube [Figure 4A][61]. The stacking mode of C_{60} in CNTs is sensitive to nanotubes' internal diameters, demonstrating the confinement effect inside nanotubes. C_{60}@SWCNTs is relatively stable below 800 °C in the vacuum state of less than 1×10^{-6} Torr, whereas fullerenes in nanotubes gradually polymerize above 1,000 ℃ or under the electron beam. A series of intermediate structures, such as a dimer, trimer, and chain, gradually transform to form complete nanotubes. Endohedral metallofullerenes have electric dipole moments caused by metal atoms within the carbon cage, which can affect their behavior inside nanotubes. Using Ce@C_{82} as a model molecule, the influence of the dipolar interactions on molecular orientations in CNTs was investigated by using HR-TEM[93] [Figure 4B]. The molecules have a tendency to align their dipolar moments along the nanotube axis, enhancing electrostatic interactions between nearby molecules, which does not occur in Ce@C_{82} crystals or solutions.

Because of the exact geometrical match between fullerene and the interior of a nanotube, some globular non-fullerene molecules, such as o-carborane[94], octasiloxane [Figure 4C][95], metal-organic cluster[14], polyoxometalates (POM) [Figure 4D][89], were also tried to fill inside the CNTs. Because it has a smaller

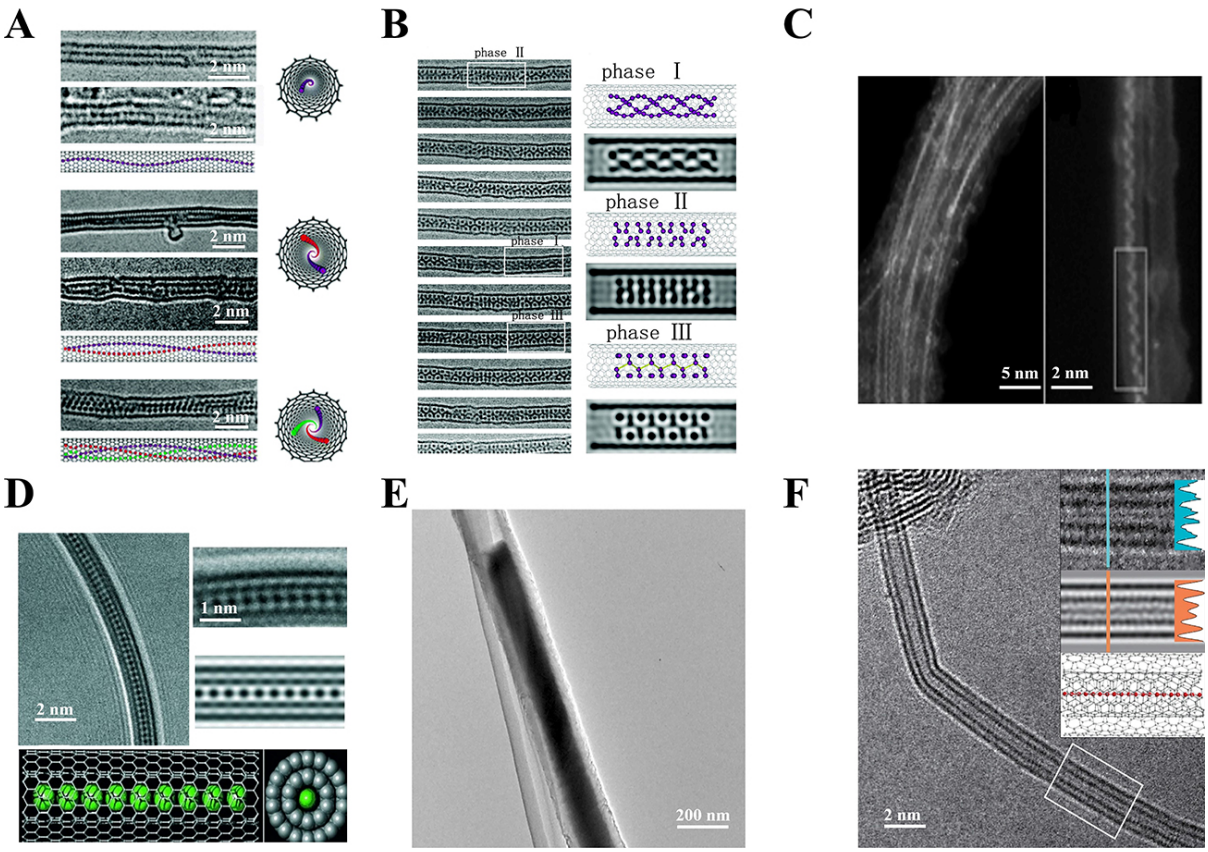

Figure 3. Elemental filling examples: (A) HR-TEM images and schematic illustrations of the chains of iodine filled in SWCNTs (Reproduced with permission[76]. Copyright 2007, American Chemical Society). (B) The phase transition of iodine from atomic chains to crystalline structures (Reproduced with permission[76]. Copyright 2007, American Chemical Society). (C) High magnifying STEM ADF image of Te-filled CNTs (Reproduced with permission[77]. Copyright 2020, Springer Nature). (D) HR-TEM image and simulated diagram of Eu's single chain filled in DWCNTs (Reproduced with permission[48]. Copyright 2009, Wiley). (E) TEM image of Sn nanowire formed in CNTs (Reproduced with permission[15]. Copyright 2016, Elsevier). (F) LLCC@DWCNT Partial HRTEM images of heterogeneous structures. Inset: a magnified portion of heterostructure (top), a simulated HR-TEM image (middle), and a molecular model (bottom) (Reproduced with permission[84]. Copyright 2016, Springer Nature).

diameter than C_{60}, octasiloxane can enter narrower CNTs than fullerenes[95]. The octasiloxane produces a zigzag packing in the SWCNT, with h-atoms in the corner of the cube in direct contact with the inner surface. In the POM@SWCNT heterostructure, electrons were transferred from SWCNTs to POM clusters, and hybrid materials formed spontaneously in an aqueous solution. Furthermore, many functional metal-organic clusters were also filled inside the CNTs to investigate new nanodevices, such as a spin valve[96] or memory device[97].

Except for the globular molecules, plane molecules can also be filled into the cavity of CNTs. For example, encapsulation of organic salt 1,1′-didodecyl-4,4′-bipyridinium dihexafluorophosphate (Viol) into metallic SWCNTs results in the formation of a semiconductor by opening the band gap [Figure 4E][21]. Small organic molecules, such as perylene and coronene-filled CNTs[16], are used as precursors to produce graphene nanoribbons by high-temperature polymerization.

Metallic inorganic compounds

Varied metallic compounds containing oxides, carbides[98], halides[99], and chalcogenides[100] have been encapsulated inside CNTs using different filling techniques. Many published reviews have discussed

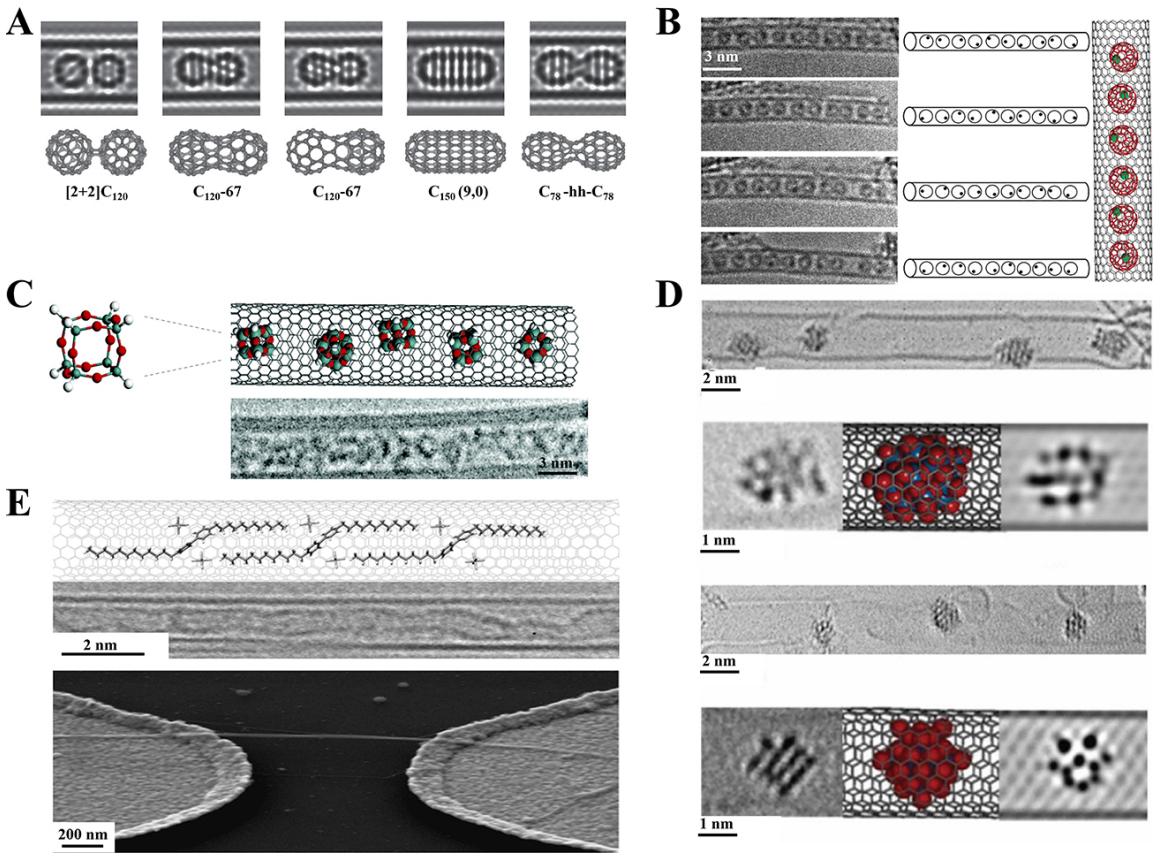

Figure 4. Organic compounds filling: (A) A series of high-resolution images of C_{60} molecules gradually bonded (Reproduced with permission[61]. Copyright 2010, Springer Nature). (B) A series of successive HRTEM images of (Ce@C_{82})@SWCNT and their schematic representation (Reproduced with permission[93]. Copyright 2004, Wiley). (C) Structural diagram of octasiloxane $Si_8H_8O_{12}$; HRTEM micrograph and structural diagram of $Si_8H_8O_{12}$@SWCNT (Reproduced with permission[95]. Copyright 2005, American Chemical Society). (D) AC-HRTEM and simulated images of @SWCNT and {W_{12}}@SWCNT, respectively (Reproduced with permission[89]. Copyright 2019, Wiley). (E) Model illustration of Viol inside a metallic SWCNT, representative AC-HRTEM image of Viol@SWCNT and SEM image of a Viol@SWCNT (Reproduced with permission[21]. Copyright 2017, Wiley).

previously studied examples such as metal oxide[44,101], carbides[61,84], and halides[102-104]. This section will concentrate on some novel structures and systems, such as transition metal dichalcogenides (TMDs)[18,50,56,57,70,101,105-108] and perovskite[53].

Many materials, which are hard to stabilize under normal conditions, form new phases with unique coordination properties in the lumen of CNTs. Under high temperatures, a PbI_2 SWCNT with a diameter ranging from ~3 to 7 nm is first realized inside the hollow nanospace of MWCNT [Figure 5A][109]. The SWCNTs are expected to be steady in the absence of carbon atom protection, and their electronic structure is diameter independent. Recently, Kashtiban *et al.* reported the formation of four isolated halide perovskite nanowires inside ~1.2-1.6 nm SWCNTs via melt insertion of $CsPbBr_3$ and $CsSnI_3$ [Figure 5B][53]. One of the four nanowires has a perovskite-like lamellar structure with polyhedral Sn_4Ix layers, while the other three are ABX_3 perovskite archetypes. Vasylenko *et al.* created SnTe nanowires that filled in CNTs with monatomic, curvilinear chains, hyperbolic chains, and 2 × 2 rock structures by varying the diameter of the CNTs[18]. The study of halide perovskite nanowires and SnTe nanowires filled in CNTs revealed that the structure of the internal filling can be manipulated to design its electronic behavior by changing the diameter of the CNTs.

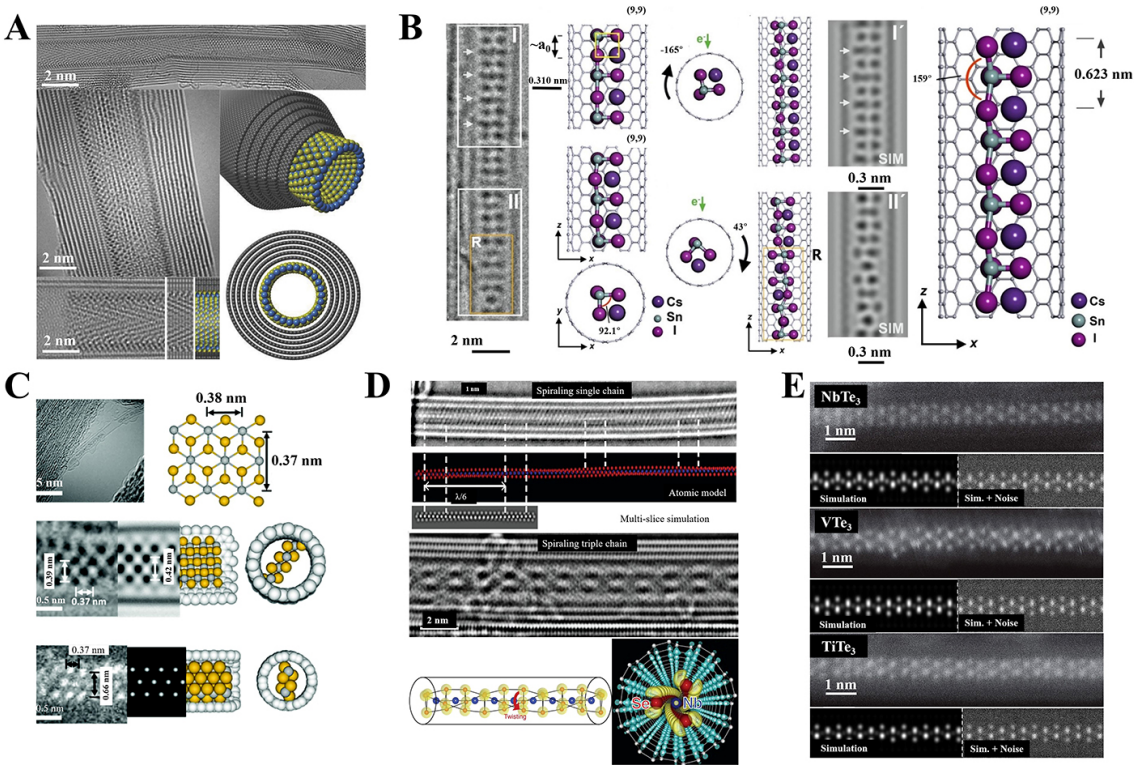

Figure 5. Compounds filling: (A) ACTEM analysis and schematic representation of the PbI_2@SWCNT. Blue: Pb atoms; yellow: I atoms (Reproduced with permission[109]. Copyright 2013, Wiley). (B) HRTEM image and corresponding simulation image of an encapsulated bilayer $CsSnI_3$ perovskite-like polymeric structure derived from $CsSnI_3$ (Reproduced with permission[53]. Copyright 2023, Wiley). (C) ACTEM photos, crystal structure, and geometric optimization models of PtS_2 (Reproduced with permission[106]. Copyright 2017, The Royal Society of Chemistry). (D) TEM and ACTEM images of $NbSe_3$ single strand in DWCNTs, atomic structure model (red: Se, blue: Nb) (Reproduced with permission[51]. Copyright 2018, The American Association for the Advancement of Science). (E) From top to bottom are the ADF-STEM images of MTe_3 single-stranded carbon nanotubes. Illustration below ADF-STEM: ADF-STEM image simulation (left) with the appropriate microscope condition noise added from the structure calculated by the DFT (right) (Reproduced with permission[50]. Copyright 2021, American Chemical Society).

Spurred by the novel electronic, optical, magnetic, and structural properties of graphene nanoribbons[110], isolating and manipulating ultra-fine nanoribbons of 2D materials (e.g., TMDs) has become popular in recent years. However, ultra-fine nanoribbons are difficult to separate and manipulate and may be highly air-sensitive due to the abundance of suspended bonds on the edges of the nanoribbons[111]. Encapsulation of metastable materials inside small-diameter nanotubes has emerged as a novel approach to creating new quasi-1D nanostructures. Cain *et al.* reported a gas-phase synthesis method for producing ultra-fine TaS_2 nanoribbons in CNTs[107]. The boundary and number of nanoribbons were limited by the diameter of the CNTs. Botos *et al.* prepared $[MS_2]_n$@SWCNT (M = Mo or W, average d_{NT} = 1.4 nm) by sequentially transforming $M(CO)_6$ (M = Mo or W) nanocluster to nanoribbons[70]. Two $[MS_2]_n$ nanoribbons, well-ordered crystalline hexagonal structures with zigzag edges, grow inward from both ends of SWCNTs. The nanoribbon's width is strictly regulated due to the limitation of the nanotube diameter. Furthermore, the nanoribbon is twisted rows in the CNTs due to the edge defect. Similar nanoribbon structures were also exhibited in the WS_2@MWCNT[16], $MnTe_2$@SWCNT[105], ReS_2@SWCNT[56], $HfTe_2$@SWCNT[57], and PtS_2@SWCNT [Figure 5C][106] heterostructures. Surprisingly, Nagata *et al.* prepared single MoTe nanowires using CNT as a template and partially oxidized $MoTe_2$ as a precursor[101]. They propose that the MoO_x oxidizes $MoTe_2$ to MoTe and TeO_2. TEM shows that MoTe nanowires exhibit unusual distortion under the confinement of carbon nanotubes, which may provide the possibility for the application of nanowires.

Another type of novel material is composed of 1D chains that are weakly held together by van der Waals interactions. Transition metal tri chalcogenides MX_3 (TMTs, M = transition metal, X= S, Se, Te) are representative examples that allow unusual ground states and collective mode electronic transport in bulk. It is fascinating to isolate and manipulate quasi-1D bulk materials in the few-chain limit because new physics can be induced by the new degree of low dimensionality. In 2018, Pham *et al.* synthesized the single- or few-chain limit of $NbSe_3$ encapsulated in protective MWCNT cavities [Figure 5D][51]. Static and dynamic charge-induced structural torsional waves observed by TEM are not found in bulk $NbSe_3$. Following that, the few-to-single chain limits of $HfTe_3$[108] in the MWCNT cavity were achieved. They discovered that the typically parallel chains in the $HfTe_3$@MWCNT system spiral around each other once three chains are reached, while at the same time, a short-wavelength trigonal antiprismatic rocking distortion takes place, opening a prominent energy gap. Later, they concentrate on MX_3 family members that are not stable in bulk and have been synthesized in the few to a single-chain limit of MTe_3 (M = Nb, V, Ti) within the nanoconfined cavity of MWCNTs [Figure 5E][50].

Electronic structure of filled CNTs heterostructures

Spectroscopy can energetically analyze the interaction between fillers and carbon nanotubes, allowing for a preliminary understanding of the filling material on the electronic structure[112]. Common types of the spectrum include optical absorption spectroscopy (OAS), Raman spectroscopy, and X-ray absorption spectroscopy (XAS).

Optical absorption spectroscopy (OAS)

Optical absorption spectroscopy (OAS) is an experimental technique that measures the ability of a sample to absorb light at different wavelengths. Since energy states are continuous, a substance can only absorb photons with a specific energy in a continuous spectrum. By measuring the amount of light absorbed by the sample, information about the material's electronic and molecular structure can be determined, resulting in spectral information[113]. OAS is a clear and accurate method to investigate the electronic structure of the filled CNTs heterostructures. The OAS technique also has some limitations. One of the main drawbacks is that it can only provide information on the surface or near-surface of the sample, and it is difficult to obtain information about deeper structures. OAS has been used to characterize $CoBr_2$[114], FeX_2[115], AgX[102], CdX_2[116], ZnX_2, CuX[103] (X = Cl, Br, I), $PrCl_3$[117], $TbCl_3$[118], GaSe[119], GaTe[49], Bi_2Se_3[49], SnTe[120], and Bi_2Te_3[52].

The following takes the four heterostructures systems selected in Figure 6A-D as examples to briefly explain the influence of material filling on SWCNTs. The curve of unfilled SWCNTs has several obvious absorption peaks, and the first two peaks, S1 (E^S_{11}) and S2 (E^S_{22}) are connected with the bandgap transition between Van-Hove singularities in semiconductor SWCNTs[102]. The appearance of the M1 (E^M_{11}) peak at about 1.8 eV is because of the inter-band transition of the first Van-Hove singularity in the metal tube. The last peak around 2.4 eV corresponds to a shift in E^S_{33} semiconductor SWCNTs.

Compared with the original data, the OAS of filled heterostructures changed significantly. The change in the spectrum is caused by the local interaction between the carbon atom and the filling atom, which further proves that the change in the electronic properties of SWCNTs is caused by the filling of the inner channel of the carbon tube[103]. The most significant and common phenomenon after being filled with foreign materials is that the optical transition at E^S_{11} is inhibited or even completely quenched because of a charge transfer between the packed substances and the carbon wall[116]. The direction and path of the charge transfer hinge on the properties of the filled materials. Metal halides usually act as electron acceptors, leading to the depletion of electrons in CNTs[115]. Another obvious feature is that all the peaks move towards the low energy region, which can be explained by the shrinking of the energy gap between Van-Hove

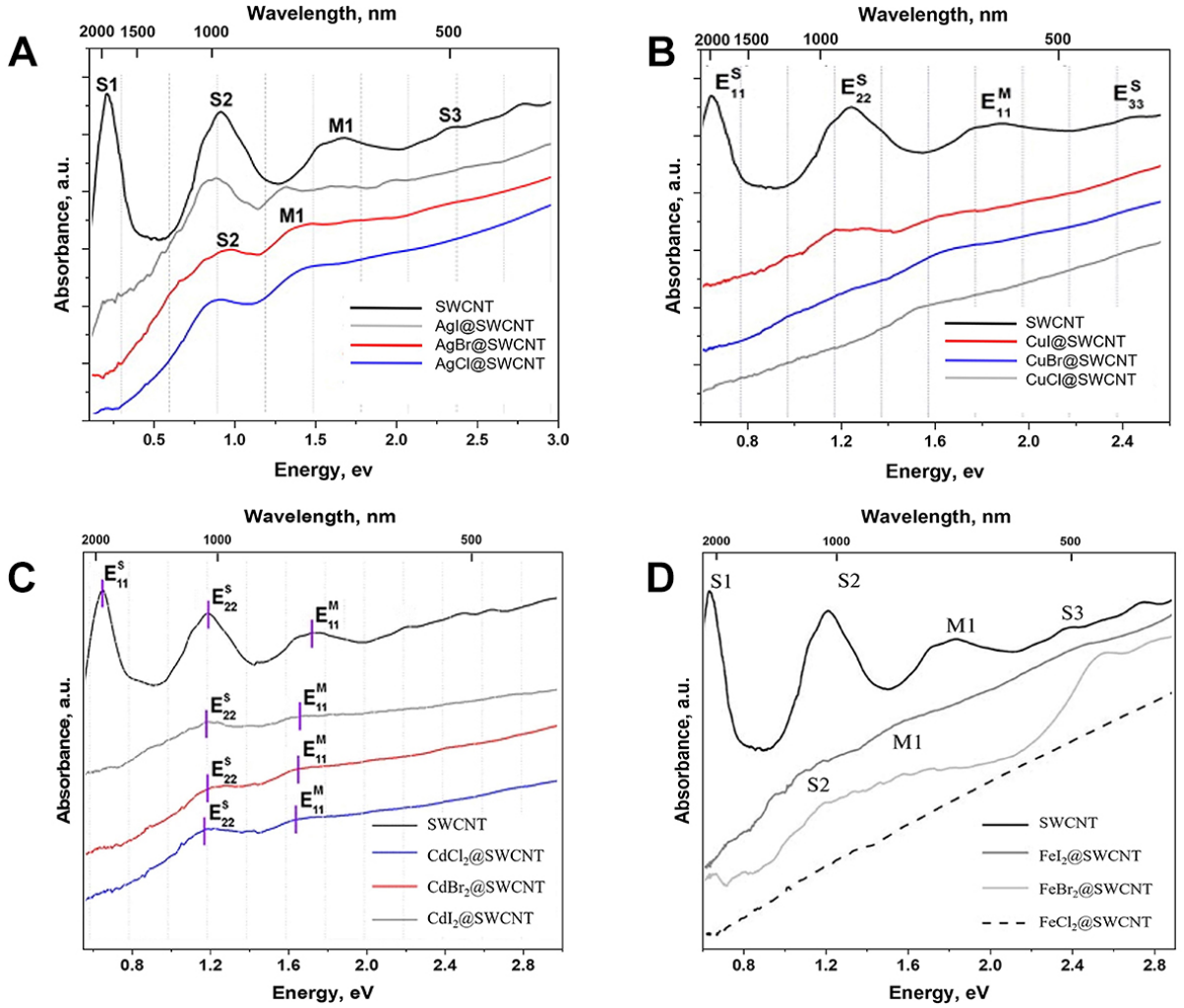

Figure 6. OAS characterization of CNT nanopeapods: (A) OAS of SWCNTs and AgX@SWCNTs (X = Cl, Br, I) (Reproduced with permission[102]. Copyright 2010, Elsevier). (B) OAS of SWCNTs and CuX@SWCNTs (X = Cl, Br, I) (Reproduced with permission[103]. Copyright 2012, Elsevier). (C) OAS of SWCNTs and CdX_2@SWCNTs (X = Cl, Br, I) (Reproduced with permission[116]. Copyright 2013, Springer Nature). (D) OAS of SWCNTs and FeX_2@SWCNTs (X = Cl, Br, I) (Reproduced with permission[115]. Copyright 2009, Springer Nature).

singularities after filling. Notably, the trend of E^S_{22} and E^M_{11} peaks was positively correlated with the electron negativity of halogen atoms (Cl > Br > I)[121]. This phenomenon is most obvious in the CuX@SWCNT and FeX_2@SWCNT systems.

Raman spectroscopy

Raman scattering is a kind of inelastic scattering that occurs when incident light interacts with phonons, and its intensity is typically only one-thousandth of Rayleigh scattering[122]. The energy difference between the scattered light and the incident light can be used to judge the lattice vibration information of carbon nanotubes[122]. Transition metal halide (MX)@CNTs were studied by Raman spectroscopy, such as MnCl, $MnBr_2$[123], $CoBr_2$[114], NiCl, $NiBr_2$[124], ZnCl[104], ZnX_2[104], FeX_2[115], AgX[102], CuX[103] (X = Cl, Br, I), rare earth metal halide, $TbBr_3$, TbI_3[125], $CdCl_2$[126], $LuCl_3$, LuI_3[126], GaSe, GaTe[119], SnS, SnTe[49], Ag[79], Cu, Ni[127], and other complexes.

Kharlamova[123] investigated the $MnCl_2$@SWCNT and $MnBr_2$@SWCNT heterostructures using Raman spectroscopy [Figure 7A and B]. The positions of the RBM peak and G peak of MnX_2 are shifted upward, reflecting the change of carbon-carbon bond energy. It is represented by the change in electronic structure during the filling process. Peak G is shifted in the Raman spectrum of MnX_2@SWCNT, reflecting the charge transfer between the carbon wall and encapsulated materials, which leads to the transition of metallic CNTs to a semiconductor state. The resonance excitation of CNTs of the corresponding diameter can be observed using a laser of specific energy[123]. Metallic SWCNTs with diameters of 1.50 and 1.41 nm were effectively excited at the laser energy of 1.58 eV. The 2.41 eV laser corresponds to a semiconductor SWCNT with a diameter of 1.35 nm. NiX_2@SWCNTs were also studied using Raman spectroscopy [Figure 7C and D]. The peak value of RBM decreased slightly, reflecting the change in CNTs diameter during the filling process. The position of peak G also changed greatly from typical metal nanotubes to semiconductor nanotubes. One possible explanation of the G peak change is that the metal SWCNTs transformed into a semiconductor state after being filled by 1D NiX_2 (X = Cl, Br) nanocrystals; that is, the gap was opened.

The Raman signal enhancement effect is also observed in filled CNTs heterostructure. Nascimento *et al.* reported that the chiral sulfur chains encapsulated in the SWCNTs with a diameter of 0.89 nm can significantly enhance the Raman signal of the SWCNTs[128]. They suggested that the small diameter and hybrid state formed by overlapping orbitals of the sulfur chains and SWCNTs in the excited part of the single-particle electronic spectra are key factors in enhancing the Raman signal. Li *et al.* further discovered that the long polymeric sulfur chains inside HiPco-SWCNTs strongly interact with the sidewalls of the carbon nanotubes, resulting in a decrease in the intensity of the high-frequency Raman spectral peaks and the appearance of new, very strong absorption peaks at 319, 395, and 715 cm^{-1}, all of which originate from the strong electron-phonon coupling between the SWCNT excitons and the S-S vibrations[129]. These findings provide new points to explain previously reported Raman signal abnormal phenomena for other filled CNTs heterostructures.

As a fingerprint characterization, Raman spectra are a simple and effective method to study the electronic structure of filled carbon-nanotube heterostructures. However, the disadvantages of Raman characterization are also obvious. For example, other morphological characterization methods are required for carbon nanotube positioning during large-area characterization. The characterization efficiency is very low when point-by-point scanning is used[126].

X-ray absorption spectrum (XAS)

X-ray absorption spectrum (XAS) refers to the measurement of the attenuation of X-rays as they pass through a material at varying energies. It provides information about the electronic structure and chemical composition of the material, including the types of atoms present, their oxidation states, and their coordination environments. This is achieved by examining the energy-dependent changes in the absorption of X-rays due to different core-level transitions in the atoms of the material[130]. XAS has several advantages and limitations. One of the main advantages is its ability to provide information on the local structure of a material at the atomic level, including the valence state and coordination geometry of the absorbing atom. XAS is also a non-destructive technique, allowing for the repeated analysis of a sample without altering its properties. However, XAS has some limitations, such as providing information only on the absorbing atom and not the surrounding environment. The XAS spectrum of SWCNTs filled with FeX_2[115], NiX_2[124], ZnX_2[104], CdX_2[116], AgX[102], CuX (X = Cl, Br, I)[103], $HgCl_2$[131] and other substances has been documented in the literatures.

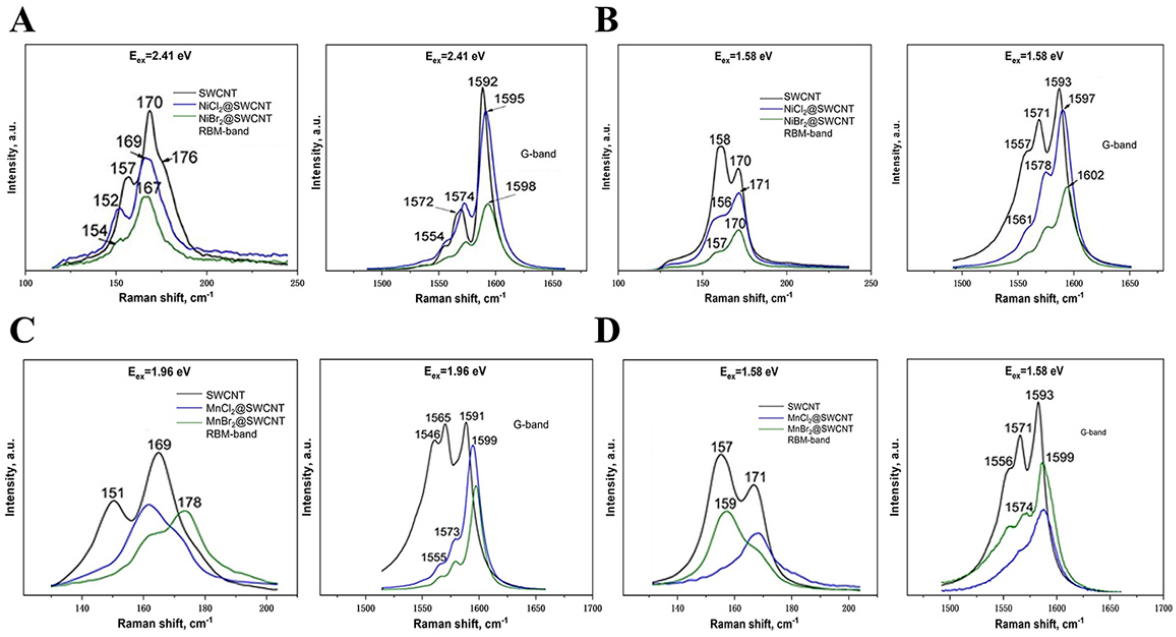

Figure 7. Raman characterization of carbon-nanotube nanopeapods: (A) Raman of MnX_2@SWCNT heterostructures at 1.96 eV laser energy (Reproduced with permission[123]. Copyright 2012, IOP Science). (B) Raman of MnX_2@SWCNTs heterostructures at 1.58 eV laser energy (Reproduced with permission[123]. Copyright 2012, IOP Science). (C) Raman of SWCNTs and NiX_2@SWCNTs at 2.41 eV laser energy (Reproduced with permission[124]. Copyright 2012, Wiley). (D) Raman of SWCNTs and NiX_2@SWCNTs at 1.58 eV laser energy (Reproduced with permission[124]. Copyright 2012, Wiley).

XAS spectra of NiX_2@SWCNTs (X = Cl, Br) heterostructures measured by Kharlamova *et al.* are shown in Figure 8A[124]. Partial information on nickel halide nanotubes can be obtained from the absorption peaks of C 1s. C 1s can be simply understood as the minimum energy required to excite an electron in a 1s orbital. An additional spectral feature A* appears below the p formant A. This property can be attributed to the interaction between the wall and the filling material. Compared with the spectra of AgX@SWCNTs and the original nanotubes [Figure 8B], SWCNTs interact with the AgX crystal of the plugged layer[102]. This additional spectrum characteristic can be attributed to the energy level that is reduced by electron transition to the reduction of the transfer of the plug-in charge.

FUNCTIONAL APPLICATIONS OF FILLED CARBON-NANOTUBE HETEROSTRUCTURES

Carbon nanotubes have excellent conductivity[132], optical[133], and thermal properties[5], mechanical properties[4], and flexibility[134], which can be applied to them in nano-electronics[2], photovoltaic[135], thermoelectric power generation[136], energy storage[137], catalytic[138], and other important areas. SWCNTs can be a metal or semiconductor, depending on their atomic structure[139]. The method of filling can not only control its electronic structure[12] but also retain the above many excellent properties, which greatly accelerates the industrialization application of carbon nanotubes.

Nanoelectronics

Charge transfer between the filled materials and CNT is common, which alters the electrical transport properties in a CNT. Li *et al.* prepared field-effect transistors (FET) with C_{60} and C_{70}@SWCNT peapods as channel materials and measured the transfer characteristics at room temperature [Figure 9A][26]. The I_{DS}-V_g curves of the C_{60} and C_{70} peapods FET show P-type hole-dominate transport characteristics, which are similar to those of pristine SWCNTs. When C_{60} is replaced with azafullerene ($C_{59}N$ and $C_{69}N$), the FETs exhibit typical N-type electron-dominate transport characteristics [Figure 9B][26]. Furthermore, a

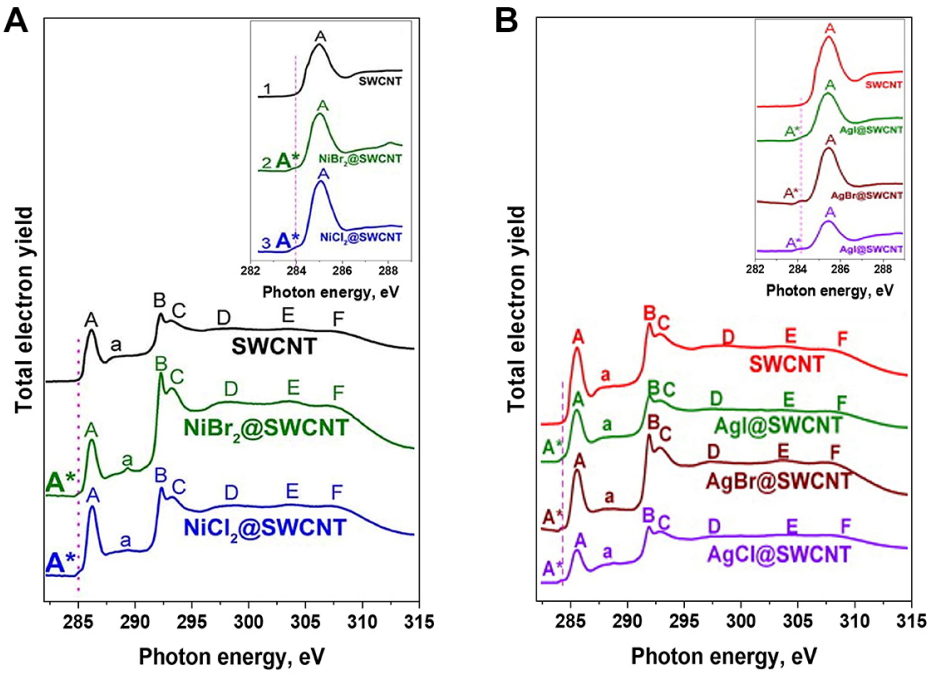

Figure 8. XAS characterization of carbon-nanotube nanopeapods: (A) XAS of SWCNTs and NiX_2@SWCNTs (X = Cl, Br) (Reproduced with permission[124]. Copyright 2012, Wiley). (B) XAS of SWCNTs and AgX@SWCNTs (X = Cl, Br, I) (Reproduced with permission[102]. Copyright 2010, Elsevier).

photoswitching behavior was also observed in $C_{59}N$ peapods FET devices, indicating the charge transfer from azafullerene to SWCNT [Figure 9C][140]. Shimada *et al.* investigated the transport characteristics of M@C_{82} (M = Gd, Dy) metallofullerenes nanopeapods FETs with ambipolar behavior. However, in the case of C_{90}-peapods, all devices exhibited metallic properties [Figure 9D][63].

Yang *et al.* further studied the temperature-dependent charge transport characteristics of Dy@C_{82} peapods FET. A transition from p-type to n-type conduction has been observed as the temperature decreases from room temperature to 265 K, indicating that charge transfers from the Dy@C_{82} to the conductance band of carbon nanotubes at low temperatures [Figure 9E][23]. At a temperature lower than 215 K, metallic behavior occurred, suggesting that additional electrons are continuously injected into the conductance band, shifting the Fermi level into the conduction band. Under 75 K, the device became a single-electron transistor with irregular coulomb blockade oscillation, meaning that the inside Dy@C_{82} splits the tube into discrete quantum dots. The transport properties of other fullerene nanopeapods FET are also investigated [Figure 9F].

It is also possible to produce p-n junctions within individual CNTs by partially filling the acceptor or donor. The examples were demonstrated in the heterostructures of partially filled CsI, CsC_{60}[25], and Fe[141] nanoparticles inside the SWCNTs where ultimate heterostructures of electron donor and acceptor were realized within the cavity of a SWCNT, yielding the air-stable rectifying performance.

Additional means can be used to tune the properties of the heterostructure-based electronic device if the target filler substance has a unique property, such as a spin-crossover (SCO) molecule[96] or magnetic cluster[14]. Giménez-López Mdel *et al.* encapsulated $Mn_{12}Ac$, a single-molecule magnet (SMM), into MWCNTs, resulting in a new type of heterostructure that combines the magnetic properties of the SMM

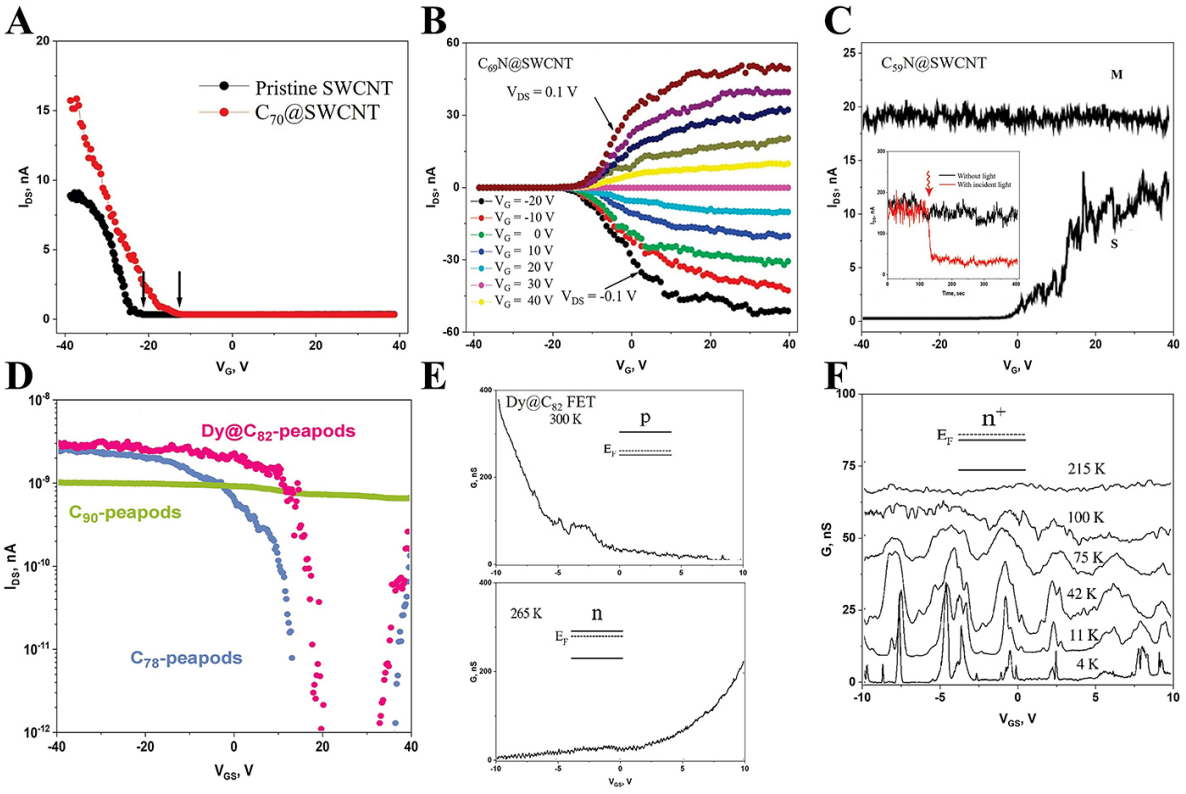

Figure 9. Electrical characterization of fullerene-peapods FETs: (A) Transfer curves for a pristine (unfilled) SWCNT FET and a C_{70} nanopeapods FET device (Reproduced with permission[26]. Copyright 2010, American Chemical Society). (B) Transfer curves measured for $C_{69}N$ nanopeapods FET (Reproduced with permission[26]. Copyright 2010, American Chemical Society). (C) I_{DS}-V_G characteristics measured at room temperature for an n-type semiconducting $C_{59}N$@SWCNT and a metallic $C_{59}N$@SWCNT without light (V_{DS} = 0.1 V). The inset shows the I_{DS} characteristic of the semiconducting $C_{59}N$@SWCNT, which is measured as a function of time without and with incident light (400 nm wavelength) (Reproduced with permission[140]. Copyright 2009, American Chemical Society). (D) Transfer characteristics of C_{78}, C_{90}, and Dy@C_{82}-peapods (V_{DS} = 20 mV, T = 23 K) (Reproduced with permission[63]. Copyright 2003, Elsevier). (E) V_G dependence of conductance measured at various temperatures (V_{DS} = 4) (Reproduced with permission[23]. Copyright 2001, AIP Publishing). (F) Conductance of Dy@C_{82}-peapods at temperatures from 4 to 215 K. The insets in (E) and (F) are band diagrams (Reproduced with permission[23]. Copyright 2001, AIP Publishing).

with the functional properties of the CNT [Figure 10][14]. At low temperatures, due to the molecule orientation of the SMM molecule arrangement inside the CNTs, the electrical resistance of the host CNTs exhibited anisotropic behavior. Villalva *et al.* synthesized the Fe-based SCO molecules filled SWCNTs heterostructures (Fe-SCO@SWCNT). The electronic transport measurements indicated that the SCO switch of the molecules triggers large conductance bistability via the SWCNT[96].

In the above, various nanoelectronic devices suggested that the filled CNT is an effective method for tuning and extending the function of pristine SWCNT.

Energy

Lithium-ion battery

Filling CNTs with suitable materials can increase their practical capacity, and their electrochemical properties are very suitable for battery preparation. Yu *et al.* tested the battery performance of FeS@CNTs [Figure 11A][54]. The battery was stable over multiple cycles, with higher cycle stability per cycle than graphite and FeS batteries. Another paper[142] demonstrated that even after one thousand cycles at a highly charged current of 2,000 mA g^{-1}, the FeS_2@CNTs battery could achieve a specific capacity of 525 mAh g^{-1}.

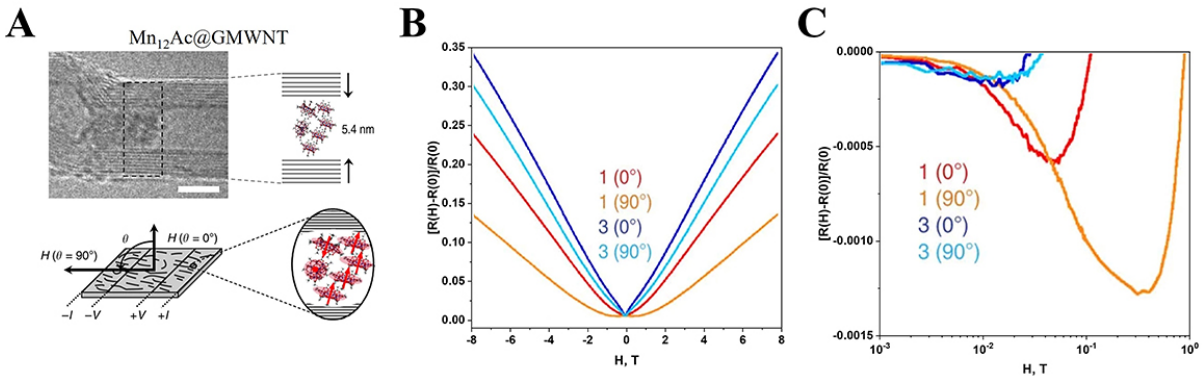

Figure 10. Effect of magnetic molecular filling on the resistance of CNTs (Reproduced with permission[14]. Copyright 2011, Springer Nature): (A) TEM of MWCNT filled with $Mn_{12}Ac$, scale bar is 5 nm, and schematic of magnetoresistance measurement apparatus and $Mn_{12}Ac$ molecules filled in CNTs. (B) Magnetoresistance of $Mn_{12}Ac$@MWCNT (1) and the control sample of pristine MWCNT (3) at 2 K in the presence of a magnetic field (H) either perpendicular (θ = 0°) or parallel (θ = 90°) to the conducting layers. (C) Low field region of the magnetoresistance measurements.

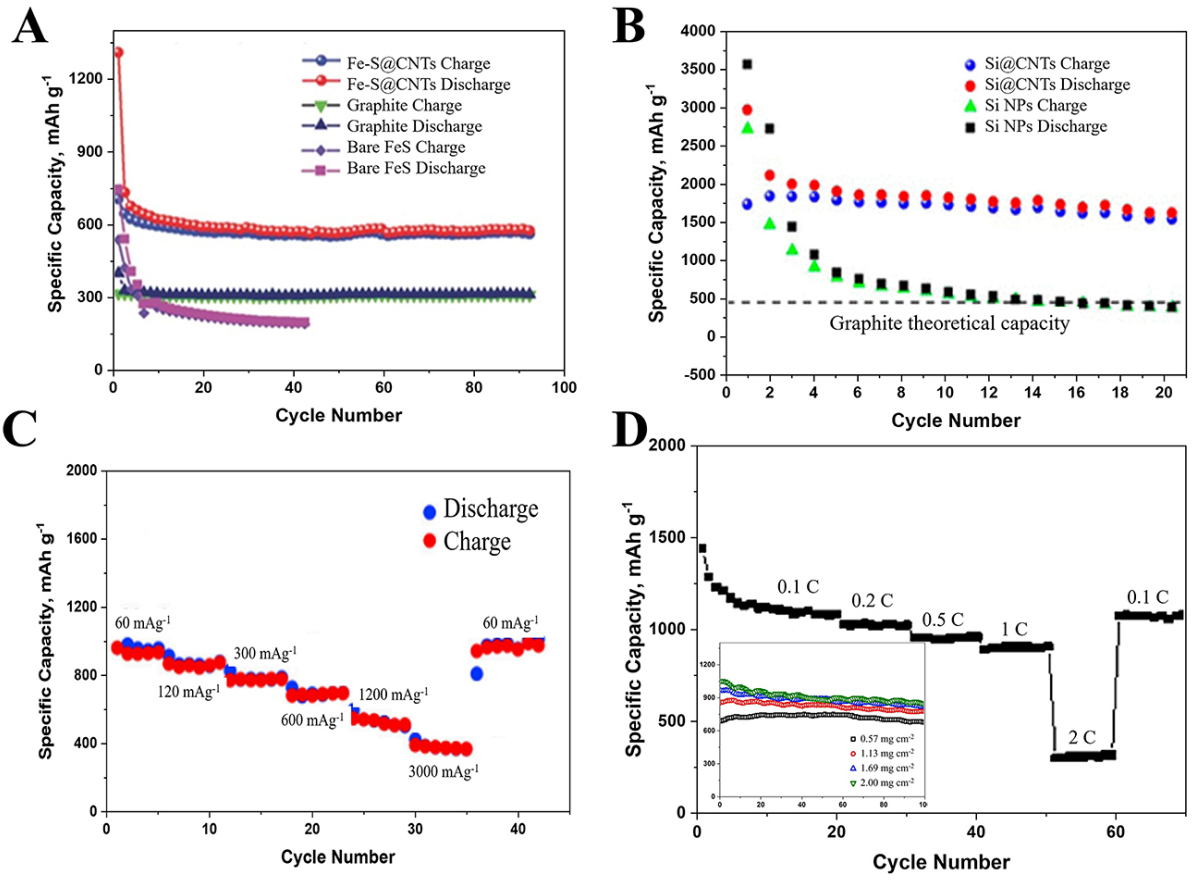

Figure 11. Properties of CNTs-filled lithium batteries: (A) Comparison of cyclic properties of three materials (Reproduced with permission[54]. Copyright 2016, Wiley). (B) Comparison of cycling properties of Si nanoparticles and Si nanoparticles@CNTs (Reproduced with permission[143]. Copyright 2015, American Chemical Society). (C) Cyclic performance of Fe_2O_3@CNTs at different current densities (Reproduced with permission[144]. Copyright 2017, American Chemical Society). (D) Rate performance of Li_2S_6@CNT thin film electrodes in the range of 0.1-2 C current density. Inset: the relationship between cycling performance and the weight of the CNTs film (Reproduced with permission[146]. Copyright 2017, Elsevier).

The reversible capacity of the Si nanoparticle @CNTs cell after 20 cycles is 1,475 mAh g^{-1} [Figure 11B], which is approximately four times that of graphite[143].

The cyclic performance of the cell prepared with Fe_2O_3@CNTs is shown in Figure 11C[144]. When the current density is 1,200 mA g^{-1}, approximately 40% of the capacity remains, and when the current rate is decreased to 60 mA g^{-1}, approximately 1,000 mA g^{-1} reversible capacity remains. Fe_3O_4-filled MWCNTs have also been studied as anode materials[145]. The specific capacity reached 220 mAh g^{-1} after 350 cycles, roughly twice that of unfilled CNTs at a current density of 2,000 mA g^{-1}. Fe_3O_4 NPs trapped within CNTs enhance the electrochemical behavior of Li-ion batteries while also preventing structural degradation.

Li-S composite system as the electrode material of high-performance batteries has been widely concerned. Kim *et al.* prepared lithium batteries using Li_2S_6@CNT conductive thin films as electrode materials and tested their performance [Figure 11D][146]. As the current density reduces from 0.1 C to 2 C, the discharge capacity decreases gradually. At the end of the cycle, when the current density returns to the initial level, the specific capacity is 1,081 mAh g^{-1} (initially 1,090 mAh g^{-1}), suggesting that the electrode has excellent stability. The illustration shows the relationship between cycle performance and film quality. This may be due to the increase in weight of CNT film, which leads to an increase in active adsorption sites in its interior, which is very favorable for the improvement of battery performance. Furthermore, Fu *et al.* investigated the chemical properties of sulfur in two types of SWCNTs with distinct diameters, produced by an electric arc (EA-SWCNTs, average diameter 1.55 nm) or high-pressure carbon monoxide (HiPco-SWCNTs, average diameter 1.0 nm), and demonstrated the electrochemical reaction activity of sulfur with lithium inside SWCNTs of different diameters[78]. Specifically, relatively larger diameter EA-SWCNTs can accommodate dissolved Li^+ ions, similar to Li-S reactions in solution. In contrast, Li^+ ions are blocked from entering the tube cavity in smaller diameter HiPco-SWCNTs. Therefore, the Li-S reaction in HiPco-SWCNTs is significantly different from when S is not encapsulated and can be attributed to interactions with π electrons passing through the carbon walls. This finding provides a new mechanism for improving the performance of lithium-ion batteries by filling CNTs.

It should be noted that the function of carbon nanotubes is more like a modifier: their participation mainly serves to modify the storage of lithium, thereby enhancing the capacity of lithium-ion batteries. However, pure carbon nanotubes are not very effective as electrode materials[147]. When filling carbon nanotubes, the mass ratio with the active material is generally 1:5, in the milligram range. If pure carbon nanotubes are used as electrode materials, they exhibit high specific capacity in the first lithium-ion insertion step but cannot be fully released in the subsequent lithium-ion extraction process[148]. This means that a large portion of the lithium ions is irreversibly consumed, leading to a decrease in the Coulombic efficiency of the battery.

The cycling rate is reflected in the electrochemical stability of the material during battery charging and discharging cycles, as well as the efficiency of ion insertion and extraction processes and the degree of material damage. CNTs can significantly improve the cycling rate performance of lithium-ion batteries, mainly due to their conductivity, their special hollow tubular structure, and cross-linked network structure, which enhance the efficiency of electron conduction in electrode materials and improve ion transport in CNTs. Firstly, CNTs provide a fast ion transport path, thereby improving the electrochemical reaction of lithium storage. Secondly, the confinement effect of CNTs allows the encapsulated active electrode material to be in close contact with the carbon tubes, shortening the distance of electron and Li^+ ion transport, which is superior to loose materials. Finally, the cross-linked conductive CNT network disperses the stress concentration phenomenon of materials, enhancing the structural strength of powder materials. The carbon nanotubes also have enough space to release induced stress expansion during the charge/discharge process,

maintaining their structural stability, so the performance of filled carbon nanotubes is significantly better than that of traditional anode materials.

Although filled carbon nanotubes show superior electrochemical performance, their performance slightly decreases during cycling due to the instability of the electrode structure, including active and non-active materials such as carbon nanotubes filled with active particles and binders. The significant expansion of carbon nanotubes during lithiation can cause cracking, deformation, and partial peeling of the electrode components during cycling, leading to the deterioration of cycling performance. To address these issues, it is important to identify the optimal filling rate for different active materials to ensure the structural stability of the expanded electrode. The use of multi-walled carbon nanotubes can further limit the range of volume expansion. Designing the battery structure based on specific materials can also improve its overall electrochemical performance.

The thermoelectric power generation

A major concern has been the potential effect of molecules encapsulated in CNTs on the thermal properties of heterostructure systems. Kodama *et al.* developed a micro-nano processing method for determining the effect of filling on thermal conductivity (κ) and thermoelectric potential (S), as shown in Figure 12[149]. The results show that the filled CNTs reduce thermal conductivity by 35%-55% and increase thermoelectric potential by about 40% compared to pristine CNTs at room temperature. Temperature-dependent measurements from 40 to 320 K show that the peak of thermal conductivity changes as temperature decreases.

Fukumaru *et al.* investigated the thermoelectric characteristics of $CoCp_2$@SWCNT heterostructures[150]. Compared with original SWCNTs, the electrical conductivity of the heterostructures was significantly improved by an order of magnitude. The negative Seebeck coefficient of -41.8 mV K^{-1} at 320 K indicates that encapsulation of cobaltocene can convert the p-type pristine semiconducting SWCNT into an n-type. Furthermore, the heterostructure has a high power factor and a low thermal conductivity (0.15 W m^{-1} K^{-1}). Such a heterogeneous structure of conductivity, power factor, and thermal conductivity is very suitable for the thermoelectric generation and is an attractive choice for the next generation of thermoelectric appliances.

Catalyst

CNTs with a large internal surface area are very stable and good catalyst carriers. Their main function is to immobilize and load nanoparticles and to provide an ideal local environment for certain chemical reactions. Aygün *et al.* investigated the catalytic performance of Ru@SWCNTs *vs.* Ru coated on the surface of SWCNTs[151]. It has been demonstrated that the reason for improving the catalytic efficiency is not only the stabilization of the catalytic particles but also the increase in the local concentration of the reactant precursor, which is critical to the catalytic effect. Chamberlain *et al.* decompose synthetic catalytic nanoparticles in SWCNTs[152]. The size and morphology of the nanoclusters were controlled by the diameter of SWCNTs, and efficient nanoparticle-filled SWCNTs provided a suitable environment for hydrogenation. SWCNTs with different diameters can compare nanometers of different sizes, which is critical for catalytic activity. The life of nanoparticles packed steadily into carbon nanotubes would be greatly extended.

Che *et al.* prepared highly aligned and monodisperse graphite-carbon nanoarrays using alumina films as templates and filled carbon nanotubes with nanoparticles (Ru and Pt/Ru)[153]. Supported catalysts are used in electrocatalytic oxygen reduction and methanol oxidation of hydrocarbons. The catalytic activity was significantly enhanced when CO and H_2O were converted to ethanol using Ru@CNTs.

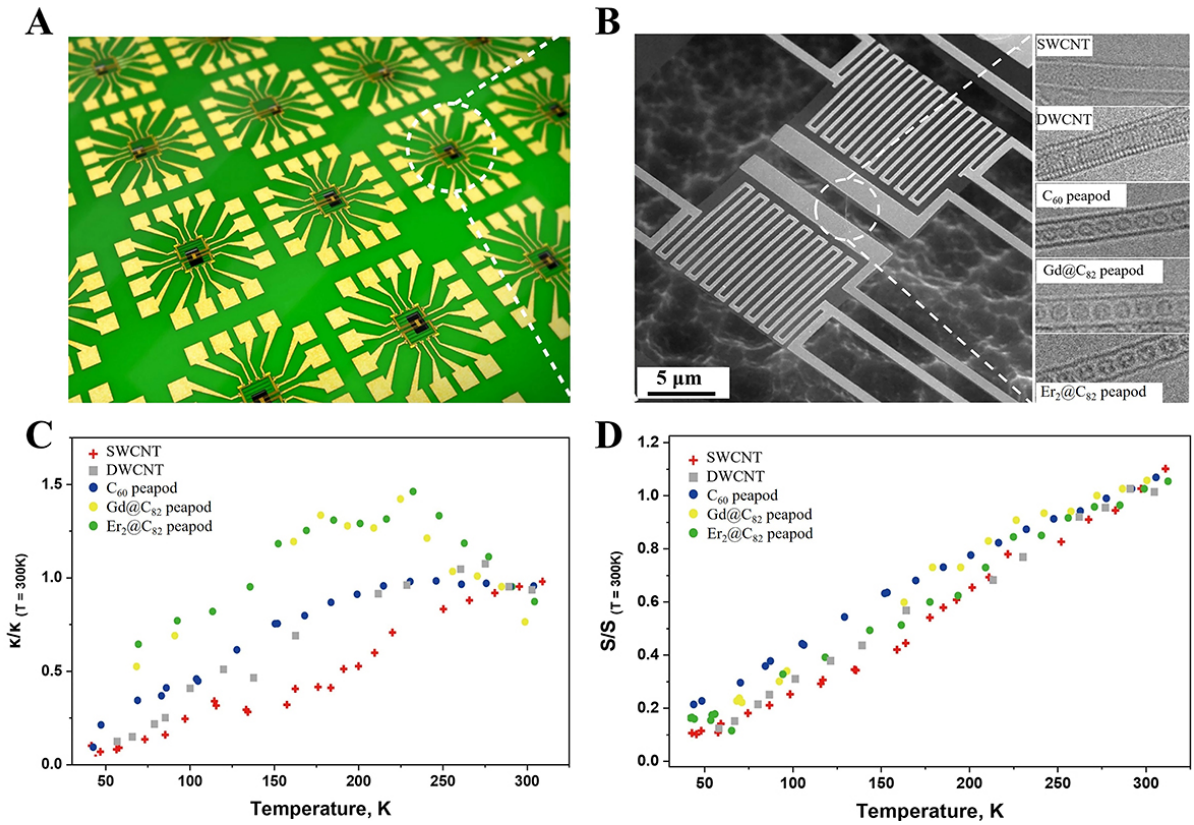

Figure 12. Properties of CNTs-filled in a thermoelectric generation (Reproduced with permission[149]. Copyright 2017, Springer Nature): (A) Schematic diagram of measuring equipment. (B) TEM photos of measuring device details. (C and D) The relationship between κ and S of CNTs and temperature after filling C_{60}, $Gd@C_{82}$, and $Er_2@C_{82}$.

Sensor

The 1D electronic properties and large adsorption area of SWCNTs can also be applied to gas sensors[154]. The ideal sensor should be highly selective[155], highly sensitive[156], completely recyclable[157], durable[158], and low in cost[159]. Although pure SWCNTs show neither specificity for gases nor are they gas-sensitive materials[160], the selection of suitable materials for filling can confer selectivity and sensitivity to X@SWCNTs heterostructures. Chimowa *et al.* used DWCNTs filled with ZnI_2 as a formaldehyde sensor[24]. The study demonstrates that it is possible to enhance the sensitivity and selectivity of the sensor by filling DWCNT. The performance of this filling is better than the surface function of nanotubes. Quang *et al.* reported the effects of ammonia adsorption at various temperatures on the electrical performance of SWCNT[161]. When the concentration of NH_3 was as low as 5 ppm, they were still able to detect the sensor's reaction to NH_3 and showed a good linear relationship. There is no obvious sign of saturation in the linear response area of the ~40 ppm concentration. Under a higher concentration, the reaction is sub-linear, but the reaction continues to increase as the concentration level increases. Nguyen *et al.* tested NH_3 sensors based on SWCNT devices under constant current conditions. The sensor's recovery and exposure time were determined by controlling the NH_3 concentration at 5 ppm[162]. After 10 min of exposure to NH_3, the electrical resistance increased by 8%. Qi *et al.* prepare a large-scale array of low-noise electronic CNT sensors for detecting gas molecules[163]. The functionalization of polymers makes SWCNTs resistant with high sensitivity and selectivity. Polyethylene amine coatings enable nanotube devices to detect nitric oxide at levels as low as 1 ppb (one billionth). Ramachandran *et al.* filled multi-wall carbon nanotubes with Ni-Co alloy nanowires for non-enzyme electrochemical sensor probes that reliably detect glucose[164]. The

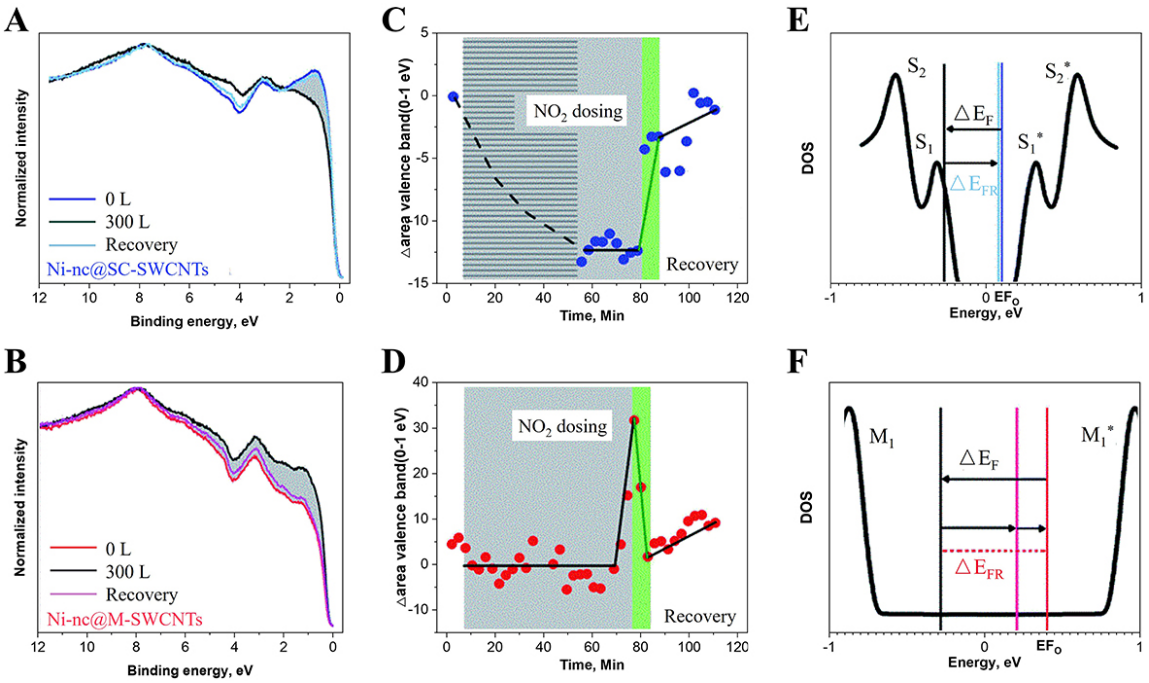

Figure 13. Properties of CNTs-filled sensors for NO_2 gas (Reproduced with permission[166].Copyright 2020, The Royal Society of Chemistry): (A and B) Photoemission spectra of Ni@sCNTs and Ni@mCNTs, respectively. (C and D) Recovery time of Ni@sCNTs and Ni@mCNTs, respectively. (E and F) Fermi level density offset plot for Ni@sCNTs and Ni@mCNTs, respectively.

outstanding electrochemical properties of the sensor are attributed to the synergy of the Ni-Co@MWCNT heterostructure. Chimowa *et al.* proposed vanadium oxide-filled MWCNTs for methane gas sensors[165]. They observed that the response time for methane gas detection decreased from 140 s (not filled) to 17 s (after filling), and the recovery time decreased from 235 s to 120 s. As a result of the metal oxide filling, the response sensitivity of the CNT was increased from 0.5% to 1.5%.

Fedi *et al.* demonstrated the feasibility of acetone nickel molecules filled SWCNTs to detect the feasibility of nitric oxide [Figure 13][166]. Figure 13A and B depict the optoelectronic transmission spectrum of the semiconductor and metal SWCNTs of Ni clusters before and after exposure to NO_2. The shaded areas in Figure 13C and D represent a 30-minute recovery time after 80 min of continuous exposure at a total NO_2 flow rate of 300 L. After 3 min, the light green stripes indicate that the recovery is nearly complete. Figure 13E and F represent the Ni cluster's Fermi level density and the Fermi level state density shift of Ni cluster metal SWCNTs. The interaction between nanotubes and sensor targets can be finely tuned by filling SWCNTs, allowing for gas adsorption and adsorption at room temperature.

CONCLUSIONS

Because of their unique properties, CNTs are a promising material in a variety of applications involving electronics, energy, and catalysis. In the last decade years, it has been experimentally demonstrated that replacing carbon atoms with other atoms, adding functional groups to the outer nanotube surface non-covalently or covalently, and filling the CNT channels are all effective ways to change the CNTs' electronic structure. This has enriched the variety of CNTs' applications and electronic properties. Filling the CNT channels is the most promising way of these to modify the nanotube characteristics because various functional materials can be encapsulated into the CNT inner channel to generate heterostructures without damaging the carbon wall structure.

In the present manuscript, we concentrated on an overview of the preparation, morphological and electronic structure characterization, and applications of filled CNTs heterostructures. With the aid of the advanced HR-TEM and AC-TEM techniques, the structures of the internal substances filling in the heterostructures are thoroughly examined *in situ*. Due to the spatial confinement effect of CNT, for some substances, the structures inside the CNT are significantly different from the bulk state and sensitive to the diameter of the CNT, which can be manipulated to design its electronic behavior. Various unstable nanomaterials have been achieved through nano chemical reactions inside the nanotubes, suggesting that the confined hollow nano space of CNTs serves as a platform for novel nanomaterials. Furthermore, spectroscopic techniques like OAS, Raman, and XAS provide researchers with simple approaches to investigate the modified electronic properties of nanotubes that occur as a result of the encapsulation of various compounds inside their channels. For example, both P and N doping of the CNT were observed when the electron donor and electron acceptor were filled. Therefore, the established methods and knowledge for modifying the electronic properties of CNTs provide the fundamentals for functioning CNTs devices.

Although various filled CNTs heterostructures have been synthesized, many challenges remain for further large-scale applications. First of all, many external factors affect the filling process, leading to low reproducibility of internal filling quality and filling yield. Therefore, it is necessary to explore and summarize more experienced filling mechanisms to guide the synthesis of high-quality samples. The yield of CNT filling may vary due to various factors, such as the size of CNTs, the properties of filling materials, the filling method, and the conditions of filling. In some cases, the yield may be high, even close to 100%, while in other cases, the yield may be relatively low or even unable to fill. Regarding the practical aspects of CNT filling, it is important to consider the expected applications and required characteristics of the filled CNTs. For example, if the filled CNTs are intended to be used as catalyst supports, the filling material should be selected based on its catalytic activity and stability, and the filling process should be optimized to ensure uniform distribution of the filling material throughout the CNTs. The filling method also has practical significance. For example, if a solvent-based filling method is used, it may be difficult to completely remove the solvent from the filled CNTs, which can affect the final performance of the material. Second, the nature of heterostructures has not been investigated in depth. Based on obtaining high-quality heterostructure samples, understanding the structural, electrical, and spectral properties of the sample from the perspective of a single tube is the next essential step in further applications. Third, it is difficult to separate high-purity semiconducting filled CNTs heterostructures for field-effect transistor applications. When the SWCNT is filled with substance, the weight and surface charge distribution of the CNT are both altered, resulting in mature separation conditions that are no longer applicable. Finally, in scenarios where filled carbon nanotubes are used in vacuum or liquid media, there is a potential for the filling material to diffuse out, reducing the stability of the structure. One potential method to minimize diffusion is to functionalize the CNT walls with appropriate chemical groups, which can help immobilize the guest material inside the CNT. Another approach is to use encapsulation techniques, such as coating the CNT with protective layers or combining the filled CNT with larger composite materials.

In conclusion, despite many challenges, the filled CNTs heterostructures would provide abundant opportunities for future interdisciplinary fundamental research and emerging applications in nanoelectronic devices, energy, storage, catalysis, and other fields.

DECLARATIONS

Authors' contributions

Conducted the literature review and drafted the original version: Teng Y, Li J

Revised the manuscript: Teng Y, Li J, Yao J, Kang L, Li Q
Conceived and supervised the project: Kang L, Li Q

Availability of data and materials
Not applicable.

Financial support and sponsorship
The authors are grateful for the technical support for Nano-X from Suzhou Institute of Nano-Tech and Nano-Bionics, Chinese Academy of Sciences (SINANO). This work was supported by the Jiangsu Province Youth Fund (BK20220289), the China Postdoctoral Science Foundation (Grant No.2022M720104), and Jiangsu Funding Program for Excellent Postdoctoral Talent.

Conflicts of interest
All authors declared that there are no conflicts of interest.

Ethical approval and consent to participate
Not applicable.

Consent for publication
Not applicable.

REFERENCES
1. Iijima S. Helical microtubules of graphitic carbon. *Nature* 1991;354:56-8. DOI
2. Peng L, Zhang Z, Qiu C. Carbon nanotube digital electronics. *Nat Electron* 2019;2:499-505. DOI
3. Saito R, Nugraha ART, Hasdeo EH, Hung NT, Izumida W. Electronic and optical properties of single wall carbon nanotubes. *Top Curr Chem* 2017;375:7. DOI PubMed
4. Yi C, Chen X, Gou F, et al. Direct measurements of the mechanical strength of carbon nanotube - aluminum interfaces. *Carbon* 2017;125:93-102. DOI
5. Zhou K, Xu N, Xie G. Thermal conductivity of carbon nanotube superlattices: comparative study with defective carbon nanotubes. *Chin Phys B* 2018;27:026501. DOI
6. Wan H, Cao Y, Lo LW, Zhao J, Sepúlveda N, Wang C. Flexible carbon nanotube synaptic transistor for neurological electronic skin applications. *ACS Nano* 2020;14:10402-12. DOI PubMed
7. Zang M. Band theory of single-walled carbon nanotubes. *IEEE Trans Nanotechnol* 2005;4:452-9. DOI
8. Desai SB, Madhvapathy SR, Sachid AB, et al. MoS_2 transistors with 1-nanometer gate lengths. *Science* 2016;354:99-102. DOI PubMed
9. Srimani T, Ding J, Yu A, et al. Comprehensive study on high purity semiconducting carbon nanotube extraction. *Adv Electron Mater* 2022;8:2101377. DOI
10. Dekker C. How we made the carbon nanotube transistor. *Nat Electron* 2018;1:518-518. DOI
11. Clément P, Xu X, Stoppiello CT, et al. Direct synthesis of multiplexed metal-nanowire-based devices by using carbon nanotubes as vector templates. *Angew Chem Int Ed* 2019;58:9928-32. DOI PubMed
12. Zhao C, Zhou X, Xie S, et al. DFT study of electronic structure and properties of N, Si and Pd-doped carbon nanotubes. *Ceram Int* 2018;44:21027-33. DOI
13. Ajayan PM, Iijima S. Capillarity-induced filling of carbon nanotubes. *Nature* 1993;361:333-4. DOI
14. Giménez-López Mdel C, Moro F, La Torre A, et al. Encapsulation of single-molecule magnets in carbon nanotubes. *Nat Commun* 2011;2:407. DOI PubMed
15. Haft M, Grönke M, Gellesch M, et al. Tailored nanoparticles and wires of Sn, Ge and Pb inside carbon nanotubes. *Carbon* 2016;101:352-60. DOI
16. Talyzin AV, Anoshkin IV, Krasheninnikov AV, et al. Synthesis of graphene nanoribbons encapsulated in single-walled carbon nanotubes. *Nano Lett* 2011;11:4352-6. DOI PubMed
17. Kharlamova MV, Kramberger C, Saito T, Pichler T. Diameter and metal-dependent growth properties of inner tubes inside

metallocene-filled single-walled carbon nanotubes. *Fuller Nanotub Carbon Nanostruct* 2020;28:20-6. DOI

18. Vasylenko A, Marks S, Wynn JM, et al. Electronic structure control of sub-nanometer 1D SnTe via Nanostructuring within single-walled carbon nanotubes. *ACS Nano* 2018;12:6023-31. DOI PubMed
19. Koizumi R, Hart AH, Brunetto G, et al. Mechano-chemical stabilization of three-dimensional carbon nanotube aggregates. *Carbon* 2016;110:27-33. DOI
20. Pan X, Bao X. The effects of confinement inside carbon nanotubes on catalysis. *ACC Chem Res* 2011;44:553-62. DOI PubMed
21. Nieto-Ortega B, Villalva J, Vera-Hidalgo M, Ruiz-González L, Burzurí E, Pérez EM. Band-gap opening in metallic single-walled carbon nanotubes by encapsulation of an organic salt. *Angew Chem Int Ed* 2017;56:12240-4. DOI PubMed
22. Ivanov VG, Kalashnyk N, Sloan J, Faulques E. Vibrational dynamics of extreme 2 × 2 and 3 × 3 potassium iodide nanowires encapsulated in single-walled carbon nanotubes. *Phys Rev B* 2018;98:125429. DOI
23. Chiu PW, Gu G, Kim GT, et al. Temperature-induced change from p to n conduction in metallofullerene nanotube peapods. *Appl Phys Lett* 2001;79:3845-7. DOI
24. Chimowa G, Yang L, Lonchambon P, et al. Tailoring of double-walled carbon nanotubes for formaldehyde sensing through encapsulation of selected materials. *Phys Status Solidi A* 2019;216:1900279. DOI
25. Kato T, Hatakeyama R, Shishido J, Oohara W, Tohji K. P-N junction with donor and acceptor encapsulated single-walled carbon nanotubes. *Appl Phys Lett* 2009;95:083109. DOI
26. Li Y, Kaneko T, Miyanaga S, Hatakeyama R. Synthesis and property characterization of c(69)n azafullerene encapsulated single-walled carbon nanotubes. *ACS Nano* 2010;4:3522-6. DOI PubMed
27. Poudel YR, Li W. Synthesis, properties, and applications of carbon nanotubes filled with foreign materials: a review. *Mater Today Phys* 2018;7:7-34. DOI
28. Eliseev AA, Kharlamova MV, Chernysheva MV, et al. Preparation and properties of single-walled nanotubes filled with inorganic compounds. *Russ Chem Rev* 2009;78:833-54. DOI
29. Yang Q, Hou P, Bai S, Wang M, Cheng H. Adsorption and capillarity of nitrogen in aggregated multi-walled carbon nanotubes. *Chem Phys Lett* 2001;345:18-24. DOI
30. Wilder JWG, Venema LC, Rinzler AG, Smalley RE, Dekker C. Electronic structure of atomically resolved carbon nanotubes. *Nature* 1998;391:59-62. DOI
31. Dujardin E, Ebbesen TW, Hiura H, Tanigaki K. Capillarity and wetting of carbon nanotubes. *Science* 1994;265:1850-2. DOI PubMed
32. Ruoff RS, Lorents DC, Chan B, Malhotra R, Subramoney S. Single crystal metals encapsulated in carbon nanoparticles. *Science* 1993;259:346-8. DOI PubMed
33. Guerret-piécourt C, Bouar YL, Lolseau A, Pascard H. Relation between metal electronic structure and morphology of metal compounds inside carbon nanotubes. *Nature* 1994;372:761-5. DOI
34. Hsu W, Li J, Terrones H, et al. Electrochemical production of low-melting metal nanowires. *Chem Phys Lett* 1999;301:159-66. DOI
35. Hirahara K, Suenaga K, Bandow S, et al. One-dimensional metallofullerene crystal generated inside single-walled carbon nanotubes. *Phys Rev Lett* 2000;85:5384-7. DOI PubMed
36. Tobias G, Shao L, Salzmann CG, Huh Y, Green ML. Purification and opening of carbon nanotubes using steam. *J Phys Chem B* 2006;110:22318-22. DOI PubMed
37. Ajayan PM, Ebbesen TW, Ichihashi T, Iijima S, Tanigaki K, Hiura H. Opening carbon nanotubes with oxygen and implications for filling. *Nature* 1993;362:522-5. DOI
38. Tsang SC, Chen YK, Harris PJF, Green MLH. A simple chemical method of opening and filling carbon nanotubes. *Nature* 1994;372:159-62. DOI
39. Hernadi K, Siska A, Thiên-nga L, Forró L, Kiricsi I. Reactivity of different kinds of carbon during oxidative purification of catalytically prepared carbon nanotubes. *Solid State Ion* 2001;141-142:203-9. DOI
40. Wiśniewski M, Terzyk AP, Hattori Y, Kaneko K, Okino F, Kruszka B. Hydrothermal opening of multiwall carbon nanotube with H_2O_2 solution. *Chem Phys Lett* 2009;482:316-9. DOI
41. Ribeiro H, Schnitzler MC, da Silva WM, Santos AP. Purification of carbon nanotubes produced by the electric arc-discharge method. *Surf Interfaces* 2021;26:101389. DOI
42. Egemen E, Nirmalakhandan N, Trevizo C. Predicting surface tension of liquid organic solvents. *Environ Sci Technol* 2000;34:2596-600. DOI
43. Eliseev A, Yashina L, Kharlamova M, Kiselev N. One-dimensional crystals inside single-walled carbon nanotubes: growth, structure and electronic properties. In: Electronic properties of carbon nanotubes. 2011. DOI
44. Sloan J, Kirkland AI, Hutchison JL, Green ML. Structural characterization of atomically regulated nanocrystals formed within single-walled carbon nanotubes using electron microscopy. *ACC Chem Res* 2002;35:1054-62. DOI PubMed
45. Wang D, Saleem MF, Javid M, et al. Formation of Sn filled CNTs nanocomposite: study of their magnetic, dielectric properties and enhanced microwave absorption performance at gigahertz frequencies. *Ceram Int* 2022;48:21961-71. DOI
46. Fujimori T, Morelos-Gómez A, Zhu Z, et al. Conducting linear chains of sulphur inside carbon nanotubes. *Nat Commun* 2013;4:2162. DOI
47. Belandria E, Millot M, Broto J, et al. Pressure dependence of Raman modes in double wall carbon nanotubes filled with 1D Tellurium. *Carbon* 2010;48:2566-72. DOI

48. Kitaura R, Nakanishi R, Saito T, Yoshikawa H, Awaga K, Shinohara H. High-yield synthesis of ultrathin metal nanowires in carbon nanotubes. *Angew Chem Int Ed* 2009;48:8298-302. DOI PubMed
49. Kharlamova MV. Comparative analysis of electronic properties of tin, gallium, and bismuth chalcogenide-filled single-walled carbon nanotubes. *J Mater Sci* 2014;49:8402-11. DOI
50. Stonemeyer S, Cain JD, Oh S, et al. Stabilization of $NbTe_3$, VTe_3 and $TiTe_3$ via nanotube encapsulation. *J Am Chem Soc* 2021;143:4563-8. DOI PubMed
51. Pham T, Oh S, Stetz P, et al. Torsional instability in the single-chain limit of a transition metal trichalcogenide. *Science* 2018;361:263-6. DOI PubMed
52. Kharlamova MV, Yashina LV, Lukashin AV. Comparison of modification of electronic properties of single-walled carbon nanotubes filled with metal halogenide, chalcogenide, and pure metal. *Appl Phys A* 2013;112:297-304. DOI
53. Kashtiban RJ, Patrick CE, Ramasse Q, Walton RI, Sloan J. Picoperovskites: the smallest conceivable isolated halide perovskite structures formed within carbon nanotubes. *Adv Mater* 2023;35:e2208575. DOI PubMed
54. Yu WJ, Liu C, Zhang L, et al. Synthesis and electrochemical lithium storage behavior of carbon nanotubes filled with iron sulfide nanoparticles. *Adv Sci* 2016;3:1600113. DOI PubMed PMC
55. Calatayud DG, Ge H, Kuganathan N, et al. Encapsulation of cadmium selenide nanocrystals in biocompatible nanotubes: DFT calculations, X-ray diffraction investigations, and confocal fluorescence imaging. *Chem Eur* 2018;7:144-58. DOI PubMed PMC
56. Norman LT, Biskupek J, Rance GA, Stoppiello CT, Kaiser U, Khlobystov AN. Synthesis of ultrathin rhenium disulfide nanoribbons using nano test tubes. *Nano Res* 2022;15:1282-7. DOI
57. Popple D, Dogan M, Hoang TV, et al. Charge-induced phase transition in encapsulated $HfTe_2$ nanoribbons. *Phys Rev Mater* 2023;7:L013001. DOI
58. Wang Z, Zhao K, Li H, et al. Ultra-narrow WS_2 nanoribbons encapsulated in carbon nanotubes. *J Mater Chem* 2011;21:171-80. DOI
59. Carter R, Suyetin M, Lister S, et al. Band gap expansion, shear inversion phase change behaviour and low-voltage induced crystal oscillation in low-dimensional tin selenide crystals. *Dalton Trans* 2014;43:7391-9. DOI PubMed
60. Wang Z, Li H, Liu Z, et al. Mixed low-dimensional nanomaterial: 2D ultranarrow MoS_2 inorganic nanoribbons encapsulated in quasi-1D carbon nanotubes. *J Am Chem Soc* 2010;132:13840-7. DOI PubMed
61. Koshino M, Niimi Y, Nakamura E, et al. Analysis of the reactivity and selectivity of fullerene dimerization reactions at the atomic level. *Nat Chem* 2010;2:117-24. DOI PubMed
62. Simon F, Kuzmany H, Rauf H, et al. Low temperature fullerene encapsulation in single wall carbon nanotubes: synthesis of N@C60@SWCNT. *Chem Phys Lett* 2004;383:362-7. DOI
63. Shimada T, Ohno Y, Okazaki T, et al. Transport properties of C78, C90 and Dy@C82 fullerenes-nanopeapods by field effect transistors. *Phys E Low Dimens Syst Nanostruct* 2004;21:1089-92. DOI
64. Luzzi DE, Smith BW, Russo R, et al. Encapsulation of metallofullerenes and metallocenes in carbon nanotubes. In AIP Conference Proceedings; 2001, pp. 622-6. DOI
65. Suenaga K, Hirahara K, Bandow S, et al. Core-level spectroscopy on the valence state of encaged metal in metallofullerene-peapods. In AIP Conference Proceedings; 2001, pp. 256-60. DOI
66. Suenaga K, Taniguchi R, Shimada T, Okazaki T, Shinohara H, Iijima S. Evidence for the intramolecular motion of Gd atoms in a $Gd_2@C_{92}$ nanopeapod. *Nano Lett* 2003;3:1395-8. DOI
67. Kuzmany H, Pfeiffer R, Simon F. The growth of nanophases in the clean room inside single-wall carbon nanotubes. *Synth Met* 2005;155:690-3. DOI
68. Zhong R, Tao J, Yang X, et al. Preparation of carbon nanotubes with high filling rate of copper nanoparticles. *Microporous Mesoporous Mater* 2022;344:112231. DOI
69. Lee J, Kim H, Kahng SJ, et al. Bandgap modulation of carbon nanotubes by encapsulated metallofullerenes. *Nature* 2002;415:1005-8. DOI PubMed
70. Botos A, Biskupek J, Chamberlain TW, et al. Carbon nanotubes as electrically active nanoreactors for multi-step inorganic synthesis: sequential transformations of molecules to nanoclusters and nanoclusters to nanoribbons. *J Am Chem Soc* 2016;138:8175-83. DOI PubMed
71. Béjar L, Mejía AA, Parra C, et al. Analysis of Raman spectroscopy and SEM of carbon nanotubes obtain by CVD. *Microsc Microanal* 2018;24:1092-3. DOI
72. Caccamo MT, Mavilia G, Magazù S. Thermal investigations on carbon nanotubes by spectroscopic techniques. *Appl Sci* 2020;10:8159. DOI
73. Banhart F. Irradiation of carbon nanotubes with a focused electron beam in the electron microscope. *J Mater Sci* 2006;41:4505-11. DOI
74. Oxley MP, Lupini AR, Pennycook SJ. Ultra-high resolution electron microscopy. *Rep Prog Phys* 2017;80:026101. DOI PubMed
75. Urban KW, Barthel J, Houben L, et al. Progress in atomic-resolution aberration corrected conventional transmission electron microscopy (CTEM). *Prog Mater Sci* 2023;133:101037. DOI
76. Guan L, Suenaga K, Shi Z, Gu Z, Iijima S. Polymorphic structures of iodine and their phase transition in confined nanospace. *Nano Lett* 2007;7:1532-5. DOI PubMed
77. Qin J, Liao P, Si M, et al. Raman response and transport properties of tellurium atomic chains encapsulated in nanotubes. *Nat Electron* 2020;3:141-7. DOI

78. Fu C, Oviedo MB, Zhu Y, et al. Confined lithium-sulfur reactions in narrow-diameter carbon nanotubes reveal enhanced electrochemical reactivity. *ACS Nano* 2018;12:9775-84. DOI PubMed
79. Corio P, Santos A, Santos P, et al. Characterization of single wall carbon nanotubes filled with silver and with chromium compounds. *Chem Phys Lett* 2004;383:475-80. DOI
80. Zhang J, Guo S, Wei J, et al. High-efficiency encapsulation of Pt nanoparticles into the channel of carbon nanotubes as an enhanced electrocatalyst for methanol oxidation. *Chemistry* 2013;19:16087-92. DOI PubMed
81. Kozhuharova R, Ritschel M, Elefant D, et al. Synthesis and characterization of aligned Fe-filled carbon nanotubes on silicon substrates. *J Mater Sci Mater Electron* 2003;14:789-91. DOI
82. Yao Y, Chen H, Lian C, et al. Fe, Co, Ni nanocrystals encapsulated in nitrogen-doped carbon nanotubes as Fenton-like catalysts for organic pollutant removal. *J Hazard Mater* 2016;314:129-39. DOI PubMed
83. Gao X, Zhang Y, Chen X, et al. Carbon nanotubes filled with metallic nanowires. *Carbon* 2004;42:47-52. DOI
84. Shi L, Rohringer P, Suenaga K, et al. Confined linear carbon chains as a route to bulk carbyne. *Nat Mater* 2016;15:634-9. DOI PubMed
85. Lenz K, Narkowicz R, Wagner K, et al. Magnetization dynamics of an individual single-crystalline Fe-filled carbon nanotube. *Small* 2019;15:e1904315. DOI PubMed
86. Aryee D, Seifu D. Shape anisotropy and hybridization enhanced magnetization in nanowires of Fe/MgO/Fe encapsulated in carbon nanotubes. *J Magn Magn Mater* 2017;429:161-5. DOI
87. Xu S, Li P, Lu Y. In situ atomic-scale analysis of Rayleigh instability in ultrathin gold nanowires. *Nano Res* 2018;11:625-32. DOI
88. Bingham JT, Proudian AP, Vyas S, Zimmerman JD. Understanding fragmentation of organic small molecules in atom probe tomography. *J Phys Chem Lett* 2021;12:10437-43. DOI PubMed
89. Jordan JW, Lowe GA, McSweeney RL, et al. Host-guest hybrid redox materials self-assembled from polyoxometalates and single-walled carbon nanotubes. *Adv Mater* 2019;31:e1904182. DOI PubMed
90. Smith BW, Monthioux M, Luzzi DE. Encapsulated C60 in carbon nanotubes. *Nature* 1998;396:323-4. DOI
91. Botos Á, Khlobystov AN, Botka B, et al. Investigation of fullerene encapsulation in carbon nanotubes using a complex approach based on vibrational spectroscopy. *Phys Status Solidi B* 2010;247:2743-5. DOI
92. Ashino M, Obergfell D, Haluska M, et al. Atomically resolved mechanical response of individual metallofullerene molecules confined inside carbon nanotubes. *Nat Nanotechnol* 2008;3:337-41. DOI PubMed
93. Khlobystov AN, Porfyrakis K, Kanai M, et al. Molecular motion of endohedral fullerenes in single-walled carbon nanotubes. *Angew Chem Int Ed* 2004;43:1386-9. DOI PubMed
94. Morgan DA, Sloan J, Green ML. Direct imaging of o-carborane molecules within single walled carbon nanotubes. *Chem Commun* 2002;20:2442-3. DOI PubMed
95. Khlobystov AN, Britz DA, Briggs GA. Molecules in carbon nanotubes. *ACC Chem Res* 2005;38:901-9. DOI PubMed
96. Villalva J, Develioglu A, Montenegro-Pohlhammer N, et al. Spin-state-dependent electrical conductivity in single-walled carbon nanotubes encapsulating spin-crossover molecules. *Nat Commun* 2021;12:1578. DOI PubMed PMC
97. Lee CH, Kang KT, Park KS, et al. The nano-memory devices of a single wall and peapod structural carbon nanotube field effect transistor. *Jpn J Appl Phys* 2003;42:5392-4. DOI
98. Friedrichs S, Sloan J, Green MLH, Meyer RR, Kirkland AI, Hutchison JL. Complete characterisation of a Sb_2O_3/(21,-8)SWNT inclusion composite. *Chem Commun* 2001;10:929-30. DOI
99. Brown G, Bailey SR, Sloan J, et al. Electron beam induced in situ clusterisation of 1D $ZrCl_4$ chains within single-walled carbon nanotubes. *Chem Commun* 2001;9:845-6. DOI
100. Eliseev AA, Chernysheva MV, Verbitskii NI, et al. Chemical reactions within single-walled carbon nanotube channels. *Chem Mater* 2009;21:5001-3. DOI
101. Nagata M, Shukla S, Nakanishi Y, et al. Isolation of single-wired transition-metal monochalcogenides by carbon nanotubes. *Nano Lett* 2019;19:4845-51. DOI PubMed
102. Eliseev A, Yashina L, Brzhezinskaya M, et al. Structure and electronic properties of AgX (X = Cl, Br, I)-intercalated single-walled carbon nanotubes. *Carbon* 2010;48:2708-21. DOI
103. Eliseev A, Yashina L, Verbitskiy N, et al. Interaction between single walled carbon nanotube and 1D crystal in CuX@SWCNT (X = Cl, Br, I) nanostructures. *Carbon* 2012;50:4021-39. DOI
104. Kharlamova MV, Yashina LV, Volykhov AA, et al. Acceptor doping of single-walled carbon nanotubes by encapsulation of zinc halogenides. *Eur Phys J B* 2012;85:34. DOI
105. Li L, Lin T, Doig J, et al. Crystal-encapsulation-induced band-structure change in single-walled carbon nanotubes: photoluminescence and Raman spectra. *Phys Rev B* 2006;74:245418. DOI
106. Stoppiello CT, Biskupek J, Li ZY, et al. A one-pot-one-reactant synthesis of platinum compounds at the nanoscale. *Nanoscale* 2017;9:14385-94. DOI PubMed
107. Cain JD, Oh S, Azizi A, et al. Ultranarrow TaS_2 nanoribbons. *Nano Lett* 2021;21:3211-7. DOI PubMed
108. Meyer S, Pham T, Oh S, et al. Metal-insulator transition in quasi-one-dimensional $HfTe_3$ in the few-chain limit. *Phys Rev B* 2019;100:4. DOI
109. Cabana L, Ballesteros B, Batista E, et al. Synthesis of PbI_2 single-layered inorganic nanotubes encapsulated within carbon nanotubes. *Adv Mater* 2014;26:2016-21. DOI PubMed

110. Wang L, Sofer Z, Bouša D, et al. Graphane nanostripes. *Angew Chem Int Ed* 2016;55:13965-9. DOI PubMed
111. Fu L, Shang C, Zhou S, Guo Y, Zhao J. Transition metal halide nanowires: a family of one-dimensional multifunctional building blocks. *Appl Phys Lett* 2022;120:023103. DOI
112. Kharlamova MV. Kinetics, electronic properties of filled carbon nanotubes investigated with spectroscopy for applications. *Nanomaterials* 2022;13:176. DOI PubMed PMC
113. Nonnenmacher M, Wickramasinghe H. Optical absorption spectroscopy by scanning force microscopy. *Ultramicroscopy* 1992;42-44:351-4. DOI
114. Kharlamova MV, Eliseev AA, Yashina LV, et al. Study of the electronic structure of single-walled carbon nanotubes filled with cobalt bromide. *JETP Lett* 2010;91:196-200. DOI
115. Kharlamova MV, Brzhezinskay MM, Vinogradov AS, et al. The formation and properties of one-dimensional $FeHal_2$ (Hal = Cl, Br, I) nanocrystals in channels of single-walled carbon nanotubes. *Nanotechnol Russ* 2009;4:634-46. DOI
116. Kharlamova MV, Yashina LV, Lukashin AV. Charge transfer in single-walled carbon nanotubes filled with cadmium halogenides. *J Mater Sci* 2013;48:8412-9. DOI
117. Kharlamova MV, Volykhov AA, Yashina LV, Egorov AV, Lukashin AV. Experimental and theoretical studies on the electronic properties of praseodymium chloride-filled single-walled carbon nanotubes. *J Mater Sci* 2015;50:5419-30. DOI
118. Kharlamova MV. Comparison of influence of incorporated 3d-, 4d- and 4f-metal chlorides on electronic properties of single-walled carbon nanotubes. *Appl Phys A* 2013;111:725-31. DOI
119. Kharlamova MV. Novel approach to tailoring the electronic properties of single-walled carbon nanotubes by the encapsulation of high-melting gallium selenide using a single-step process. *JETP Lett* 2013;98:272-7. DOI
120. Yashina LV, Eliseev AA, Kharlamova MV, et al. Growth and characterization of one-dimensional SnTe crystals within the single-walled carbon nanotube channels. *J Phys Chem C* 2011;115:3578-86. DOI
121. Si R, Fischer CF. Electron affinities of at and its homologous elements Cl, Br, and I. *Phys Rev A* 2018;98:052504. DOI
122. Jorio A, Saito R. Raman spectroscopy for carbon nanotube applications. *J Appl Phys* 2021;129:021102. DOI
123. Kharlamova MV, Eliseev AA, Yashina LV, Lukashin AV, Tretyakov YD. Synthesis of nanocomposites on basis of single-walled carbon nanotubes intercalated by manganese halogenides. *J Phys Conf Ser* 2012;345:012034. DOI
124. Kharlamova MV, Yashina LV, Eliseev AA, et al. Single-walled carbon nanotubes filled with nickel halogenides: atomic structure and doping effect. *Phys Status Solidi B* 2012;249:2328-32. DOI
125. Kharlamova MV, Kramberger C, Mittelberger A. Raman spectroscopy study of the doping effect of the encapsulated terbium halogenides on single-walled carbon nanotubes. *Appl Phys A* 2017;123:239. DOI
126. Kharlamova MV, Kramberger C, Pichler T. Semiconducting response in single-walled carbon nanotubes filled with cadmium chloride: semiconducting response in SWCNTs filled with $CdCl_2$. *Phys Status Solidi B* 2016;253:2433-9. DOI
127. Kharlamova MV, Sauer M, Saito T, et al. Doping of single-walled carbon nanotubes controlled via chemical transformation of encapsulated nickelocene. *Nanoscale* 2015;7:1383-91. DOI PubMed
128. Nascimento VV, Neves WQ, Alencar RS, et al. Origin of the giant enhanced raman scattering by sulfur chains encapsulated inside single-wall carbon nanotubes. *ACS Nano* 2021;15:8574-82. DOI PubMed
129. Li G, Fu C, Oviedo MB, et al. Giant Raman response to the encapsulation of sulfur in narrow diameter single-walled carbon nanotubes. *J Am Chem Soc* 2016;138:40-3. DOI PubMed
130. Mijit E, Trapananti A, Minicucci M, et al. Development of a high temperature diamond anvil cell for x ray absorption experiments under extreme conditions. *Radiat Phys Chem* 2020;175:108106. DOI
131. Fedoseeva YV, Orekhov AS, Chekhova GN, et al. Single-walled carbon nanotube reactor for redox transformation of mercury dichloride. *ACS Nano* 2017;11:8643-9. DOI PubMed
132. Gets AV, Krainov VP. Conductivity of single-walled carbon nanotubes. *J Exp Theor Phys* 2016;123:1084-9. DOI
133. Khosravi M, Badehian HA, Habibinejad M. Optical properties of double walled carbon nanotubes. *J Electron Spectros Relat Phenomena* 2021;248:147058. DOI
134. Shang Y, Hua C, Xu W, et al. Meter-long spiral carbon nanotube fibers show ultrauniformity and flexibility. *Nano Lett* 2016;16:1768-75. DOI PubMed
135. Chen C, Song C, Yang J, et al. Intramolecular p-i-n junction photovoltaic device based on selectively doped carbon nanotubes. *Nano Energy* 2017;32:280-6. DOI
136. Chiba T, Amma Y, Takashiri M. Heat source free water floating carbon nanotube thermoelectric generators. *Sci Rep* 2021;11:14707. DOI PubMed PMC
137. Wang JG, Liu H, Zhang X, Li X, Liu X, Kang F. Green synthesis of hierarchically porous carbon nanotubes as advanced materials for high-efficient energy storage. *Small* 2018;14:e1703950. DOI PubMed
138. Bychko IB, Abakumov AA, Lemesh NV, Strizhak PE. Catalytic activity of multiwalled carbon nanotubes in acetylene hydrogenation. *ChemCatChem* 2017;9:4470-4. DOI
139. Liu J, Lu J, Lin X, et al. The electronic properties of chiral carbon nanotubes. *Comput Mater Sci* 2017;129:290-4. DOI
140. Li Y, Kaneko T, Kong J, Hatakeyama R. Photoswitching in azafullerene encapsulated single-walled carbon nanotube FET devices. *J Am Chem Soc* 2009;131:3412-3. DOI PubMed
141. Li YF, Hatakeyama R, Shishido J, Kato T, Kaneko T. Air-stable p-n junction diodes based on single-walled carbon nanotubes encapsulating Fe nanoparticles. *Appl Phys Lett* 2007;90:173127. DOI

142. Xu L, Hu Y, Zhang H, Jiang H, Li C. Confined synthesis of FeS_2 nanoparticles encapsulated in carbon nanotube hybrids for ultrastable lithium-ion batteries. *ACS Sustain Chem Eng* 2016;4:4251-5. DOI
143. Yu WJ, Liu C, Hou PX, et al. Lithiation of silicon nanoparticles confined in carbon nanotubes. *ACS Nano* 2015;9:5063-71. DOI PubMed
144. Li S, Liu Y, Guo P, Wang C. Self-climbed amorphous carbon nanotubes filled with transition metal oxide nanoparticles for large rate and long lifespan anode materials in lithium ion batteries. *ACS Appl Mater Interfaces* 2017;9:26818-25. DOI PubMed
145. Liu Y, Wu N, Wang Z, Cao H, Liu J. Fe_3O_4 nanoparticles encapsulated in multi-walled carbon nanotubes possess superior lithium storage capability. *New J Chem* 2017;41:6241-50. DOI
146. Kim S, Song H, Jeong Y. Flexible catholyte@carbon nanotube film electrode for high-performance lithium sulfur battery. *Carbon* 2017;113:371-8. DOI
147. Landi BJ, Ganter MJ, Cress CD, Dileo RA, Raffaelle RP. Carbon nanotubes for lithium ion batteries. *Energy Environ Sci* 2009;2:638. DOI
148. Raccichini R, Varzi A, Passerini S, Scrosati B. The role of graphene for electrochemical energy storage. *Nat Mater* 2015;14:271-9. DOI PubMed
149. Kodama T, Ohnishi M, Park W, et al. Modulation of thermal and thermoelectric transport in individual carbon nanotubes by fullerene encapsulation. *Nat Mater* 2017;16:892-7. DOI PubMed
150. Fukumaru T, Fujigaya T, Nakashima N. Development of n-type cobaltocene-encapsulated carbon nanotubes with remarkable thermoelectric property. *Sci Rep* 2015;5:7951. DOI PubMed PMC
151. Aygün M, Stoppiello CT, Lebedeva MA, et al. Comparison of alkene hydrogenation in carbon nanoreactors of different diameters: probing the effects of nanoscale confinement on ruthenium nanoparticle catalysis. *J Mater Chem A* 2017;5:21467-77. DOI
152. Chamberlain TW, Earley JH, Anderson DP, Khlobystov AN, Bourne RA. Catalytic nanoreactors in continuous flow: hydrogenation inside single-walled carbon nanotubes using supercritical CO_2. *Chem Commun* 2014;50:5200-2. DOI PubMed
153. Che G, Lakshmi BB, Martin CR, Fisher ER. Metal-nanocluster-filled carbon nanotubes: catalytic properties and possible applications in electrochemical energy storage and production. *Langmuir* 1999;15:750-8. DOI
154. Ellis JE, Star A. Carbon nanotube based gas sensors toward breath analysis. *Chempluschem* 2016;81:1248-65. DOI PubMed
155. Tian R, Wang S, Hu X, et al. Novel approaches for highly selective, room-temperature gas sensors based on atomically dispersed non-precious metals. *J Mater Chem A* 2020;8:23784-94. DOI
156. Qin M, Li J, Song Y. Toward high sensitivity: perspective on colorimetric photonic crystal sensors. *Anal Chem* 2022;94:9497-507. DOI PubMed
157. Qin Z, Sun X, Zhang H, et al. A transparent, ultrastretchable and fully recyclable gelatin organohydrogel based electronic sensor with broad operating temperature. *J Mater Chem A* 2020;8:4447-56. DOI
158. Luo C, Jia J, Gong Y, Wang Z, Fu Q, Pan C. Highly sensitive, durable, and multifunctional sensor inspired by a spider. *ACS Appl Mater Interfaces* 2017;9:19955-62. DOI PubMed
159. liu H, Jiang H, Du F, Zhang D, Li Z, Zhou H. Flexible and degradable paper-based strain sensor with low cost. *ACS Sustain Chem Eng* 2017;5:10538-43. DOI
160. Kim J, Choi S, Lee J, Chung Y, Byun YT. Gas sensing properties of defect-induced single-walled carbon nanotubes. *Sens Actuator A Phys* 2016;228:688-92. DOI
161. Quang NH, Van Trinh M, Lee B, Huh J. Effect of NH_3 gas on the electrical properties of single-walled carbon nanotube bundles. *Sens Actuators B Chem* 2006;113:341-6. DOI
162. Nguyen H, Huh J. Behavior of single-walled carbon nanotube-based gas sensors at various temperatures of treatment and operation. *Sens Actuators B Chem* 2006;117:426-30. DOI
163. Qi P, Vermesh O, Grecu M, et al. Toward large arrays of multiplex functionalized carbon nanotube sensors for highly sensitive and selective molecular detection. *Nano Lett* 2003;3:347-51. DOI PubMed
164. Ramachandran K, Raj Kumar T, Babu KJ, Gnana Kumar G. Ni-Co bimetal nanowires filled multiwalled carbon nanotubes for the highly sensitive and selective non-enzymatic glucose sensor applications. *Sci Rep* 2016;6:36583. DOI PubMed PMC
165. Chimowa G, Tshabalala ZP, Akande AA, et al. Improving methane gas sensing properties of multi-walled carbon nanotubes by vanadium oxide filling. *Sens Actuators B Chem* 2017;247:11-8. DOI
166. Fedi F, Domanov O, Shiozawa H, et al. Reversible changes in the electronic structure of carbon nanotube-hybrids upon NO_2 exposure under ambient conditions. *J Mater Chem A* 2020;8:9753-9. DOI

Liu *et al. Microstructures* 2023;3:2023020
DOI: 10.20517/microstructures.2023.02

Microstructures

Review

Open Access

Check for updates

A review on pitting corrosion and environmentally assisted cracking on duplex stainless steel

Menghao Liu[1], Cuiwei Du[1], Zhiyong Liu[1], Li Wang[1], Rui Zhong[2], Xiaojie Cheng[1], Jiawei Ao[1], Teng Duan[1], Yuetong Zhu[1], Xiaogang Li[1]

[1]Institute for Advanced Material and Technology, University of Science and Technology Beijing, Beijing 100083, China.
[2]Collaborative Innovation Center of Steel Technology, University of Science and Technology Beijing, Beijing 100083, China.

Correspondence to: Prof. Cuiwei Du, Institute for Advanced Material and Technology, University of Science and Technology Beijing, Beijing 100083, China. E-mail: dcw@ustb.edu.cn

How to cite this article: Liu M, Du C, Liu Z, Wang L, Zhong R, Cheng X, Ao J, Duan T, Zhu Y, Li X. A review on pitting corrosion and environmentally assisted cracking on duplex stainless steel. *Microstructures* 2023;3:2023020. https://dx.doi.org/10.20517/microstructures.2023.02

Received: 16 Jan 2023 **First Decision:** 3 Mar 2023 **Revised:** 7 Mar 2023 **Accepted:** 28 Mar 2023 **Published:** 18 Apr 2023

Academic Editor: Xiaozhou Liao **Copy Editor:** Fangling Lan **Production Editor:** Fangling Lan

Abstract

Duplex stainless steel is widely used in the petrochemical, maritime, and food industries. However, duplex stainless steel has the problem of corrosion failures during use. This topic has not been comprehensively and academically reviewed. These factors motivate the authors to review the developments in the corrosion research of duplex stainless steel. The review found that the primary reasons for the failure of duplex stainless steels are pitting corrosion and chloride-induced stress corrosion cracking. After being submerged in water, the evolution of the passive film on the duplex stainless steel can be loosely classified into three stages: nucleation, rapid growth, and stable growth stages. Instead of dramatic rupture, the passive film rupture process is a continuous metal oxidation process. Environmental factors scarcely affect the double-layer structure of the passive film, but they affect the film's overall thickness, oxide ratio, and defect concentration. The six mechanisms of alloying elements on pitting corrosion are summarized as stabilization, ineffective, soluble precipitates, soluble inclusions, insoluble inclusions, and wrapping mechanisms. In environments containing chlorides, ferrite undergoes pitting corrosion more easily than austenite. However, the pitting corrosion resistance reverses when sufficiently large deformation is used. The mechanisms of pitting corrosion induced by precipitates include the Cr-depletion, microgalvanic, and high-stress field theories. Chloride-induced cracks always initiate in the corrosion pits and blunt when encountering austenite. Phase boundaries are both strong hydrogen traps and rapid hydrogen diffusion pathways during hydrogen-induced stress cracking.

Keywords: Duplex stainless steel, passive film, pitting corrosion, stress corrosion cracking, hydrogen embrittlement

INTRODUCTION

Duplex stainless steel has gained wide acceptance in the papermaking, petroleum, food processing, and marine industries as a material of choice for systems, structures, and components due to the combination of high strength, good toughness and excellent corrosion resistance. This is attributed to the synergistic collaboration between the ferrite and austenite phases. Duplex stainless steels are more resistant to intergranular corrosion than austenitic stainless steels, because the combination of the austenite-ferrite boundary and the ferrite phase enables the precipitation of chromium carbides without severely depleting chromium at the phase boundaries[1]. The high solubility and slow diffusion rate of hydrogen in the austenite phase of duplex stainless steel make it more difficult for hydrogen to diffuse, distinguishing duplex stainless steel from ferritic stainless steel[2].

However, as application fields have expanded, it has become clear that duplex stainless steel suffers from corrosion problems. In acidic environments, duplex stainless steels suffer from severe selective corrosion of the austenite phase[3]. In the moist H_2S environment, duplex stainless steel faces the risk of sulfide stress cracking[4]. From 2000 to 2022, several failures have been documented in journals and conferences, including *CORROSION*, *Engineering Failure Analysis*, and *Journal of Failure Analysis and Prevention*, as illustrated in Figure 1[3-8] and presented in the supplemental material [Supplementary Table 1]. Environmentally-assisted cracking (EAC), which includes hydrogen-induced stress cracking (4.55%), sulfide stress cracking (18.18%), and chloride-induced stress corrosion cracking (27.27%), accounted for 50% of the failures. Pitting corrosion-induced failures accounted for 27.27% of the failures. Additionally, both microbially-induced corrosion (MIC) and selective corrosion caused 9.09% of the failures. Crevice corrosion was responsible for 4.55% of the failures. The majority of the failures were attributed to pitting corrosion and EAC. To ensure the safety of duplex stainless steel in industrial practice, it is imperative to undertake rigorous academic investigations into these issues.

Nevertheless, current review articles mainly emphasize the production processes, such as hot working, machinability and weldments[9-14]. Only a few reviews have discussed the service processes of duplex stainless steel. de Farias Azevedo *et al.* summarized some failures of duplex stainless steels, which focused on the failures induced by improper heat treatment[15]. However, the report is deficient in academic studies concerning failures related to corrosion. Salthalaand highlighted failures in the oil and gas industry, which focus on practical advice[16]. Cassagne and Elhoud reviewed the hydrogen embrittlement of duplex stainless steels[17,18]. Since their reviews were conducted ten years ago, new findings should be added, such as the recent research on the distribution of hydrogen in the two phases and at phase boundaries. Pan performed a mini-review summarizing research on passive films using synchrotron-based analyses[19]. Han *et al.* reviewed the function of the alloying elements in duplex stainless steel, which shed little on the corrosion behavior[20]. In response to the demands of industry and the paucity of comprehensive reviews dedicated to corrosion related to practical applications, this review was undertaken to fill this knowledge gap.

This article aims to review the recent academic progress on the pitting corrosion and EAC of duplex stainless steel, which are the most common causes of failures. Because the formation and degradation of the passive film are the basis for understanding the corrosion of duplex stainless steel, this review first introduces the research on passive films from the perspective of the formation process and degradation process of the passive film. Subsequently, the progress on pitting corrosion research is reviewed and summarized from the perspectives of alloying elements and microstructures. Various distinct pitting

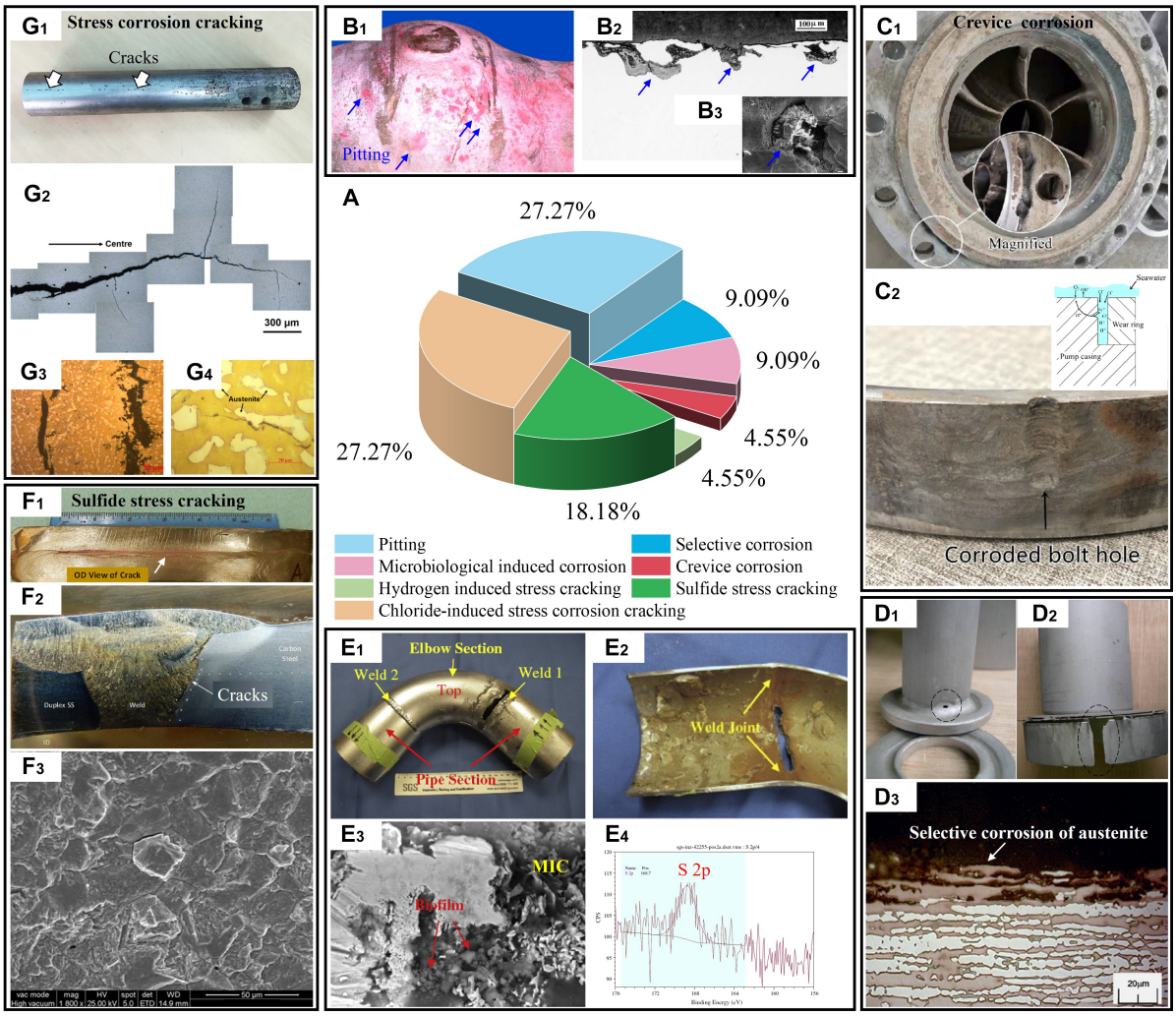

Figure 1. Environment-related failure statistics and typical cases of duplex stainless steel from 2000 to 2022. (A) Causes of failures and their proportions and (B) Failure caused by pitting corrosion (Reproduced with permission[5]. Copyright 2009, Elsevier). (B_1) Pitting corrosion was observed at the weld during the industrial inspection, (B_2) cross-sectional morphology of pitting corrosion, and (B_3) enlarged morphology of a pitted area. (C) Failure caused by crevice corrosion[6]. (Open access). (C_1) The failure point was located at the joint and (C_2) corrosion occurred along the contact area between the workpieces. A schematic diagram of the crevice corrosion mechanism is shown on the top right. (D) A failure caused by selective corrosion. (Reproduced with permission[3]. Copyright 2015, Elsevier). (D_1 and D_2) Corrosion caused perforation, and (D_3) the austenite phase was selectively corroded. (E) Failure caused by microbially-induced corrosion (MIC). (Reproduced with permission[7]. Copyright 2014, Elsevier). (E_1) Corrosion caused perforation at the weld, (E_2) the internal tube was covered with corrosion products, (E_3) biofilm was observed in the corrosion products, and (E_4) corrosion products containing sulfur element (S), indicating that corrosion was caused by sulfate-reducing bacteria (SRB) and sulfur-oxidizing bacteria (SOB). (F) Failure caused by sulfide stress cracking[8]. (Open access). (F_1) Cracking occurred near the weld/matrix interface, (F_2) cracks propagated along the side of the fusion line, and (F_3) fracture exhibited typical cleavage features. (G) Failure due to stress corrosion cracking. (Reproduced with permission[4]. Copyright 2018, Elsevier). (G_1) Cracks were visible along the length of the pipe and there was significant pitting corrosion on the pipe surface, (G_2) cross-sectional cracks with obvious dendritic bifurcations, (G_3) at the crack-propagating regions, the cracks propagated within both ferrite and austenite and (G_4) at crack-tip regions, the cracks expanded preferentially in ferrite.

corrosion mechanisms proposed in the literature to date are summarized in this section. Subsequently, the most recent studies on EAC are reviewed, and the EAC mechanisms and the most recent experimental findings are outlined. Finally, prospects for further corrosion research on duplex stainless steels are proposed.

PASSIVE FILM

Stainless steel is more corrosion-resistant than carbon steel in many applications because a dense film is formed on the surface, shielding the matrix from corrosive media. The passive film of duplex stainless steels consists of nanocrystals, hydroxides, and mixed oxides[19]. The two phases of duplex stainless steels have a gradient in their chemical composition, raising the question of whether or not their film-formation and film-degradation processes differ in any way. These issues have recently been addressed in passive film research on duplex stainless steels. This section introduces the research progress from the perspective of film formation and film degradation.

Formation of the passive film

Formation process of passive film

Chromium and molybdenum in duplex stainless steels are enriched in the ferrite phase, whereas the content of nickel and molybdenum in austenite is higher [Table 1][21-23]. The composition difference would lead to the formation difference of passive film. Overall, there is a lack of research in this area, and few studies have been published. Some scholars believe that the final passive film is dependent on the oxidation potential and ion solubility of the individual elements. Therefore, they extrapolated from the electrochemical behavior of pure metals in the environment to the composition of the passive film. Yao *et al.* predicted the passive film composition of 2,205 duplex stainless steel at different potentials by comparing the polarization curves of pure iron and pure chromium[24]. The composition of the passive film in duplex stainless steel can be readily determined using this method, which is interesting to consider. However, this view assumes that there is no interaction between the interphase passive films. This assumption might be debatable at the phase boundaries.

Another approach is to observe the passive process *in situ*. The evolution of passive films over 600 min was characterized using electrochemical atomic force microscopy (EC-AFM)[25]. Oxide particles were formed separately during the first 100 min, after which they completely covered the surface [Figure 2][25]. However, the low time resolution of EC-AFM, as compared to the rapid formation of passive films, is a drawback of this technology. Passive films form within seconds of exposure. Hence, the above study could not adequately capture the initial process of passive film formation. In recent years, researchers have also attempted to capture the formation process *in situ* at the nanometric scale using high-resolution techniques. This has yielded favorable results for the investigation of austenitic stainless steel[26,27]. Using scanning tunneling microscopes, the local oxidation of chromium was observed[26]. Therefore, a local inhomogeneity is generated once the passive film is formed. However, these studies focused on austenitic stainless steel. Further studies on the coupling process between nitrogen element and chromium element, the formation process at grain boundaries and phase boundaries, and the differences in passive film formation between ferrite and austenite from on the nanometric scale are promising for unveiling the mechanism responsible for the high corrosion resistance of duplex stainless steel. Furthermore, from a cross-sectional perspective, it is currently unknown how the passive film grows longitudinally. There are insufficient data to determine whether the oxidation is internal or external.

The study of the *in situ* passive film growth process in liquid may be another research direction because the current research is performed under electrochemical polarization conditions or in air. The state of the passive film in air differs from that in a real liquid environment. CrOOH in the passive film, which is one of the main components of the passive film in air, may react with water into other substances once it is immersed in the NaCl solution[28].

Table 1. The chemical composition of the matrix and the phases (wt.%)

Material	Phase	Cr	Mo	Ni	Mn	Ref.
UNS S32101	Total	21.69	0.36	1.56	4.92	[21]
	α	22.643	0.435	1.276	4.710	
	γ	20.735	0.280	1.857	5.247	
UNS S32205	Total	22.44	3.24	5.99	1.38	[22]
	α	23.604	4.216	5.003	1.300	
	γ	21.501	2.540	7.231	1.493	
UNS S32750	Total	24.48	4.00	6.36	0.54	[23]
	α	27.428	4.693	5.807	0.450	
	γ	24.299	3.08989	8.810	0.495	

(Reproduced with permission[21].Copyright 2019 Elsevier) (Reproduced with permission[22].Copyright 2014, Elsevier) (Reproduced with permission[23].Copyright 2015, Elsevier).

Composition and structure of the passive film

Research on passive films has focused on studying the composition and structural differences between the ferrite and austenite phases of the passive film, as shown in Figure 3[29,30]. There is a difference in the chemical composition of the passive film formed between ferrite and austenite. The contents of chromium, molybdenum and tungsten are higher in the ferritic passive film than that in the austenitic passive film. The nitrogen and nickel contents in the austenitic passive film are higher than those in the ferritic passive film[29-32]. Nickel is chemically stable and does not form oxides, which is mainly concentrated at the film/matrix interface[24]. However, both passive films are structurally composed of an outer film rich in iron and molybdenum and an inner film rich in chromium, with almost the same thickness and structure[30,32]. Other literature has shown that the passive film conductivity of the austenite phase is higher than that of the ferrite phase[33]. The crystal orientation may influence the passive film, which was identified by synchrotron hard X-ray photoemission electron microscopy (HAXPEEM)[29]. The (111) ferrite grains exhibit the lowest chromium content among the different orientations of ferrite, while the Cr_2O_3 content in the (111) ferrite grains is higher than that in the (111) austenite grain[29].

Environmental response of passive film

Environmental factors that cause corrosion failures of duplex stainless steels include pressure, temperature, sulfide, sodium hydroxide, chloride ions, vibration, and applied potentials[17]. Therefore, the effects of these factors on the composition and structure are discussed in the subsequent sections. Upon immersion in water, the structure and composition of the passive film change [Figure 4A and B][26,28]. Once immersed, the surface strain of the passive film decreases and relaxation occurs[28]. Furthermore, the content of CrOOH in the passive film decreases upon immersion in water, and when immersed in a 0.1 M NaCl solution, CrOOH vanishes [Figure 4B][28].

Based on the thermodynamic Pourbaix diagram, increasing the temperature narrows the region of metallic Fe, Cr, and Ni. Cr_2O_3 and Cr $(OH)_3$ are transformed into $FeCr_2O_4$, CrOOH, and $HCrO_2$[34]. From the perspective of the corrosion process, the temperature thickens the passive film and increases the point defects density in the passive film by analyzing the electrochemical data [Figure 4C][35]. When the temperature exceeds 40 °C, the electrochemical impendence spectra (EIS) show two-time constants, indicating that the structure changed[36]. The XPS results showed that increasing the temperature could also increase the Cr/Fe ratio in the passive film [Figure 4C][36]. However, the above conclusions were mostly drawn from electrochemical studies. Moreover, these structural changes require further verification.

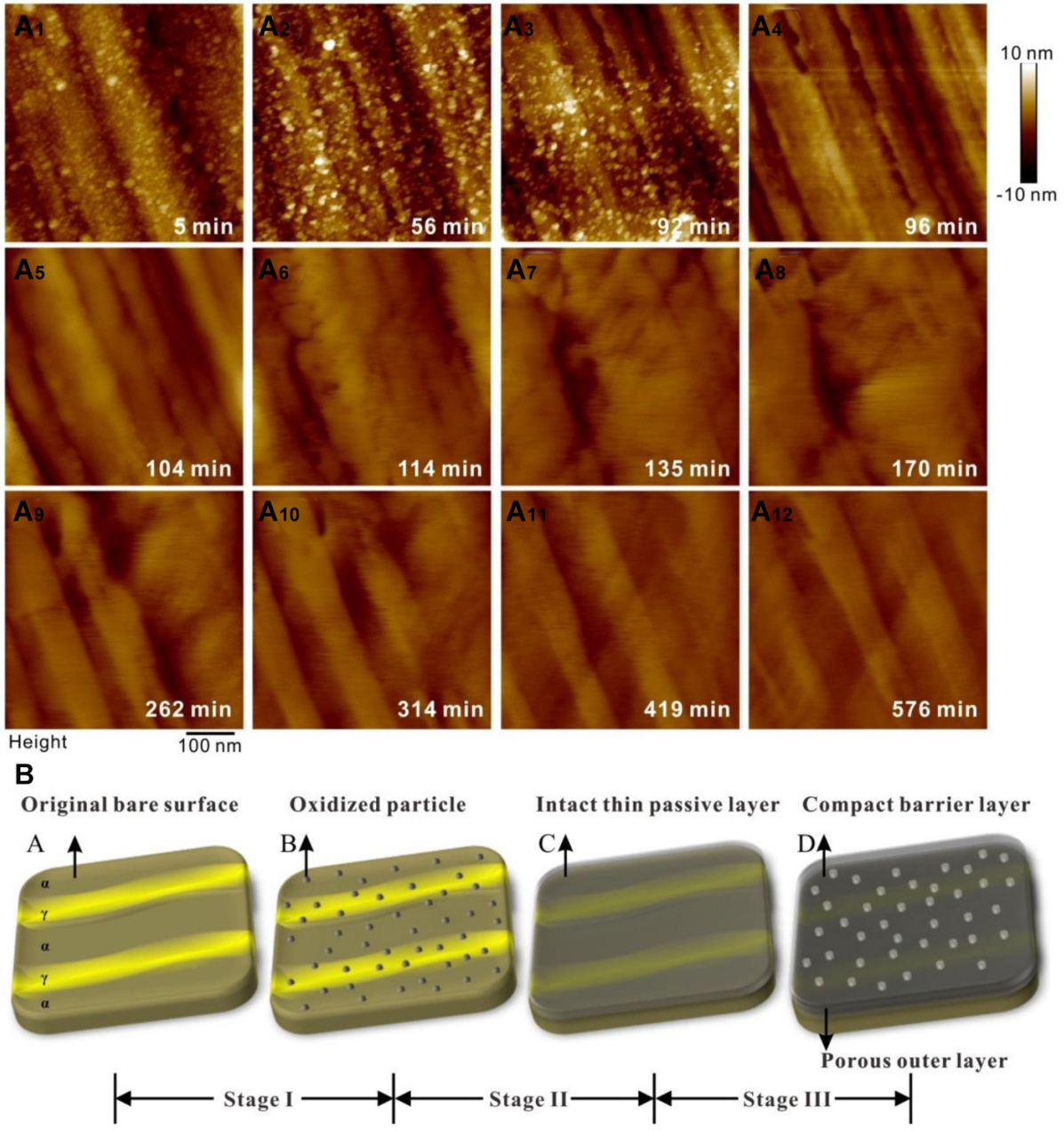

Figure 2. Evolution of the passive film on 2,205 duplex stainless steel[25]. (Open access). (A) The surface morphology changes within 600 min and (B) a schematic diagram of the passive film evolution.

Hydrostatic pressure is inevitable when considering the use of deep-sea counterparts. On the one hand, hydrostatic pressure decreases the Nyquist impedance and Cr_2O_3 proportion of the passive film [Figure 4D][37]. These changes indicate that hydrostatic pressure may reduce the compactness of the passive film[37]. On the other hand, potentiodynamic results show that hydrostatic pressure promotes the hydrogen evolution reaction by accelerating hydrogen adsorption on the metal surface and inhibiting the transfer of H_2 molecules[37]. However, the changes to the passive film due to hydrostatic pressure have not been adequately investigated. Therefore, elucidating the relationship between the changes in the passive film and the hydrogen evolution reaction may help clarify the mechanism. Cui *et al.* used the High Field Model and

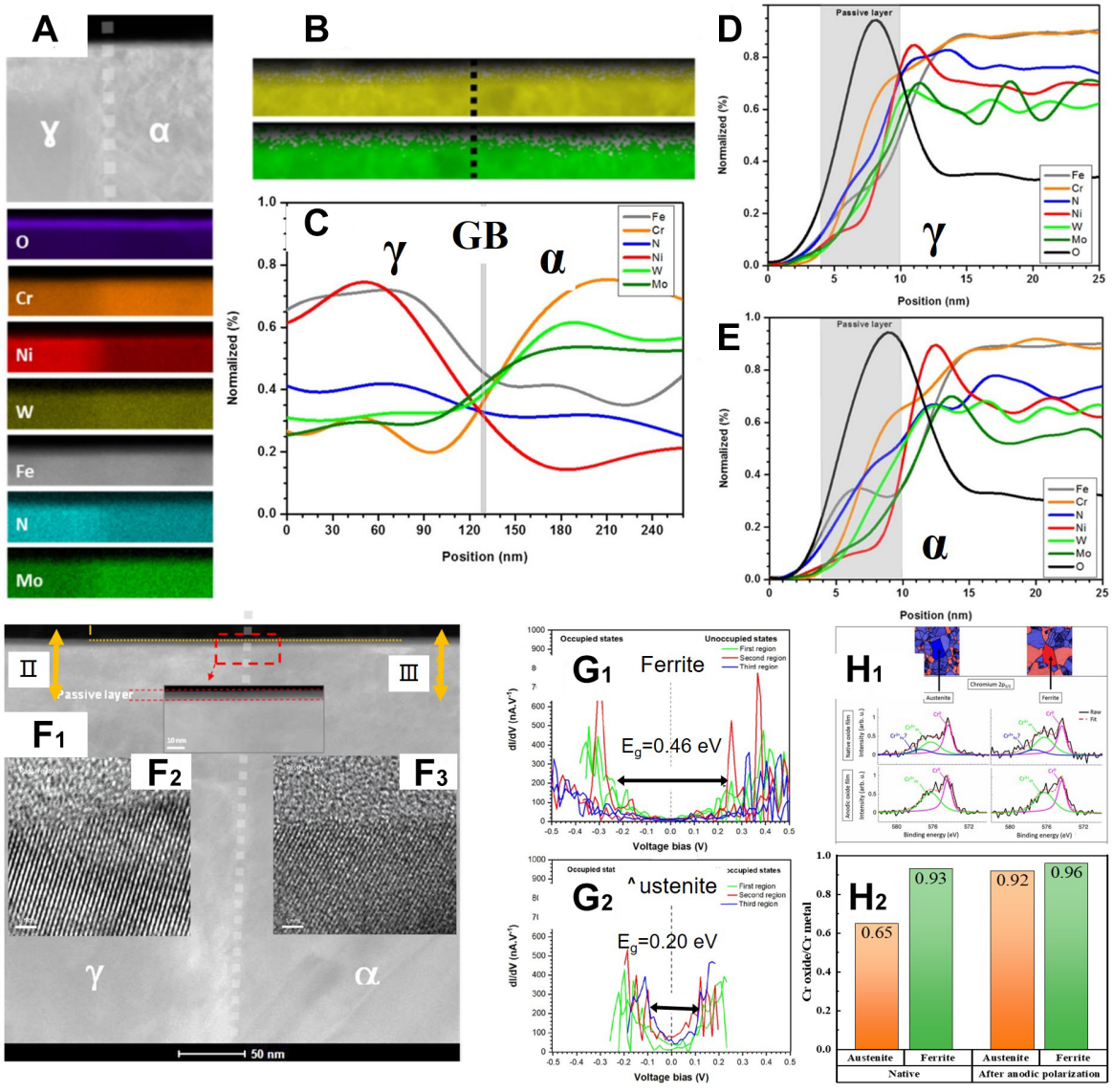

Figure 3. (A-C) EDS analyses revealed that the elements in the passive film are unevenly distributed. (Reproduced with permission[30]. Copyright 2019, Elsevier). Chromium, molybdenum and tungsten are enriched in the passive film on the ferrite phase. Nitrogen and nickel are enriched in the passive film on the austenite phase. (D and E) Line-scanning from the passive film to the matrix revealed that nickel is enriched at the film/matrix interface. (Reproduced with permission[30].Copyright 2019, Elsevier). (F) FIB analyses demonstrated that the passive film thicknesses of ferrite and austenite phases are already the same. (Reproduced with permission[30]. Copyright 2019, Elsevier). (G_1 and G_2) Scanning tunneling spectroscopy (STS) results show that the energy gap (E_g) of passive film on the ferrite phase is higher than that of the austenite phase, which means that passive film on the ferrite phase has a higher local energy gap between different semi-conductive characteristics (local conduction band potential and local valence band potential) (Reproduced with permission[30].Copyright 2019, Elsevier). (H_1 and H_2) The chromium oxide content of the passive film on the ferrite phase is higher than that on the austenite phase[29]. (Open access).

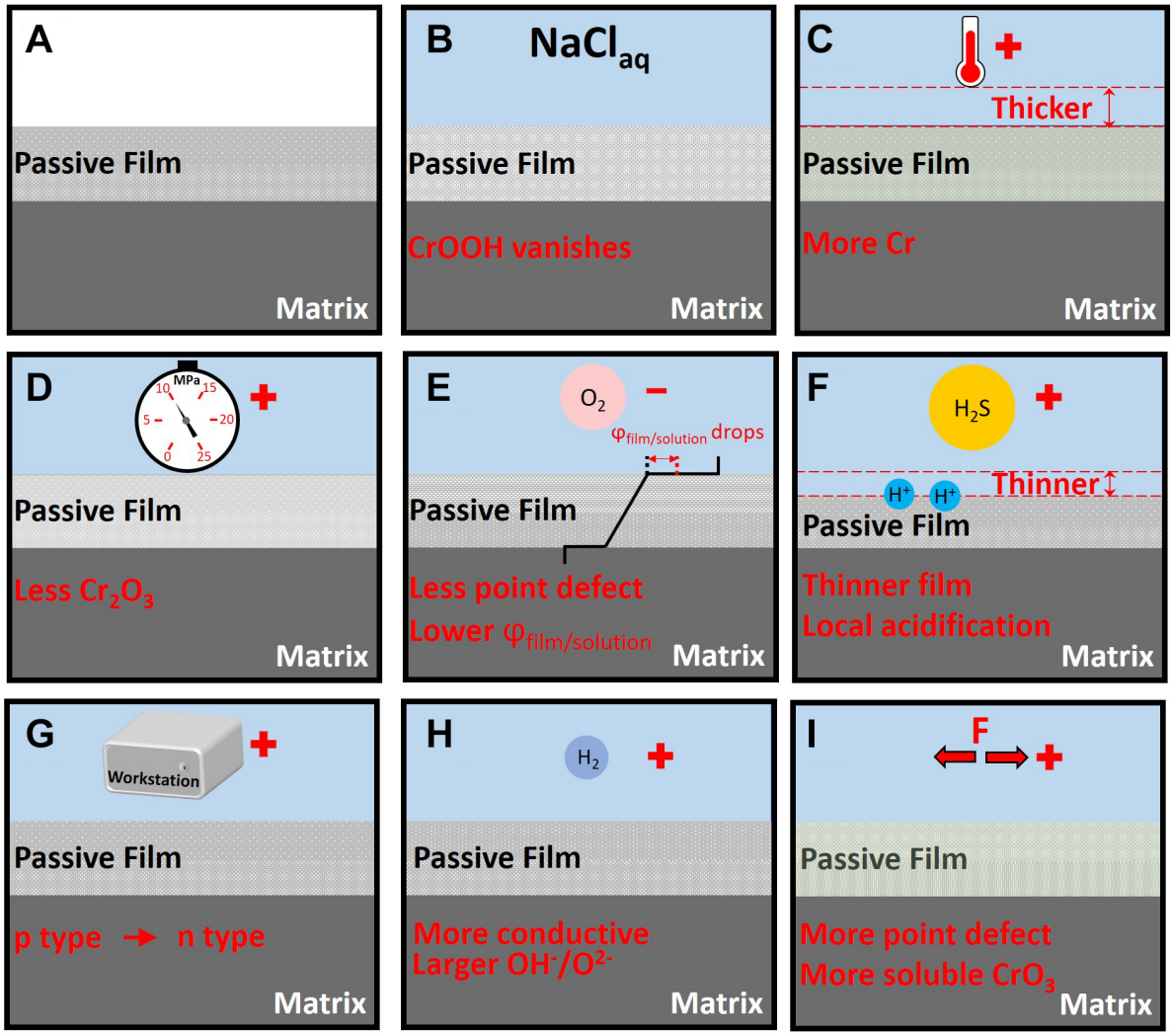

Figure 4. The effect of environmental variables on the passive film. (A) The passive film in the open air is constituted by a two-layer structure, specifically, the Cr-rich inner layer and the Fe-rich outer layer. (B) When immersion in the solutioncontaining chlorides, the CrOOH disappears[28]. (C) When the temperature increases, the passive film thickens and becomes more enriched in Cr[35]. (D) When the hydrostatic pressure increases, less Cr_2O_3 is detected[37]. (E) Removing oxygen decreases the point defects in the passive film and lowers the film/solution potential drop[35]. (F) Hydrogen sulfide accelerates the film dissolution process and local acidification processes[38]. (G) Increasing the anodic potential transforms the passive film from p-type to n-type[36]. (H) Hydrogen charging makes the passive film more conductive and imparts it with a larger OH^-/O^{2-} ratio[39,40]. (I) Stress creates more point defects and more soluble CrO_3 in the passive film[41,42].

Point Defect Model (PDM) and proposed that reducing the oxygen content in the solution can reduce the potential difference of the field/substrate interface and decreases the point defect diffusivity [Figure 4E][35].

Hydrogen sulfide generates hydrogen ions via the reacidification effect [Figure 4F][38]. Adding hydrogen sulfide does not change the semiconductor type of the passive film, but thins the film [Figure 4F][38]. A higher anodic current indicates that it accelerates the dissolution of the passive film. When the concentration was increased, the number of oxygen vacancies increased and Fe^{2+} in the passive film was consumed.

The influence of the applied potential on the passive film can be divided into anodic potentials and cathodic potentials, compared with the corrosion potential. One research strategy is focused on the composition change. At low anodic potentials, the passive film exhibits p-type semiconductor characteristics, because the passive film is composed of Cr_2O_3, FeO, NiO, and MoO_2, which contain many cationic vacancies. At high anodic potentials, the main components are Fe_2O_3, FeOOH, CrO_3, and MoO_3. The passive film resembles the n-type semiconductor [Figure 4G][36]. Therefore, the conductivity of the passive film decreases when the applied anodic potential increases[36]. Another research thought focuses on the film evolution modes under applied potentials[35]. At low anodic potentials, the passive film grows and thickens. When the applied potential shifts to the transpassive potential range, electron removal increases the number of the valent species and the passive film dissolves.

The applied cathodic potential is related to the hydrogen evolution reaction. Time-of-flight secondary ion mass spectrometry (TOF-SIMS) analyses showed that hydrogen accumulates preferentially on the grain boundaries and phase boundaries of the duplex stainless steel[39]. *In situ* AFM revealed that hydrogen charging causes a height difference on the sample surface[39]. Further studies showed that hydrogen-charged specimens exhibit an increased conductivity, and that the increase in conductivity in the austenite phase is larger than that in the ferrite phase[40]. The composition analysis of the passive film demonstrates that hydrogen charging promotes the presence of oxygen atoms in the form of hydroxide [Figure 4H][39,40].

Elastic stress and tensile stress both increase the donor and acceptor densities as determined using Mott-Schottky measurements [Figure 4I][41,42]. Stress increases the number of dislocations on the surface. According to the PDM models, dislocations promote the formation of vacancies in passive films[42].

In summary, the study on the environmental response of passive films focuses on their semiconductor properties, compositions, and structural response characteristics. As the thickness of the passive film is only a few nanometers, the above parameters are mostly obtained by substituting the macroscopic data into the existing model. Therefore, its accuracy is debatable. The specific evolution process of the influence of environmental factors on passive films is not clear. Further research can be conducted using high-resolution observation methods coupled with an environmental test bench.

Degradation of the passive film

It was believed that the rupture of the passive film was caused by the reaction from the trivalent chromium to the soluble tetravalent chromium at a certain potential, which was consistent with the sudden current increase. However, new experimental results do not support this view. Using *in situ* synchrotron grazing-incidence X-ray diffraction (GIXRD), a new phenomenon was observed that the passive film would thicken, accompanied by accelerating iron dissolution, and crystallinity decreases of the passive film when the potential increased in the passivation zone [Figure 5A-D][43]. This indicates that the rupture of the passive film is not only a valence change process but also a structural change process. As the applied potential increases to the breakdown potential, the composition and structure change simultaneously. Chromium, nickel and molybdenum in the passive film react and form soluble substances [Figure 5E and F][44]. The passive film becomes loose, whereas the film/matrix interface becomes dense owing to the enrichment of nickel and molybdenum[44]. These phenomena indicate that the rupture process of the passive film is a continuous degradation process over a wide potential range, rather than a sudden change as per the traditional definition [Figure 5G][44].

Nevertheless, there are also some factors that still need to be defined. Firstly, the difference in the degradation process of passive film between the austenite and ferrite phases is not fully understood. The

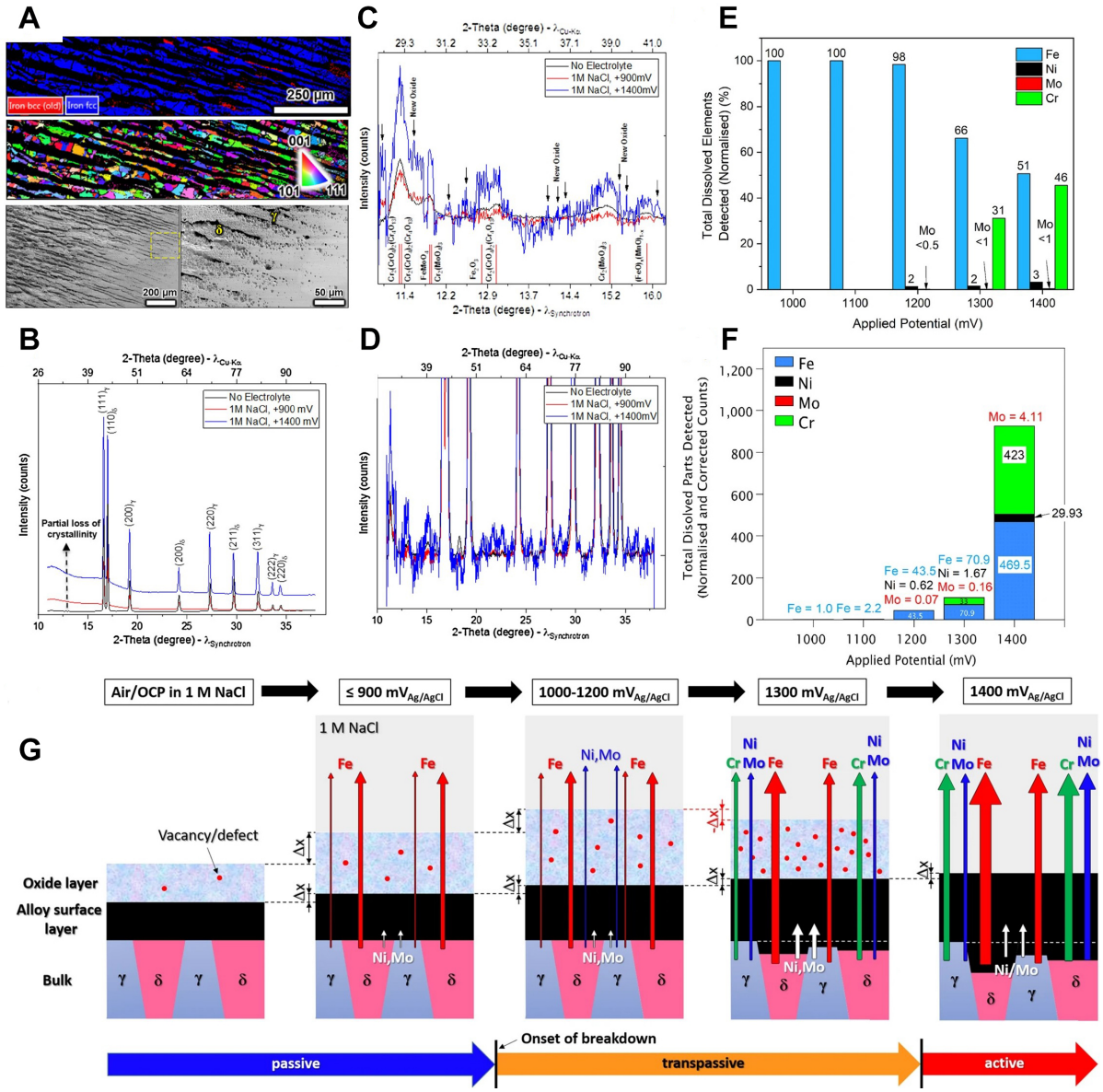

Figure 5. Study of the passive film degradation of duplex stainless steel after anodic polarization at 900 and 1400 mV (*vs.* Ag/AgCl) in 1 M NaCl (aq). (A) During the polarization test, selective dissolution occurred on the ferrite phase and the austenite phase was corroded as well. (Reproduced with permission[43].Copyright 2018, Elsevier). (B) The main composition was ferrite and austenite.(Reproduced with permission[43].Copyright 2018, Elsevier). (C) The small diffraction peaks corresponded to multiple crystal oxides (Reproduced with permission[43].Copyright 2018, Elsevier). (D) Chromium oxide is the major compound of crystal oxides. The random noise represents the nano-crystalline structure of the oxides. (Reproduced with permission[43].Copyright 2018, Elsevier). (E and F) The X-Ray Fluorescence (XRF) data for Fe, Cr, Ni, and Mo after applying different anodic polarization at room temperature[44].(Open access). (G) The degradation mechanism of 2,507 duplex stainless steel under the applied potential[44].(Open access).

studies mentioned above were conducted on the entire surface of the samples, and the exact phases cannot be distinguished. The morphological results show that both ferrite and austenite are corroded[43]. Secondly, the hydrogen evolution reaction, in addition to anodic polarization, could also degrade the passive film, since current research all focuses on the transpassive process of the passive film. This type of degradation is still not clearly understood. The mechanism by which the passive film changes if the hydrogen reaction occurs is yet to be explored.

PITTING CORROSION

The pitting corrosion mechanism includes both initiation and propagation mechanisms. The initiation and stabilization mechanisms of metastable pitting are still not comprehensively understood. Research on the pitting corrosion mechanism is mostly performed on single-phase austenitic materials, and there is little research on duplex stainless steel, which is more complicated. Current research on the pitting corrosion of duplex stainless steels mostly focuses on the correlation between various material factors with the pitting corrosion resistance and their mechanisms. These material factors include alloying composition and microstructure. As duplex stainless steels are mainly applied in chloride-containing environments, the default environment is a Cl-containing reducing environment unless specifically mentioned.

Alloying elements

Nitrogen element

Nitrogen is the element that solves the welding problems of duplex stainless steels and makes it widely commercially available. Nitrogen slightly increases the pitting potential and protection potential of duplex stainless steels[45]. When the nitrogen content in 2,507 is increased from 0.15 wt.% to 0.27 wt.%, the corrosion rate decreases by approximately 85%[46]. However, previous studies mainly focused on corrosion evaluation and not on the corrosion mechanism, and some topics remain debatable. Nitrogen is mainly distributed in the austenite phase in duplex stainless steels, and the solubility of nitrogen in the ferrite phase is extremely low. In austenitic stainless steel, nitrogen exists as NH_4^+ in the passive film[47]. Therefore, the addition of nitrogen leads to a larger difference between the Pitting Resistance Equivalence Number (PREN) values of the two phases. According to the point of view that the phase with the lowest PREN represents the pitting corrosion resistance, the addition of nitrogen has little effect on the pitting corrosion resistance, which is not consistent with the experimental results.

Molybdenum element

Molybdenum can significantly increase the pitting corrosion resistance of duplex stainless steels. When molybdenum content is below 1.0 wt.%, molybdenum exhibits no obvious improvement in pitting corrosion resistance[48]. However, adding 1.5 wt.% Mo can increase the pitting potential by at least 150 mV[49]. This is mainly attributed to two reasons. Firstly, molybdenum exists in the passive film in the form of MoO_2, MoO_3, and MoO_4^{2-}. These oxides render the passive film more stable[49]. Secondly, molybdenum accumulates in the pits and hinders further dissolution[50]. Additionally, Tian *et al.* found that tetravalent Mo species only exist in the passive film of 2,205 duplex stainless steel, as compared to single ferrite phase or single austenite phase[51]. This indicates that molybdenum plays an important role in the interaction between the austenite and ferrite phases. However, the exact interaction between the austenite and ferrite phases is unclear. The influence mechanism of molybdenum on austenite and ferrite in different stages of pitting corrosion still needs to be comprehensively understood.

Nickel element

Nickel changes the composition of the passive film by introducing metallic Ni, NiO, $Ni(OH)_2$, and $NiCl_2$[52]. This is beneficial for pitting corrosion resistance[46]. A nickel content of 5-13 wt.% increases the pitting potential in 1 M hydrochloric acid by 500 mV[53]. Nickel also narrows the protection potential range[53]. However, the content change of nickel causes a significant change in the ratio of the two phases[54], and the ratio of the two phases has a greater impact on the pitting corrosion ability. When studying the influence of nickel, it is necessary to control the ratio of the two phases by heat treatment. Additionally, the influence of nickel on pitting corrosion is still mainly observed using electrochemical tests, and comprehensive research needs to be conducted from the perspective of the corrosion morphology and the corrosion rate.

Tungsten element

Kim *et al.* reported that adding 4 wt.% tungsten increases the pitting potential and critical pitting temperature of the duplex stainless steel. It could also promote the repassivation process[52]. Tungsten exists as WO_3 and W^M in passive films. However, Torres *et al.* reported that adding 2.1 wt.% tungsten to the duplex stainless steel decreases the critical pitting temperature when aged at 920 °C for 60 s[55]. This change correlates with the fact that tungsten favors the precipitation of the chi phase. The opposite results that were obtained for tungsten are not only because the heat treatment varied but also because the steel used in the research was not a single variable. That is, industrial steels were used as the test samples[52,55], in which the contents of molybdenum, silicon and other elements vary, which also influences the pitting corrosion resistance and may obscure the influence of tungsten. Another study that controlled element tungsten more accurately showed that tungsten is slightly beneficial in resisting pitting corrosion when in the solid solution state[56]. However, tungsten is detrimental when detrimental phases containing tungsten precipitate.

Copper element

Copper exists in duplex stainless steels in the form of the solid solution state or epsilon-Cu, the latter of which exists when the sample is aged at 700-800 °C[57,58]. The addition of copper in the solid solution state has few beneficial or even negative effects[59]. Although copper is more stable than iron, the corrosion product of copper dissolves into complex ions containing Cu[57], which have not been fully understood until now. Epsilon-Cu has been reported to be more active than the ferrite and austenite phases[60], which means that it dissolves preferentially and forms nucleation sites for pitting corrosion. However, the electrochemical test is the main test method on this topic which cannot reflect the corrosion mechanisms microscopically. Additionally, *in situ* observation of the pitting corrosion process caused by epsilon-Cu is still lacking. The change in the pitting nucleation and pitting propagation stages after the addition of solid-solution copper is also vague.

Manganese element

Manganese exists in passive films in the form of oxidation states II and IIII[61]. Jang reported that adding 0.8 wt.% manganese to CD4MCU cast duplex stainless steel negatively impacts the pitting corrosion resistance, but the pitting corrosion resistance recovers by adding 2 wt.% manganese[62]. Jang attributed these changes to the proportion of austenite/ferrite[62]. Mass loss tests showed that increasing the manganese content from 1.7 to 3.3 wt.% significantly decreases the pitting corrosion resistance[49]. However, the pitting potential slightly increased when adding 8.03 wt.% in the solid solution state to duplex stainless steel[63]. Feng *et al.* reported that manganese is detrimental when aging at 800 °C for forming precipitants[64]. Therefore, it can be concluded that manganese increases the number of pit nucleation sites when it exists in the form of precipitants (inclusions or secondary phases). However, the current research shows that manganese-containing inclusions exhibit different dissolution modes, and the specific mechanisms of these different dissolution modes still need clarification. Additionally, existing studies have shown that solid-solution-state manganese does not seem to have a significant effect on the pitting corrosion of duplex stainless steels.

Titanium, niobium and tantalum

Titanium is a strong nitride-forming element which means TiN would form upon Ti is added to duplex stainless steels. Firstly, titanium could form TiN. Secondly, titanium in the solid solution state forms oxides. Zhang *et al.* has reported adding 0.01 wt.% titanium increased the pitting potential[65]. However, when 0.15 wt.% titanium was added, the pitting potential decreased. The authors attributed this change to the size of TiN. However, no direct evidence was provided to support this.

Adding 0.25 wt.% Nb to the duplex stainless steel increases the pitting potential by more than 100 mV. Niobium forms the Z phase that surrounds the anodic inclusions[66]. Furthermore, the Z phase has a low mismatch with the matrix, and there is no gap between the matrix and Z phases[66]. Therefore, niobium addition decreases the number of pitting nucleation sites.

It has been reported that tantalum additions can hinder the precipitation of harmful phases, which improves the pitting corrosion resistance[67,68]. Further studies showed that tantalum forms nitrides that coat the CaS and (Al, Ca) oxides. When CaS and (Al, Ca) oxides dissolve, stable nitrides containing tantalum prevents further propagation of pitting corrosion[69].

Other elements

Aluminum was found to have a negative effect on pitting corrosion. The negative effect is not obvious when contents are below 1 wt.%, but it is obvious when the contents are above 1.5 wt.%[70]. This is because the Al_2O_3 film formed by aluminum is porous. Studies have reported that Al_2O_3 forms an Al_2O_3 layer on the surface only when the content is above 4-6 wt.%.

The addition of 0.2 wt.% silver is detrimental to pitting corrosion resistance. Silver increases the fraction of secondary austenite[71]. Pits preferentially initiate at secondary austenite. Additionally, the solubility of silver in steel is very low, and pitting corrosion is preferentially initiated at the interface between the Ag-containing precipitates and the matrix.

Sulfur addition of 0.001 to 0.053 wt.% increases the pitting nucleation sites by approximately 3.5 times[72]. Manganese sulfides increase significantly, which deteriorates the pitting corrosion resistance. The pitting potential decreases by approximately 700 mV in 3 M NaCl[72].

Rare earth metals (REMs) exist in duplex stainless steels in the form of precipitates. The addition of REMs can refine polygonal Mn inclusions into uniform-shaped REM oxides[73]. These REMs oxides are ball-shaped at the interface and act as cathodes during corrosion[74]. Pitting corrosion occurs at the matrix near the oxide/matrix interface, rather than at the oxide[74]. The frequency of metastable pitting also decreases[74]. However, Kim *et al.* did not clarify why pitting corrosion initiates in the matrix near the oxide/matrix interface instead of in the matrix away from the REM oxides[74].

Adding 0.01-0.2 wt.% tin was also found to improve corrosion resistance, and its effect was better when it was compounded with copper[75], but the specific mechanism is still unclear.

Ruthenium addition of approximately 0.28 wt.% can increase the pitting corrosion potential in sulfuric acid by 100 mV[76]. The passive current decreases dramatically with the addition of ruthenium. This indicates that ruthenium can hinder anodic dissolution. However, in the only report on this topic, the conclusion was mainly drawn using macroscopic electrochemistry and weight loss, and the partition and influence mechanism of ruthenium between the two phases is yet to be understood.

In summary, the mechanism of alloying elements on the pitting corrosion of duplex stainless steels can be roughly divided into six mechanisms. In the stabilization mechanism [Figure 6A][49], elements accumulate in the passive film and at the bottom of pits, which stabilize the passive film and hinder further dissolution in the corrosion pits. This mechanism has been verified for molybdenum in the solid solution state[49]. In the ineffective mechanism [Figure 6B][49,59], the element does not stabilize or deteriorate the passive film. When pitting corrosion propagates, this kind of element is also corroded. This mechanism applies to manganese

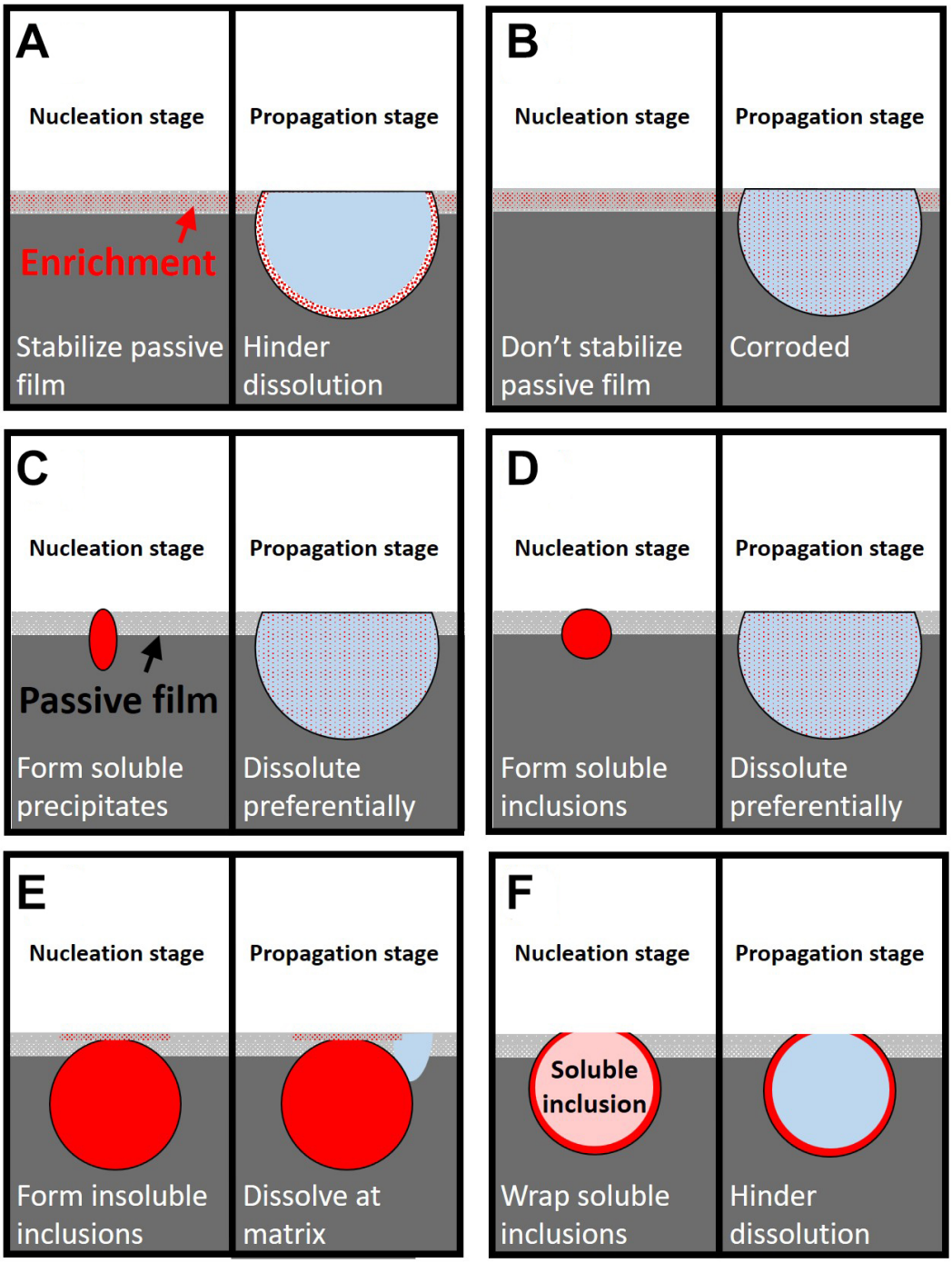

Figure 6. The six mechanisms of alloying elements on the pitting corrosion of duplex stainless steels. (A) Stabilize the passive film and hinders further dissolution in the corrosion pits. This mechanism has been verified for molybdenum[49]. (B) Does not stabilize or deteriorate the passive film. When pitting propagates, the element is also corroded. This mechanism applies to both manganese[49] and copper[59] in the solid solution state. (C) Forms soluble precipitates, which dissolve preferentially and nucleate pits. This mechanism applies to copper after aging during which epsilon-Cuis formed[60]. (D) Forms soluble inclusions. The inclusions dissolve preferentially and nucleate pits. This mechanism is applied to sulfur[72]. (E) Forms insoluble inclusions, which do not corrode. Pitting corrosion occurs in the matrix near the inclusions. This mechanism has been reported for titanium[65]. (F) Wraps soluble inclusions. When the inclusions dissolve, the protective layer protects the matrix from pitting corrosion. This mechanism applies to adding niobium[66].

and copper in the solid solution state[57]. In the soluble precipitates mechanism [Figure 6C][60], the element preferentially promotes the formation of soluble precipitates and dissolves, promoting pit nucleation. This mechanism applies to copper after aging during which epsilon-Cu is formed. Epsilon-Cu corrodes and initiates pitting[60]. In the soluble inclusions mechanism [Figure 6D][72], the alloying elements forms soluble inclusions. The inclusions preferentially dissolve and nucleate pits. This mechanism applies to the addition of sulfur[72]. In the insoluble inclusions mechanism [Figure 6E][65], the alloying elements form insoluble inclusions, which do not corrode. Pitting corrosion occurs in the matrix near the inclusions. This mechanism has been previously reported for titanium[65]. The last mechanism is the wrapping mechanism [Figure 6F][66]. The element forms a protective layer that wraps the soluble inclusions. When the inclusions dissolve, the protective layer protects the matrix from pitting corrosion[66,69].

Microstructure

Ferrite and austenite

The Volta potential difference between the ferrite and austenite phases is approximately 50-100 mV [Figure 7A][28,77]. The potentiodynamic results show that the dissolution potentials of austenite and ferrite are -281 mV_{SCE} and -323 mV_{SCE} in 1 M H_2SO_4, respectively[78]. Theoretically, the potential difference should induce micro-galvanic corrosion and accelerate the corrosion of the ferrite[79]. However, duplex stainless steel has excellent corrosion resistance. Xiao proposed that there is feedback during the corrosion process[80]. The corrosion of the ferrite phase can change the passive film of the austenite phase. Xiao also believed that the potential difference is no longer the main electrochemical inhomogeneity in corrosive media, where both phases can be passivated[80]. Tian *et al.* found that the passive current density of the duplex stainless steel was lower than that of the single-phase structure[51]. The two phases in the duplex stainless steel may interact during the corrosion process. Cheng *et al.* found that the defect density in the two-phase passive film is lower than that of single austenite phase or single ferrite phase[81]. They proposed that the two-phase galvanic corrosion effect improves the corrosion resistance of the duplex stainless steel. However, the exact galvanic corrosion mechanism is unclear. Additionally, the existing test methods are controversial. The single-phase structure obtained by anodic dissolution is honeycomb-like. Therefore, the single-phase samples have more interfaces, which increases the risk of crevice corrosion of the samples during electrochemical testing.

Pitting corrosion after deformation has also been studied[28,78]. Örnek and Engelberg reported that the ferrite phase of 2,205 undergoes pitting corrosion preferentially before cold deformation, whereas the austenite phase preferentially pits after a 40% cold deformation[77]. Luo *et al.* also found that when the cold deformation of UNS S31803 exceeds 70%, pitting corrosion preferentially initiates in the austenite phase[82]. Molyndal *et al.* proposed that the corrosion resistance of ferrite decreases monotonically with strain but not in the austenite phase[78]. Slip bands and subgrains are formed in austenite under a small deformation, which barely deteriorate the pitting corrosion resistance. High-angle grain boundaries are formed in austenite under large deformation, which deteriorates the pitting corrosion resistance[78]. Therefore, the relative pitting corrosion resistance between ferrite and austenite reverses as the cold deformation increases [Figure 7B1 and B2][83]. However, the above studies were based on the correspondence between pitting corrosion behavior and microstructural changes after deformation. Evidence for the direct correlation between microstructural changes (dislocation configuration, slip banding, and subgrain boundaries) and pitting corrosion is still lacking.

The phase ratio affects the pitting corrosion as well [Figure 7C1 and C2][23]. Ha *et al.* stated that the smaller the PREN difference between the two phases, the stronger the pitting corrosion resistance of the entire matrix[21,22]. This view was verified in 2,205 and 2,101 duplex stainless steels. However, the pitting corrosion resistance of different phase ratios in 2,507 stainless steel The pitting corrosion resistance with different

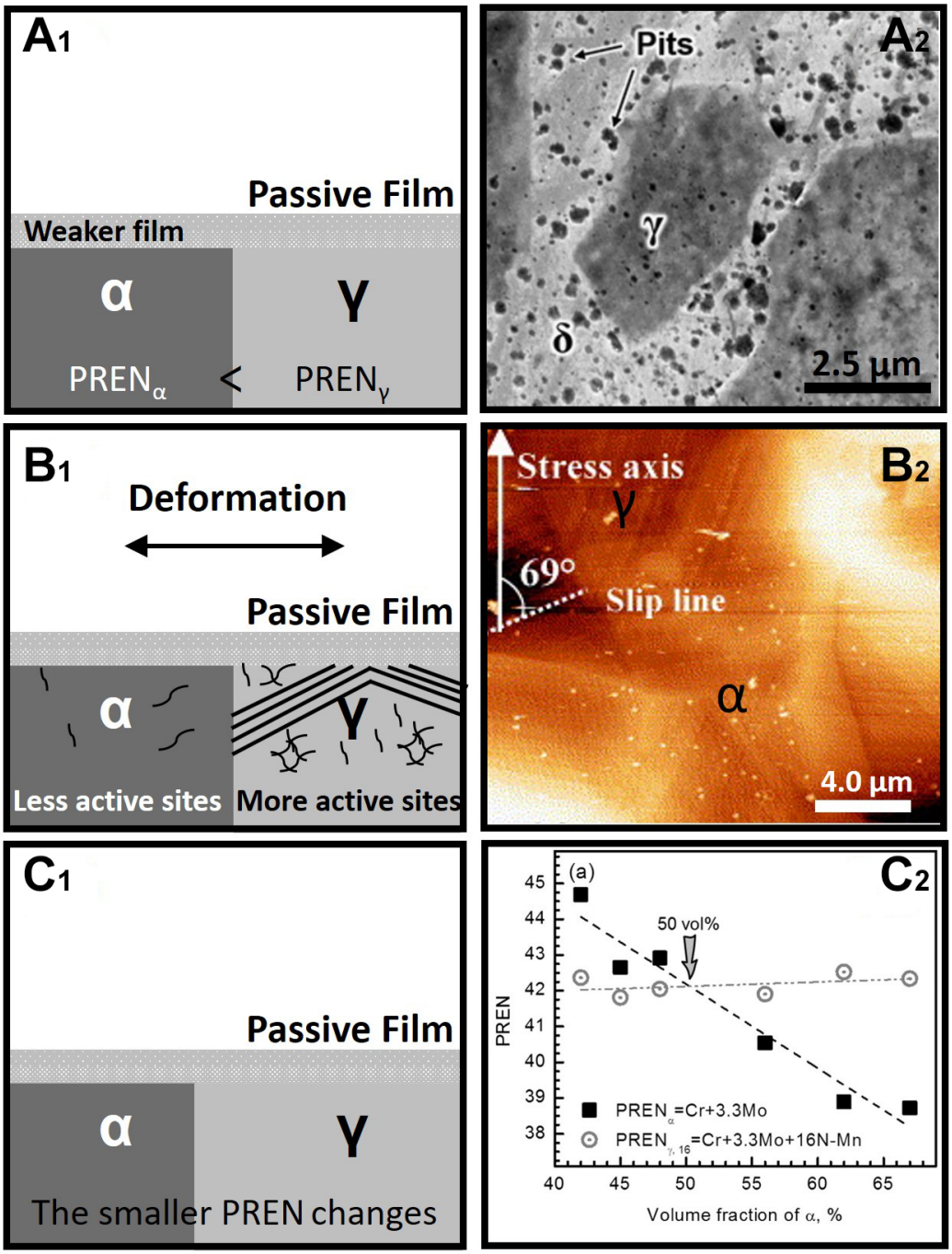

Figure 7. Summary of the studies on the pitting corrosion resistance between ferrite and austenite. (A_1) The pitting resistance equivalent number of the ferrite phase is smaller than that of austenite. Therefore, the passive film of ferrite is unstable, and pitting corrosion occurs preferentially in ferrite. (A_2) In the chloride-containing environment, the amount of pitting corrosion initiated in the ferrite phase is significantly more than that in the austenite phase[28] (Open Access) (B_1) Under plastic deformation conditions, austenite forms more dislocation walls, slip bands, and dislocation outcropping defects. Therefore, more active sites appear on the surface of the austenite phase, and the pitting corrosion resistance gap between ferrite and austenite becomes smaller and even reversed. (B_2) After plastic deformation, the defects in austenite increase significantly, whereas that in the ferrite phase changes little. (Reproduced with permission[83]. Copyright 2006, Elsevier). (C_1) Element diffusion occurs during the heat treatment process to change the phase ratio. The minimum value of the pitting resistance equivalent number changes, and the pitting corrosion resistance of duplex stainless steel changes. (C_2) UNS S32750 with different phase ratios exhibits different pitting potentials. (Reproduced with permission[23]. Copyright 2015, Elsevier.

phase ratios is not highly correlated with PREN. but it is well correlated to the two-phase micro-galvanic corrosion depth[23]. The authors believed that this is because PREN mainly reflects the initiation process of pitting corrosion. This is suitable for 2,205 and 2,101 duplex stainless steels, which are not resistant to pitting corrosion. The corrosion resistance of 2,507 duplex stainless steel is higher. Therefore, the pitting corrosion performance mainly depends on the pitting propagation process. However, according to the pitting corrosion model proposed by Li *et al.* and Frankel *et al.*, the propagation process plays a decisive role in materials that are not resistant to corrosion[84,85]. This opinion contradicts that of Ha *et al.*[21,22]. However, the model proposed by Li *et al.* has not been verified in the duplex stainless steel system[84,85]. Therefore, the mechanism of the phase ratios on the pitting corrosion requires further clarification.

Precipitates

Harmful phases precipitate in duplex stainless steels during welding and isothermal aging processes. In metals, precipitates typically have a deleterious effect on pitting resistance[86]. There are three opinions on interpretations of the pitting corrosion mechanisms of secondary precipitates.

The first theory is the Cr-depletion theory [Figure 8A1], where the precipitates are enriched with chromium or molybdenum, which forms a surrounding depleted zone. The passive film at the depleted zone is weak or absent. Pitting corrosion occurs in these areas. This theory is applicable to secondary austenite, sigma phase (σ phase), chi phase (χ phase), CrN, and Cr_2N [Figure 8A2 and A3][87-90]. Zhang *et al.* showed that after tempering at 700 °C for a sufficient duration, the pitting initiation site of S82441 duplex stainless steel transformed from austenite to the Cr-depleted zone[91]. The higher the quantity of the sigma phase, the lower the breakdown potential. However, the pitting corrosion resistance recovers to a certain degree after aging for a sufficient time. Once the sigma phase is fully precipitated, further aging causes tungsten and molybdenum to diffuse into the Cr-depleted secondary austenite[92].

The Cr-depleted α phase formed by spinodal decomposition can also induce pitting corrosion, but it is not as strong as the σ phase[93]. The micro-galvanic corrosion model has been proposed to interpret this phenomenon [Figure 8B1][94,95]. Cathodic phases enriched in chromium surround anodic phases depleted in chromium [Figure 8B2 and B3][94]. Microgalvanic corrosion induces pitting corrosion in the Cr-depleted phase, which has been proposed recently and is appliable to the α and α' phases.

The pitting corrosion that occurs around the G phase is still under debate. The stress concentration model assumes that a large strain field is generated around the square precipitate, which promotes the initiation of pitting corrosion preferentially at this location [Figure 8C1]. A high-stress field has been verified using HAFFT [Figure 8C2 and C3][96]. Another hypothesis is that pitting corrosion is related to the Cr-depleted zone around the G phase, which is caused by the growth of the G phase. Silva *et al.* recently suggested that the pitting corrosion around the G phase is due to galvanic corrosion[94].

In summary, research on microscale precipitates and nanoscale precipitates has yielded a unified understanding of the σ and χ phases, whereas the knowledge of nanoscale precipitates, such as the G phase, α phase and α' phase, is still lacking. Transmission electron microscopy (TEM) has been adapted to trace the initiation sites and propagation tendency in austenite stainless steel and got good results on Cu-rich phases and MnS[97]. This technology is promising in studying the pitting corrosion related to nanoscale precipitates in duplex stainless steel. The second tendency is from static research to dynamic research. The precipitation growth process of secondary phases leads to the diffusion of alloying elements, which affects the pitting corrosion resistance. Moreover, research on the surface passive films of the precipitates is still lacking. Current research has reported that TiB_2 nanoparticles help suppress pitting initiation, because it is easier to

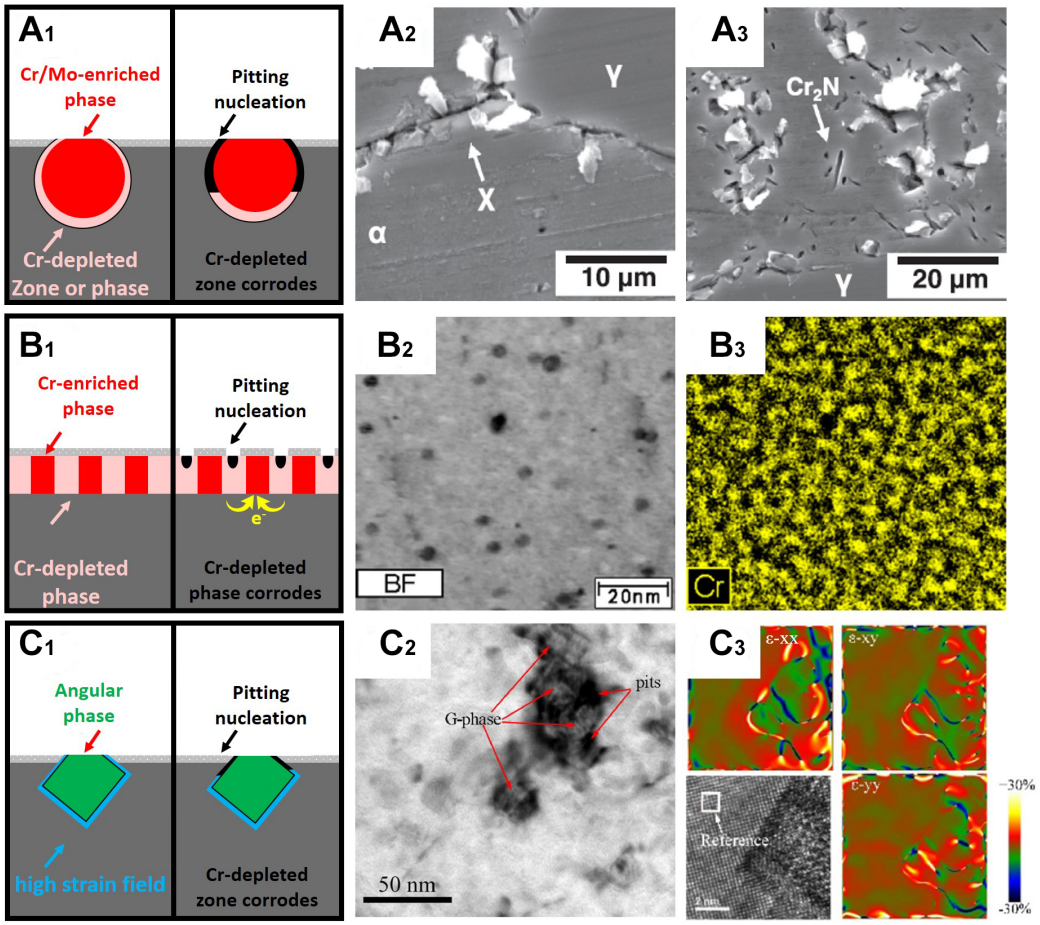

Figure 8. The proposed pitting corrosion mechanisms of the precipitants. (A) When secondary phases are enriched in chromium or molybdenum, a surrounding depleted zone is formed. The passive film at the depleted zone is weak or absent. Pitting corrosion occurred at the Cr-depleted zone. This theory is applicable to σ phase, χ phase and CrN. (Reproduced with permission[87]. Copyright 2014, Elsevier). (B) Cathodic Cr-enriched secondary phases surround anodic Cr-depleted phases. The micro-galvanic corrosion induces pitting corrosion in the Cr-depleted phase. This theory has been recently proposed and is applicable to α and α′ phases. (Reproduced with permission[94]. Copyright 2022, Elsevier). (C) A large strain field is generated around the square precipitate, which promotes the initiation of pitting corrosion preferentially at this location. (Reproduced with permission[96]. Copyright 2020, Elsevier). This opinion has been proposed to interpret the pitting corrosion around the G phase, which is still under discussion.

passivate[98]. This research indicates that the passive film on the precipitates is meaningful for further understanding the role of precipitates in pitting corrosion.

ENVIRONMENTALLY-ASSISTED CRACKING

The main causes of EAC in duplex stainless steels are chloride-induced stress corrosion cracking, hydrogen-induced stress cracking, and sulfide stress cracking, which was deduced from the failure investigation in the Introduction Section. These failures are caused by a combination of the anodic dissolution mechanism and the hydrogen embrittlement mechanism. Additionally, the stacking fault energy of the austenite phase is significantly lower than the ferrite phase. Dislocations cross-slip more easily in austenite. Therefore, dislocations move differently between the phases. This causes the crack to propagate in different ways between the phases. Nevertheless, there is a lack of discussion on this important topic.

Environmentally assisted cracking (EAC) is the main failure cause in duplex stainless steel. EAC is caused by the combined effects of materials, stress, and a corrosive environment[99]. At the mesoscopic scale, the suggested mechanisms include: (1) The anodic dissolution mechanism, which suggests that the nucleation and propagation of cracks result from the preferential dissolution of atoms at the crack tip[100]; (2) The adsorption-induced dislocation emission theory, where absorbed ions reduce the bonding force of the atoms at the crack tip, which promotes dislocations nucleation. Dislocations connect the holes, thereby inducing crack propagation[101]; (3) The weak bond theory, where hydrogen atoms generated by the electrochemical reaction are adsorbed at the crack tip. Hydrogen reduces the bonding force between the atoms at the crack tip and promotes crack propagation[102]; (4) Hydrogen promotes local plastic deformation theory. Hydrogen promotes the movement of dislocations in the plastic zone. Therefore, slip/microvoids accumulate in the local plastic deformation zone and the crack propagates[103]; and (5) The membrane rupture theory, which assumes that the crack tip moves because the brittle product film at the crack tip ruptures under the action of an external force[104].

This section reviews the mechanisms and the recent studies on the main type of failures [Figure 9][105-109]. Overall, research on the EAC mechanism in duplex stainless steels is still lacking. The current research mainly focuses on how environmental variables affect EAC susceptibility.

Chloride-induced stress corrosion cracking

Although duplex stainless steel is more resistant to stress corrosion cracking than austenitic stainless steel, it still suffers from chloride-induced stress corrosion cracking under certain conditions[4], which include seawater and alkaline environments[110]. The cracking mechanism of chloride-induced stress corrosion cracking is associated with ferrite dissolution and hydrogen embrittlement[105]. The mechanism states that in the chloride-containing environments, chloride ions penetrate the passive film of duplex stainless steel [Figure 9A1 and A2]. Owing to the poor stability of the passive film, pitting corrosion is preferentially initiated in the ferrite phase. An autocatalytic effect occurs at the bottom of the pits, which hinders the repassivation of the matrix [Figure 9A3][105]. Under the action of stress, cracks initiate at the bottom of the pits. Distinct chloride-induced cracks are branched. When cracks propagate into the austenite phase, they are arrested [Figure 9A4][105]. Therefore, the cracks mainly propagate along the ferrite/ferrite boundaries and austenite/ferrite phase boundaries.

Wu *et al.* reported that the sensitivity of 2,205 duplex stainless steel in a simulated marine atmosphere increases with a decrease in the pH, and the main control mechanisms are the anodic dissolution mechanism and the hydrogen embrittlement mechanism[111]. The susceptibility of 2,101 duplex stainless steel increases with increasing temperature, then decreases when the temperature is above 50 °C[106]. This is because high temperatures intensify the anodic dissolution and weaken the hydrogen embrittlement[106]. The addition of 5,600 ppm of nitrate prolongs the rupture time of 2,507 duplex stainless steel in 30 wt.% $MgCl_2$ by nine-fold because it can reduce the adsorption sites of chloride ions[112].

The crack propagation resistance of ferrite is weaker than that of austenite[113]. However, some researchers believe that the anodic dissolution crack initiation in ferrite is not due to pitting corrosion. Wickström suggested that the chloride-induced cracks in ferrite in water droplet evaporation experiments were due to surface dealloying[114]. Not all circumstances make the ferrite more prone to chloride-induced stress corrosion cracking. For example, Örnek found that the austenite in 2,205 duplex stainless steel suffers from chloride-induced stress corrosion cracking in the drop test[115].

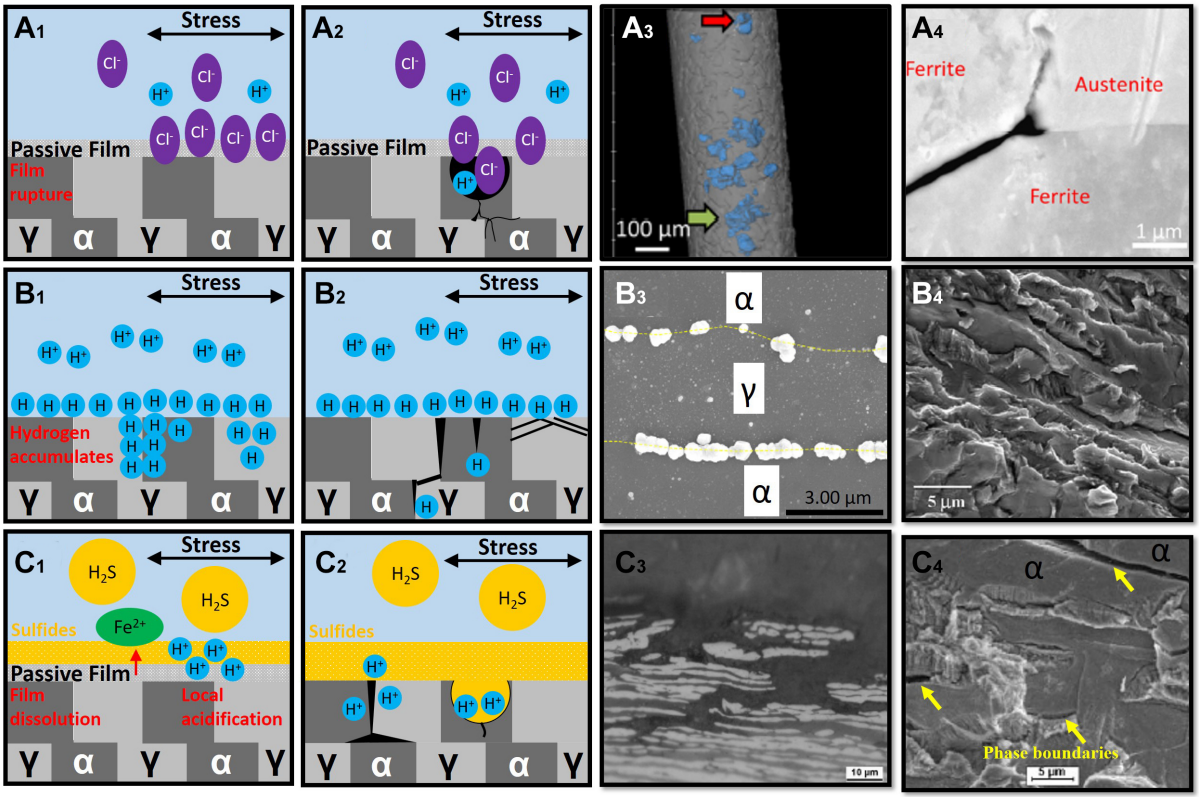

Figure 9. The mechanisms of (A_1-A_4) chloride-induced stress cracking, (B_1-B_4) hydrogen-induced stress cracking (C_1-C_4) and sulfide stress cracking. (A_1) In chloride-containing environments, chloride ions penetrate the passive film of the duplex stainless steel. (A_2) Due to the poor stability of the passivation film, pitting corrosion is preferentially initiates in the ferrite phase, and the autocatalytic effect occurs at the bottom of the pits, which hinders the repassivation of the matrix and initiates cracks under the action of stress. The crack is branched and stops when it propagates into the austenite phase. The crack propagates along the ferrite and austenite/ferrite phase boundaries. (A_3) Three-dimensional pitting corrosion on the surface of the duplex stainless steel. (Reproduced with permission[105]. Copyright 2021, Elsevier). (A_4) The crack blunts when it reaches the austenite phase and propagates along the ferrite and phase boundaries. (Reproduced with permission[105]. Copyright 2021, Elsevier). (B_1) Hydrogen atoms diffuse and accumulate at the phase boundaries. (B_2) Cracks initiate in the ferrite phase and ferrite/austenite phase boundaries and propagate in a zig-zag manner. Hydrogen promotes dislocation slip in austenite. (B_3) Hydrogen accumulates at the ferrite/austenite boundaries (Reproduced with permission[107]. Copyright 2022, Elsevier). (B_4) Both cracked ferrite and austenite exhibit brittle fracture characteristics. (Reproduced with permission[108]. Copyright 2006, Elsevier). (C_1) In sulfide environments, the passivation film dissolves and a layer of sulfide is formed on the surface. The surface is partially acidified, and the acidification effect produces corrosion. (C_2) Corrosion pits are formed in the ferrite phase. The reacidification and the autocatalytic effects generate hydrogen. Cracks initiate in the ferrite phase. Hydrogen generated at the corrosion product/substrate interface also preferentially diffuses to the phase boundaries and initiates cracks. (C_3) A sulfide corrosion product film forms on the surface of the sample, and the ferrite phase preferentially dissolves. (Reproduced with permission[106]. Copyright 2014, Elsevier). (C_4) Secondary cracks preferentially initiate at the phase boundaries and ferrite (Reproduced with permission[109]. Copyright 2006, Elsevier).

Hydrogen-induced stress cracking

Hydrogen-induced stress cracking mainly occurs under the conditions of the low cathodic protection potential and the deep-sea environment[116]. The mechanism is as follows. Hydrogen atoms diffuse and accumulate at the phase boundaries [Figure 9B1 and B3][107]. The decohesion effect of hydrogen causes the boundaries and planes to crack more easily [Figure 9B2]. A combination of the applied stress and the residual stress cause the specimen to crack. The cracks initiate in the ferrite phase and at the ferrite/austenite phase boundaries [Figure 9B4][108,117],which then propagate in a zig-zag manner[108].

Hydrogen charging in the pre-strained duplex stainless steel can induce dislocation multiplication[118]. Hydrogen can cause more obvious lattice deformation in austenite than ferrite[119]. Further studies interpreted this phenomenon by stating that hydrogen causes slip planarity and martensite formation in austenite[120,121]. Larsson *et al.* reported that hydrogen absorption causes compressive strains without stress[122]. This may be due to the expansion effect after austenite accommodates more hydrogen atoms.

The solubility of hydrogen atoms in the ferrite phase is significantly lower than that in austenite, whereas the diffusion rate in ferrite is considerably faster than that in austenite. Therefore, the ferrite phase is more prone to cracking during hydrogen embrittlement[123]. The remarkable role of the phase boundaries in hydrogen-induced stress cracking was recently recognized. The binding energies of phase boundaries, ferrite boundaries and austenite boundaries are 43.6, 26.5, and 13.5 kJ/mol, respectively[107]. Wu *et al.* used experiments, numerical simulations, and theoretical analysis to demonstrate that the phase boundaries are not only strong hydrogen traps but also act as fast hydrogen diffusion pathways[107].

Sulfide stress cracking

Sulfide stress cracking is common in the petrochemical industry. The occurrence of sulfide stress cracking is related to the dissolution of the passive film, sulfide formation, localized corrosion, and hydrogen embrittlement[124]. In the sulfide environment, the passivation film dissolves, and a layer of sulfide is formed on the surface[124]. The surface is partially acidified, and the acidification effect results in corrosion [Figure 9C1 and 9C3][106]. Corrosion pits are then formed in the ferrite phase. The reacidification and the autocatalytic effects generate hydrogen atoms. Cracks initiate in the ferrite phase [Figure 9C2]. Hydrogen atoms generate at the corrosion product/substrate interface also preferentially diffuse to the phase boundaries and initiate cracks [Figure 9C4][109].

Zucchi reported that adding sulfide to seawater increases the cracking sensitivity of 2,205 duplex stainless steel in neutral seawater[108]. The main control mechanism is the hydrogen embrittlement mechanism. The sensitivity of 2,101 duplex stainless steel after adding 10^{-3} M thiosulfate to a 20 wt.% NaCl environment is as high as 40%, but when the pH is increased to above 4.5, 2,101 is not sensitive to 10^{-2} M thiosulfate[106]. This indicates that the sulfide stress cracking is closely related to the acidification effect. The σ phase, which preferentially precipitates in the ferrite phase, also easily becomes the initiation point. The σ phase may crack first and the crack spreads along the interface between the ferrite phase and the σ phase[125].

CONCLUSIONS

This article first summarizes the failures in the last 20 years and identifies the main corrosion-related types leading to failures of duplex stainless steels. Then the study on the formation and degradation of passive films is reviewed. The mechanisms by which the alloying elements and microstructure affect the pitting corrosion are summarized. Finally, the academic progress of EAC is reviewed. The main conclusions are as follows.

(1) Among the reported failures, pitting corrosion and chloride-induced stress corrosion cracking are the main causes. Sulfide stress cracking, Hydrogen-induced stress cracking, MIC, selective corrosion and crevice corrosion are other failure causes. Therefore, academic studies should focus on the causes of such failures.

(2) The evolution of passive films after immersion in water can be roughly divided into three-stage, namely, the nucleation, rapid growth, and stable growth stages. The rupture process of the passive film is a continuous metal oxidation process rather than a sudden rupture. The film structure and composition

change simultaneously during the breakdown process.

(3) The film structure and film thickness of ferrite and austenite are very similar, whereas the chemical composition differs. Environment variables hardly change the double-layer structure of the passive film, but they change the overall thickness, oxide ratio, and defect concentration.

(4) The influence mechanisms of the alloying elements on pitting corrosion are summarized as the stabilization, ineffective, soluble precipitates, soluble inclusions, insoluble inclusions, and wrapping mechanisms. When the state of existence of the same alloying element changes, the influence mechanism varies.

(5) In the chloride-containing environment, ferrite is more prone to pitting corrosion than austenite. However, reversion of the pitting corrosion resistance occurs when a sufficiently large deformation is applied to duplex stainless steel. This is attributed to the greater number of defects generated in austenite.

(6) Three theories can be used to interpret the pitting corrosion mechanism of precipitants, namely (1) the Cr-depletion theory suggests that Cr-depleted zones surrounding precipitates cause pitting corrosion; (2) the microgalvanic theory proposes that the microgalvanic effect between Cr-enriched phase and Cr-depleted phase causes pitting corrosion; and (3) the high-stress field theory suggests that the high-stress field around the precipitates causes pitting corrosion.

(7) In chloride-induced stress corrosion cracking, chloride-induced cracks always initiate at corrosion pits and blunt upon contact with the austenite phase. In hydrogen-induced stress cracking, phase boundaries are not only strong hydrogen traps but also fast hydrogen diffusion pathways. The occurrence of sulfide stress cracking is closely related to the acidification effect of sulfide.

PROSPECTS

Owing to its high corrosion resistance, low economic cost, and good mechanical properties, duplex stainless steel is an ideal material for constructing future industrial societies. However, research on the corrosion of duplex stainless steel is still lacking. This review proposes important scientific issues and promising research directions in recent years.

(1) Studies on passive film formation are still lacking. The difference between the two phases at the micro-nanoscale and the longitudinal growth process of the passivation film from the cross-sectional perspective is still unclear. The effect of the cathodic potential on the passive film is still unclear. Therefore, it is necessary to use *in situ* scanning tunneling microscopy, high-resolution transmission microscopy, and theoretical model calculations to further explore this. Researchers need to pay more attention to the diffusion of elements along the phase boundaries.

(2) Studies on the nucleation and repassivation process of metastable pitting and the initiation process of submerged pitting corrosion are still lacking. Therefore, it is necessary to use *in situ* scanning tunneling microscopy and neutron scattering technology to study this. It is also necessary to perform quasi-*in situ* experiments, such as SKPFM and GIXRD, to understand these phenomena.

(3) The detailed mechanism of alloying elements to improve pitting corrosion still needs to be clarified because the alloying elements may play different roles in different stages of pitting corrosion. The coupling

law of more than two elements in pitting corrosion still needs to be explored. Therefore, it is necessary to use electrochemical corrosion combined with a pitting corrosion model to study this.

(4) Studies on the EAC of duplex stainless steels are not sufficient compared to the proportion of failures it has caused. The apparent regularity and microstructural mechanism of alloying elements on EAC are still unclear. Therefore, materials computing, metallurgy and electrochemistry should be used to study this and propose theoretical models.

(5) Duplex stainless steels are increasingly being used in a variety of applications. Therefore, it is necessary to study their corrosion behavior and mechanisms in more practical applications. Based on this, new types of corrosion-resistant, economical and high-strength duplex stainless steels should be developed.

DECLARATIONS

Authors' contributions

Made substantial contributions to the conception and design of the study and performed data acquisition, data analysis and interpretation: Liu M
Provided administrative and technical support: Du C, Liu Z, Li X, Wang L
Performed data acquisition: Zhong R, Cheng X, Ao J, Duan T, Zhu Y

Availability of data and materials

Not applicable.

Financial support and sponsorship

None.

Conflicts of interest

All authors declared that there are no conflicts of interest.

Ethical approval and consent to participate

Not applicable.

Consent for publication

Not applicable.

REFERENCES

1. Cobb HM. The history of stainless steel. ASM International; 2010. DOI
2. Silva B, Salvio F, Santos DD. Hydrogen induced stress cracking in UNS S32750 super duplex stainless steel tube weld joint. *Int J Hydrog Energy* 2015;40:17091-101. DOI
3. Colombo A, Trasatti S. Corrosion of an UNS S31803 distillation column for acetic acid recovery. *Eng Fail Anal* 2015;55:317-26. DOI
4. Chandra K, Singh A, Kain V, Kumar N. Sulphide stress cracking of a valve stem of duplex stainless steel. *Eng Fail Anal* 2018;94:41-6. DOI
5. Atxaga G, Irisarri A. Study of the failure of a duplex stainless steel valve. *Eng Fail Anal* 2009;16:1412-9. DOI
6. Wang H, Yang Y, Yang Z, Xu Z, Chai Y, Zhang Z. Corrosion failure analysis of duplex stainless steel in marine environment. *Int J Electrochem Sci* 2022;17:2. DOI
7. Liu W. Rapid MIC attack on 2205 duplex stainless steel pipe in a yacht. *Eng Fail Anal* 2014;42:109-20. DOI
8. Corleto CR, Argade GR. Failure analysis of dissimilar weld in heat exchanger. *Eng Fail Anal* 2017;9:27-34. DOI

9. Jebaraj A, Ajaykumar L, Deepak CR, Aditya KV. Weldability, machinability and surfacing of commercial duplex stainless steel AISI2205 for marine applications - a recent review. *J Adv Res* 2017;8:183-99. DOI PubMed PMC
10. Gowthaman P, Jeyakumar S, Saravanan B. Machinability and tool wear mechanism of duplex stainless steel - a review. *Mater Today Proc* 2020;26:1423-9. DOI
11. Westin EM. Hot cracking in duplex stainless steel weldments - a review. *Weld World* 2022;66:1483-99. DOI
12. Zhang D, Liu A, Yin B, Wen P. Additive manufacturing of duplex stainless steels - a critical review. *J Manuf Process* 2022;73:496-517. DOI
13. Verma J, Taiwade RV. Effect of welding processes and conditions on the microstructure, mechanical properties and corrosion resistance of duplex stainless steel weldments-a review. *J Manuf Process* 2017;25:134-52. DOI
14. Fan Y, Liu T, Xin L, Han Y, Lu Y, Shoji T. Thermal aging behaviors of duplex stainless steels used in nuclear power plant: a review. *J Nucl Mater* 2021;544:152693. DOI
15. Farias Azevedo CR, Boschetti Pereira H, Wolynec S, Padilha AF. An overview of the recurrent failures of duplex stainless steels. *Eng Fail Anal* 2019;97:161-88. DOI
16. Saithala JR, Kharusi A, Ghafri M, Nabhani T, Kulkarni M, Behlani N. After 30 years of duplex stainless steel experience in oil & gas-do we still face challenges? In: AMPP Annual Conference + Expo, San Antonio, TX, USA; 2022. Available from: https://onepetro.org/amppcorr/proceedings-abstract/AMPP22/4-AMPP22/D041S042R006/488731 [Last accessed on 11 April 2023].
17. Cassagne T, Embrittlement F. A review on hydrogen embrittlement of duplex stainless steels. Available from: https://onepetro.org/NACECORR/proceedings-abstract/CORR05/All-CORR05/NACE-05098/115159 [Last accessed on 11 April 2023].
18. Elhoud A, Renton N, Deans W. Hydrogen embrittlement of super duplex stainless steel in acid solution. *Int J Hydrog Energy* 2010;35:6455-64. DOI
19. Pan J. Studying the passivity and breakdown of duplex stainless steels at micrometer and nanometer scales - the influence of microstructure. *Front Mater* 2020;7:133. DOI
20. Han Y, Liu Z, Wu C, et al. A short review on the role of alloying elements in duplex stainless steels. *Tungsten* 2022:00168. DOI
21. Ha H, Lee T, Lee C, Yoon H. Understanding the relation between pitting corrosion resistance and phase fraction of S32101 duplex stainless steel. *Corros Sci* 2019;149:226-35. DOI
22. Ha H, Jang M, Lee T, Moon J. Interpretation of the relation between ferrite fraction and pitting corrosion resistance of commercial 2205 duplex stainless steel. *Corros Sci* 2014;89:154-62. DOI
23. Ha H, Jang M, Lee T, Moon J. Understanding the relation between phase fraction and pitting corrosion resistance of UNS S32750 stainless steel. *Mater Charact* 2015;106:338-45. DOI
24. Yao J, Macdonald DD, Dong C. Passive film on 2205 duplex stainless steel studied by photo-electrochemistry and ARXPS methods. *Corros Sci* 2019;146:221-32. DOI
25. Yao J, Qi Z, Dong C. Real-time evolution and characterization of passive films on individual ferrite and austenite phases of duplex stainless steel. *Electrochem Commun* 2022;137:107265. DOI
26. Ma L, Wiame F, Maurice V, Marcus P. Origin of nanoscale heterogeneity in the surface oxide film protecting stainless steel against corrosion. *NPJ Mater Degrad* 2019;3:1-9. DOI
27. Ma L, Wiame F, Maurice V, Marcus P. Stainless steel surface structure and initial oxidation at nanometric and atomic scales. *Appl Surf Sci* 2019;494:8-12. DOI
28. Örnek C, Långberg M, Evertsson J, et al. Influence of surface strain on passive film formation of duplex stainless steel and its degradation in corrosive environment. *J Electrochem Soc* 2019;166:C3071-80. DOI
29. Långberg M, Örnek C, Zhang F, et al. Characterization of native oxide and passive film on austenite/ferrite phases of duplex stainless steel using synchrotron HAXPEEM. *J Electrochem Soc* 2019;166:C3336-40. DOI
30. Rahimi E, Kosari A, Hosseinpour S, Davoodi A, Zandbergen H, Mol JM. Characterization of the passive layer on ferrite and austenite phases of super duplex stainless steel. *Appl Surf Sci* 2019;496:143634. DOI
31. Vignal V, Krawiec H, Heintz O, Mainy D. Passive properties of lean duplex stainless steels after long-term ageing in air studied using EBSD, AES, XPS and local electrochemical impedance spectroscopy. *Corros Sci* 2013;67:109-17. DOI
32. Gardin E, Zanna S, Seyeux A, Allion-maurer A, Marcus P. Comparative study of the surface oxide films on lean duplex and corresponding single phase stainless steels by XPS and ToF-SIMS. *Corros Sci* 2018;143:403-13. DOI
33. Gardin E, Zanna S, Seyeux A, Allion-maurer A, Marcus P. XPS and ToF-SIMS characterization of the surface oxides on lean duplex stainless steel - Global and local approaches. *Corros Sci* 2019;155:121-33. DOI
34. Liu H, Sun J, Qian J, et al. Revealing the temperature effects on the corrosion behaviour of 2205 duplex stainless steel from passivation to activation in a CO_2-containing geothermal environment. *Corros Sci* 2021;187:109495. DOI
35. Cui Z, Chen S, Dou Y, et al. Passivation behavior and surface chemistry of 2507 super duplex stainless steel in artificial seawater: influence of dissolved oxygen and pH. *Corros Sci* 2019;150:218-34. DOI
36. Cui Z, Wang L, Ni H, et al. Influence of temperature on the electrochemical and passivation behavior of 2507 super duplex stainless steel in simulated desulfurized flue gas condensates. *Corros Sci* 2017;118:31-48. DOI
37. Kan B, Wu W, Yang Z, Zhang X, Li J. Effects of hydrostatic pressure and pH on the corrosion behavior of 2205 duplex stainless steel. *J Electroanal Chem* 2021;886:115134. DOI
38. Wang L, Dou Y, Han S, Wu J, Cui Z. Influence of sulfide on the passivation behavior and surface chemistry of 2507 super duplex stainless steel in acidified artificial seawater. *Appl Surf Sci* 2020;504:144340. DOI

39. Yao J, Li N, Grothe H, Qi Z, Dong C. Determination of the hydrogen effects on the passive film and the micro-structure at the surface of 2205 duplex stainless steel. *Appl Surf Sci* 2021;554:149597. DOI
40. Guo LQ, Qin SX, Yang BJ, Liang D, Qiao LJ. Effect of hydrogen on semiconductive properties of passive film on ferrite and austenite phases in a duplex stainless steel. *Sci Rep* 2017;7:3317. DOI PubMed PMC
41. Chen L, Liu W, Dong B, et al. Insight into electrochemical passivation behavior and surface chemistry of 2205 duplex stainless steel: effect of tensile elastic stress. *Corros Sci* 2021;193:109903. DOI
42. Lv J, Guo W, Liang T. The effect of pre-deformation on corrosion resistance of the passive film formed on 2205 duplex stainless steel. *J Alloys Compd* 2016;686:176-83. DOI
43. Örnek C, Långberg M, Evertsson J, et al. In-situ synchrotron GIXRD study of passive film evolution on duplex stainless steel in corrosive environment. *Corros Sci* 2018;141:18-21. DOI
44. Långberg M, Örnek C, Evertsson J, et al. Redefining passivity breakdown of super duplex stainless steel by electrochemical operando synchrotron near surface X-ray analyses. *NPJ Mater Degrad* 2019;3:1-11. DOI
45. Ha HY, Lee CH, Lee TH, Kim S. Effects of nitrogen and tensile direction on stress corrosion cracking susceptibility of Ni-free FeCrMnC-based duplex stainless steels. *Materials* 2017;10:294. DOI PubMed PMC
46. Yan Z. Effects of Ni, Mn and N on microstructure and properties of 2507 super duplex stainless steel (In Chinese). In Harbin University of Science and Technology; 2014.
47. Baba H, Kodama T, Katada Y. Role of nitrogen on the corrosion behavior of austenitic stainless steels. *Corros Sci* 2002;44:2393-407. DOI
48. Merello R, Botana F, Botella J, Matres M, Marcos M. Influence of chemical composition on the pitting corrosion resistance of non-standard low-Ni high-Mn-N duplex stainless steels. *Corros Sci* 2003;45:909-21. DOI
49. An L, Cao J, Wu L, Mao H, Yang Y. Effects of Mo and Mn on pitting behavior of duplex stainless steel. *J Iron Steel Res Int* 2016;23:1333-41. DOI
50. Sun Y, Tan X, Lei L, Li J, Jiang Y. Revisiting the effect of molybdenum on pitting resistance of stainless steels. *Tungsten* 2021;3:329-37. DOI
51. Tian H, Cheng X, Wang Y, Dong C, Li X. Effect of Mo on interaction between α/γ phases of duplex stainless steel. *Electrochimica Acta* 2018;267:255-68. DOI
52. Kim JS, Xiang PJ, Kim KY. Effect of tungsten and nickel addition on the repassivation behavior of stainless steel. *Corros Sci* 2005;61:174-83. DOI
53. Potgieter J, Olubambi P, Cornish L, Machio C, Sherif EM. Influence of nickel additions on the corrosion behaviour of low nitrogen 22% Cr series duplex stainless steels. *Corros Sci* 2008;50:2572-9. DOI
54. Muthupandi V, Bala Srinivasan P, Shankar V, Seshadri S, Sundaresan S. Effect of nickel and nitrogen addition on the microstructure and mechanical properties of power beam processed duplex stainless steel (UNS 31803) weld metals. *Mater Lett* 2005;59:2305-9. DOI
55. Torres C, Hazarabedian MS, Quadir Z, Johnsen R, Iannuzzi M. The Role of tungsten on the phase transformation kinetics and its correlation with the localized corrosion resistance of 25Cr super duplex stainless steels. *J Electrochem Soc* 2020;167:081510. DOI
56. Ji L. Effect of tungsten on microstructure and properties of super duplex stainless steel $00Cr_{25}Ni_7Mo_{3.5}WCuN$ (In Chinese). In: Kunming University of Science and Technology; 2011.
57. Ran Q, Li J, Xu Y, Xiao X, Yu H, Jiang L. Novel Cu-bearing economical 21Cr duplex stainless steels. *Mater Des* 2013;46:758-65. DOI
58. Zhao Y, Liu X, Li X, Wang Y, Zhang W, Liu Z. Pitting corrosion behavior in novel Mn-N alloyed lean duplex stainless steel containing Cu. *J Mater Sci* 2018;53:824-36. DOI
59. Li P, Zhao Y, Liu Y, et al. Effect of Cu addition to 2205 duplex stainless steel on the resistance against pitting corrosion by the pseudomonas aeruginosa biofilm. *J Mater Sci Technol* 2017;33:723-7. DOI
60. Fuertes N, Pettersson R. Review-passive film properties and electrochemical response of different phases in a Cu-alloyed stainless steel after long term heat treatment. *J Electrochem Soc* 2016;163:C377-85. DOI
61. Fredriksson W, Edström K, Olsson C. XPS analysis of manganese in stainless steel passive films on 1.4432 and the lean duplex 1.4162. *Corros Sci* 2010;52:2505-10. DOI
62. Jang Y, Kim S, Lee J. Effect of different mo contents on tensile and corrosion behaviors of CD4MCU cast duplex stainless steels. *Metall Mat Trans A* 2005;36:1229-36. DOI
63. Li J, Xu Y, Xiao X, Zhao J, Jiang L, Hu J. A new resource-saving, high manganese and nitrogen super duplex stainless steel 25Cr-2Ni-3Mo-*x*Mn-N. *Mater Sci Eng A* 2009;527:245-51. DOI
64. Feng Z, Yang Y, Wang J. Effect of Mn addition on the precipitation and corrosion behaviour of 22% Cr economical duplex stainless steel after isothermal aging at 800 °C. *J Alloys Compd* 2017;699:334-44. DOI
65. Zhang J, Hu X, Chou K. Effects of Ti addition on microstructure and the associated corrosion behavior of a 22Cr-5Ni duplex stainless steel. *Mater Corros* 2021;72:1201-14. DOI
66. Li H. Dressing inclusions with "Niobium Armor": a new approach to improve the corrosion resistance of duplex stainless steels using niobium microalloying (In Chinese). In The 11th National Conference on Corrosion and Protection; 2021. DOI
67. Eleonora B, Raghuveer G, Karin A, Guocai C, Christina H, Siriki R. New duplex stainless steel 2018. (EP 3631031A1).
68. Junichiro K, Natsuki N, Nii H, Sato T. Duplex stainless steel material and duplex stainless steel tube; 2015. (EP 2947169A1).

69. Kawamori M, Kinugasa J, Fukuta Y, et al. Pitting corrosion resistance of Ta-bearing duplex stainless steel. *Mater Trans* 2021;62:1359-67. DOI
70. Meng Q, La P, Yao L, Zhang P, Wei Y, Guo X. Effect of Al on microstructure and properties of hot-rolled 2205 dual stainless steel. *Adv Mater Sci Eng* 2016;2016:1-8. DOI
71. Huang W, Chen C, Chou Y, Lin D, Yang S. Pitting corrosion behavior of silver-containing 2205 duplex stainless steel as secondary austenitic phase existed. *Mater Trans* 2013;54:553-60. DOI
72. Jeon S, Kim S, Lee J, Lee I, Park Y. Effects of sulfur addition on the formation of inclusions and the corrosion behavior of super duplex stainless steels in chloride solutions of different pH. *Mater Trans* 2012;53:1617-26. DOI
73. Kim SM, Kim JS, Kim KT, Park K, Lee CS. Effect of Ce addition on secondary phase transformation and mechanical properties of 27Cr-7Ni hyper duplex stainless steels. *Mater Sci Eng A* 2013;573:27-36. DOI
74. Kim S, Jeon S, Lee I, Park Y. Effects of rare earth metals addition on the resistance to pitting corrosion of super duplex stainless steel - part 1. *Corros Sci* 2010;52:1897-904. DOI
75. Shinji T, Yusuke O, Hiroshi U, Haruhiko K. Duplex stainless steel, duplex stainless steel slab, and duplex stainless steel material; 2014. (US 2014255244A1).
76. Potgieter JH, Ellis P, Bennekom AV. Investigation of the active dissolution behaviour of a 22% chromium duplex stainless steel with small ruthenium additions in sulphuric acid. *ISIJ Int* 1995;35:197-202. DOI
77. Örnek C, Engelberg D. SKPFM measured volta potential correlated with strain localisation in microstructure to understand corrosion susceptibility of cold-rolled grade 2205 duplex stainless steel. *Corros Sci* 2015;99:164-71. DOI
78. Mondal R, Bonagani SK, Lodh A, et al. Relating general and phase specific corrosion in a super duplex stainless steel with phase specific microstructure evolution. *Corrosion* 2019;75:1315-26. DOI
79. Tsai W, Chen J. Galvanic corrosion between the constituent phases in duplex stainless steel. *Corros Sci* 2007;49:3659-68. DOI
80. Jimei X. Metallography of stainless steel (In Chinese). Beijing: Metallurgical Industry Press; 1983. p. 122-3.
81. Cheng X, Wang Y, Dong C, Li X. The beneficial galvanic effect of the constituent phases in 2205 duplex stainless steel on the passive films formed in a 3.5% NaCl solution. *Corros Sci* 2018;134:122-30. DOI
82. Luo H, Wang X, Dong C, Xiao K, Li X. Effect of cold deformation on the corrosion behaviour of UNS S31803 duplex stainless steel in simulated concrete pore solution. *Corros Sci* 2017;124:178-92. DOI
83. Fréchard S, Martin F, Clément C, Cousty J. AFM and EBSD combined studies of plastic deformation in a duplex stainless steel. *Mater Sci Eng A* 2006;418:312-9. DOI
84. Frankel GS, Li T, Scully JR. Perspective-localized corrosion: passive film breakdown *vs.* pit growth stability. *J Electrochem Soc* 2017;164:C180-1. DOI
85. Li T, Scully JR, Frankel GS. Localized corrosion: passive film breakdown *vs.* pit growth stability: part V. Validation of a new framework for pit growth stability using one-dimensional artificial pit electrodes. *J Electrochem Soc* 2019;166:C3341-54. DOI
86. Li M, Seyeux A, Wiame F, Marcus P, Światowska J. Insights on the Al-Cu-Fe-Mn intermetallic particles induced pitting corrosion of Al-Cu-Li alloy. *Corros Sci* 2020;176:109040. DOI
87. Jeon S, Kim H, Park Y. Effects of inclusions on the precipitation of chi phases and intergranular corrosion resistance of hyper duplex stainless steel. *Corros Sci* 2014;87:1-5. DOI
88. Zhang Z, Jing H, Xu L, Han Y, Zhao L. The influence of microstructural evolution on selective corrosion in duplex stainless steel flux-cored arc welded joints. *Corros Sci* 2017;120:194-210. DOI
89. Santos DCD, Magnabosco R, de Moura-neto C. Influence of sigma phase formation on pitting corrosion of an aged UNS S31803 duplex stainless steel. *Corrosion* 2013;69:900-11. DOI
90. Jinlong L, Tongxiang L, Limin D, Chen W. Influence of sensitization on microstructure and passive property of AISI 2205 duplex stainless steel. *Corros Sci* 2016;104:144-51. DOI
91. Zhang Z, Zhao H, Zhang H, et al. Effect of isothermal aging on the pitting corrosion resistance of UNS S82441 duplex stainless steel based on electrochemical detection. *Corros Sci* 2015;93:120-5. DOI
92. Hong J, Han D, Tan H, Li J, Jiang Y. Evaluation of aged duplex stainless steel UNS S32750 susceptibility to intergranular corrosion by optimized double loop electrochemical potentiokinetic reactivation method. *Corros Sci* 2013;68:249-55. DOI
93. Melo EB, Magnabosco R. Evaluation of microstructural effects on the degree of sensitization (DOS) of a UNS S31803 duplex stainless steel aged at 475 °C. *Corrosion* 2015;71:1490-9. DOI
94. Silva R, Vacchi G, Kugelmeier C, et al. New insights into the hardening and pitting corrosion mechanisms of thermally aged duplex stainless steel at 475 °C: a comparative study between 2205 and 2101 steels. *J Mater Sci Technol* 2022;98:123-35. DOI
95. Silva R, Kugelmeier C, Vacchi G, et al. A comprehensive study of the pitting corrosion mechanism of lean duplex stainless steel grade 2404 aged at 475 °C. *Corros Sci* 2021;191:109738. DOI
96. Chen Y, Yang B, Zhou Y, Wu Y, Zhu H. Evaluation of pitting corrosion in duplex stainless steel $Fe_{20}Cr_9Ni$ for nuclear power application. *Acta Mater* 2020;197:172-83. DOI
97. Zhang B, Ma X. A review-Pitting corrosion initiation investigated by TEM. *J Mater Sci Technol* 2019;35:1455-65. DOI
98. Pan S, Dong S, Xu M. Electrochemical origin for mitigated pitting initiation in AA7075 alloy with TiB2 nanoparticles. *Appl Surf Sci* 2022;601:154275. DOI
99. Raja V, Shoji T. Stress corrosion cracking: theory and practice. Elsevier; 2011. Available from: https://www.researchgate.net/publication/297926155_Stress_corrosion_cracking_Theory_and_practice [Last accessed on 15 Apr 2023].

100. Scully JC. Mechanism of dissolution-controlled cracking. *Metal Sci* 1978;12:290-300. DOI
101. Liu H. A unified model of environment-assisted cracking. *Acta Mater* 2008;56:4339-48. DOI
102. Mcmahon C. Hydrogen-induced intergranular fracture of steels. *Eng Fract Mech* 2001;68:773-88. DOI
103. Birnbaum H, Robertson I, Sofronis P, Teter D. Mechanisms of hydrogen related fracture-a review. In: Second International Conference on Corrosion-Deformation Interactions; 1996. pp. 172-95. Available from: https://www.researchgate.net/publication/287494691_Mechanisms_of_hydrogen_related_fracture_-_a_review_in_T_Magnin_Ed [Last accessed on 15 Apr 2023].
104. Barnes A, Senior NA, Newman RC. Film-induced cleavage of Ag-Au alloys. *Metall Mat Trans A* 2009;40:58-68. DOI
105. Eguchi K, Burnett TL, Engelberg DL. X-ray tomographic observation of environmental assisted cracking in heat-treated lean duplex stainless steel. *Corros Sci* 2021;184:109363. DOI
106. Zanotto F, Grassi V, Balbo A, Monticelli C, Zucchi F. Stress corrosion cracking of LDX 2101® duplex stainless steel in chloride solutions in the presence of thiosulphate. *Corros Sci* 2014;80:205-12. DOI
107. Wu W, Zhang X, Li W, et al. Effect of hydrogen trapping on hydrogen permeation in a 2205 duplex stainless steel: role of austenite-ferrite interface. *Corros Sci* 2022;202:110332. DOI
108. Zucchi F, Grassi V, Monticelli C, Trabanelli G. Hydrogen embrittlement of duplex stainless steel under cathodic protection in acidic artificial sea water in the presence of sulphide ions. *Corros Sci* 2006;48:522-30. DOI
109. Klyk-spyra K, Sozańska M. Quantitative fractography of 2205 duplex stainless steel after a sulfide stress cracking test. *Mater Charact* 2006;56:384-8. DOI
110. Laitinen A, Hänninen H. Chloride-induced stress corrosion cracking of powder metallurgy duplex stainless steels. *Corrosion* 1996;52:295-306. DOI
111. Wu W, Liu Z, Hu S, Li X, Du C. Effect of pH and hydrogen on the stress corrosion cracking behavior of duplex stainless steel in marine atmosphere environment. *Ocean Eng* 2017;146:311-23. DOI
112. Raman RS, Siew W. Role of nitrite addition in chloride stress corrosion cracking of a super duplex stainless steel. *Corros Sci* 2010;52:113-7. DOI
113. Rajaguru J, Arunachalam N. Investigation on machining induced surface and subsurface modifications on the stress corrosion crack growth behaviour of super duplex stainless steel. *Corros Sci* 2018;141:230-42. DOI
114. Wickström L, Mingard K, Hinds G, Turnbull A. Microcrack clustering in stress corrosion cracking of 22Cr and 25Cr duplex stainless steels. *Corros Sci* 2016;109:86-93. DOI
115. Örnek C, Zhong X, Engelberg DL. Low-temperature environmentally assisted cracking of grade 2205 duplex stainless steel beneath a $MgCl_2$:$FeCl_3$ salt droplet. *Corrosion* 2016;72:384-99. DOI
116. Sofia Hazarabedian M, Viereckl A, Quadir Z, et al. Hydrogen-induced stress cracking of swaged super duplex stainless steel subsea components. *Corrosion* 2019;75:824-38. DOI
117. Maeda MY, Koyama M, Nishimura H, Cintho OM, Akiyama E. Hydrogen-assisted damage evolution in nitrogen-doped duplex stainless steel. *Int J Hydrog Energy* 2021;46:2716-28. DOI
118. Liang X, Dodge M, Kabra S, Kelleher J, Lee T, Dong H. Effect of hydrogen charging on dislocation multiplication in pre-strained super duplex stainless steel. *Scr Mater* 2018;143:20-4. DOI
119. Örnek C, Larsson A, Harlow GS, et al. Metastable precursor structures in hydrogen-infused super duplex stainless steel microstructure - an operando diffraction experiment. *Corros Sci* 2020;176:109021. DOI
120. Claeys L, Depover T, De Graeve I, Verbeken K. First observation by EBSD of martensitic transformations due to hydrogen presence during straining of duplex stainless steel. *Mater Charact* 2019;156:109843. DOI
121. Barnoush A, Zamanzade M, Vehoff H. Direct observation of hydrogen-enhanced plasticity in super duplex stainless steel by means of *in situ* electrochemical methods. *Scr Mater* 2010;62:242-5. DOI
122. Örnek C, Larsson A, Harlow GS, et al. Time-resolved grazing-incidence X-ray diffraction measurement to understand the effect of hydrogen on surface strain development in super duplex stainless steel. *Scr Mater* 2020;187:63-7. DOI
123. Tong H, Sun Y, Su Y, Pang X, Gao K. Investigation on hydrogen-induced cracking behavior of 2205 duplex stainless steel used for marine structure (In Chinese). *J Chin Soc Corros Prot* 2019;39:130-7. DOI
124. El-Sherik MA. Trends in oil and gas corrosion research and technologies; 2017. pp. 271-92. DOI
125. Saithala JR, Sudhakar M, Ubhi HS, Atkinson JD. Environmental-assisted cracking behaviour of sigmatied super duplex stainless steel in oil field production brine. 2012. DOI

Zhao *et al. Microstructures* 2023;3:2023022
DOI: 10.20517/microstructures.2022.46

Microstructures

Research Article

Open Access

Check for updates

Low-pressure-driven barocaloric effects at colinear-to-triangular antiferromagnetic transitions in $Mn_{3-x}Pt_{1+x}$

Xueting Zhao[1,2], Kun Zhang[1,2], Ji Qi[1,2], Peng Liu[1,2], Zhao Zhang[1,2], Lin Qu[1,2], Zhidong Zhang[1,2], Bing Li[1,2]

[1]Shenyang National Laboratory for Materials Science, Institute of Metal Research, Chinese Academy of Sciences, Shenyang 110016, Liaoning, China.
[2]School of Materials Science and Engineering, University of Science and Technology of China, Shenyang 110016, Liaoning, China.

Correspondence to: Prof. Bing Li, Shenyang National Laboratory for Materials Science, Institute of Metal Research, Chinese Academy of Sciences, 72 Wenhua Road, Shenyang 110016, Liaoning, China. E-mail: bingli@imr.ac.cn; Prof. Kun Zhang, Shenyang National Laboratory for Materials Science, Institute of Metal Research, Chinese Academy of Sciences, 72 Wenhua Road, Shenyang 110016, Liaoning, China. E-mail: kzhang@imr.ac.cn

How to cite this article: Zhao X, Zhang K, Qi J, Liu P, Zhang Z, Qu L, Zhang Z, Li B. Low-pressure-driven barocaloric effects at colinear-to-triangular antiferromagnetic transitions in $Mn_{3-x}Pt_{1+x}$. *Microstructures* 2023;3:2023022. https://dx.doi.org/10.20517/microstructures.2022.46

Received: 29 Dec 2022 **First Decision:** 31 Jan 2023 **Revised:** 23 Mar 2023 **Accepted:** 21 Apr 2023 **Published:** 28 Apr 2023

Academic Editor: Fei Li **Copy Editor:** Fangling Lan **Production Editor:** Fangling Lan

Abstract

A large driving pressure is required for barocaloric effects (BCEs) in intermetallics, usually above 100 MPa. Here, we report barocaloric effects in $Mn_{3-x}Pt_{1+x}$ alloys saturated at about 60 MPa, the lowest pressure reported in intermetallics to date. A first-order phase transition occurs from the colinear antiferromagnetic phase to the triangular antiferromagnetic phase as temperature decreases. The transition temperature strongly depends on the composition x, ranging from 331 K for x = 0.18 to 384 K for x = 0.04, and is sensitive to pressure, with dT_t/dP up to 139 K/GPa. However, the maximum pressure-induced entropy changes are as small as 13.79 J kg^{-1} K^{-1}, attributed to the mutual cancellation of lattice and magnetic entropy changes. The small driving pressure and total entropy changes are due to the special magnetic geometric frustration.

Keywords: Barocaloric effects, magnetoelastic coupling, magnetic transition, geometrical spin frustration, colinear antiferromagnetic

INTRODUCTION

Refrigeration technology is of great significance for both industry and everyday life. Current refrigeration systems are mostly based on conventional vapor compression technology. Although highly optimized in recent decades, they still have a considerable undesirable impact on the environment[1]. Frequently used refrigerants have thousand-time stronger global warming potentials compared to CO_2. To achieve carbon neutrality, solid-state refrigeration technology based on the caloric effects of solids has been proposed as an alternative solution. Various phase transitions caused by some calorimeter materials under external fields are accompanied by huge latent heat, which can be utilized for cooling purposes through designated thermodynamic cycles. Magnetocaloric effects (MCEs) is one of the most studied caloric effects, which is usually linked to magnetic-field-induced first-order transitions. Barocaloric effects (BCEs), as the counterpart and extension of the (MCEs), is defined as the change in the isothermal entropy or adiabatic temperature of the material during the application or withdrawal of the external pressure field. Materials with first-order phase transition are more likely to be the most potential barocaloric effect materials due to the sensitivity of the lattice to pressure.

Initially observed around 2,000 years, BCEs has been found in $Pr_{1-x}La_xNiO_3$[2] and CeSb[3]. Subsequent studies of magneto-elastically coupled materials for MCEs have revealed larger BCEs, such as in magnetic shape memory alloys including NiMnIn[4], $La(Fe,Si)_{13}$[5,6], $Gd_5Si_2Ge_2$[7], $MnCoGe_{0.99}In_{0.01}$[8], FeRh[9,10], and others. These materials exhibit a strong coupling between magnetic and lattice degrees of freedom. Usually, there is a magnetic phase with a larger volume and a magnetic phase with a smaller volume. The application of a sufficiently large hydrostatic pressure induces a change of the system from the large-volume to the small-volume phase, and simultaneously the magnetic phase transition takes place. Typically, the required driving pressures in these systems are as high as several hundred MPa, and a comparable pressure-induced entropy change to that induced by a magnetic field can be obtained.

In recent years, a great variety of materials have been reported with larger BCEs, such as AgI[11], organic-inorganic hybrid chalcogenide $[TPrA][Mn(dca)_3]$[12], ferroelectric $(NH_4)_2SO_4$[13,14], spin-crossover complexes[15-18], and even natural rubber[19,20]. First-principles calculations also predicted sizable BCEs for lithium-ion conductor materials[21], fluorine ion conductor materials[22], and graphene[23]. In plastic crystals, the extensive molecular orientation disorder in plastic crystals leads to huge entropy changes larger than 100 J kg^{-1} K^{-1}, and the driving pressures have been significantly reduced down to below 100 MPa, for which they are termed as colossal barocaloric effects[24-26].

Antiferromagnetic materials are effective in releasing their entropy change by pressure in addition to the magnetic field[10,27], with remarkably reduced driving pressures, especially in frustrated antiferromagnets. Recent research has found that larger BCEs are observed at phase transitions from frustrated antiferromagnetic (AFM) to paramagnetic states in nitrides (Mn_3GaN[28], Mn_3NiN[29]) with an anti-perovskite structure. This indicates that even small hydrostatic pressures (as low as 90 MPa in plastic crystals) can effectively act on the AFM system. In this work, we report on the barocaloric properties of $Mn_{3-x}Pt_{1+x}$ alloys at first-order phase transitions from low-temperature triangle-lattice frustrated to high-temperature colinear AFM states. The composition-dependent phase transition temperature (T_t) is about 331 K for the $Mn_{2.82}Pt_{1.18}$. The pressure-dependent calorimetric measurements suggest that entropy changes are saturated at around 60 MPa.

EXPERIMENTS

Polycrystalline samples of $Mn_{3-x}Pt_{1+x}$ with different Mn contents (x = 0.04, 0.08, 0.1, and 0.18) were prepared by arc-melting the high-purity (99.9%) elements under an Ar atmosphere. The true composition was

determined using a ThermoFisher iCAP6300 Inductive Coupled Plasma Emission Spectrometer (ICP). The ingots were remelted three times to ensure homogeneity. 2wt.% excessive Mn elements were added to compensate for losses during the melting process. The as-prepared ingots were annealed in encapsulated quartz tubes at 973 K for 120 h and followed by furnace cooling. The nature of the single-phase was checked using a Rigaku MiniFlex 600 X-ray diffractometer. The temperature-dependent X-ray diffraction (XRD) patterns were collected using Bruker D8 Advance X-ray diffractometer. The diffraction patterns were fitted to a cubic unit cell (space group $Pm\bar{3}m$) in Jana2006[30]. The calorimetric data were collected as a function of temperature and pressure using a high-pressure differential scanning calorimeter (μDSC7, Setaram). The samples were enclosed in a high-pressure vessel made of Hastelloy. Constant pressure scans were performed at 0.1, 30, 60, and 90 MPa in the temperature region from 290 to 390 K, respectively. After subtracting the baseline background, the heat flow data can be converted to entropy changes. The magnetic properties are characterized using a Magnetic Properties Measurement System (MPMS-XL, Quantum Design) and a Physical Property Measurement System (PPMS-14T, Quantum Design).

RESULTS AND DISCUSSIONS

$Mn_{3-x}Pt_{1+x}$ crystallizes in the ordered Cu_3Au-type structure[31,32], where Mn atoms are located on the face centers of the cubic lattice formed by Pt atoms, as shown in Figure 1A. The compound with the stoichiometric composition magnetically orders into a colinear AFM state at about T_t ~365 K (magnetic transition temperature of Mn_3Pt in the literature[32]), where a negligibly small tetragonal distortion is observed. As depicted, magnetic moments carried by Mn atoms are aligned along the *c*-axis, and the magnetic unit cell is constructed along the *c*-axis with doubled chemical unit cell. Note that the Mn atoms located on the *ab*-plane carry no ordered magnetic moment. The four Mn atoms form a square lattice, and the diagonal magnetic moments are parallel while the adjacent ones are anti-parallel. Spaced by the non-magnetic Mn atom, the magnetic moments of the two layers of the square lattices are antiferromagnetically coupled. As the temperature decreases below T_t, such a colinear AFM state transforms into a triangle-lattice AFM state, where magnetic moments are located on the (111) plane and point in the <211> direction, leading to a two-dimensional geometric spin frustration. This arrangement of magnetic moments ensures that the magnetic unit cell is identical to the chemical unit cell. This phase transition is a typical first-order magnetic phase transition, even if the lattice symmetry is maintained[33]. Based on the triangular AFM structure, anomalous Hall effects have been predicted and observed in films as well as bulk single crystals[34,35].

In the $Mn_{3-x}Pt_{1+x}$ system, the magnetic properties, in particular, T_t, are strongly dependent on the composition *x*. Shown in Figure 1B is the heat flow data of the $x = 0.1$ alloy under ambient pressure, where an endothermic peak is found at 360 K while an exothermic peak at 340 K with a thermal hysteresis of about 20 K, which is a signature of the first-order phase transition. The temperature corresponding to the peak in the heat flow curve is defined as the phase transition temperature. In this paper, we uniformly regard the transition temperature of the cooling process as the phase transition temperature of the sample. The entropy change at this transition is derived from being about 12.31 J kg^{-1} K^{-1}, which is kind of small compared to other systems that exhibit strong first-order transitions. The reason will be clarified afterward. For example, the entropy change is 22.3 J kg^{-1} K^{-1} in Mn_3GaN[28] while 43 J kg^{-1} K^{-1} in Mn_3NiN[29]. The temperature-dependent XRD was used to monitor the lattice distortion during the phase transition. The contour plots of the XRD patterns are shown in Figure 1C as a function of temperature (*T*) and scattering vector (*Q*). The patterns can be indexed based on the reported cubic structure. Within our resolution, there is no distinguishable symmetry change in the temperature from 300 to 410 K. Four strong Bragg peaks are observed, and the (210) peak obviously shifts towards the lower *Q* around 360 K. The determined lattice constant displays a sudden jump at 360 K [Figure 1D], corresponding to relative changes in lattice constant

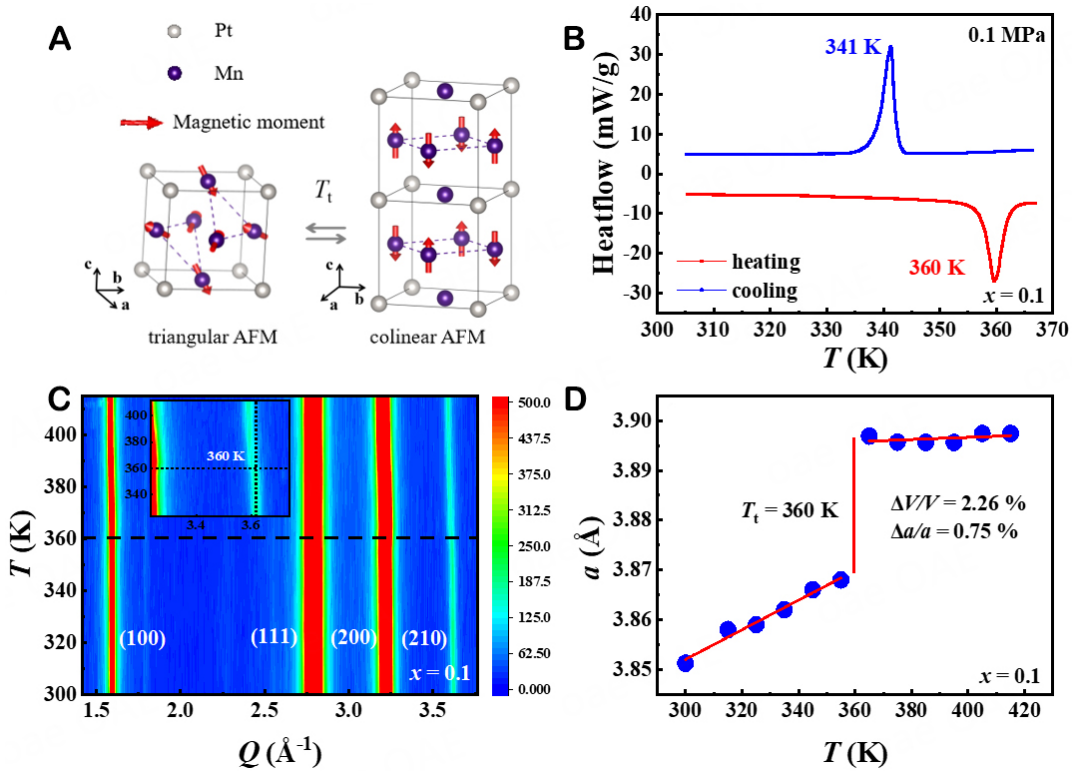

Figure 1. (A) Magnetic structures of Mn_3Pt alloys with triangular AFM and colinear AFM phases as reported by Tao *et al.*[27]. (B-D) heat flow *vs.* temperature curves, the contour plots of the variable temperature XRD patterns and lattice constant *vs.* temperature curves for sample x = 0.1, respectively. The inset in (C) is an enlarged image of the high Q region.

and unit cell volume of 0.75% and 2.26%, respectively. These values are similar to those reported in other literature[36,37]. In addition, the structurally determined T_t is well consistent with the thermally determined one.

After confirming the first-order phase transition as the core of this study typically occurs at x = 0.1, we systematically extend the magnetic characterizations to x = 0.04, 0.08, 0.1, and 0.18. Their field-cooled magnetizations as a function of temperature are plotted in Figure 2A-D. As the temperature decreases, magnetizations abruptly drop at 331 K for x = 0.18, 336 K for x = 0.1, 355 K for x = 0.08, and 384 K for x = 0.04, indicating the first-order phase transitions. As for x = 0.1, the determined T_t at the magnetization is a few kelvins lower than that in the heat flow data. We summarize the T_t values of these four samples, along with their lattice constants at room temperature, in Figure 2E. As x changes from 0.18 to 0.04, T_t monotonically increases while the lattice constant a decrease. Unlike the linear behavior of a, T_t exhibits a saturation feature, remaining nearly constant when x is greater than 0.1. Such a tendency is consistent with the previous report[31,32,36]. This phenomenon is also explained in the literature[31] based on the theoretical phase diagram of Mn_3Pt in the molecular field approximation.

Selecting x = 0.18 as an example, the high-field isothermal magnetization is considered at 300 and 380 K, where the compound is in the triangular AFM and colinear AFM states, respectively. As shown in Figure 2F, the magnetizations essentially obey a linear relation as a function of applied fields up to 14 T, which reflects the dominating AFM interactions. However, the low-field regions (the inset of Figure 2F) show a weak nonlinearity at both temperatures, which might be attributed to the uncancelled moments due to the off-stoichiometry. In particular, there are small remanence and coercivity at 300 K. The exact origin is

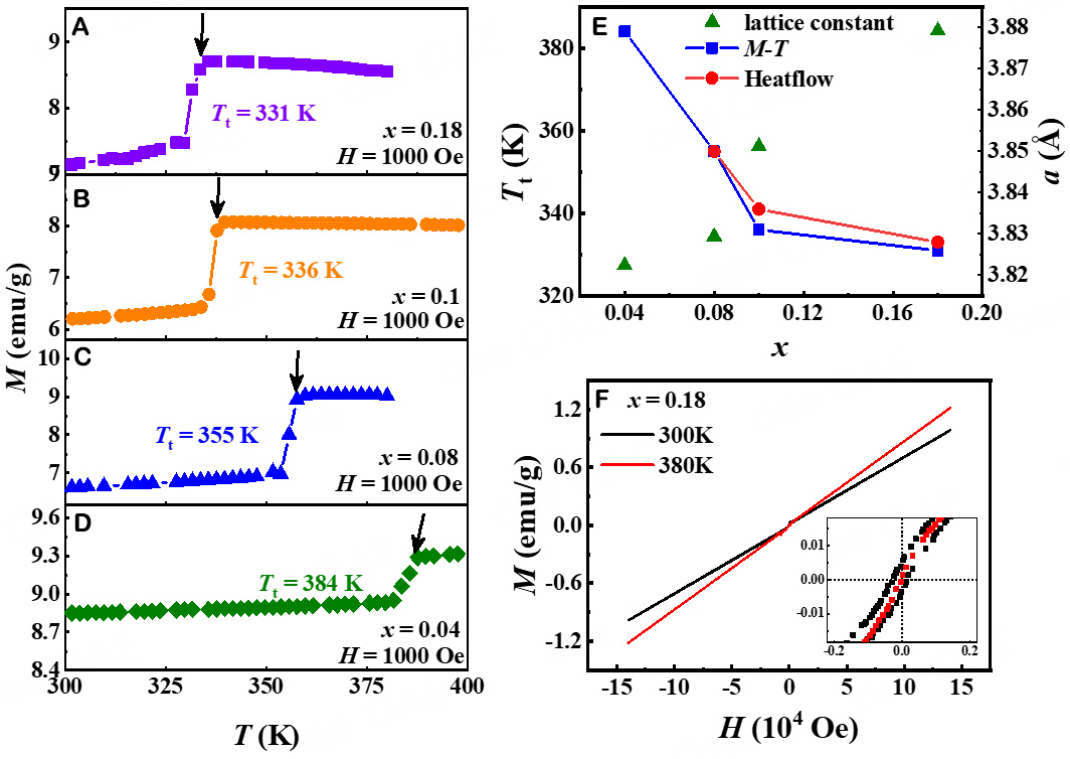

Figure 2. (A-D) Magnetization curves for samples x = 0.18, 0.1, 0.08, and 0.04, respectively. (E) Curves of phase transition temperature *vs.* manganese content x (blue squares and red dots indicate measurement by M-T and heat flow, respectively) and lattice constant *vs.* manganese content x for the samples. (Taking x = 0.08 as an example, the fitting parameters obtained using the lebail method to fit the XRD curve are: GOF = 1.47, Rp = 4.18, Rwp = 5.99). (F) The magnetization loop of x = 0.18. The inset shows the enlarged plot at low fields.

still unknown. Previous studies have also shown that a ferromagnetic component perpendicular to the (111) plane is allowed on both Mn and Pt atoms, except for the component in the (111) plane pointing in the [112] direction in the magnetic structure of the triangular AFM phase[31]. Furthermore, it has been pointed out that the origin of this ferromagnetism may be because the third site of the colinear AFM phase generates a net magnetic moment due to electron interactions at low temperatures of 100 K or even lower[38]. In contrast to the presence of net moments along the <111> direction, the magnetization curve of the single-crystal material along the <111> direction did not show ferromagnetic behavior[34].

Except for the influence of magnetic fields on the first-order phase transitions, we explore the impact of applied hydrostatic pressures. Heat flow data as a function of temperature are plotted under 0.1, 30, 60, and 90 MPa for x = 0.08 and x = 0.18 in Figure 3A and B, respectively. As the pressure increases, the endothermic and exothermic peaks move toward the high-temperature region simultaneously. The peak intensity has a small increase with pressure, while the peak width has a tendency to narrow, which is especially obvious in the x = 0.18 sample. In addition, the thermal hysteresis at 0.1 MPa for the x = 0.08 sample is the same as that at x = 0.1, which is 19 K. However, the thermal hysteresis at atmospheric pressure for x = 0.18 sample is 9 K and decreases to 5 K at 90 MPa with increasing pressure.

Entropy changes at the phase transition under constant pressure, ΔS_P, are determined by integrating the heat flow data. The pressure-induced entropy changes ($\Delta S_{P_0 \to P}$) when pressure is increased from ambient pressure (P_0) to applied pressure (P) is defined as $\Delta S_{P_0 \to P} = \Delta S_P - \Delta S_{P_0}$. Figure 3C and D show $\Delta S_{P_0 \to P}$ at the

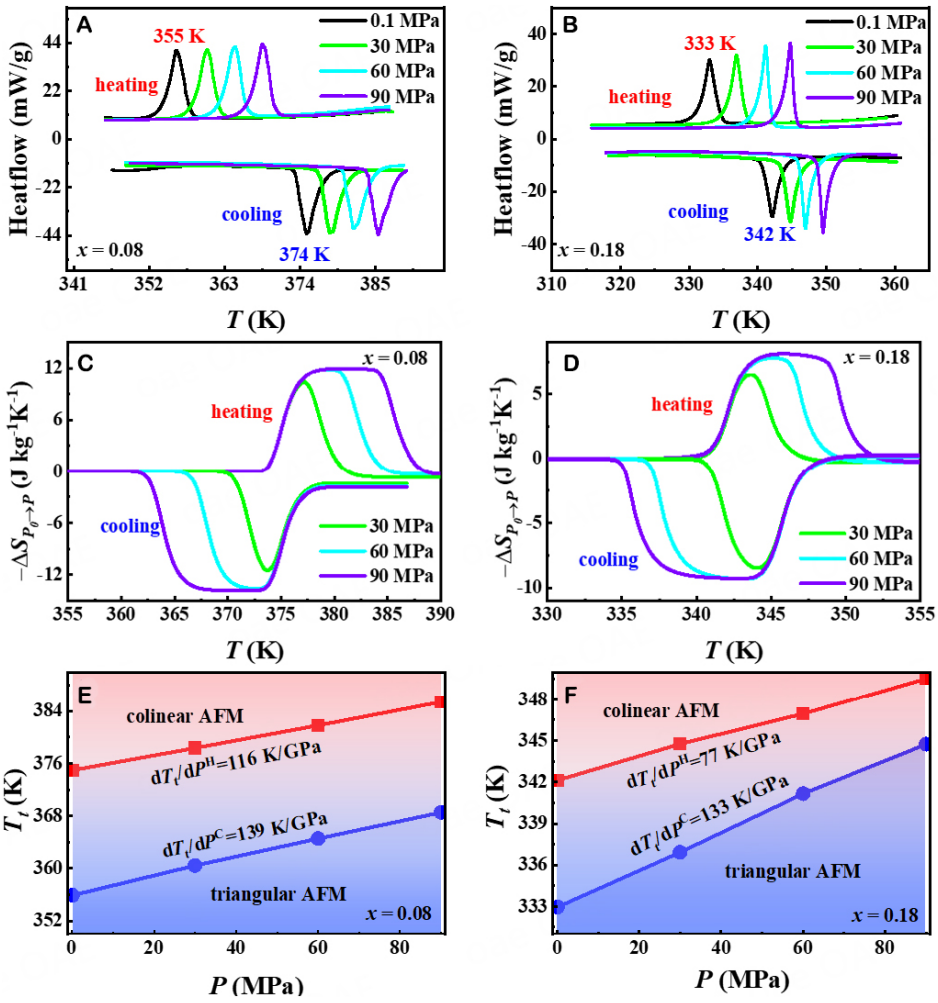

Figure 3. (A and B) Heat flow data as a function of temperature for x = 0.08 and x = 0.18 at 0.1, 30, 60, and 90 MPa pressure, respectively. (C and D) Entropy change curves for x = 0.08 and x = 0.18 at different pressures, respectively. (E and F) The temperature-pressure phase diagrams for x = 0.08 and x = 0.18, respectively.

final pressure of 30, 60, and 90 MPa for x = 0.08 and 0.18, respectively. It can be seen that more than 80% of the maximum entropy changes are achieved at pressures as low as 30 MPa, and the entropy changes tend to be saturated at about 60 MPa. Note that the maximum entropy of 13.79 J kg^{-1} K^{-1} acquired in x = 0.08 at 90 MPa is larger than that in x = 0.18 whereas the so-called reversible region (overlapped region for the cooling and heating curves) is much larger for x = 0.18. The temperature-pressure phase diagrams are constructed based on the heat flow data [Figure 3E and F]. It can be seen that the thermal hysteresis is much smaller in x = 0.18, which is the reason why its reversible region is larger[14]. Furthermore, its thermal hysteresis is obviously reduced at higher pressures.

To understand the uniqueness of this system, Table 1 compares its barocaloric factors to those of other typical compounds, including organic plastic crystals, inorganic salts, magnetocaloric intermetallics, and other frustrated AFM systems. The slope of the phase boundary (dT_t/dP) of this system is the largest, and the driving pressure (ΔP) is the smallest among all intermetallics, which are impressively comparable to those of prototype plastic crystal neopentyl glycol with colossal BCEs. However, the larger dT_t/dP must lead to smaller entropy changes in terms of the Clausius-Clapeyron relation[39], even though the volume change

Table 1. Performance summary of several typical barocaloric materials

Material	T_t (K)	dT_t/dP (K GPa^{-1})	P (MPa)	V/V (%)	$\Delta S_{P_0 \rightarrow P}$ (J kg^{-1}K^{-1})	Ref.
NPG	313	133	45	-	389	[24]
$C_2B_{10}H_{12}$	277	380	60	-	106.2	[44]
NH_4I	243	810	20	-	89	[45]
NH_4SCN	364	300	20	5	128.7	[46]
$Fe_{49}Rh_{51}$	310	60	250	1	12	[9,10]
$MnNiSi_{0.61}FeCoGe_{0.39}$	311	70	260	-	44	[47]
$Ni_{0.95}Fe_{0.05}S$	274	75	100	2	39.6	[48]
Mn_3GaN	290	65	90	1	21.6	[28]
Mn_3NiN	262	13.5	280	0.4	35	[29]
$Mn_{2.92}Pt_{1.08}$	355	139	60	2.26*	13.79	This work

*determined for $Mn_{2.9}Pt_{1.1}$.

is not too small. The small entropy change at this first-order phase transition is due to unique magnetic fluctuations in nature. Magnetic fluctuation refers to the fluctuation of magnetic (electron spin) moment in magnetic systems[40]. The interaction between the local moment and the itinerant electron matrix may enhance spin fluctuation. Frustration structures are often accompanied by strong spin fluctuations[41,42]. Neutron diffraction measurements suggest that the ordered moment is 3.3 μ_B/Mn atom in the colinear AFM state, whereas 2.2 μ_B/Mn atom in the triangular AFM[37]. The reduction in the latter should be attributed to spin fluctuations due to geometric frustration. As a result, the triangle-lattice AFM state is magnetically less ordered than the colinear AFM one, which leads to an increase of magnetic entropy across T_t. At the same time, the crystal lattice shows a normal contraction, and a reduction of entropy of the lattice subsystem is expected. We infer that the contributions of individuals to the total entropy change partially cancel each other out, and the remaining entropy change represents the overall entropy change of the material. According to the previous theoretic study, the system can be described by a nearest-neighboring exchange interaction J_1 and a next-nearest-neighboring exchange interaction J_2. J_1 is always negative, but J_2 can be negative or positive, dependent on the interatomic distance between Mn atoms[31]. At T_t, J_2 just changes its sign due to the shrinkage of the Mn-Mn distance. In this sense, such a picture is similar to the exchange striction observed in NiMnIn alloys[43].

CONCLUSIONS

In summary, the first-order phase transitions of $Mn_{3-x}Pt_{1+x}$ (x = 0.04, 0.08, 0.1, and 0.18) compounds have been studied at varying temperatures, pressures, and magnetic fields. At the phase transitions, both magnetizations and lattice constants showed abrupt drops as the temperature decreased. While the phase transition temperatures decreased at lower Mn content, they increased at higher pressures. This system is highly susceptible to pressure, and the pressure-induced entropy changes are saturated at 60 MPa, which is the lowest among current intermetallics. This may be due to the intense geometric magnetic frustration.

DECLARATIONS

Authors' contributions

Prepared the samples, collected the data, performed data analysis and contributed to the writing and revisions: Zhao X

Conceived the study, designed the study, and contributed to the writing and revisions: Li B, Zhang K

Collected some of the data and provided technical support: Qi J, Liu P, Zhang Z (Zhang Zhao), Qu L

Revision of articles: Zhang Z (Zhang Zhidong)

Availability of data and materials

The datasets used and analyzed during the current study are available from the corresponding author upon reasonable request.

Financial support and sponsorship

The work was supported by the Ministry of Science and Technology of China (Grant nos. 2021YFB3501201, 2022YFE0109900, and 2020YFA0406002) and the Key Research Program of Frontier Sciences of Chinese Academy of Sciences (Grant no. ZDBS-LY-JSC002).

Conflicts of interest

All authors declared that there are no conflicts of interest.

Ethical approval and consent to participate

Not applicable.

Consent for publication

Not applicable.

REFERENCES

1. Sari O, Balli M. From conventional to magnetic refrigerator technology. *Int J Refrig* 2014;37:8-15. DOI
2. Müller K, Fauth F, Fischer S, Koch M, Furrer A, Lacorre P. Cooling by adiabatic pressure application in $Pr_{1-x}La_xNiO_3$. *Appl Phys Lett* 1998;73:1056-8. DOI
3. Strässle T, Furrer A, Lacorre P, Müller K. A novel principle for cooling by adiabatic pressure application in rare-earth compounds. *J Alloys Compd* 2000;303-304:228-31. DOI
4. Mañosa L, González-Alonso D, Planes A, et al. Giant solid-state barocaloric effect in the Ni-Mn-In magnetic shape-memory alloy. *Nat Mater* 2010;9:478-81. DOI
5. Mañosa L, González-Alonso D, Planes A, et al. Inverse barocaloric effect in the giant magnetocaloric La-Fe-Si-Co compound. *Nat Commun* 2011;2:595. DOI
6. Fujieda S, Fujita A, Fukamichi K. Strong pressure effect on the curie temperature of itinerant-electron metamagnetic $La(Fe_{0.88}Si_{0.12})_{13}Hy$ and $La_{0.7}Ce_{0.3}(Fe_{0.88}Si_{0.12})_{13}Hy$. *Mater Trans* 2009;50:483-6. DOI
7. Yuce S, Barrio M, Emre B, et al. Barocaloric effect in the magnetocaloric prototype $Gd_5Si_2Ge_2$. *Appl Phys Lett* 2012;101:071906. DOI
8. Wu RR, Bao LF, Hu FX, et al. Giant barocaloric effect in hexagonal Ni_2In-type Mn-Co-Ge-In compounds around room temperature. *Sci Rep* 2015;5:18027. DOI PubMed PMC
9. Stern-taulats E, Gràcia-condal A, Planes A, et al. Reversible adiabatic temperature changes at the magnetocaloric and barocaloric effects in $Fe_{49}Rh_{51}$. *Appl Phys Lett* 2015;107:152409. DOI
10. Stern-taulats E, Planes A, Lloveras P, et al. Barocaloric and magnetocaloric effects in $Fe_{49}Rh_{51}$. *Phys Rev B* 2014;89:214105. DOI
11. Aznar A, Lloveras P, Romanini M, et al. Giant barocaloric effects over a wide temperature range in superionic conductor AgI. *Nat Commun* 2017;8:1851. DOI PubMed PMC
12. Bermúdez-García JM, Sánchez-Andújar M, Castro-García S, López-Beceiro J, Artiaga R, Señarís-Rodríguez MA. Giant barocaloric effect in the ferroic organic-inorganic hybrid $[TPrA][Mn(dca)_3]$ perovskite under easily accessible pressures. *Nat Commun* 2017;8:15715. DOI PubMed PMC
13. Lloveras P, Stern-Taulats E, Barrio M, et al. Giant barocaloric effects at low pressure in ferrielectric ammonium sulphate. *Nat Commun* 2015;6:8801. DOI PubMed PMC
14. Mikhaleva E, Gorev M, Bondarev V, Bogdanov E, Flerov I. Comparative analysis of elastocaloric and barocaloric effects in single-crystal and ceramic ferroelectric $(NH_4)_2SO_4$. *Scripta Mater* 2021;191:149-54. DOI
15. Yu C, Huang J, Qi J, et al. Giant barocaloric effects in formamidinium iodide. *APL Mater* 2022;10:011109. DOI
16. Salgado-beceiro J, Nonato A, Silva RX, et al. Near-room-temperature reversible giant barocaloric effects in $[(CH_3)_4N]Mn[N_3]_3$ hybrid perovskite. *Mater Adv* 2020;1:3167-70. DOI
17. Ranke P, Alho B, Ribeiro P. First indirect experimental evidence and theoretical discussion of giant refrigeration capacity through the

reversible pressure induced spin-crossover phase transition. *J Alloys Compd* 2018;749:556-60. DOI

18. Szafrański M, Wei W, Wang Z, Li W, Katrusiak A. Research update: tricritical point and large caloric effect in a hybrid organic-inorganic perovskite. *APL Mater* 2018;6:100701. DOI
19. Bom NM, Imamura W, Usuda EO, Paixão LS, Carvalho AMG. Giant barocaloric effects in natural rubber: a relevant step toward solid-state cooling. *ACS Macro Lett* 2018;7:31-6. DOI
20. Miliante CM, Christmann AM, Usuda EO, et al. Unveiling the origin of the giant barocaloric effect in natural rubber. *Macromolecules* 2020;53:2606-15. DOI
21. Sagotra AK, Chu D, Cazorla C. Room-temperature mechanocaloric effects in lithium-based superionic materials. *Nat Commun* 2018;9:3337. DOI PubMed PMC
22. Cazorla C, Errandonea D. Giant mechanocaloric effects in fluorite-structured superionic materials. *Nano Lett* 2016;16:3124-9. DOI PubMed
23. Ma N, Reis MS. Barocaloric effect on graphene. *Sci Rep* 2017;7:13257. DOI PubMed PMC
24. Li B, Kawakita Y, Ohira-Kawamura S, et al. Colossal barocaloric effects in plastic crystals. *Nature* 2019;567:506-10. DOI
25. Aznar A, Lloveras P, Barrio M, et al. Reversible and irreversible colossal barocaloric effects in plastic crystals. *J Mater Chem A* 2020;8:639-47. DOI
26. Lloveras P, Tamarit J. Advances and obstacles in pressure-driven solid-state cooling: a review of barocaloric materials. *MRS Energy Sustain* 2021:8;3-15. DOI
27. Tao K, Song W, Lin J, et al. Giant reversible barocaloric effect with low hysteresis in antiperovskite $PdNMn_3$ compound. *Scripta Mater* 2021;203:114049. DOI
28. Matsunami D, Fujita A, Takenaka K, Kano M. Giant barocaloric effect enhanced by the frustration of the antiferromagnetic phase in Mn_3GaN. *Nat Mater* 2015;14:73-8. DOI PubMed
29. Boldrin D, Mendive-tapia E, Zemen J, et al. Multisite exchange-enhanced barocaloric response in Mn_3NiN. *Phys Rev X* 2018;8:041035. DOI
30. Dusek M, Petricek V. Towards the routine application of computing system Jana2000. *Acta Crystallogr A Found Crystallogr* 2005;61:c104-5. DOI
31. Krén E, Kádár G, Pál L, Sólyom J, Szabó P, Tarnóczi T. Magnetic structures and exchange interactions in the Mn-Pt system. *Phys Rev* 1968;171:574-85. DOI
32. Krén E, Kádár G, Pál L, Szabó P. Investigation of the first-order magnetic transformation in Mn_3Pt. *J Appl Phys* 1967;38:1265-6. DOI
33. Tomiyoshi S, Yasui H, Kaneko T, et al. Magnetic excitations in Mn_3Pt at high energies by the TOF method. *J Magn Magn Mater* 1990;90-91:203-4. DOI
34. Zuniga-Cespedes BE, Manna K, Noad HML, et al. Observation of an anomalous hall effect in single-crystal Mn_3Pt. *Mater Sci* 2022;2209:05865. DOI
35. An N, Tang M, Hu S, et al. Structure and strain tunings of topological anomalous hall effect in cubic noncollinear antiferromagnet Mn_3Pt epitaxial films. *Sci China Phys Mech Astron* 2020;63:297511. DOI
36. Yasui H, Kaneko T, Yoshida H, Abe S, Kamigaki K, Mori N. Pressure dependence of magnetic transition temperatures and lattice parameter in an antiferromagnetic ordered alloy Mn_3Pt. *J Phys Soc Jpn* 1987;56:4532-9. DOI
37. Yasui H, Ohashi M, Abe S, et al. Magnetic order-order transformation in Mn_3Pt. *J Magn Magn Mater* 1992;104-107:927-8. DOI
38. Ricodeau JA. Model of the antiferromagnetic-antiferromagnetic transition in Mn_3Pt alloys. *J Phys F Met Phys* 1974;4:1285-303. DOI
39. Boldrin D. Fantastic barocalorics and where to find them. *Appl Phys Lett* 2021;118:170502. DOI
40. Ehrenreich H, Spaepen F. Solid state physics: advances in research and applications. Amsterdam Boston: Academic Press; 2006.
41. Hemberger J, von Nidda HA, Tsurkan V, Loidl A. Large magnetostriction and negative thermal expansion in the frustrated antiferromagnet $ZnCr_2Se_4$. *Phys Rev Lett* 2007;98:147203. DOI PubMed
42. Broholm C, Aeppli G, Espinosa GP, Cooper AS. Antiferromagnetic fluctuations and short-range order in a Kagomé lattice. *Phys Rev Lett* 1990;65:3173-6. DOI
43. Li B, Ren WJ, Zhang Q, et al. Magnetostructural coupling and magnetocaloric effect in Ni-Mn-In. *Appl Phys Lett* 2009;95:172506. DOI
44. Zhang K, Song R, Qi J, et al. Colossal barocaloric effect in carboranes as a performance tradeoff. *Adv Funct Mater* 2022;32:2112622. DOI
45. Ren Q, Qi J, Yu D, et al. Ultrasensitive barocaloric material for room-temperature solid-state refrigeration. *Nat Commun* 2022;13:2293. DOI PubMed PMC
46. Zhang Z, Li K, Lin S, et al. Thermal batteries based on inverse barocaloric effects. *Sci Adv* 2023;9:eadd0374. DOI PubMed PMC
47. Lloveras P, Samanta T, Barrio M, et al. Giant reversible barocaloric response of $MnNiSi)_{1-x}(FeCoGe)_x$ (x = 0.39, 0.40, 0.41). *APL Mater* 2019;7:061106. DOI
48. Greca LG, Lehtonen J, Tardy BL, Guo J, Rojas OJ. Biofabrication of multifunctional nanocellulosic 3D structures: a facile and customizable route. *Mater Horiz* 2018;5:408-15. DOI

Wang *et al. Microstructures* 2023;3:2023023
DOI: 10.20517/microstructures.2023.04

Microstructures

Research Article

Open Access

Check for updates

High energy storage properties of $0.94Bi_{0.5}Na_{0.5}TiO_3$-$0.06BaTiO_3$ ceramics by incorporating $Sr_{0.8}Bi_{0.1}\square_{0.1}Ti_{0.8}Zr_{0.2}O_{2.95}$

Cheng Wang[1], Xiaojie Lou[2]

[1]Gansu Vocational College of Architecture, Lanzhou 730050, Gansu, China.
[2]Frontier Institute of Science and Technology, and State Key Laboratory for Mechanical Behavior of Materials, Xi'an Jiaotong University, Xi'an 710049, Shaanxi, China.

Correspondence to: Prof. Xiaojie Lou, Frontier Institute of Science and Technology, and State Key Laboratory for Mechanical Behavior of Materials, Xi'an Jiaotong University, No. 1 West Building, 99 Yanxiang Road, Yanta District, Xi'an 710049, Shaanxi, China. E-mail: xlou03@163.com

How to cite this article: Wang C, Lou X. High energy storage properties of $0.94Bi_{0.5}Na_{0.5}TiO_3$-$0.06BaTiO_3$ ceramics by incorporating $Sr_{0.8}Bi_{0.1}\square_{0.1}Ti_{0.8}Zr_{0.2}O_{2.95}$. *Microstructures* 2023;3:2023023. https://dx.doi.org/10.20517/microstructures.2023.04

Received: 16 Jan 2023 **First Decision:** 17 Feb 2023 **Revised:** 22 Mar 2023 **Accepted:** 5 May 2023 **Published:** 19 May 2023

Academic Editor: Shujun Zhang **Copy Editor:** Fangling Lan **Production Editor:** Fangling Lan

Abstract

Ceramics with high-energy storage density are in high demand across various industries. In this regard, lead-free relaxor ferroelectric ceramics were synthesized using the conventional solid-state reaction method with the composition $(1-x)[0.94Bi_{0.5}Na_{0.5}TiO_3-0.06BaTiO_3]-xSr_{0.8}Bi\gamma_{0.1}Ti_{0.8}Zr_{0.2}O_{0.95}$, abbreviated as BNBT-*x*SBTZ. The incorporation of SBTZ in BNBT ceramics significantly improved their relaxation properties. Specifically, the 0.91BNBT-0.09SBTZ ceramics displayed a breakdown electric field of up to 230 kV/cm, with a recoverable energy storage density (*Wr*) of 2.68 J/cm^3 and an energy storage efficiency (η) of 74.4%. Additionally, this sample demonstrated remarkable temperature stability and fatigue resistance, with only an 11% decrease in *Wr* observed from room temperature to 140 °C and a 13.3% reduction in *Wr* after 10^5 electrical cycles. Therefore, the 0.91BNBT-0.09SBTZ ceramic is a promising dielectric material suitable for energy-storage dielectric capacitors.

Keywords: Energy storage properties, lead-free ceramics, temperature stability, fatigue resistance

INTRODUCTION

The global community is facing the challenge of climate change and environmental issues, which

necessitates the exploration of alternative energy sources such as solar and wind power. However, the intermittent nature of these energy sources presents limitations on their practical applications. Therefore, it is crucial to develop new energy storage technologies. Currently, the primary electrical energy storage devices include batteries, chemical capacitors, and ceramic capacitors. Ceramic capacitors, in particular, offer many advantages, such as high-power density, rapid charging and discharging rates, and a broad operating temperature range. As a result, they are widely used in various applications, including pulsed power supplies, microwave circuits, and electric vehicles. Nevertheless, the low energy storage density of ceramic capacitors compared to chemical batteries restricts their potential applications. Consequently, there is an urgent need to develop ceramic capacitors with higher energy storage density to address the growing energy challenges.

The key performance indicators of ceramic capacitors comprise the recoverable energy storage density (W_r), total energy storage density (W), and energy storage efficiency (η). These parameters can be derived from the electrical hysteresis loops (P-E) of ceramics or calculated by following Equation (1-3)[1,2]:

$$W = \int_0^{P_m} EdP \tag{1}$$

$$W_r = \int_{P_r}^{P_m} EdP \tag{2}$$

$$\eta = \frac{W_r}{W} \tag{3}$$

where P_m is the maximum polarization, and P_r is the remanent polarization.

Equations (1-3) indicate that achieving high energy storage capacity (W_r) and efficiency (η) requires a large polarization (P_m) and a small remnant polarization (P_r). The ferroelectric ceramic $Na_{0.5}Bi_{0.5}TiO_3$ (BNT) possesses a large P_m, making it a promising candidate for developing high-energy storage capacitors. However, pristine BNT ceramic has a large P_r, resulting in low W_r and η. Recent studies have focused on developing BNT-based ceramics with large P_m and small P_r through doping, which can significantly reduce the grain size of the ceramics and increase their dielectric breakdown strength (DBS), W_r, and η[3]. For instance, Qi *et al.* prepared linear-like anti-ferroelectric BNT-based ceramics with a W_r of 7.02 J/cm^3 and η of 85%[4]. Similar results have been reported in other studies[5-8]. Therefore, chemical doping of pure BNT is an important method for preparing ceramics with high-energy storage properties.

The material $0.94Na_{0.5}Bi_{0.5}TiO_3$-$0.06BaTiO_3$ (BNT-BT) is a type of relaxor ferroelectric material that exhibits a morphotropic phase boundary (MPB) structure. When an external electric field is applied, this material undergoes a reversible transition from a relaxor state to a long-range ferroelectric order, resulting in a large P_m and a lower P_r[9,10]. However, the dielectric breakdown electric field of BNT-BT is relatively low. In general, the breakdown electric field of dielectric ceramics increases with decreasing grain size. Therefore, in this study, we aim to improve the breakdown electric field and enhance the energy storage properties of BNT-BT by using $Sr_{0.8}Bi_{0.1}\gamma_{0.1}Ti_{0.8}Zr_{0.2}O_{2.95}$ (SBTZ) as a modifier to regulate the relaxation behavior and decrease the grain size. SBTZ is a newly developed relaxor ferroelectric material obtained by doping Bi^{3+} and Zr^{4+} into the cubic-phase perovskite material of $SrTiO_3$. The introduction of Bi^{3+} and Zr^{4+} ions into the A-site of $SrTiO_3$ reduces the chemical ratio of Bi^{3+} and creates an A-site vacancy, which disrupts the ferroelectric order and results in relaxation behavior[11,12]. It is expected that the energy storage performance of BNT-BT

will be improved due to the enhanced relaxation property and breakdown electric field.

MATERIALS AND METHODS

Ceramic samples of (1-*x*)[0.94$Bi_{0.5}Na_{0.5}TiO_3$-0.06$BaTiO_3$]-*x*$Sr_{0.8}Biγ_{0.1}Ti_{0.8}Zr_{0.2}O_{0.95}$ (abbreviated as: (1-*x*)BNBT-*x*SBTZ, *x* = 0.07, 0.08, 0.09, and 0.10) were synthesized using the solid-state reaction method. The starting materials used were Bi_2O_3 (99.9%), Na_2CO_3 (99.5%), $BaCO_3$ (99.9%), $SrCO_3$ (99%), TiO_2 (99.6%), and ZrO_2 (99.99%). The raw powders were mixed and ball-milled for 16 h in polyethylene pots with zirconia balls and ethanol as the milling medium. The use of ethanol was preferred due to its low ion dissolution properties, which minimized the introduction of unwanted ions. The milled powder was dried, sieved, and formed into cylindrical pellets before being sintered for 4 h at 850 °C The sintered pellets were then crushed, re-milled for 10 h, and cold isostatically pressed into pellets with a diameter of 10 mm under a pressure of 250 MPa. The pellets were sintered at 1150 °C for 2 h in alumina crucibles in an air atmosphere. To compensate for the loss of sodium oxides and bismuth, the pellets were buried in prepared powders of the same composition. Finally, the sintered pellets were polished to a final thickness of approximately 0.6 mm, and silver electrodes were coated on both surfaces and fired at 550 °C for 30 min for electrical testing.

The phase structure was determined through the use of X-ray diffractometry (XRD, Advanced), while the surface morphology was analyzed by means of scanning electron microscopy (SEM) (Carle Zeiss GeminiSEM 500, Germany). In addition, the dielectric properties were measured using a precision impedance analyzer (Agilent E4980A), while Raman spectra were obtained using a Raman spectrometer (Horiba Allmentation LabRam). Finally, the polarization hysteresis loops (*P-E*) were assessed via a standard ferroelectric analyzer (TF Analyzer 2000).

RESULTS AND DISCUSSION

The X-ray diffraction patterns of BNBT-*x*SBTZ ceramics were analyzed in the range of 20° to 75°, as shown in Figure 1A. The results indicate that each sample has a single perovskite structure, with no presence of any secondary phase. This suggests that SBTZ is fully incorporated into the lattice[13]. Furthermore, Figure 1B displays the expanded XRD patterns around the diffraction peak of (111), which reveals that the diffraction peaks shift towards higher diffraction angles as the SBTZ doping content increases. This shift indicates a reduction in the lattice constant[14,15]. Additionally, the absence of peak splitting at around 40° suggests that all samples possess a highly symmetrical pseudocubic structure[16].

The Raman spectra of (1-*x*)BNBT-*x*SBTZ ceramics were analyzed in the range of 100-1,000 cm^{-1}, as depicted in Figure 1C. The spectra were categorized into four regions, each representing distinct chemical bonding behavior[17]. The modes below 200 cm^{-1} were found to be associated with A-site atomic vibrations, while the high-frequency band between 200 and 380 cm^{-1} corresponded to the vibrations of BO bonds, including Zr^{2+}, Zr^{4+}, and Ti^{4+} ions. The modes near 550 cm^{-1} and 610 cm^{-1} were linked to Ti/Zr-O_6 vibrations, and it was observed that the two peak positions became separated, indicating an increased intensity of oxygen octahedron vibration and enhanced relaxation characteristics with increasing doping content[18]. The section with modes above 700 cm^{-1} was considered to be the superposition of various vibration modes.

The SEM images of (1-*x*)BNBT-*x*SBTZ ceramics, as depicted in Figure 2A-D, indicate that the ceramics have been effectively sintered with minimal surface pores. The grain size of the ceramics initially decreases and then increases with increasing dopant concentration. This phenomenon can be attributed to the appearance of low melting point regions in the ceramics after SBTZ doping. During the sintering and cooling process, these regions are more prone to nucleation and grain growth, resulting in a decrease in grain size. However, at higher doping concentrations, the liquid phase melting regions further increase,

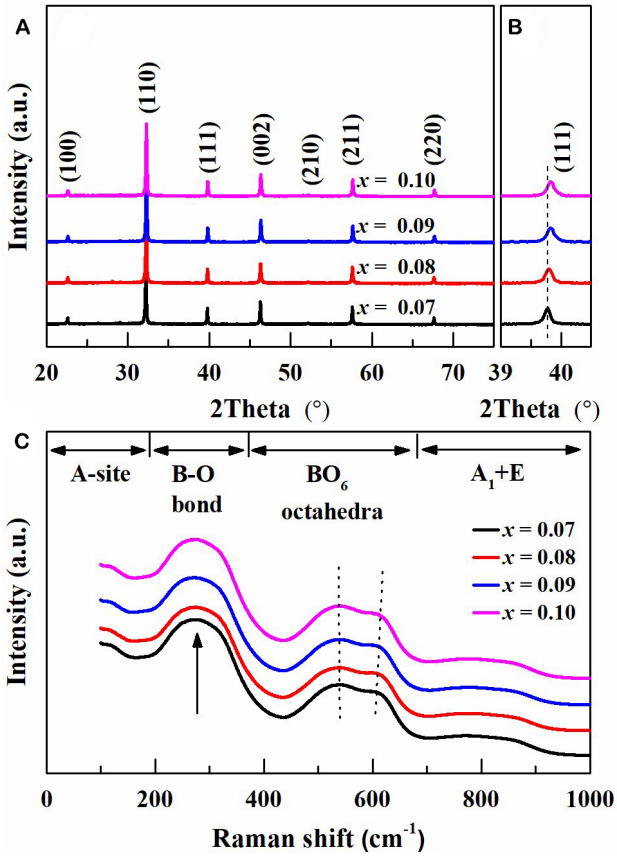

Figure 1. XRD patterns and Raman spectra of the sintered ceramics. (A) XRD patterns from 20° to 75°; (B) expanded XRD patterns at around peak (111); (C) Raman spectra in the range of 100-900 cm^{-1}.

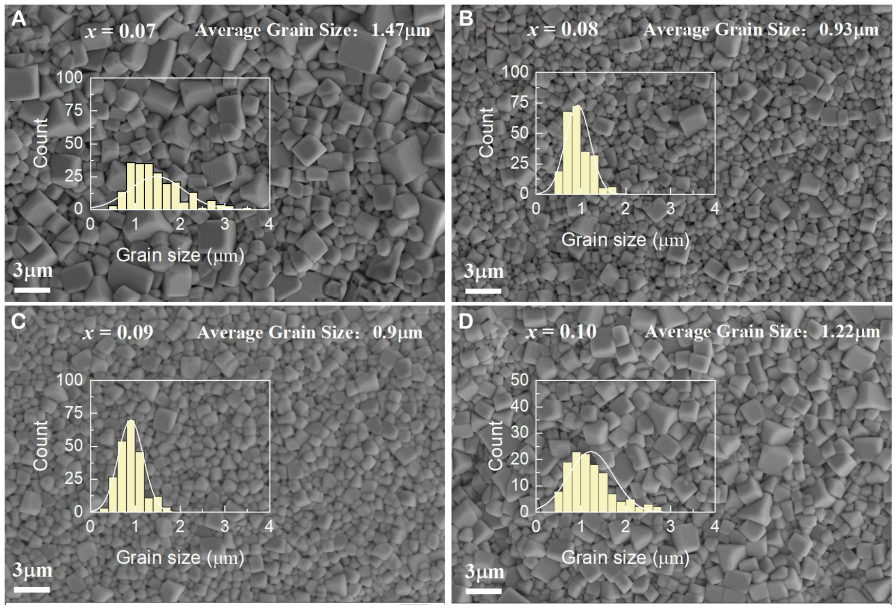

Figure 2. The surface morphology of the (1-*x*)BNBT-*x*SBTZ ceramics and distribution of grain size. (A) *x* = 0.07, (B) *x* = 0.09, (C) *x* = 0.09, and (D) *x* = 0.10.

leading to the emergence of smaller grain sizes[19]. The breakdown field of ceramics is significantly influenced by the grain size, with smaller grain sizes resulting in higher breakdown electric fields[18]. Therefore, the addition of SBTZ at low doping levels is advantageous for achieving high energy storage properties. Specifically, when the SBTZ content is 0.07, 0.08, 0.09, and 0.1, the average grain sizes are 1.47 μm, 0.93 μm, 0.90 μm, and 1.22 μm, respectively.

Figure 3 depicts the dielectric behavior of (1-x)BNBT-xSBTZ ceramics over a temperature range of 35-400 °C and at frequencies of 1 kHz, 10 kHz, 1 MHz, 10 MHz, and 20 MHz, respectively. The curves illustrate that the ceramics exhibit relaxation behavior with double dielectric peaks. The shape of the curves remains consistent across varying SBTZ doping levels, with the dielectric peak T_m becoming broader, indicating an enhanced relaxation characteristic[20]. The second peak T_m, which corresponds to the maximum dielectric constant (ε_m), represents the relaxation of the rhombohedral-tetragonal phase transition brought about by the polar nanoregions[21]. As the doping level increases, the ε_m of the ceramics tends to decrease, indicating a weakening of the ferroelectric properties. The low dielectric losses (tan δ) of the samples demonstrate their excellent insulating properties, which play a crucial role in improving the energy storage performance of ceramics.

In order to conduct a more thorough investigation into the relaxor transition in ceramics, an adaptation of the Curie-Weiss Law was implemented, which can be expressed as follows:

$$\ln(1/\varepsilon - 1/\varepsilon_{max}) = \gamma \ln(T - T_m) + C \quad (4)$$

where ε is the dielectric constant, T is the temperature, T_m is the temperature at which ε reaches its maximum value ε_{max}, C is a constant, and is the diffuse degree. The value of γ ranges from 1 for typical ferroelectrics to 2 for ideal relaxor ferroelectrics.

Figure 4 depicts the relationship between $\ln(T-T_m)$ and $\ln(1/\varepsilon - 1/\varepsilon_{max})$ for the examined samples. The calculated value of γ ranges from 1.76 to 2.01, indicating a strong relaxation behavior of the sintered ceramics.

The dielectric breakdown strength (DBS) of the ceramics was evaluated, as depicted in Figure 5A. By utilizing the Weibull distribution as Equation (5-7)[22]:

$$P_i = i(n+1) \quad (5)$$

$$X_i = \ln(E_i) \quad (6)$$

$$Y_i = \ln(\ln(1/(1-P_i))) \quad (7)$$

where i is the group number, X_i and Y_i are parameters in Weibull distribution functions, E_i is the DBS of sample i, P_i is associated with dielectric breakdown, and n is the sum of specimens of each sample. The electric field is ranged as Equation (8).

$$E_1 \le E_2 \le ... \le E_i \le ... \le E_n \quad (8)$$

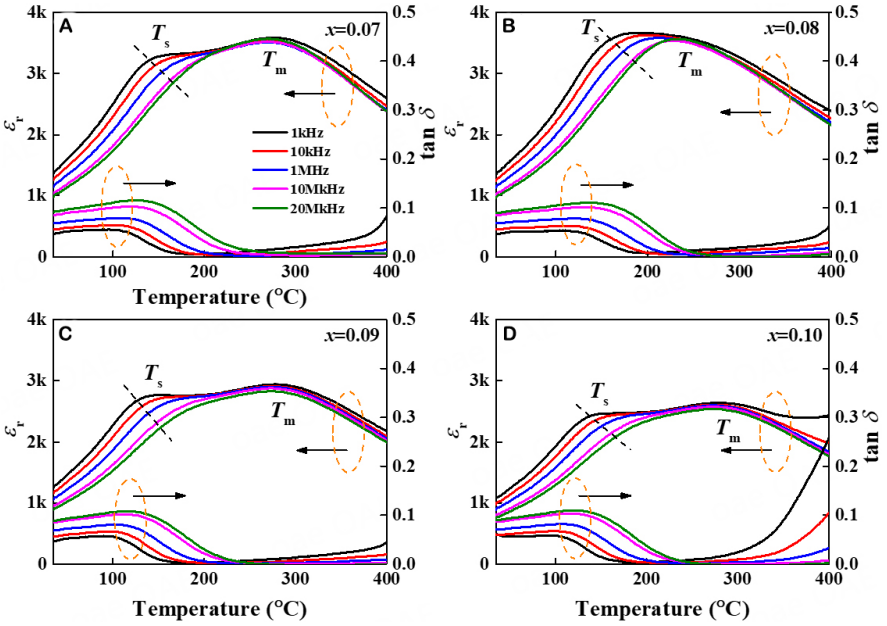

Figure 3. Temperature-dependent dielectric permittivity and loss of (1-*x*)BNBT-*x*SBTZ ceramics from 70 to 400 °C at 1 kHz, 10 kHz, 1 MHz, 10 MHz, and 20 MHz, respectively. (A) *x* = 0.07, (B) *x* = 0.09, (C) *x* = 0.09, and (D) *x* = 0.10.

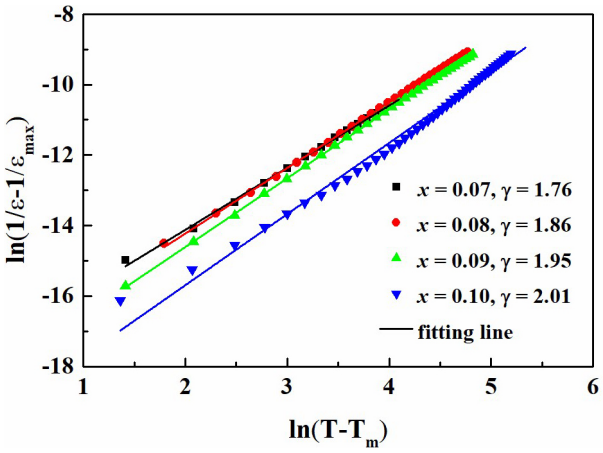

Figure 4. Plots of ln(1/ε-1/ε_{max}) as a function of ln(T-T_m) at 1 kHz by the modified Curie-Weiss law.

According to the Weibull distribution model, there is a linear relationship between X_i and Y_i, as shown in Equation (9).

$$Y_i = mX_i + b \tag{9}$$

where m represents the dispersion degree of all experimental data, and a larger m indicates more reliable experimental results.

The determination of the magnitude of DBS can be derived from the intercept on the ln(E_i) axis. The results obtained from the fitted calculations in Figure 5A indicate that the DBS gradually increases and then

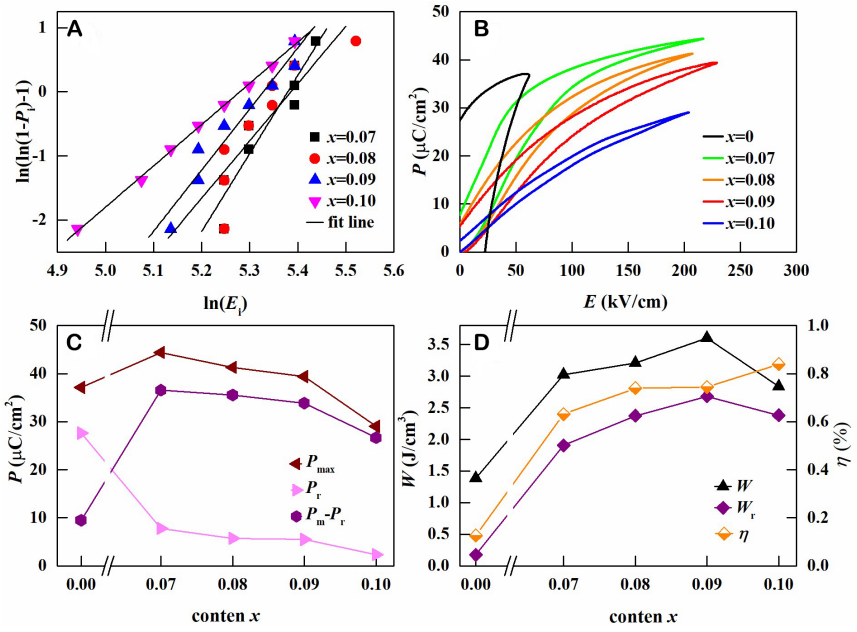

Figure 5. Energy storage studies of sintered (1-*x*)BNBT-*x*SBTZ ceramics. (A) Weibull distribution of the breakdown electric field; (B) *P-E* loops as a function of *x*; (C) P_m, P_r, and P_m-P_r as a function of *x*; (D) W_r, *W*, and η as a function of *x*.

decreases with the increase of SBTZ content, which is consistent with the shift in the average grain size. The DBS values obtained for increasing dopant concentrations were 215 kV/cm, 230 kV/cm, 245 kV/cm, and 218 kV/cm, respectively. The DBS is influenced by several factors, including porosity, grain size, and extrinsic measurement conditions such as sample thickness, sample area, and electrode configuration. In this study, all the samples had almost the same phase structure and measurement condition, but there was a slight difference in grain size. Generally, smaller grain size contributes to an enhanced DBS, and furthermore, the DBS exhibits an opposite variation tendency with grain size[23-25].

The polarization hysteresis (*P-E*) loops of the sintered BNBT-xSBTZ ceramics were measured and shown in Figure 5B. The test electric field was loaded near the breakdown field. The *P-E* loops were observed to be flat and slender, indicating weak ferroelectricity and enhanced relaxation properties. This is a crucial factor in achieving high energy storage density and efficiency[26]. As the doping content increased, P_{max}, P_r, and P_{max}-P_r gradually decreased, as depicted in Figure 5C. The trend of decreasing polarization intensity also suggests a decline in ferroelectricity. The sample with 0.93BNBT-0.07SBTZ exhibited the highest P_{max} of 44.38 μC/cm², but its W_r was not the highest due to its high P_r. In contrast, the 0.9BNBT-0.1SBTZ sample had a lower P_{max} of 29.04 μC/cm² and P_r of 2.36 μC/cm². Figure 5D illustrates the values of *W*, W_r, and η for all samples. It was observed that W_r reached its maximum value at x=0.09, while η was highest at x=0.10. The values of *W*, W_r, and η are presented in Table 1.

The practical application of energy storage ceramics requires good temperature stability. To investigate the temperature stability of the 0.91BNBT-0.09SBTZ ceramic, energy storage characteristics were examined at various temperatures. *P-E* hysteresis loops were measured at 170 kV/cm, with temperatures ranging from 25 °C to 140 °C, as depicted in Figure 6A. The *P-E* loops did not exhibit significant changes, with P_{max} decreasing from 34.7 μC/cm² at 25 °C to 31.6 μC/cm² at 140 °C. Additionally, W_r decreased from 1.71 J/cm³ to 1.52 J/cm³, as shown in Figure 6B. Despite the temperature variations, W_r and η remained at a relatively high level, indicating excellent temperature stability.

Table 1. Energy storage properties of (1-*x*)BNBT-*x*SBTZ ceramics

x	*W* (J/cm^3)	W_r (J/cm^3)	*E* (kV/cm)	η
0	1.38	0.174	60	12.6%
0.07	3.02	1.91	215	63.1%
0.08	3.21	2.37	230	73.9%
0.09	3.60	2.68	245	74.4%
0.10	2.84	2.38	218	83.9%

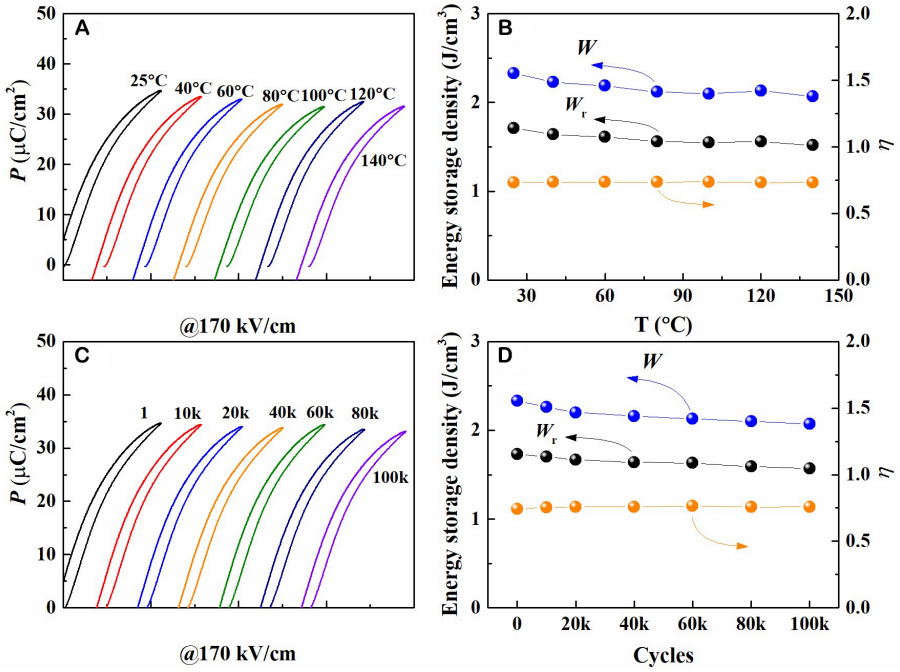

Figure 6. Temperature stability and fatigue resistance of the sintered ceramics. (A) *P-E* hysteresis loops at 25 °C to 140 °C; (B) W_r and η as a function of temperature; (C) fatigue behavior measured at various electrical cycles; (D) W_r and η as a function of electrical cycles.

In addition to examining the temperature stability of ceramics, their fatigue resistance behavior was also investigated. The fatigue behavior was assessed at room temperature under a frequency of 10 Hz and a voltage of 170 kV/cm, with a cycling number of 10^5. The *P-E* loops at different cycles were depicted in Figure 6C, while the changes in P_{max} and W_r with an increase in the number of charging/discharging cycles were illustrated in Figure 6D. After 10^5 cycles, W_r remained at a relatively high level of 1.5 J/cm^3, which was only 13.3% lower than its initial value of 1.73 J/cm^3, indicating favorable fatigue resistance properties. It is worth noting that P_{max} and W_r exhibited a slight decrease, which was attributed to the local phase decomposition caused by switching-induced charge injection, as suggested by Lou *et al.*[27-29].

CONCLUSIONS

This study investigated the dielectric and energy storage properties of (1-*x*)(0.94$Bi_{0.5}Na_{0.5}TiO_3$-0.06$BaTiO_3$) -*x*$Sr_{0.8}Bi_{0.1}\gamma_{0.1}Ti_{0.8}Zr_{0.2}O_{2.95}$ ceramics, prepared through the solid-state method. X-ray diffraction analysis revealed a single perovskite structure in all ceramic samples, indicating successful incorporation of SBTZ into the BNBT lattice. Doping with SBTZ resulted in notable relaxation properties and excellent energy storage capabilities. Specifically, 0.91BNBT-0.09SBTZ ceramics demonstrated a breakdown electric field of 230 kV/cm, with W_r of 2.68 J/cm^3 and η of 74.4%. Additionally, the energy storage properties of the ceramics

exhibited remarkable temperature stability and fatigue resistance. The energy storage density only decreased by 11% from room temperature to 140 °C, and after 10^5 electrical cycles, the energy storage density decreased by only 5.2%. Overall, these findings suggest that 0.91BNBT-0.09SBTZ ceramics have great potential as dielectric materials for energy-storage dielectric capacitors.

DECLARATIONS

Authors' contributions

Made substantial contributions to the conception and design of the study and performed data analysis and interpretation: Wang C

Performed data acquisition and provided administrative, technical, and material support: Lou X

Availability of data and materials

Not applicable.

Financial support and sponsorship

This work was supported by the Education Science and Technology Innovation Project of Gansu Province, China, the year of 2022; the project: Study on the mechanism of the fatigue behavior of sodium-bismuth-titanate based relaxor ferroelectric capacitors after electrical charge-discharge cycles (Grant No. 2022QB-213) and the National Natural Science Foundation of China (NSFC NO.52172125).

Financial support and sponsorship

None.

Conflicts of interest

Both authors declared that there are no conflicts of interest.

Ethical approval and consent to participate

Not applicable.

Consent for publication

Not applicable.

REFERENCES

1. Yang L, Kong X, Li F, et al. Perovskite lead-free dielectrics for energy storage applications. *Prog Mater Sci* 2019;102:72-108. DOI
2. Zou K, Dan Y, Xu H, et al. Recent advances in lead-free dielectric materials for energy storage. *Mater Res Bull* 2019;113:190-201. DOI
3. Shi P, Li T, Zhu X, et al. High strain in $Bi_{0.5}Na_{0.5}TiO_3$-based relaxors by adding two modifiers featuring with morphotropic phase boundary. *Scripta Mater* 2022;218:114674. DOI
4. Qi H, Zuo R. Linear-like lead-free relaxor antiferroelectric $(Bi_{0.5}Na_{0.5})TiO_3$-$NaNbO_3$ with giant energy-storage density/efficiency and super stability against temperature and frequency. *J Mate Chem A* 2019;8:3971-8. DOI
5. Zhu X, Shi P, Gao Y, et al. Enhanced energy storage performance of $0.88(0.65Bi_{0.5}Na_{0.5}TiO_3$-$0.35SrTiO_3)$-$0.12Bi(Mg_{0.5}Hf_{0.5})O_3$ lead-free relaxor ceramic by composition design strategy. *Chem Eng J* 2022;437:135462. DOI
6. Lv J, Li Q, Li Y, et al. Significantly improved energy storage performance of NBT-BT based ceramics through domain control and preparation optimization. *Chem Eng J* 2021;420:129900. DOI
7. Luo C, Feng Q, Luo N, et al. Effect of Ca^{2+}/Hf^{4+} modification at A/B sites on energy-storage density of $Bi_{0.47}Na_{0.47}Ba_{0.06}TiO_3$ ceramics. *Chem Eng J* 2021;420:129861. DOI
8. Yao Y, Li Y, Sun N, et al. Enhanced dielectric and energy-storage properties in ZnO-doped $0.9(0.94Na_{0.5}Bi_{0.5}TiO_3$-$0.06BaTiO_3)$-$0.1NaNbO_3$ ceramics. *Ceram Int* 2018;44:5961-6. DOI

9. Ma C, Tan X, Dul'kin E, Roth M. Domain structure-dielectric property relationship in lead-free (1-*x*)($Bi_{1/2}Na_{1/2}$)TiO_3-*x*$BaTiO_3$ ceramics. *J Appl Phys* 2010;108:104105. DOI
10. Ma C, Guo H, Beckman SP, Tan X. Creation and destruction of morphotropic phase boundaries through electrical poling: a case study of lead-free ($Bi_{1/2}Na_{1/2}$)TiO_3-$BaTiO_3$ piezoelectrics. *Phys Rev Lett* 2012;109:107602. DOI
11. Li T, Lou X, Ke X, et al. Giant strain with low hysteresis in a-site-deficient ($Bi_{0.5}Na_{0.5}$)TiO_3-based lead-free piezoceramics. *Acta Mater* 2017;128:337-44. DOI
12. Cao W, Li W, Feng Y, et al. Defect dipole induced large recoverable strain and high energy-storage density in lead-free $Na_{0.5}Bi_{0.5}TiO_3$-based systems. *Appl Phys Lett* 2016;108:202902. DOI
13. Liu Z, Ren P, Long C, Wang X, Wan Y, Zhao G. Enhanced energy storage properties of $NaNbO_3$ and $SrZrO_3$ modified $Bi_{0.5}Na_{0.5}TiO_3$ based ceramics. *J Alloy Compd* 2017;721:538-44. DOI
14. Zhang L, Pu Y, Chen M, et al. High energy-storage density under low electric fields and improved optical transparency in novel sodium bismuth titanate-based lead-free ceramics. *J Eur Ceram Soc* 2020;40:71-7. DOI
15. Wang C, Lou X, Xia T, Tian S. The dielectric, strain and energy storage density of BNT-BKH_xT_{1-x} piezoelectric ceramics. *Ceram Int* 2017;43:9253-8. DOI
16. Zhu X, Shi P, Kang R, et al. Enhanced energy storage density of $Sr_{0.7}Bi_xTiO_3$ lead-free relaxor ceramics via a-site defect and grain size tuning. *Chem Eng J* 2021;420:129808. DOI
17. Liu L, Fan H, Fang L, Chen X, Dammak H, Thi MP. Effects of Na/K evaporation on electrical properties and intrinsic defects in $Na_{0.5}K_{0.5}NbO_3$ ceramics. *Mater Chem Phys* 2009;117:138-41. DOI
18. Shi P, Zhu X, Lou X, et al. Tailoring ferroelectric polarization and relaxation of BNT-based lead-free relaxors for superior energy storage properties. *Chem Eng J* 2022;428:132612. DOI
19. Grace MAL, Sambasivam R, Perumal RN, Athikesavan V. Enhanced synthesis, structure, and ferroelectric properties of Nb-modified 1-*x*[$Bi_{0.5}(Na_{0.4}K_{0.1})(Ti_{1-x}Nb_x)$]$O_3$-*x*($Ba_{0.7}Sr_{0.3}$)$TiO_3$ ceramics for energy storage applications. *J Aust Ceram Soc* 2020;56:157-65. DOI
20. Viola G, Ning H, Wei X, et al. Dielectric relaxation, lattice dynamics and polarization mechanisms in $Bi_{0.5}Na_{0.5}TiO_3$-based lead-free ceramics. *J Appl Phys* 2013;114:014107. DOI
21. Shi P, Zhu X, Lou X, et al. $Bi_{0.5}Na_{0.5}TiO_3$-based lead-free ceramics with superior energy storage properties at high temperatures. *Compos Part B Eng* 2021;215:108815. DOI
22. Chen P, Chu B. Improvement of dielectric and energy storage properties in Bi($Mg_{1/2}Ti_{1/2}$)O_3-modified $(Na_{1/2}Bi_{1/2})_{0.92}Ba_{0.08}TiO_3$ ceramics. *J Eur Ceram Soc* 2016;36:81-8. DOI
23. Li W, Zhou D, Pang L. Enhanced energy storage density by inducing defect dipoles in lead free relaxor ferroelectric $BaTiO_3$-based ceramics. *Appl Phys Lett* 2017;110:132902. DOI
24. Zhao L, Liu Q, Gao J, Zhang S, Li JF. Lead-free antiferroelectric silver niobate tantalate with high energy storage performance. *Adv Mater* 2017;29:1701824. DOI
25. Wang T, Jin L, Li C, Hu Q, Wei X, Lupascu D. Relaxor ferroelectric $BaTiO_3$-Bi($Mg_{2/3}Nb_{1/3}$)O_3 ceramics for energy storage application. *J Am Ceram Soc* 2015;98:559-66. DOI
26. Shi P, Hong Z, Zhu X, et al. Enhancement of energy storage properties of $Bi_{0.5}Na_{0.5}TiO_3$-based relaxor ferroelectric under moderate electric field. *Appl Phys Lett* 2022;120:132903. DOI
27. Lou XJ. Polarization fatigue in ferroelectric thin films and related materials. *J Appl Phys* 2009;105:024101. DOI
28. Lou XJ, Zhang M, Redfern SAT, Scott JF. Fatigue as a local phase decomposition: a switching-induced charge-injection model. *Phys Rev B* 2007:75. DOI
29. Lou XJ, Zhang M, Redfern SA, Scott JF. Local phase decomposition as a cause of polarization fatigue in ferroelectric thin films. *Phys Rev Lett* 2006;97:177601. DOI PubMed

Li *et al. Microstructures* 2023;3:2023024
DOI: 10.20517/microstructures.2023.09

Microstructures

Review

Open Access

Check for updates

Recent developments in metal nanocluster-based catalysts for improving photocatalytic CO_2 reduction performance

Huan Li[1], Huitong Du[2], Huanhuan Luo[2], Hua Wang[3], Wenlei Zhu[2], Yang Zhou[1]

[1]Key Laboratory of Organic Electronics and Information Displays, Institute of Advanced Materials (IAM), Nanjing University of Posts & Telecommunications, Nanjing 210023, Jiangsu, China.
[2]State Key Laboratory of Analytical Chemistry for Life Science, State Key Laboratory of Pollution Control and Resource Reuse, Frontiers Science Center for Critical Earth Material Cycling, School of Chemistry and Chemical Engineering, School of the Environment, Nanjing University, Nanjing 210023, Jiangsu, China.
[3]Huzhou Key Laboratory of Medical and Environmental Applications Technologies, School of Life Sciences, Huzhou University, Huzhou 313000, Zhejiang, China.

Correspondence to: Prof. Wenlei Zhu, State Key Laboratory of Analytical Chemistry for Life Science, State Key Laboratory of Pollution Control and Resource Reuse, Frontiers Science Center for Critical Earth Material Cycling, School of Chemistry and Chemical Engineering, School of the Environment, Nanjing University, Nanjing 210023, Jiangsu, China. E-mail: wenleizhu@nju.edu.cn; Prof. Yang Zhou, Key Laboratory of Organic Electronics and Information Displays, Institute of Advanced Materials (IAM), Nanjing University of Posts & Telecommunications, Nanjing 210023, Jiangsu, China. E-mail: iamyangzhou@njupt.edu.cn

How to cite this article: Li H, Du H, Luo H, Wang H, Zhu W, Zhou Y. Recent developments in metal nanocluster-based catalysts for improving photocatalytic CO_2 reduction performance. *Microstructures* 2023;3:2023024. https://dx.doi.org/10.20517/microstructures.2023.09

Received: 3 Feb 2023 **First Decision:** 16 Mar 2023 **Revised:** 26 Apr 2023 **Accepted:** 8 May 2023 **Published:** 22 May 2023

Academic Editor: Chunqiang Zhuang **Copy Editor:** Fangling Lan **Production Editor:** Fangling Lan

Abstract

Photocatalytic reduction of carbon dioxide (CO_2) is a promising technology for carbon recycling that offers both environmental and economic benefits. Among the potential photocatalysts, metal nanoclusters (MNCs) stand out as a class of materials with remarkable photophysical and photochemical properties. Despite the growing number of studies on MNCs-based photocatalytic reduction of CO_2 in recent years, a systematic and comparative overview of these studies is still lacking. This review provides a concise and comprehensive summary of the latest research on MNCs-based catalysts for enhancing photocatalytic CO_2 reduction performance. Moreover, this review highlights the challenges and opportunities in this field based on the current development trends.

Keywords: Photocatalysis, CO_2 reduction, nanoclusters, photocatalyst

INTRODUCTION

Fossil fuels have been the dominant source of energy for various applications such as production, transportation, and power generation throughout human history. However, the excessive consumption of fossil fuels has led to the massive emission of carbon dioxide (CO_2), which poses serious threats to energy security and environmental quality[1-9]. Numerous carbon fixation strategies have been developed to address these challenges, such as CO_2 emission reduction, CO_2 capture and storage (CCS), and CO_2 utilization[10-12]. CO_2 emission reduction involves the use of innovative technologies to lower the amount of CO_2 produced during the production stage. However, these methods are often associated with high costs that are difficult for the general public to bear. The CCS also received significant attention, but the high cost and leakage risk limit its application on a large scale. CO_2 utilization, in contrast, is the most attractive path. Chemical reforming, electrochemical reduction, biological reduction, and photochemical reduction are the leading CO_2 utilization technologies. Photocatalytic CO_2 reduction (PCR) is a sustainable process. It does not produce any toxic byproducts or cause any environmental pollution. PCR process can harness solar energy to reduce CO_2 and produce valuable energy sources such as methane or methanol. Moreover, the PCR process is usually operating under mild conditions of ambient temperature and pressure. These advantages make PCR a highly desirable method for completing the carbon cycle[13-20].

In the past few decades, the development of PCR catalysts has shifted from early bulky metals to nanostructured materials with specific properties[21]. Nanoclusters (NCs) are a new class of materials comprising a few to several hundred atoms surrounded by ligands. NCs have three components: the inner core, the outer atoms, and the surface ligands (as shown in Figure 1)[22]. NCs exhibit distinct physical and chemical properties compared to nanoparticles and molecules due to their distinctive electronic and geometric structures. The majority of the current NCs are metal nanoclusters (MNCs) with sizes ranging from 0.1 to 5 nm (typically < 2 nm for MNCs)[23], which is close to the Fermi wavelength (approximately 0.7 nm). Due to the quantum size effect, a single atomic change can drastically alter the electronic structure and the physical and chemical properties of the clusters. Compared to conventional nanoparticles, MNCs possess a much higher proportion of surface atoms. The surface atoms of MNCs have a low coordination number, which results in high activity[24]. Furthermore, MNCs are easier to synthesize than individual atoms and also have a larger surface area and more catalytic sites than bulk materials[25].

Taking advantage of these inherent advantages, MNCs have been used as catalysts in various catalytic processes. For example, Kurashige *et al.* investigated Au NCs as co-catalysts for H_2 evolution[26]. Gautam *et al.* presented a series of Au_n(GSH) NCs as co-catalysts on $BaLa_4TiO_{15}$ for photocatalytic water splitting[27]. Numerous efforts also have been devoted to the development of MNCs-based photocatalysts to further improve PCR performance[28]. For instance, Shoji *et al.* reported Cu_xO NCs as a general co-catalyst and can be used in combination with various semiconductors to construct low-cost and efficient PCR systems[29]. Similarly, Gao *et al.* also reported Ag NCs as co-catalysts for selective CO_2 photoreduction to CO[30]. Additionally, Bo *et al.* bridged Au NCs with ultrathin nanosheets via ligands for enhancing charge transfer in PCR[31]. All these relevant reports above confirm that MNCs are promising catalyst candidates for PCR.

However, the synthesis and utilization of MNCs for PCR remain challenging. It requires a comprehensive understanding of their properties and catalytic reaction mechanisms. In this review, we provide a systematic overview of the recent advances in MNCs-based catalysts for PCR applications. We first introduce a general

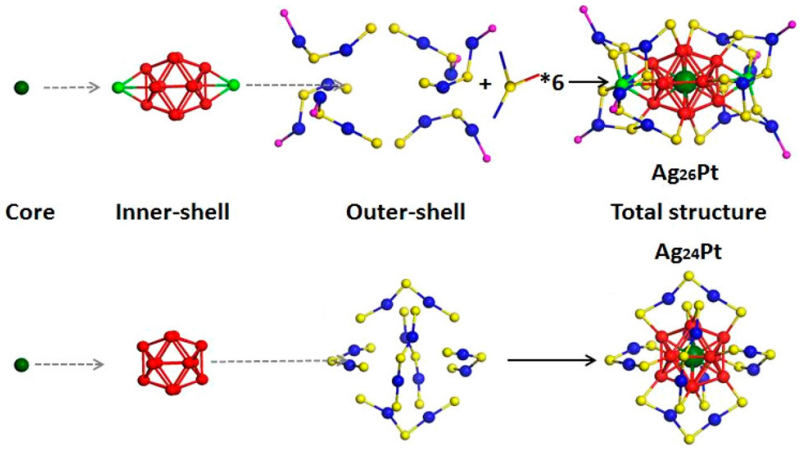

Figure 1. Structures of MNCs of $Ag_{26}Pt$ and $Ag_{24}Pt$[22]. Copyright 2018, American Chemical Society.

method for preparing MNCs. Next, we review how MNCs can enhance the PCR process as catalysts. We then classify the MNCs into two major categories: noble and nonnoble MNCs and summarize their advantages for PCR applications. Finally, we discuss the current challenges and prospects of MNCs for PCR. We hope this review will stimulate further research and innovation in this emerging field.

ADVANTAGES OF MNCS AND COMMON SYNTHESIS METHODS

Advantages of MNCs

MNCs show a very different energy level structure in comparison with large-size nanoparticles (as shown in Figure 2). MNCs change the electron energy level near the Fermi level from quasi-continuous to discrete, resulting in energy level splitting or energy gap widening[32,33]. The discrete energy levels allow the electrons in MNCs to jump between energy levels and interact with light, which enhances the separation of electrons and holes[34]. Additionally, MNCs also have a small energy gap and absorb light in the visible and near-infrared regions[35,36]. Furthermore, MNCs are stable against oxidation or reduction by photogenerated electrons or holes[37,38]. More importantly, MNCs have a high specific surface area, a high fraction of low-coordinated atoms, a quantum size effect, a tunable composition, and a unique surface structure (e.g., pocket-like sites) due to their ultra-small size. These unique features of MNCs make them an emerging class of photocatalytic materials with increasing interest[39]. Moreover, their precise atomic-level structures enable fundamental research on the photocatalytic mechanisms, which provides theoretical guidance for the design of new photocatalytic materials and improves catalytic performance[40].

The synthesis methods of MNCs

There has been much research into the synthesis of MNCs, so we have summarized the commonly reported synthesis methods in the literature as follows[41]:

(1) Reduction growth method[42] (as shown in Figure 3 a→c): The metal core is created by reducing the respective metal ions. Therefore, the strength of the chosen reducing agent and the kinetic regulation of the reduction process are crucial for synthesizing the desired product.

(2) Seed growth method[43] (as shown in Figure 3 c→d): Smaller-sized MNCs are used as seeds to induce nucleation, resulting in the growth of larger-sized MNCs over time. The regulation of the crystal growth process is noteworthy.

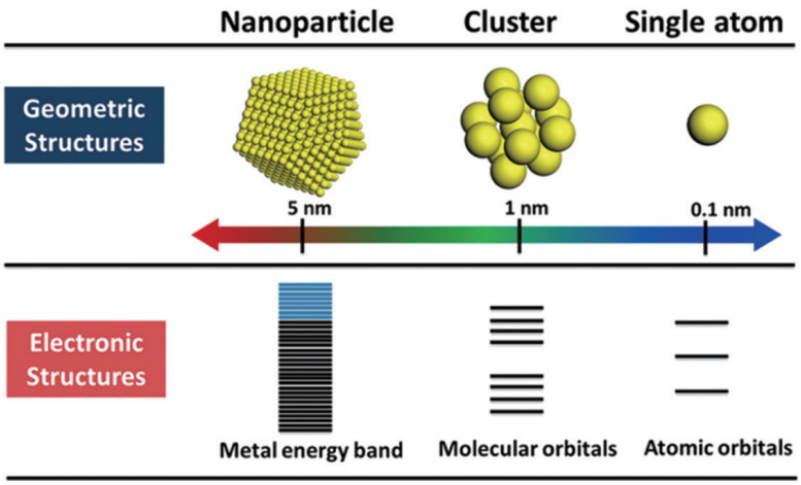

Figure 2. Geometric and electronic structures of single atoms, NCs, and nanoparticles[23]. Copyright 2018 American Chemical Society.

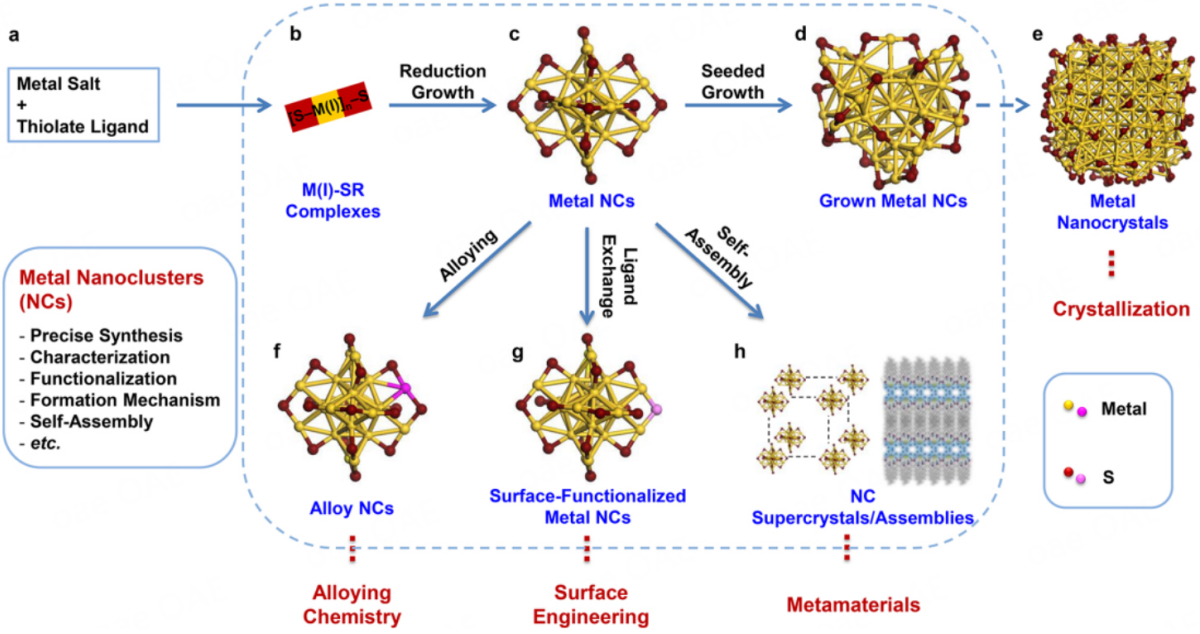

Figure 3. Common methods for the synthesis of MNCs: (a→b) formation of M(I)-SR complexes, metal atom (M(I)), thiolate ligand (SR), (b→c) reduction growth, (c→d) seeded growth, (c→f) alloying reaction, (c→g) ligand-exchange process, (c→h) self-assembly of metal NCs, and (d→e) evolution from metal NCs to metal nanocrystals[41]. Copyright 2016, American Chemical Society.

(3) Alloying method[44] (as shown in Figure 3 c→f): The introduction of other metals for doping could be accomplished through the template exchange method, where the difference in electrode potential between the two metals serves as the driving force for the substitution reaction.

(4) Ligand exchange method (as shown in Figure 3 c→g): In principle, the ligand exchange method is similar to the alloying method in that both involve an exchange process, but the objects exchanged differ. For example, template exchange generates alloying NCs, whereas ligand exchange refers to preparing MNCs by exchanging the protective ligand layers on their periphery.

(5) The current atomically precise nano-chemistry is indeed moving toward the programmable synthesis of MNCs with control over the structure, such as the bcc, fcc, hcp, decahedra, icosahedra, multi-tetrahedral network, *etc.* (as shown in Figure 4)[45,46]. This programmable synthesis of MNCs offers promising opportunities for designing their structures and enhancing their catalytic performance[47].

THE PCR MECHANISM OVER MNCS-BASED PHOTOCATALYSTS

PCR involves multielectron reduction, and various products can be obtained via different reduction pathways, such as CO, CH_4, HCOOH, C_2H_4, HCHO, and CH_3OH. Below are the reduction potentials (E_0, V *vs.* NHE) required for these products:[48]

$$CO_2 + e^- \rightarrow CO_2^- \; E_0 = -1.900 \text{ V} \quad (1)$$

$$CO_2 + 2H^+ + 2e^- \rightarrow HCOOH \; E_0 = -0.610 \text{ V} \quad (2)$$

$$CO_2 + 2H^+ + 2e^- \rightarrow CO + H_2O \; E_0 = -0.530 \text{ V} \quad (3)$$

$$2CO_2 + 2H^+ + 2e^- \rightarrow H_2C_2O_4 \; E_0 = -0.913 \text{ V} \quad (4)$$

$$CO_2 + 4H^+ + 4e^- \rightarrow HCHO + H_2O \; E_0 = -0.480 \text{ V} \quad (5)$$

$$CO_2 + 6H^+ + 6e^- \rightarrow CH_3OH + H_2O \; E_0 = -0.380 \text{ V} \quad (6)$$

$$CO_2 + 8H^+ + 8e^- \rightarrow CH_4 + 2H_2O \; E_0 = -0.240 \text{ V} \quad (7)$$

$$2CO_2 + 12H^+ + 12e^- \rightarrow C_2H_4 + 4H_2O \; E_0 = -0.349 \text{ V} \quad (8)$$

$$2CO_2 + 14H^+ + 14e^- \rightarrow C_2H_6 + 4H_2O \; E_0 = -0.270 \text{ V} \quad (9)$$

$$3CO_2 + 18H^+ + 18e^- \rightarrow C_3H_7OH + 5H_2O \; E_0 = -0.310 \text{ V} \quad (10)$$

The ultra-small size of NCs gives them a strong quantum size effect, exhibiting discrete energy levels that allow electrons to undergo a leap from the highest occupied molecular orbital (HOMO) to the lowest unoccupied molecular orbital (LUMO), and electron-hole separation occurs. The energy gap of MNCs is typically less than 2.2 eV, allowing photocatalytic reactions under visible light irradiation. Therefore, MNCs can be considered semiconductor nanomaterials for photocatalytic reactions with small band gaps.

The mechanism of MNCs as catalysts in the PCR process is as follows (as shown in Figure 5)[49,50]. After irradiating the MNCs-based catalyst with light with photon energy equal to or greater than the band gap energy, the electrons transfer from the valence band (VB) to the conduction band (CB) to generate photogenerated electrons and holes. The photogenerated holes are transferred to the surface active sites for the oxidation reaction, as shown in process (1) of Figure 5[51]. In process (3) of Figure 5, photogenerated electrons are transferred to the surface-active site for the reduction reaction. Therefore, the photocatalytic performance is affected by the incident light absorption capacity and charge separation efficiency. To fully utilize the energy from solar radiation, the band gap of the photocatalyst should be below 3.1 eV to maximize light absorption[52]. Most of the solar radiation energy reaching Earth is in the visible spectrum. Additionally, the generated electrons and holes do not always migrate to the surface of the photocatalyst

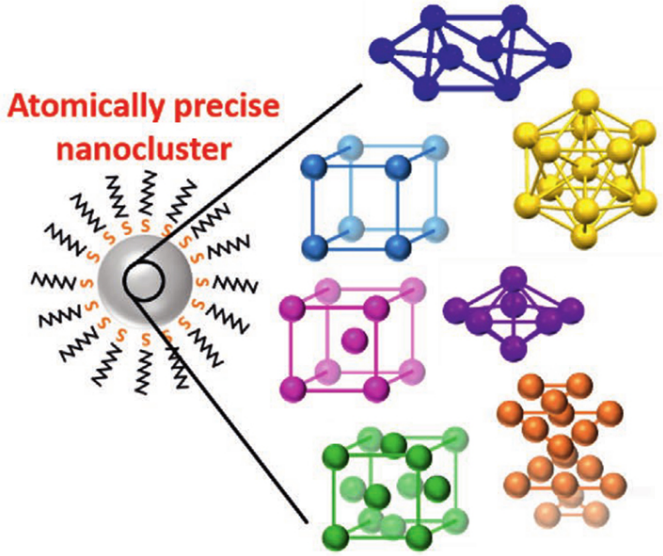

Figure 4. Programmable atomic packing into different crystal structures of Au NCs[45]. Copyright 2021, Wiley-VCH.

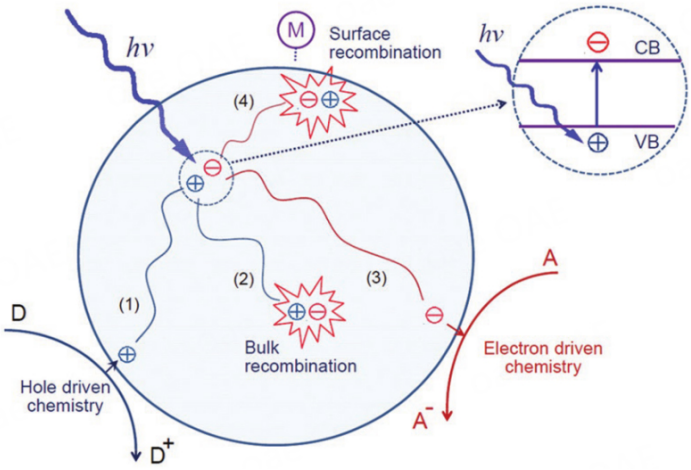

Figure 5. Photocatalytic process of MNCs[49]. Copyright 1995, American Chemical Society.

and react optimally. Occasionally, photogenerated electrons and holes will combine inside the catalyst [as shown in process (2) in Figure 5] or on the surface [as shown in process (4) in Figure 5] in a brief period, releasing energy in the form of heat or light that can result in a significant reduction in photocatalytic efficiency.

Therefore, the MNCs-based materials used to improve the PCR process must satisfy the following conditions: (1) Smaller energy gaps, typically exhibiting significant absorption in the visible or near-infrared region, make it easier to form photogenerated electron-hole pairs; (2) Good photostability, not readily oxidized or reduced by photogenerated holes or electrons. Long lifetimes of photogenerated electrons and holes so that the electron-hole pairs can participate more in redox reduction; and (3) The large specific surface area provides more catalytic sites, allowing free electrons to react with CO_2 via charge transfer to the composite surface[53].

PROGRESS OF MNCS-BASED CATALYSTS IN PCR

MNCs have garnered attention for their potential to improve PCR performance due to their unique and desirable properties. Several reasons contribute to the focus on MNCs for PCR, including:

(1) High catalytic activity: The small size and high surface area-to-volume ratio of MNCs result in a high catalytic activity, which can enhance the efficiency of the PCR.

(2) Improved charge transfer: MNCs have been shown to improve the charge separation and transfer processes in photocatalytic systems, leading to higher photocatalytic activity.

(3) Tailor-made properties: The properties of MNCs can be easily tuned or customized by controlling the size, shape, and composition, allowing for better control of their catalytic activity.

Overall, MNCs have shown great potential for enhancing PCR performance. Continued research on MNCs can contribute to the development of sustainable and efficient CO_2 reduction systems. Many strategies have been proposed to use MNCs as catalysts for improving PCR performance. This section reviews the recent advances in MNCs-based catalysts for enhancing PCR performance. We classify the MNCs-based catalysts into two subsections, nonnoble (e.g., Cu[54], CdS[55], Fe, Co[56], Ni, Cu) and noble MNCs-based (e.g., Au[57], Ag[58], Pt) catalysts[59]. Then, we describe their respective roles as catalysts for improving the PCR process. The photocatalytic performance of various MNCs-based catalysts under visible-light irradiation is presented in Table 1.

Nonnoble MNCs-based catalysts in PCR

Nonnoble MNCs offer a wide range of material selection options, and commonly available and inexpensive metals such as Fe, Ni, Cu, and Al can be used to prepare MNCs. Additionally, they are generally less costly compared to noble MNCs, resulting in lower preparation costs. In addition, semiconductor materials with wide energy gaps, such as TiO_2, $SrTiO_3$, $BiVO_4$, Ta_3N_5, g-C_3N_4, CdS, and MoS_2, are the most widely used photocatalysts[60]. However, most required light sources are in the ultraviolet spectrum, with low solar utilization and high electron-hole complexation rates, resulting in low photocatalytic reaction efficiency[61-63]. Consequently, using nonnoble MNCs as co-catalysts is suitable for overcoming these disadvantages[64]. Due to the advantages mentioned above, nonnoble MNCs-based catalysts are primarily employed for surface modification of semiconductor materials to enhance PCR performance. The reaction process for nonnoble MNCs-based catalysts to improve PCR performance by surface modification techniques has two steps, namely visible-light-induced interfacial charge transfer (IFCT) between the MNCs and semiconductor materials and the multielectron reduction of oxygen molecules mediated by the co-catalytic promoter effect of the MNCs[65].

Preparation of nonnoble MNCs-based catalysts by impregnation to enhance PCR performance

Photocatalysts composed of nonnoble MNCs and semiconducting materials are typically fabricated by the impregnation method[66]. Impregnation is a method of incorporating one material into another by soaking or spraying the material onto the surface of the other. Impregnation involves the following steps: The prepared semiconducting material is soaked or sprayed with the MNCs' solvent, which contains a suspension of MNCs, and allowed to dry. The MNCs are then deposited onto the surface of the semiconducting material. The impregnated semiconducting material is then calcined at high temperatures to remove the solvent and stabilize the MNCs on the surface of the semiconducting material. The impregnation method allows for the controlled deposition of MNCs onto the surface of semiconducting materials, thereby preparing materials with good photocatalytic activity.

Table 1. Performance of various noble & nonnoble MNCs used for PCR

Sample	Performance	References
Cu (II)-TiO_2	CO_2 generation rate = 0.13 μmol/h; quantum efficiency = 27.7%	[67]
Cu(II)-Nb-doped TiO_2	CO_2 generation rate = 0.20 μmol/h; quantum efficiency = 25.3%	[69]
Cu(II)-TiO_2 after the coordination of oxygen and metal	CO_2 generation rate = 0.40 μmol/h; quantum efficiency = 68.7%	[75]
Fe(III)-TiO_2	CO_2 generation rate = 0.40 μmol/h; quantum efficiency = 53.5%	[77]
Fe(III)-Ti(IV)-TiO_2	CO_2 generation rate = 0.69 μmol/h; quantum efficiency = 92.2%	[79]
Ni/TiO_2	CH_3CHO production rate = 1.42 μmol g-cat^{-1}	[81]
TiO_{2-x}/CoO_x	CO production rate = 1.2473 μmol/g/h; CH_4 production rate = 0.0903 μmol/g/h	[82]
CeO_x-S/$ZnIn_2S_4$	CO productivity of 1.8 mmol/g$^{/}$ with a rate of 0.18 mmol/g/h	[83]
Au NCs/TiO_2/Ti_3C_2 with CBD method	CO yield of 27.5 μmol/g in 3 h; CH_4 yield of 42.11 μmol/g in 3 h	[87]
SNO/CdSe–DET	CO production rate = 36.16 μmol/g/h	[102]
Au-NC@UiO-68-NHC	CO production rate = 57.57 μmol/g/h	[107]

The initial focus of the research was to improve the visible light sensitivity of TiO_2 semiconductors by using Cu(II) or Fe(III) NCs as co-catalysts (as shown in Figure 6)[67,68]. However, this photocatalytic system has limited catalytic efficiency because IFCT occurs only at the TiO_2/MNCs interface. Liu *et al.* designed a TiO_2 photocatalyst that can respond to visible light based on the principle of energy level matching[69]. The energy level occupied by the N-doped particles below the conduction band of TiO_2 matches the potential of the Cu^{2+}/Cu^{+} redox couple in the Cu(II) NCs. The matched energy levels facilitate the efficient transfer of photogenerated electrons from the doped Nb state to the Cu(II) NCs, thereby contributing to the efficient multielectron reduction of oxygen molecules (as shown in Figure 7)[69,70]. This method provides a practical and strategic approach to creating new MNCs materials with effective photocatalytic properties.

Nonnoble MNCs-based catalysts improve PCR performance by increasing vacancies and defects

Nonnoble MNCs-based catalysts are not limited to simple grafting modifications as co-catalysts. It was discovered that the performance of PCR could be enhanced by increasing the vacancies and defects. By generating oxygen vacancies, these modifications increase the surface negative charge density[71]. Upon exposure to light, the oxygen vacancies accumulate additional negative charges that contribute to the extension of the visible light absorption of semiconductor material, making the metal oxide capable of activating CO_2[72].

Nolan *et al.* present a study of electron and hole localization in low-coordinated titanium and oxygen sites of free and metal oxide-supported TiO_2 nanocrystals (as shown in Figure 8A)[73]. This approach highlights how nonnoble MNCs can enhance oxygen and metal coordination by modifying semiconductor materials. The structure of MNCs as catalysts in semiconductors reveals a significantly different metal and oxygen coordination environment compared to that of the unmodified semiconductor[74,75]. Low-coordinated metal and oxygen sites are crucial as charge carrier capture sites and active sites for target molecules, such as carbon dioxide and water[76]. Thus, Liu *et al.* developed a more sophisticated synthesis strategy by employing MNCs with poorly coordinated metal and oxygen sites as catalysts[77,78]. Liu *et al.* also demonstrated that amorphous Ti(IV) NCs promoted the oxidation of organic compounds effectively (as shown in Figure 8B) and that TiO_2 with Fe(III) and Ti(IV) NCs as catalysts achieved a Q.E. of 90% (as shown in Figure 8C)[79]. Additionally, Cheng *et al.* recently published the first study on Cu clusters mediated into Cd vacancies at the edges of CdS nanorods for photocatalytic CO_2 conversion[80]. Billo *et al.* reported a Ni-NCs/TiO_2 catalyst with improved PCR performance[81]. The Ni-NCs and O vacancies provide energetically stable CO_2 binding sites for CO_2 reduction, allowing for rapid electron transport for enhanced solar energy harvesting[81]. This method enhances the photocatalytic activity and selectivity of Ni/TiO_2 via a synergistic interaction in which

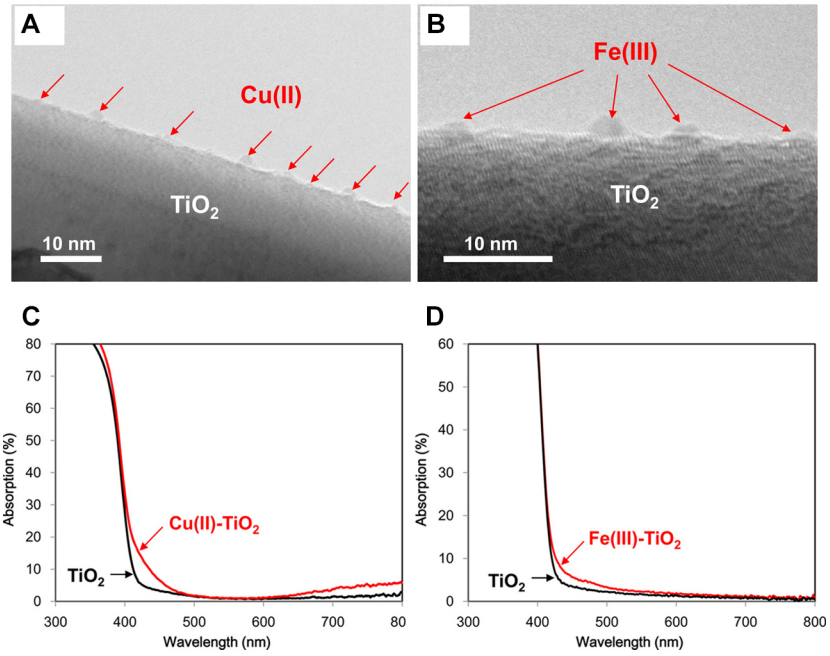

Figure 6. Cu (II) (A) and Fe (III) (B) NCs-grafted TiO_2 images captured by TEM. UV-Vis absorption spectra for Cu(II) (C) and Fe(III) (D) NCs-grafted TiO_2[70]. Copyright 2016, American Chemical Society.

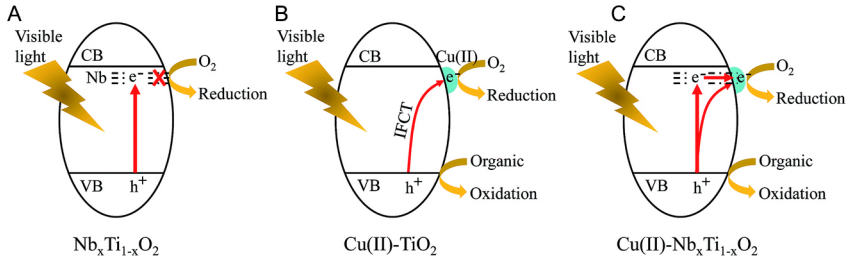

Figure 7. Proposed photocatalytic processes for (A) $Nb_xTi_{1-x}O_2$, (B) Cu(II)-TiO_2, and (C) Cu(II)-$Nb_xTi_{1-x}O_2$, respectively[70]. Copyright 2016, American Chemical Society.

the active center increases activity by lowering the activation barrier energy for CO_2 dissociation, and CO_2 molecules can bind to Ni and defect sites. Li *et al.* developed an effective photothermal catalyst by modifying TiO_2 nanotubes with a minute amount of CoO_x and oxygen vacancies. The results demonstrated that introducing oxygen vacancies facilitated the charge separation and dispersion of CoO_x co-catalysts, in which grafted CoO_x acted as hole traps and promoted the release of more protons (as shown in Figure 9)[82]. In addition, Hou *et al.* have significantly enhanced the activity by constructing CeO_x NCs with surface defect sites via a "partial sulfation" technique. The underlying principle of this strategy is improving the surface electronic properties of CeO_x-S NCs, which in turn induces the appearance of several Ce^{3+} and oxygen vacancies[83]. The photogenerated electrons were captured by oxygen vacancies on the CeO_x-S/$ZnIn_2S_4$ catalyst and subsequently transferred to CO_2, promoting CO_2 activation (as shown in Figure 10). This discovery also provides information regarding the optimization of PCR.

Noble MNCs-based catalysts in PCR

While the high cost of noble MNCs limits their use in large quantities, they possess large energy bandwidths and high electron densities that enable them to rapidly receive and release electrons. This results in the high

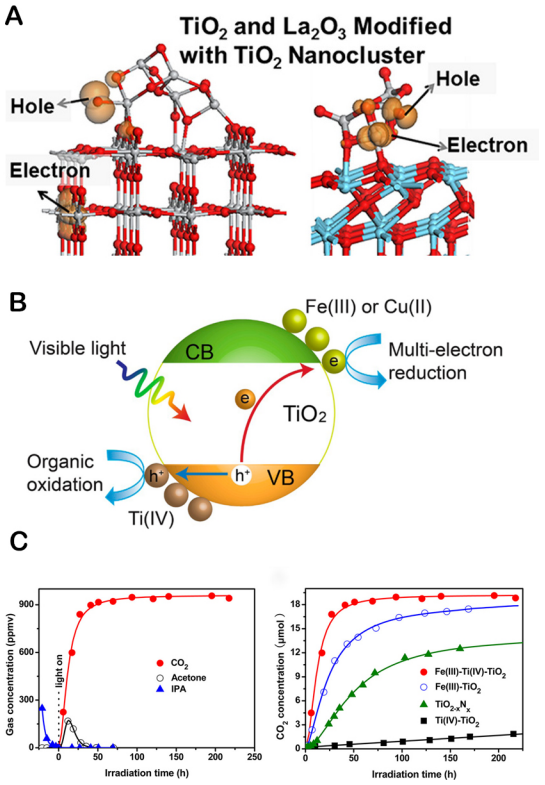

Figure 8. (A) Atomic structure of TiO_2 and La_2O_3 modified with TiO_2 NCs[73]. Copyright 2014, American Chemical Society. (B) Proposed photocatalysis processes. (C) Photocatalytic performance of the Fe(III)-Ti(IV)-TiO_2 nanocomposites[79]. Copyright 2014, American Chemical Society.

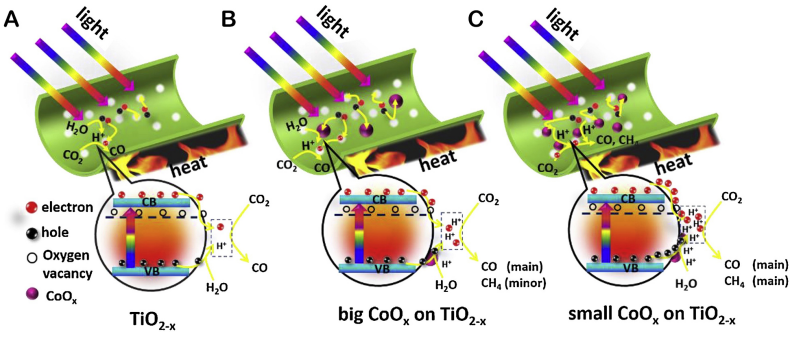

Figure 9. Scheme of photothermocatalytic reaction over three typical samples: (A) TiO_{2-x}. (B) big CoO_x clusters modified TiO_{2-x}. (C) small CoO_x clusters modified TiO_{2-x}[82]. Copyright 2018, Elsevier.

catalytic activity of noble MNCs[84]. Noble MNCs are also known to exhibit unique electrical and thermodynamic properties, which allow them to perform reactions that other catalysts cannot. For instance, they are being utilized in biological research.

Noble MNCs-based catalysts improve PCR performance by cluster beam deposition

The acids and ligands used in conventional surface modification techniques have a chemical contamination effect on the MNCs (the effect causes the change of a single atom to have a significant physical and chemical effect on the MNCs). Cluster beam deposition (CBD) was proposed to avoid the chemical contamination of

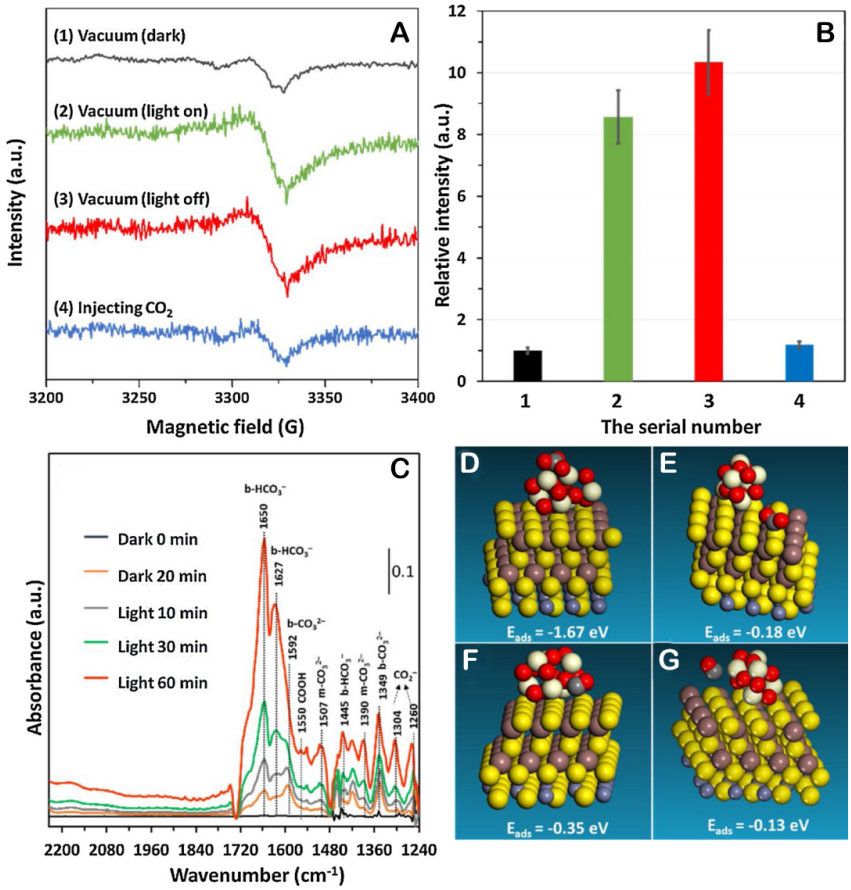

Figure 10. Investigation of the promotional role of CeO_x-S clusters in electron transfer and the subsequent surface reaction. (A) *In situ* EPR signals of CeO_x-S/$ZnIn_2S_4$. (B) Quantitative analysis by the double integral of the EPR signals in a. (C) *In situ* FTIR spectra for the adsorption, activation, and reduction of CO_2 under visible light over CeO_x-S/$ZnIn_2S_4$. (D and E) Adsorption energies of CO_2 and (F and G) CO at different sites of Ce_6O_{10}-$ZnIn_2S_4$ (0001) determined by DFT calculations[83]. Copyright 2018, Elsevier.

MNCs. CBD produces cluster-modified semiconductor materials with exceptional photocatalytic properties by forming clusters in a gaseous environment and then soft-landing them on supports with precise control over their size, shape, and composition (as shown in Figure 11)[85]. After deposition, unlike wet chemistry, no additional calcination or activation steps are required[86]. The vapor-phase Au NCs deposition method permits the placement of all active particles on the surface. Li *et al.* also prepared Au NCs/TiO_2/Ti_3C_2 and Au nanoparticles/TiO_2/Ti_3C_2 by deposition and precipitation[87]. The optimized Au NCs/TiO_2/Ti_3C_2 exhibited higher yields of reduced CO_2 to CO and CH_4 than Au-nanoparticles/TiO_2/$TiCO_2$ and P-Au-nanoparticles/TiO_2/$TiCO_2$ (as shown in Figure 12)[87]. CBD for MNCs synthesis not only reduces the risk of chemical contamination but also ensures that the MNCs are evenly distributed over the semiconductor surface and reduces costs.

Preparation of Noble MNCs-based catalysts by preventing clusters from aggregating improve PCR performance

Due to their large specific surface area and high surface energy, noble MNCs are typically thermodynamically unstable and susceptible to migration and agglomeration under light irradiation or high-temperature conditions, resulting in a substantial decrease in catalytic activity and selectivity[88,89]. Therefore, strategies to prevent cluster aggregation on the carrier are necessary to enhance their photocatalytic performance[90].

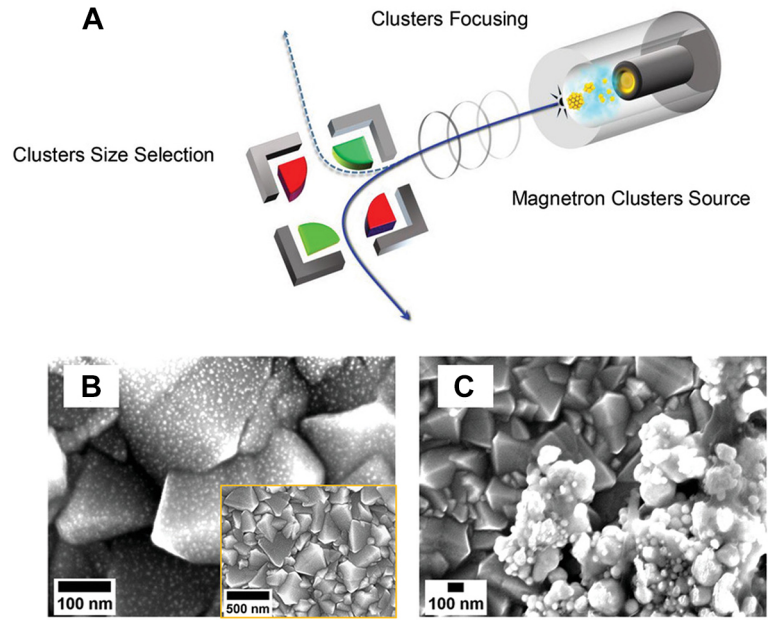

Figure 11. (A) Schematic illustration of magnetron CBD technology. High-Resolution SEM images of (B) Au NCs modified FTO and (C) colloidal Au modified FTO. The inset image in (B) shows the global view of deposited Au NCs[85]. Copyright 2021, Wiley-VCH.

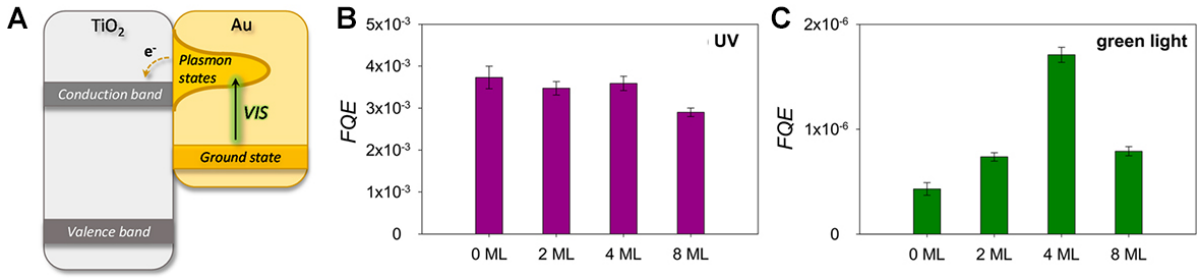

Figure 12. (A) Schematic illustration of hot electron transfer from an excited plasmonic state on the gold nanoparticle to the TiO_2 conduction band. Formal Quantum Efficiency (FQE) under (B) UV and (C) green light illumination as a function of Au NCs coverage on TiO_2 P25[86]. Copyright 2018, Wiley-VCH.

Bard proposed traditional Z-scheme photocatalysts in 1979[91], which can improve charge separation efficiency and retain strong redox capabilities. This system consists of two semiconducting materials with appropriate intermediate couples, such as Fe^{3+}/Fe^{2+}, IO^{3-}/I^-, and I^{3-}/I^-[92]. These two semiconductors have band structure configurations that differ. In a perfect process, photogenerated holes in the VB of PC I react with electron donors to produce electron acceptors. Photogenerated electrons in PC II's CB react with electron acceptors to produce electron donors. Then, photogenerated electrons in PC I's CB and holes in PC II's VB participate in the reduction and oxidation reactions, respectively (as shown in Figure 13)[93,94]. This mode of charge transfer can endow this system with powerful redox capability and spatially distinct redox reaction sites. Deng *et al.* developed PCR catalysts based on Z-scheme Au NCs (as shown in Figure 14)[95]. By combining with the photogenerated electrons in the coupled semiconductor, the photogenerated holes in the Au NCs can be consumed. This combination prevents the self-oxidative aggregation of Au NCs and increases their stability, thereby enhancing their photocatalytic activity[95]. Therefore, it is essential to combine NCs with suitable semiconductors when constructing a Z-scheme heterojunction system.

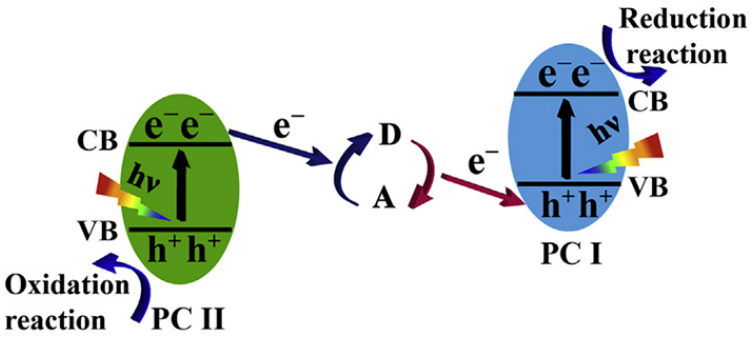

Figure 13. Schematic illustration of charge transfer in traditional Z-scheme heterojunction photocatalysts. D in the figure indicates electron donors, and A in the figure indicates electron acceptors[94]. Copyright 2020, Elsevier Inc.

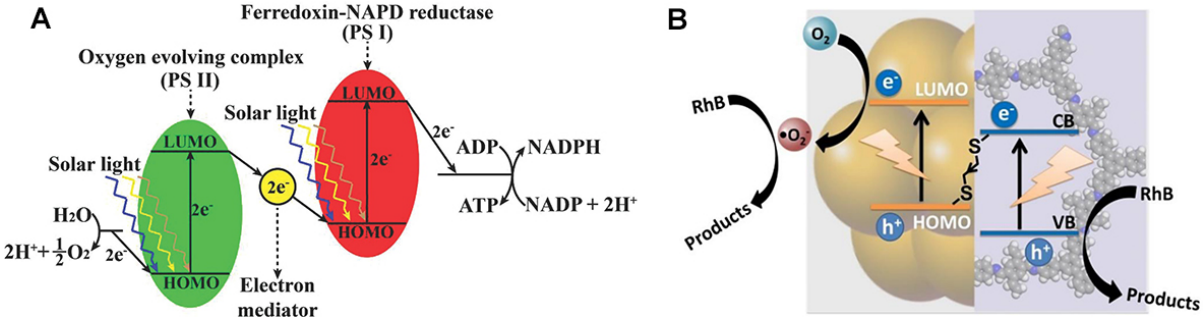

Figure 14. (A) A Z-scheme photocatalytic mechanism in natural photosynthesis system[90]. Copyright 2014, WILEY-VCH. (B) Photogenerated electron transport rules between Au NCs and COF support[95]. Copyright 2020, Wiley-VCH.

In addition to Z-scheme heterojunction structures, S-scheme heterojunctions are utilized to fabricate catalysts for improving PCR performance. (as shown in Figure 15A)[96]. S-scheme heterojunction has the following advantages: (1) the photocatalytic system can have both a wide photo-response range and a strong redox ability; (2) the large internal contact area and the rapid separation of carriers in the S-scheme system suppress the photo-induced electron-hole pair combination, which further improves the photocatalytic ability[97-101]. Ke *et al.* initially fabricated a novel S-scheme SNO/CdSe-DET composite and investigated its PCR activity (as shown in Figure 15B)[102]. The SNO/CdSe-DET composites exhibited excellent CO_2 photoreduction stability. Such a superior activity should be ascribed to the S-scheme system, which benefits the separation of the photogenerated carriers and promotes the synergy between CdSe-DET nanorods and SNO nanosheets by strong chemical-bonding coordination.

The encapsulation of MNCs in metal-organic frameworks (MOFs) has also garnered considerable interest[103,104]. By encapsulating MNCs within the environment of the MOFs structure, their fluctuations and aggregation can be effectively reduced, resulting in improved stability and catalytic efficiency. The MOFs structure prevents MNCs from interacting with undesirable species in the reaction environment, which can have a detrimental impact on their performance. Furthermore, the highly porous and interconnected structure of MOFs enables the efficient mass transfer of molecules to and from the active sites of MNCs, thereby enhancing their catalytic activity[105]. Overall, the MOFs-encapsulated MNCs show enhanced stability and improved performance, making them highly attractive for improving PCR performance. Indrani Choudhuri and Donald G. Truhlar studied a composite material containing a Cd_6Se_6 cluster in the pore of NU-1000 MOF. The Cd_6Se_6@NU-1000 composite permits electron transfer from the visible-light photo-excited organic linker to the lowest unoccupied orbital of the inorganic cluster, which can result in

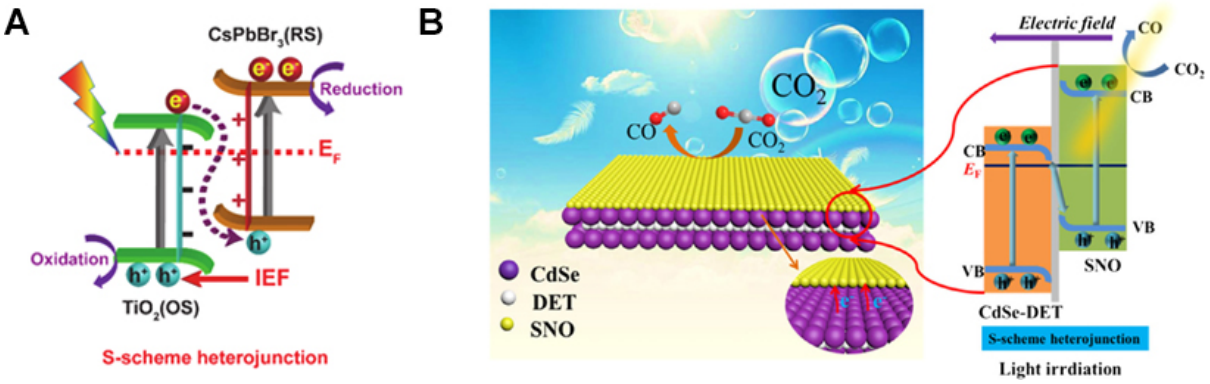

Figure 15. (A) S-scheme heterojunction. (B) The S-scheme SNO/CdSe-DET heterojunction charge migration and separation diagram under light irradiation[102]. Copyright 2021, Wiley-VCH.

charge separation (as shown in Figure 16A and B)[106]. Jiang *et al.* present a heterogeneous nucleation strategy for stabilizing and dispersing ultrasmall Au NCs in an NHC-functionalized porous matrix (as shown in Figure 16C)[107]. The Au NCs are embedded in the MOF material to prevent cluster aggregation. It gives the composite material a high degree of photostability and chemical stability. During the PCR process, the Au-NC@MOF composite demonstrates outstanding and consistent activity (as shown in Figure 16D)[107]. Therefore, MOFs are ideally suited for photocatalysis design.

Noble MNCs-based catalysts improve PCR performance by photosynthetic biohybrid system

Noble MNCs exhibit excellent biocompatibility, minimizing interference with the inherent functions of living organisms. This advantage allows noble MNCs to be used in the biological field. To link pre-assembled biosynthetic pathways with inorganic light absorbers, a photosynthetic biohybrid system (PBS) was developed. Both the high light-harvesting efficiency of solid-state semiconductors and the superior catalytic performance of whole-cell microorganisms are inherited by this strategy[108]. For instance, Zhang *et al.* utilized Au NCs as biocompatible intracellular light absorbers in PBS[109]. A biocompatible light absorber circumvents slow electron transfer kinetics and functions of the existing PBS as an inhibitor of reactive oxygen species to maintain high bacterial activity. With the dual advantages of light absorption and biocompatibility, this PBS can efficiently absorb sunlight and transfer photogenerated electrons to cellular metabolism, allowing for several days of continuous CO_2 fixation (as shown in Figure 17)[109]. The method of constructing PBSs offers a novel concept for PCR.

To summarize, compared to noble MNCs-based catalysts, nonnoble MNCs-based catalysts have a lower price, greater availability, a more comprehensive selection of materials, and better stability. The disadvantage is that the catalytic effect of the PCR process is inferior to that of noble MNCs. Furthermore, noble MNCs-based catalysts exhibit better biocompatibility. However, the scarcity of precious metals causes them to be expensive. The high specific surface area of noble MNCs-based catalysts can cause aggregation. Maintaining the long-term stability of the composites under *in situ* light conditions is challenging, a bottleneck in developing noble MNCs-based catalysts for practical applications. Thus, adopting strategies to prevent cluster aggregation on the carrier (such as Z/S-scheme heterojunction or MOF structure) is essential for their photocatalytic performance.

SUMMARY AND PROSPECTS

Artificial carbon fixation has stimulated the development of PCR as a promising technology. MNCs are a new potential photocatalyst with unique physical and chemical properties. To improve PCR performance,

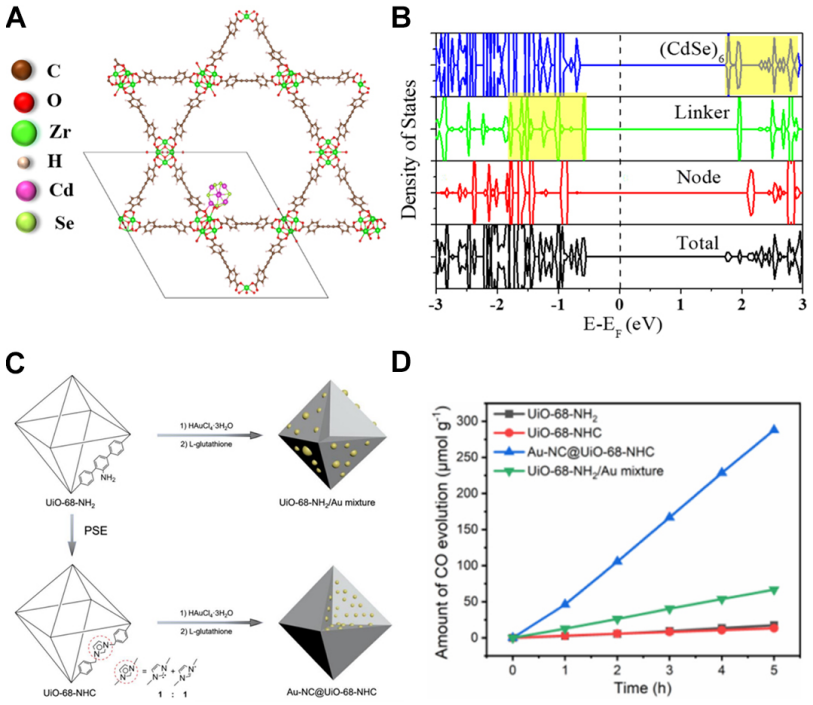

Figure 16. (A) Structure of the Cd_6Se_6 cluster encapsulated in NU-1000 at a node site (Cd_6Se_6@NU-1000). The unit cell of the system is denoted by a solid line. (B) Total and partial density of states of Cd_6Se_6@NU-1000. The Fermi level is set to zero and denoted by a black dashed line. The highest occupied crystal orbital (HOCO) is on the linker, and the lowest unoccupied crystal orbital (LUCO) is on the cluster. The highest-energy occupied orbitals on the linker and the lowest-energy unoccupied orbitals on the cluster are highlighted in yellow[106]. Copyright 2020, American Chemical Society (C) Schematic presentation for the synthesis of UiO-68-NHC, Au-NC@UiO-68-NHC, and UiO-68-NH_2/Au mixture. (D) Time courses of CO evolution by PCR using UiO-68-NHC, Au-NC@UiO-68-NHC, UiO-68-NH_2, and Au/UiO-66-NH_2 as photocatalysts upon AM 1.5 G irradiation[107]. Copyright 2021 Wiley-VCH.

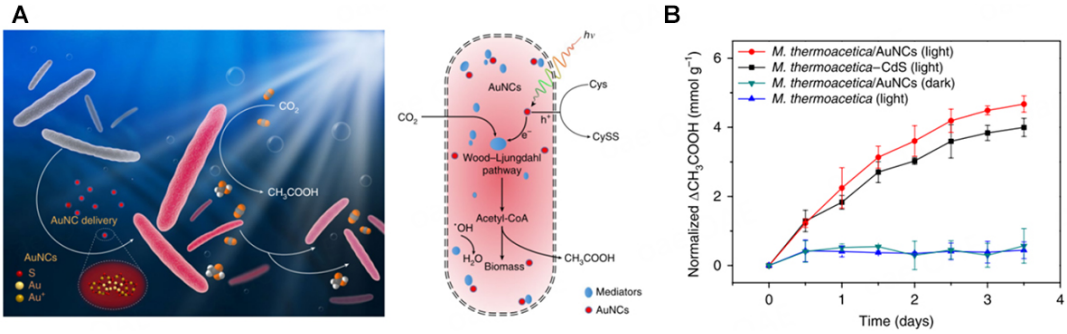

Figure 17. (A) Schematic diagram of the M. thermoacetica/Au NCs hybrid system. (B) photosynthesis behavior of different systems[109]. Copyright 2018, Springer Nature.

various advanced techniques have been widely explored. Due to the fast progress of this field, a summary of recent studies is essential for both new and experienced researchers in related fields. In this review, we summarize the recent advances in MNCs-based catalysts for PCR. We first introduce the synthesis of MNCs. Then, we explain the mechanism of photocatalysis based on MNCs-based catalysts. Finally, in the section on advanced MNCs-based catalysts for PCR, we classify MNCs into nonnoble MNCs and noble MNCs and summarize their role as catalysts in enhancing PCR performance. In the future, it is believed that there will be more strategies to optimize the design of MNCs-based catalysts for PCR. Therefore, we want to

emphasize the outlook for catalysts based on MNCs:

(1) The majority of current research is devoted to the development of transition MNCs. However, other types of NCs, such as alloy NCs, also merit investigation and consideration.

(2) The selectivity of CO_2 reduction by MNCs-based catalysts used to enhance the PCR process is still not good, and most systems can only reduce CO_2 to C_1 products such as CO. Therefore, how to improve the selectivity of PCR through material and system design is an important challenge at present.

(3) In the PCR process, MNCs are mostly used as co-catalysts/photosensitizers for semiconductor nanomaterials. It is hoped that in the future, there will be MNCs that can be used directly in PCR with excellent performance.

(4) The PCR efficiencies are still lower than commercial targets, and a firm understanding of how these rich structures of MNCs affect catalytic performance has yet to be fully achieved. The reaction pathways at the atomic level have yet to be determined. Therefore, further research should be dedicated to enhancing the activity of PCR processes and monitoring the structure of MNCs during reactions to further establish the precise correlation between structure and catalytic performance.

DECLARATIONS

Authors' contributions

Conceptualization, investigation, writing-original draft: Li H
Writing-review & editing: Luo H, Du H
Writing-review & editing, supervision, and funding acquisition: Wang H, Zhu W, Zhou Y

Availability of data and materials

Not applicable.

Financial support and sponsorship

This work was supported by the National Natural Science Foundation of China (22176086), the Natural Science Foundation of Jiangsu Province (BK20210189), State Key Laboratory of Pollution Control and Resource Reuse (PCRR-ZZ-202106), the Fundamental Research Funds for the Central Universities (021114380183, 021114380189, 021114380199), the Research Funds from the Nanjing Science and Technology Innovation Project for Chinese Scholars Studying Abroad (13006003), the Research Funds from Frontiers Science Center for Critical Earth Material Cycling of Nanjing University, and Research Funds for Jiangsu Distinguished Professor. Y.Z. would like to acknowledge the support from the National Natural Science Foundation of China (22276100), Natural Science Foundation of Jiangsu Province (SBK2022044384), Key Laboratory for Organic Electronics & Information Displays (GZR2022010010), Nanjing Science and Technology Innovation Project for Chinese Scholars Studying Abroad (NJKCZYZZ2022-01), Research Fund for Jiangsu Distinguished Professor (RK030STP22001), and the Research startup fund of NJUPT (NY221006).

Conflicts of interest

All authors declared that there are no conflicts of interest.

Ethical approval and consent to participate

Not applicable.

Consent for publication

Not applicable.

REFERENCES

1. Arneth A, Sitch S, Pongratz J, et al. Historical carbon dioxide emissions caused by land-use changes are possibly larger than assumed. *Nat Geosci* 2017;10:79-84. DOI
2. Liu LX, Fu J, Jiang LP, Zhang JR, Zhu W, Lin Y. Highly efficient photoelectrochemical reduction of CO_2 at low applied voltage using 3D Co-Pi/$BiVO_4$/SnO_2 nanosheet array photoanodes. *ACS Appl Mater Interfaces* 2019;11:26024-31. DOI
3. Yuan Y, Lu J. Demanding energy from carbon. *Carbon Energy* 2019;1:8-12. DOI
4. Liu J, Fu J, Zhou Y, Zhu W, Jiang LP, Lin Y. Controlled synthesis of EDTA-modified porous hollow copper microspheres for high-efficiency conversion of CO_2 to multicarbon products. *Nano Lett* 2020;20:4823-8. DOI
5. Liu J, Cai Y, Song R, et al. Recent progress on single-atom catalysts for CO_2 electroreduction. *Mater Today* 2021;48:95-114. DOI
6. Salemdeeb R, Saint R, Clark W, Lenaghan M, Pratt K, Millar F. A pragmatic and industry-oriented framework for data quality assessment of environmental footprint tools. *Resour Environ Sustain* 2021;3:100019. DOI
7. Dou X, Wang Y, Ciais P, et al. Near-real-time global gridded daily CO_2 emissions. *Innovation* 2022;3:100182. DOI PubMed PMC
8. Du H, Liu LX, Li P, et al. Enriching reaction intermediates in multishell structured copper catalysts for boosted propanol electrosynthesis from carbon monoxide. *ACS Nano* 2023;17:8663-70. DOI
9. Zhao Q, Yu P, Mahendran R, et al. Global climate change and human health: pathways and possible solutions. *Eco-Environ Health* 2022;1:53-62. DOI
10. Fu J, Li P, Lin Y, et al. Fight for carbon neutrality with state-of-the-art negative carbon emission technologies. *Eco-Environ Health* 2022;1:259-79. DOI
11. Li K, Cai Y, Yang X, et al. H_2S Involved photocatalytic system: a novel syngas production strategy by boosting the photoreduction of CO_2 while recovering hydrogen from the environmental toxicant. *Adv Funct Mater* 2022;32:2113002. DOI
12. Yang X, Li K, Wang G, et al. 2D Catalysts for CO_2 photoreduction: discussing structure efficiency strategies and prospects for scaled production based on current progress. *Chemistry* 2022;28:e202201881. DOI
13. Ran J, Jaroniec M, Qiao SZ. Cocatalysts in semiconductor-based photocatalytic CO_2 reduction: achievements, challenges, and opportunities. *Adv Mater* 2018;30:1704649. DOI PubMed
14. Fu J, Jiang K, Qiu X, Yu J, Liu M. Product selectivity of photocatalytic CO_2 reduction reactions. *Mater Today* 2020;32:222-43. DOI
15. Schäppi R, Rutz D, Dähler F, et al. Drop-in fuels from sunlight and air. *Nature* 2022;601:63-8. DOI
16. Tian J, Zhong K, Zhu X, et al. Highly exposed active sites of Au nanoclusters for photocatalytic CO_2 reduction. *Chem Eng J* 2023;451:138392. DOI
17. Yang J, Yang Z, Yang K, et al. Indium-based ternary metal sulfide for photocatalytic CO_2 reduction application. *Chin J Catal* 2023;44:67-95. DOI
18. Zhu L, Hu F, Sun B, Gu S, Gao T, Zhou G. Recent advances on multivariate MOFs for photocatalytic CO_2 reduction and H_2 evolution. *Adv Sustain Syst* 2023;7:2200394. DOI
19. Zhu Z, Xuan Y, Liu X, Zhu Q. Revealing the stochastic kinetics evolution of photocatalytic CO_2 reduction. *Nanoscale* 2023;15:730-41. DOI
20. Zuo Q, Cui R, Wang L, et al. High-loading single cobalt atoms on ultrathin MOF nanosheets for efficient photocatalytic CO_2 reduction. *Sci China Chem* 2023;66:570-7. DOI
21. Liu H, Zhu Y, Ma J, Zhang Z, Hu W. Recent advances in atomic-level engineering of nanostructured catalysts for electrochemical CO_2 reduction. *Adv Funct Mater* 2020;30:1910534. DOI
22. He L, Yuan J, Xia N, et al. Kernel tuning and nonuniform influence on optical and electrochemical gaps of bimetal nanoclusters. *J Am Chem Soc* 2018;140:3487-90. DOI
23. Bootharaju MS, Baek W, Lee S, Chang H, Kim J, Hyeon T. Magic-sized stoichiometric II-VI nanoclusters. *Small* 2021;17:e2002067. DOI
24. Busatto S, de Mello Donega C. Magic-size semiconductor nanostructures: where does the magic come from? *ACS Mater Au* 2022;2:237-49. DOI PubMed PMC
25. Wang Y, Zhou Y, Zhang Y, Buhro WE. Magic-size II-VI nanoclusters as synthons for flat colloidal nanocrystals. *Inorg Chem* 2015;54:1165-77. DOI
26. Kurashige W, Kumazawa R, Ishii D, et al. Au_{25}-loaded $BaLa_4Ti_4O_{15}$ water-splitting photocatalyst with enhanced activity and durability produced using new chromium oxide shell formation method. *J Phys Chem C* 2018;122:13669-81. DOI
27. Gautam A, Gore PM, Kandasubramanian B. Nanocluster materials in photosynthetic machines. *Chem Eng J* 2020;385:123951. DOI
28. Nitopi S, Bertheussen E, Scott SB, et al. Progress and perspectives of electrochemical CO_2 reduction on copper in aqueous electrolyte. *Chem Rev* 2019;119:7610-72. DOI

29. Shoji S, Yin G, Nishikawa M, Atarashi D, Sakai E, Miyauchi M. Photocatalytic reduction of CO_2 by CuO nanocluster loaded $SrTiO_3$ nanorod thin film. *Chem Phys Lett* 2016;658:309-14. DOI
30. Gao Y, Sun L, Bian J, Zhang Z, Li Z, Jing L. Accelerated charge transfer of g-C_3N_4/$BiVO_4$ Z-scheme 2D heterojunctions by controllably introducing phosphate bridges and Ag nanocluster co-catalysts for selective CO_2 photoreduction to CO. *Appl Surf Sci* 2023;610:155360. DOI
31. Bo Y, Du P, Li H, et al. Bridging Au nanoclusters with ultrathin LDH nanosheets via ligands for enhanced charge transfer in photocatalytic CO_2 reduction. *Appl Catal B Environ* 2023;330:122667. DOI
32. Chen J, Zhang QF, Bonaccorso TA, Williard PG, Wang LS. Controlling gold nanoclusters by diphospine ligands. *J Am Chem Soc* 2014;136:92-5. DOI
33. Zhu Q, Huang X, Zeng Y, et al. Controllable synthesis and electrocatalytic applications of atomically precise gold nanoclusters. *Nanoscale Adv* 2021;3:6330-41. DOI
34. Liu L, Corma A. Metal Catalysts for heterogeneous catalysis: from single atoms to nanoclusters and nanoparticles. *Chem Rev* 2018;118:4981-5079. DOI PubMed PMC
35. Chakraborty I, Pradeep T. Atomically precise clusters of noble metals: emerging link between atoms and nanoparticles. *Chem Rev* 2017;117:8208-71. DOI PubMed
36. Lu H, Chen B, Li Y, et al. Benzyl-rich ligand engineering of the photostability of atomically precise gold nanoclusters. *Chem Commun* 2022;58:2395-8. DOI
37. Fang J, Zhang B, Yao Q, Yang Y, Xie J, Yan N. Recent advances in the synthesis and catalytic applications of ligand-protected, atomically precise metal nanoclusters. *Coord Chem Rev* 2016;322:1-29. DOI
38. Chai OJH, Liu Z, Chen T, Xie J. Engineering ultrasmall metal nanoclusters for photocatalytic and electrocatalytic applications. *Nanoscale* 2019;11:20437-48. DOI
39. Sun Y, Cai X, Hu W, Liu X, Zhu Y. Electrocatalytic and photocatalytic applications of atomically precise gold-based nanoclusters. *Sci China Chem* 2021;64:1065-75. DOI
40. Wu J, Xia W, Lan M, et al. Artificial photosynthetic assemblies constructed by the self-assembly of synthetic building blocks for enhanced photocatalytic hydrogen evolution. *J Mater Chem A* 2020;8:21690-9. DOI
41. Yao Q, Chen T, Yuan X, Xie J. Toward total synthesis of thiolate-protected metal nanoclusters. *ACC Chem Res* 2018;51:1338-48. DOI
42. Luo Z, Nachammai V, Zhang B, et al. Toward understanding the growth mechanism: tracing all stable intermediate species from reduction of Au(I)-thiolate complexes to evolution of Au_{25} nanoclusters. *J Am Chem Soc* 2014;136:10577-80. DOI
43. Yao Q, Yuan X, Fung V, et al. Understanding seed-mediated growth of gold nanoclusters at molecular level. *Nat Commun* 2017;8:927. DOI PubMed PMC
44. Wang S, Li Q, Kang X, Zhu M. Customizing the structure, composition, and properties of alloy nanoclusters by metal exchange. *ACC Chem Res* 2018;51:2784-92. DOI
45. Li Y, Zhou M, Jin R. Programmable metal nanoclusters with atomic precision. *Adv Mater* 2021;33:e2006591. DOI
46. Li G, Jin R. Atomically precise gold nanoclusters as new model catalysts. *ACC Chem Res* 2013;46:1749-58. DOI
47. Zhou M, Higaki T, Li Y, et al. Three-stage evolution from nonscalable to scalable optical properties of thiolate-protected gold nanoclusters. *J Am Chem Soc* 2019;141:19754-64. DOI
48. Pan H, Heagy MD. Photons to formate-a review on photocatalytic reduction of CO_2 to formic acid. *Nanomaterials* 2020;10:2422. DOI PubMed PMC
49. Linsebigler AL, Lu G, Yates JT. Photocatalysis on TiO_2 surfaces: principles, mechanisms, and selected results. *Chem Rev* 1995;95:735-58. DOI
50. Habisreutinger SN, Schmidt-mende L, Stolarczyk JK. Photokatalytische reduktion von CO_2 an TiO_2 und anderen halbleitern. *Angew Chem Int Ed* 2013;125:7516-57. DOI
51. Yan J, Teo BK, Zheng N. Surface chemistry of atomically precise coinage-metal nanoclusters: from structural control to surface reactivity and catalysis. *ACC Chem Res* 2018;51:3084-93. DOI PubMed
52. Hou B, Kim B, Lee HKH, et al. Multiphoton absorption stimulated metal chalcogenide quantum dot solar cells under ambient and concentrated irradiance. *Adv Funct Mater* 2020;30:2004563. DOI
53. Guo K, Zhu X, Peng L, et al. Boosting photocatalytic CO_2 reduction over a covalent organic framework decorated with ruthenium nanoparticles. *Chem Eng J* 2021;405:127011. DOI
54. Kuhl KP, Cave ER, Abram DN, Jaramillo TF. New insights into the electrochemical reduction of carbon dioxide on metallic copper surfaces. *Energy Environ Sci* 2012;5:7050. DOI
55. Zhou M, Wang S, Yang P, Huang C, Wang X. Boron carbon nitride semiconductors decorated with CdS nanoparticles for photocatalytic reduction of CO_2. *ACS Catal* 2018;8:4928-36. DOI
56. Nguyen D, Nguyen C, Do T. Rational one-step synthesis of cobalt clusters embedded-graphitic carbon nitrides for the efficient photocatalytic CO_2 reduction under ambient conditions. *J Catal* 2020;392:88-96. DOI
57. Hansen HA, Varley JB, Peterson AA, Nørskov JK. Understanding trends in the electrocatalytic activity of metals and enzymes for CO_2 reduction to CO. *J Phys Chem Lett* 2013;4:388-92. DOI
58. Rosen BA, Salehi-Khojin A, Thorson MR, et al. Ionic liquid-mediated selective conversion of CO_2 to CO at low overpotentials. *Science* 2011;334:643-4. DOI

59. Palencia C, Yu K, Boldt K. The future of colloidal semiconductor magic-size clusters. *ACS Nano* 2020;14:1227-35. DOI PubMed
60. Chang X, Wang T, Gong J. CO_2 photo-reduction: insights into CO_2 activation and reaction on surfaces of photocatalysts. *Energy Environ Sci* 2016;9:2177-96. DOI
61. Peng S, Zeng X, Li Y. Titanate nanotube modified with different nickel precursors for enhanced Eosin Y-sensitized photocatalytic hydrogen evolution. *Int J Hydrog Energy* 2015;40:6038-49. DOI
62. Zhang W, Li Y, Zeng X, Peng S. Synergetic effect of metal nickel and graphene as a cocatalyst for enhanced photocatalytic hydrogen evolution via dye sensitization. *Sci Rep* 2015;5:10589. DOI PubMed PMC
63. Li Y, Xiang Y, Peng S, Wang X, Zhou L. Modification of Zr-doped titania nanotube arrays by urea pyrolysis for enhanced visible-light photoelectrochemical H_2 generation. *Electrochim Acta* 2013;87:794-800. DOI
64. Yin G, Nishikawa M, Nosaka Y, et al. Photocatalytic carbon dioxide reduction by copper oxide nanocluster-grafted niobate nanosheets. *ACS Nano* 2015;9:2111-9. DOI
65. Park D, Jeong Y, Lee J, Lee J, Moon S. Interfacial charge-transfer loss in dye-sensitized solar cells. *J Phys Chem C* 2013;117:2734-9. DOI
66. Irie H, Miura S, Kamiya K, Hashimoto K. Efficient visible light-sensitive photocatalysts: Grafting Cu(II) ions onto TiO_2 and WO_3 photocatalysts. *Chem Phys Lett* 2008;457:202-5. DOI
67. Irie H, Kamiya K, Shibanuma T, et al. Visible light-sensitive Cu(II)-grafted TiO_2 photocatalysts: activities and X-ray absorption fine structure analyses. *J Phys Chem C* 2009;113:10761-6. DOI
68. Yu H, Irie H, Shimodaira Y, et al. An efficient visible-light-sensitive Fe(III)-grafted TiO_2 photocatalyst. *J Phys Chem C* 2010;114:16481-7. DOI
69. Liu M, Qiu X, Hashimoto K, Miyauchi M. Cu(II) nanocluster-grafted, Nb-doped TiO_2 as an efficient visible-light-sensitive photocatalyst based on energy-level matching between surface and bulk states. *J Mater Chem A* 2014;2:13571-9. DOI
70. Miyauchi M, Irie H, Liu M, et al. Visible-light-sensitive photocatalysts: nanocluster-grafted titanium dioxide for indoor environmental remediation. *J Phys Chem Lett* 2016;7:75-84. DOI
71. Kong L, Wang C, Wan F, Zheng H, Zhang X. Synergistic effect of surface self-doping and Fe species-grafting for enhanced photocatalytic activity of TiO_2 under visible-light. *Appl Surf Sci* 2017;396:26-35. DOI
72. Ji Y, Luo Y. New Mechanism for photocatalytic reduction of CO_2 on the anatase TiO_2 (101) surface: the essential role of oxygen vacancy. *J Am Chem Soc* 2016;138:15896-902. DOI PubMed
73. Nolan M, Iwaszuk A, Gray KA. Localization of photoexcited electrons and holes on low coordinated Ti and O sites in free and supported TiO_2 nanoclusters. *J Phys Chem C* 2014;118:27890-900. DOI
74. Hurum D, Agrios A, Crist S, Gray K, Rajh T, Thurnauer M. Probing reaction mechanisms in mixed phase TiO_2 by EPR. *J Electron Spectros Relat Phenomena* 2006;150:155-63. DOI
75. Li G, Gray KA. The solid-solid interface: explaining the high and unique photocatalytic reactivity of TiO_2-based nanocomposite materials. *Chem Phys* 2007;339:173-87. DOI
76. Pacchioni G. Oxygen vacancy: the invisible agent on oxide surfaces. *Chemphyschem* 2003;4:1041-7. DOI PubMed
77. Liu M, Qiu X, Miyauchi M, Hashimoto K. Energy-level matching of Fe(III) ions grafted at surface and doped in bulk for efficient visible-light photocatalysts. *J Am Chem Soc* 2013;135:10064-72. DOI PubMed
78. Liu M, Sunada K, Hashimoto K, Miyauchi M. Visible-light sensitive Cu(II)-TiO_2 with sustained anti-viral activity for efficient indoor environmental remediation. *J Mater Chem A* 2015;3:17312-9. DOI
79. Liu M, Inde R, Nishikawa M, et al. Enhanced photoactivity with nanocluster-grafted titanium dioxide photocatalysts. *ACS Nano* 2014;8:7229-38. DOI
80. Cheng L, Li B, Yin H, Fan J, Xiang Q. Cu clusters immobilized on Cd-defective cadmium sulfide nano-rods towards photocatalytic CO_2 reduction. *J Mater Sci Technol* 2022;118:54-63. DOI
81. Billo T, Fu FY, Raghunath P, et al. Ni-nanocluster modified black TiO_2 with dual active sites for selective photocatalytic CO_2 reduction. *Small* 2018;14:1702928. DOI
82. Li Y, Wang C, Song M, Li D, Zhang X, Liu Y. TiO_{2-x}/CoO_x photocatalyst sparkles in photothermocatalytic reduction of CO_2 with H_2O steam. *Appl Catal B Environ* 2019;243:760-70. DOI
83. Hou T, Luo N, Cui Y, et al. Selective reduction of CO_2 to CO under visible light by controlling coordination structures of CeO_x-S/$ZnIn_2S_4$ hybrid catalysts. *Appl Catal B Environ* 2019;245:262-70. DOI
84. Mrowetz M, Villa A, Prati L, Selli E. Effects of Au nanoparticles on TiO_2 in the photocatalytic degradation of an azo dye. *Gold Bull* 2007;40:154-60. DOI
85. Yadav A, Li Y, Liao TW, et al. Enhanced methanol electro-oxidation activity of nanoclustered gold. *Small* 2021;17:e2004541. DOI
86. Liao TW, Verbruggen SW, Claes N, et al. TiO_2 films modified with Au nanoclusters as self-cleaning surfaces under visible light. *Nanomaterials* 2018;8:30. DOI PubMed PMC
87. Li Y, Yang Y, Chen G, Fan J, Xiang Q. Au cluster anchored on TiO_2/Ti_3C_2 hybrid composites for efficient photocatalytic CO_2 reduction. *Rare Met* 2022;41:3045-59. DOI
88. Xiao FX, Zeng Z, Hsu SH, Hung SF, Chen HM, Liu B. Light-induced *in situ* transformation of metal clusters to metal nanocrystals for photocatalysis. *ACS Appl Mater Interfaces* 2015;7:28105-9. DOI PubMed
89. Liu S, Xu YJ. Photo-induced transformation process at gold clusters-semiconductor interface: implications for the complexity of gold clusters-based photocatalysis. *Sci Rep* 2016;6:22742. DOI

90. Zhou P, Yu J, Jaroniec M. All-solid-state Z-scheme photocatalytic systems. *Adv Mater* 2014;26:4920-35. DOI
91. Bard AJ. Photoelectrochemistry and heterogeneous photo-catalysis at semiconductors. *J Photochem* 1979;10:59-75. DOI
92. Li H, Tu W, Zhou Y, Zou Z. Z-scheme photocatalytic systems for promoting photocatalytic performance: recent progress and future challenges. *Adv Sci* 2016;3:1500389. DOI PubMed PMC
93. Maeda K. Z-scheme water splitting using two different semiconductor photocatalysts. *ACS Catal* 2013;3:1486-503. DOI
94. Xu Q, Zhang L, Cheng B, Fan J, Yu J. S-scheme heterojunction photocatalyst. *Chem* 2020;6:1543-59. DOI
95. Deng Y, Zhang Z, Du P, et al. Embedding ultrasmall Au clusters into the pores of a covalent organic framework for enhanced photostability and photocatalytic performance. *Angew Chem Int Ed* 2020;132:6138-45. DOI
96. Xu Q, Wageh S, Al-ghamdi AA, Li X. Design principle of S-scheme heterojunction photocatalyst. *J Mater Sci Technol* 2022;124:171-3. DOI
97. Li X, Xiong J, Gao X, et al. Novel BP/BiOBr S-scheme nano-heterojunction for enhanced visible-light photocatalytic tetracycline removal and oxygen evolution activity. *J Hazard Mater* 2020;387:121690. DOI
98. Xia P, Cao S, Zhu B, et al. Designing a 0D/2D S-scheme heterojunction over polymeric carbon nitride for visible-light photocatalytic inactivation of bacteria. *Angew Chem Int Ed* 2020;59:5218-25. DOI
99. Xu F, Meng K, Cheng B, Wang S, Xu J, Yu J. Unique S-scheme heterojunctions in self-assembled TiO_2/$CsPbBr_3$ hybrids for CO_2 photoreduction. *Nat Commun* 2020;11:4613. DOI PubMed PMC
100. Wageh S, A. Al-ghamdi A, Liu L. S-scheme heterojunction photocatalyst for CO_2 photoreduction. *Acta Physico-Chimica Sinica* 2021;37:2010024. DOI
101. Zhang L, Zhang J, Yu H, Yu J. Emerging S-scheme photocatalyst. *Adv Mater* 2022;34:e2107668. DOI
102. Ke X, Zhang J, Dai K, Fan K, Liang C. Integrated S-scheme heterojunction of amine-functionalized 1D CdSe nanorods anchoring on ultrathin 2D $SnNb_2O_6$ Nanosheets for robust solar-driven CO_2 conversion. *Solar RRL* 2021;5:2000805. DOI
103. Férey G. Hybrid porous solids: past, present, future. *Chem Soc Rev* 2008;37:191-214. DOI PubMed
104. Long JR, Yaghi OM. The pervasive chemistry of metal-organic frameworks. *Chem Soc Rev* 2009;38:1213-4. DOI PubMed
105. Bernales V, Ortuño MA, Truhlar DG, Cramer CJ, Gagliardi L. Computational design of functionalized metal-organic framework nodes for catalysis. *ACS Cent Sci* 2018;4:5-19. DOI PubMed PMC
106. Choudhuri I, Truhlar DG. Photogenerated charge separation in a CdSe nanocluster encapsulated in a metal-organic framework for improved photocatalysis. *J Phys Chem C* 2020;124:8504-13. DOI
107. Jiang Y, Yu Y, Zhang X, et al. N-heterocyclic carbene-stabilized ultrasmall gold nanoclusters in a metal-organic framework for photocatalytic CO_2 reduction. *Angew Chem Int Ed* 2021;60:17388-93. DOI
108. Sakimoto KK, Kornienko N, Yang P. Cyborgian material design for solar fuel production: the emerging photosynthetic biohybrid systems. *ACC Chem Res* 2017;50:476-81. DOI PubMed
109. Zhang H, Liu H, Tian Z, et al. Bacteria photosensitized by intracellular gold nanoclusters for solar fuel production. *Nat Nanotechnol* 2018;13:900-5. DOI

Chen *et al. Microstructures* 2023;3:2023025
DOI: 10.20517/microstructures.2023.12

Microstructures

Review

Open Access

Check for updates

Strong metal-support interaction of Pt-based electrocatalysts with transition metal oxides/nitrides/carbides for oxygen reduction reaction

Min Chen, Peng Rao, Zhengpei Miao, Junming Luo, Jing Li, Peilin Deng, Wei Huang, Xinlong Tian

State Key Laboratory of Marine Resource Utilization in South China Sea, Hainan Provincial Key Lab of Fine Chemistry, School of Chemical Engineering and Technology, Hainan University, Haikou 570228, Hainan, China.

Correspondence to: Prof. Zhengpei Miao, State Key Laboratory of Marine Resource Utilization in South China Sea, Hainan Provincial Key Lab of Fine Chemistry, School of Chemical Engineering and Technology, Hainan University, Haikou 570228, Hainan, China. E-mail: zpmiao92@hainanu.edu.cn; Prof. Xinlong Tian, State Key Laboratory of Marine Resource Utilization in South China Sea, Hainan Provincial Key Lab of Fine Chemistry, School of Chemical Engineering and Technology, Hainan University, Haikou 570228, Hainan, China. E-mail: tianxl@hainanu.edu.cn

How to cite this article: Chen M, Rao P, Miao Z, Luo J, Li J, Deng P, Huang W, Tian X. Strong metal-support interaction of Pt-based electrocatalysts with transition metal oxides/nitrides/carbides for oxygen reduction reaction. *Microstructures* 2023;3:2023025. https://dx.doi.org/10.20517/microstructures.2023.12

Received: 6 Mar 2023 **First Decision:** 4 Apr 2023 **Revised:** 26 Apr 2023 **Accepted:** 8 May 2023 **Published:** 6 Jun 2023

Academic Editor: Chunqiang Zhuang **Copy Editor:** Fangling Lan **Production Editor:** Fangling Lan

Abstract

The practical application of carbon-supported Pt-based catalysts for the oxygen reduction reaction (ORR) in proton exchange membrane fuel cells (PEMFCs) still faces many limitations, including carbon corrosion and their weak interaction with Pt-based nanoparticles (NPs). Harnessing the strong metal-support interaction (SMSI) effects at the interface between Pt-based nanoparticles and alternative corrosion-resistant non-carbon support is an effective strategy to address these issues. The rational design of Pt-based catalysts with favorable SMSI and elucidation of the mechanisms underlying such interactions is indispensable for achieving desirable activity and stability. In this review, first, the basic principles of the ORR are briefly introduced. Next, the formation process of SMSI, construction strategies, and the advantages and drawbacks of representative supports, including transition metal oxides, nitrides, and carbides (TMOs, TMCs, and TMNs, respectively), are fully discussed. Finally, the challenges and prospects in promoting the practical applications of the SMSI effect for ORR are highlighted.

Keywords: Fuel cells, oxygen reduction reaction, strong metal-support interaction, stability

INTRODUCTION

The accelerated global population growth and massive consumption of fossil fuel energy have induced imbalanced energy shortages and severe environmental disruption. Thus, the development of environment-friendly and sustainable energy technologies has attracted widespread attention to mitigate these phenomena[1-3]. Benefiting from their high energy density and zero carbon emissions, proton exchange membrane fuel cells (PEMFCs) have been considered as one of the most promising energy conversion technologies in residential applications, automobile transportation, and other stationary power systems[4-6]. However, the sluggish kinetics of the cathodic oxygen reduction reaction (ORR) is the major barrier to the further scale-up of PEMFC for large-scale commercialization[7-9]. Carbon-supported Pt nanoparticles (Pt/C) have been widely employed as the ORR electrocatalysts, while the weak interaction between Pt and carbon frequently causes the aggregation, dissolution, Ostwald ripening/coalescence, or detachment of Pt from the carbon support, thus deteriorating the ORR activity and stability[10,11]. Furthermore, carbon supports tend to experience severe corrosion, especially under the high potential encountered during the start-up or shut-down stages. The strong acidic environment (pH < 1) also contributes to catalyst inactivation and short lifetime[8,12], which is a non-negligible factor.

To overcome such shortcomings of carbon support, different types of alternative supports have been exploited to improve the stability of Pt-based catalysts towards ORR in highly oxidative and acidic environments, including graphitic carbon nitride (g-C_3N_4), transition metal oxides, carbides and nitrides (TMOs, TMCs, and TMNs, respectively), 2D metal-organic frameworks (MOFs), covalent-organic framework (COFs), layered double hydroxide (LDH), and so on[13-22]. Among them, TMOs, TMNs, and TMCs are considered to be the most promising alternative supports due to their superior corrosion resistance and strong metal-support interaction (SMSI) with Pt nanoparticles (NPs). The driving force of SMSI is defined as minimizing the surface energy of Pt NPs by covering the mobile support suboxides, which provide a variety of possibilities to modulate the catalytic activity, selectivity, and stability of the active species, opening up opportunities for developing highly active and stable ORR catalysts. To be specific, the SMSI of Pt-support usually involves interfacial electron transfer/donation and structural reconstruction at the metal-support interface (defined as electronic and geometric effects), which has the capacity to alter the adsorption energies of the reactants and reaction intermediates at the catalytic active sites situated on the catalyst surface, thereby affecting the activity and stability of catalysts[23,24]. In addition, SMSI is usually accompanied by the encapsulation of supported metal particles by the support, which effectively stabilizes the metal particles, thus improving the stability of the catalyst. Recently, several review articles have shed much new light on SMSI, which provides an effective method to design catalysts with high activity and durability. For example, Wang *et al.* summarized several new routes to construct SMSI involving reductive/oxidative induced SMSI, adsorbate-mediated SMSI (A-SMSI), and wet-chemistry SMSI (wcSMSI) to improve the sinter resistance and catalytic performances of the supported metal catalysts[25]. Luo *et al.* provided an overview of the developments of SMSI and covered its applicability in both thermocatalysis and electrocatalysis systems[26]. Pu *et al.* reviewed various spectroscopic and microscopic techniques capable of characterizing the SMSI phenomena and systematically explored the effect of SMSI on catalytic activity/selectivity[27]. However, these SMSI analyses were largely limited to catalytic reactions involving CO, CH_4, CO_2, or methanol as the main reactant, lacking relevant summaries and mechanistic elucidation in the field of ORR.

In this review, particular attention is paid to the recent progress in the design, construction, and emerging applications of SMSI in ORR catalysts. Particularly, we start by optimizing the intrinsic activity of TMOs, TMNs, and TMCs supports. By elaborately selecting their compositions, precisely modulating the synthesis methods, and further adjusting the metal-support interaction, we aim to improve the ORR activity and stability of the catalysts. This distinguishes our view from the previous review articles[27,28]. Firstly, the basic principles of the ORR, some descriptors of the computational activity, and electrochemical activity are briefly introduced. Secondly, detailed strategies of manipulating SMSI through rational design of catalyst structures and different atmosphere treatments in recent years are summarized. In addition, the precise synthetic methods and effective improvement strategies of several TMO-, TMN-, and TMC-supported Pt-based catalysts applications for ORR are discussed. Finally, the prospects and challenges of SMSI for ORR catalysts are provided.

BASIC PRINCIPLES OF THE ORR

Mechanisms of the ORR

The ORR process generally consists of four steps as follows: (1) diffusion and adsorption of O_2 on the electrocatalyst surface; (2) electron migration from the electrode to adsorbed O_2 molecules; (3) weakening and splitting of O=O bonds; and (4) removal of the generated species to the electrolyte[29]. Typically, O_2 can be reduced to H_2O or H_2O_2 through two different electron transfer pathways: the direct four-electron transfer pathway (Eq. 1) and the indirect two-electron transfer pathway (Eq. 2). Four-electron transfer occurs to reduce molecular oxygen to water, facilitating the ORR process. However, it is always accompanied by the reduction of the two-electron pathway, resulting in the partial reduction of oxygen to hydrogen peroxide products, which reduces the electrocatalytic selectivity. Both four- and two-electron transfer pathways involve various oxygen-containing intermediates such as *O, *OH, or *OOH (*represents the active catalytic site)[30-32]. More specifically, there are three possible reaction mechanisms: dissociative, associative, and peroxo mechanisms, as shown in Figure 1A. For the dissociative and associative mechanisms of the four-electron transfer pathway, their difference depends on whether they involve the formation of *OOH intermediate[33].

$$O_2 + 4H^+ + 4e^- \rightarrow 2H_2O,\ E^0 = 1.229\ \text{V}\ vs.\ \text{RHE} \quad (1)$$

$$O_2 + 2H^+ + 2e^- \rightarrow 2H_2O_2,\ E^0 = 0.695\ \text{V}\ vs.\ \text{RHE} \quad (2)$$

where RHE represents the reversible hydrogen electrode.

Linear scaling relationships

Density functional theory (DFT) calculations have been extensively used to understand the free energies of those intermediates and further estimate the ORR performance. By extending the calculations to various close-packed metal surfaces, the scaling relationship between ORR activity and oxygen adsorption energy (ΔE_o) have been eventually plotted in "volcano plots" with Pt located at the extreme tip of the linear currently (as shown in Figure 1B)[34]. Generally, the ΔE_o of Pt-based catalysts is determined by the position of the *d*-band center relative to the Femi level, while the shift of the *d*-band center can be modulated by alloy with other elements (ligand effect), such as Ni, Co, Fe, *etc.*[33,35]. An ideal candidate metal should have a moderate affinity for oxygen. More specifically, if the metals bind oxygen too strong, the ORR will be retarded due to the difficulty in removing intermediates (O* or OH*) formed by proton-coupled electron transfer, whereas the metals bind oxygen too weak, the O_2 adsorption and later dissociation to form O* will be constrained. Additionally, a series of catalysts with the SMSI effect, compared to PtM/C catalysts, can rapidly accelerate the electron transfer in the metal-support interface and precisely regulate the *d*-band

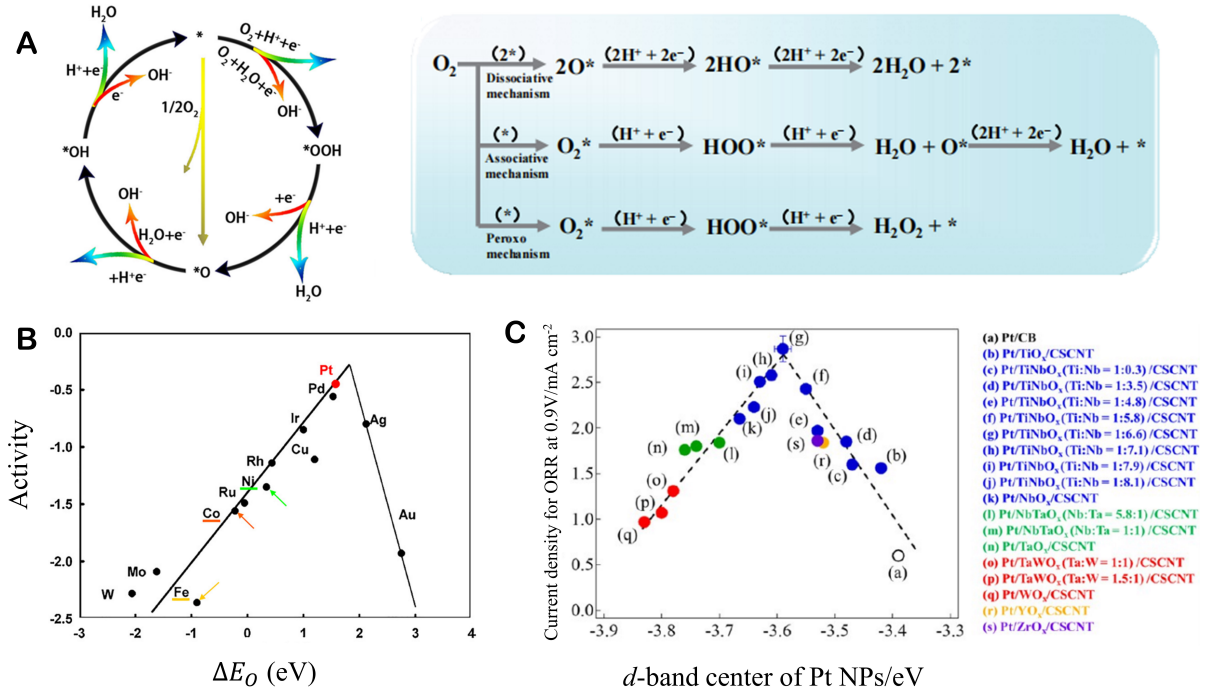

Figure 1. (A) ORR mechanism in acidic (blue line) and alkaline (red line) electrolytes and proposed pathways for ORR. Reproduced with the permission of Ref.[31] Copyright 2021, Elsevier. (B) Trends in oxygen reduction activity plotted as a function of the oxygen binding energy. Reproduced with permission of Ref.[34] Copyright 2004, American Chemical Society. (C) Relationship between the *d*-band center of Pt and the current density at 0.9 V (*vs.* RHE) for the ORR. The Pt NPs were deposited on support materials (a)-(s) shown on the right. Reproduced with the permission of Ref.[36] Copyright 2021, American Chemical Society.

center of the catalyst. Inspired by this, Ando *et al.* constructed a similar "volcano-type" of a series of binary transition metal oxides/cup-stacked carbon nanotubes supported Pt NPs (Pt/$M_1M_2O_x$/CSCNTs) catalysts to demonstrate that the *d*-band center values of Pt/$M_1M_2O_x$/CSCNTs catalysts can be downshift in a controlled manner by reasonable selection and precise regulation of M_1 and M_2 in the $M_1M_2O_x$/CSCNTs support (as shown in Figure 1C)[36]. The Pt/TiNbO$_x$ (Ti/Nb = 1:6.6 in atomic ratio)/CSCNTs catalysts with ca. 0.2 eV downshift of the *d*-band center from that of Pt exhibited the maximum ORR activity and stability, resulting from the ligand effect in the metal-support structure and the SMSI effect as well.

METHODS TO INDUCE THE STRONG METAL-SUPPORT INTERACTIONS

With the rapid development in the field of SMSI, the methods to induce SMSI have also been continuously developed and evolved for improving the sinter resistance and catalytic performance of the supported metal catalysts. To date, several SMSIs construction strategies, including SMSI, oxidative strong metal-support interaction (O-SMSI), A-SMSI, wcSMSI, reaction-induced SMSI (R-SMSI), and laser-induced SMSI (L-SMSI) have been reported with different construction conditions[26], such as reduction, oxidation, adsorbates, photo-treatment, *etc*. Tuning the SMSI behaviors has also been proven to be one of the most efficient methods for manipulating catalytic performance. Here, we briefly summarize the recent progress in SMSI, focusing on different methods for constructing SMSI and their advantages and disadvantages. The timeline for different types of SMSI is shown in Figure 2.

Strong metal-support interaction (SMSI)

Since the first report[37] and follow-up work[38] in the late 1970s by Tauster *et al.*, the classical strong metal-support interaction (SMSI), a term coined to describe a phenomenon that the loss of small molecules (such

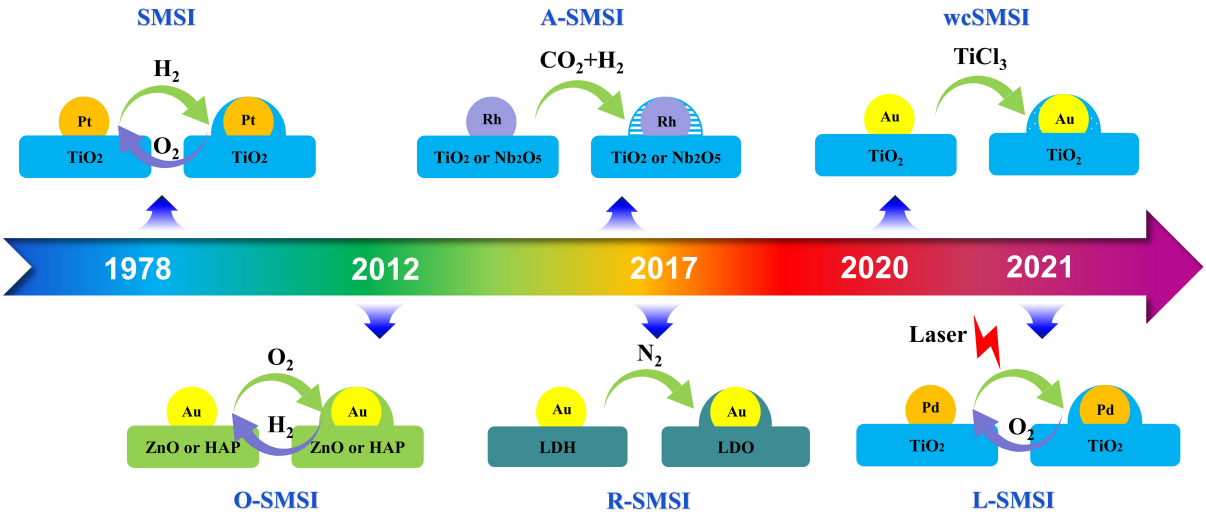

Figure 2. A timeline of representative achievements in the field of SMSI.

as CO and H_2) chemisorption of titania-supported platinum group metals (PGMs) after high-temperature reduction (HTR) with hydrogen (as shown in Figure 3A), has garnered a great deal of interest and attention in the field of heterogeneous catalysis. Initially, the inhibition of chemisorption was assigned to the electron perturbation of the system, i.e., the intermetallic bonding between PGMs and Ti cations under hydrogen atmospheres[10]. Subsequently, an increasing number of studies have shown that the primary reason for the CO adsorption suppression is the partially reduced layer of TiO_2 encapsulating its supported PGMs, thereby obscuring the metal surface adsorption sites[10,39-41]. With the application of high-resolution real-space methods, the primary characteristics of SMSI have been revealed successively and eventually identified by four criteria, including: (1) remarkable suppression of the chemisorption of small molecules on the metal; (2) mass transport induced by metal NPs encapsulated by the reduced support; (3) electron transfer from the support to metal NPs; and (4) a reversal of the above phenomena on reoxidation[25,42]. The electronic/geometric effects and synergistic interactions between metal and support arising from these features endow the catalysts with great tunability and stability for their structure and properties[43,44]. However, metals with high surface energy and large work functions are believed to be indispensable for the formation of SMSI, that is, a series of low work function and surface energy IB group metals NPs, such as Au, Cu, and Ag, fail to manifest SMSI behaviors on TiO_2, as shown in Figure 3B[45-48]. Additionally, the SMSI effect is limited existing on reducible oxide supports, which inevitably influences the catalyst performance owing to the low electrical conductivity. Furthermore, the traditional method for inducing SMSI requires a high-temperature reduction in the H_2 atmosphere to activate the surface of reducible metal oxide support, which usually causes the aggregation of metal NPs before forming the barriers under harsh reduction conditions, in turn affecting the catalytic performance. Therefore, it is necessary to develop several new routes for constructing SMSI to elucidate its universality in catalytic systems.

Oxidative strong metal-support interaction (O-SMSI)

O-SMSI, a novel strategy to construct SMSI by high-temperature oxidative treatment, was first reported by Liu *et al.* in an Au/ZnO-nanorod catalyst[49]. The reversible encapsulation of Au NPs by a thin layer of zinc oxide and reduction of small-molecule adsorption are identical to the traditional SMSI except that the electron transfer of O-SMSI is from Au NPs to support. This new discovery not only broadens the occurrence of SMSI but also points to new directions in the study of SMSI for Au-based catalysts. Subsequently, a series of studies extended the support of SMSI from oxide to non-oxide systems such as

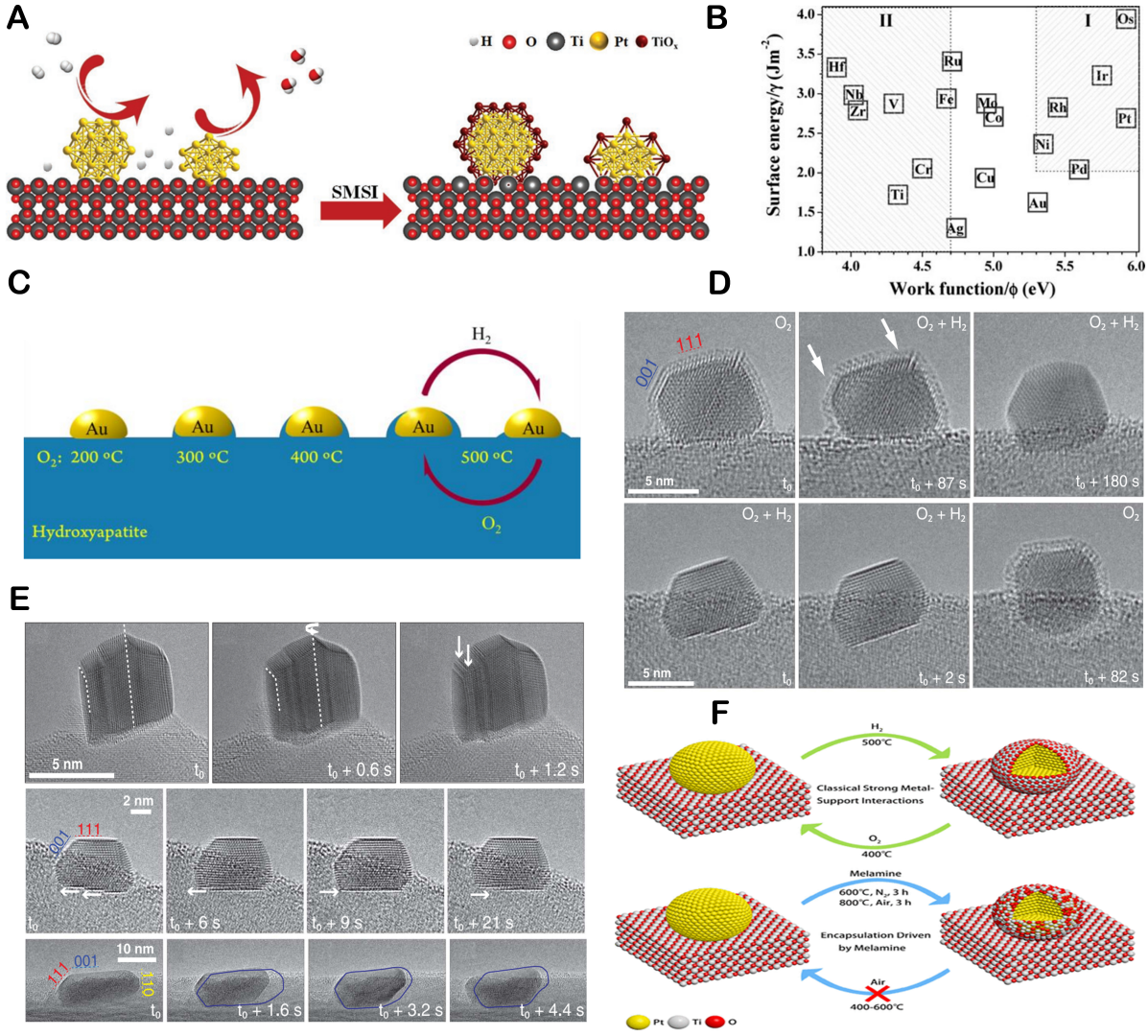

Figure 3. (A) Schematic illustrations of the formation process of SMSI in Pt/TiO_2. Reproduced with the permission of Ref.[26] Copyright 2022, John Wiley and Sons. (B) Relationship between surface energy (γ_M) and work function (φ) of different transition metals. Reproduced with the permission of Ref.[48] Copyright 2005, American Chemical Society. (C) Schematic illustrations of the formation process of O-SMSI in Au/HAP. Reproduced with the permission of Ref.[50] Copyright 2016, American Chemical Society. HRTEM images of (D) The destabilization of overlayer and (E) the dynamic behavior of Pt NPs on the support interface. Reproduced with the permission of Ref.[10] Copyright 2022, Science. (F) Different encapsulation functions between O-SMSI and classical SMSI in Pt/TiO_x. Reproduced with the permission of Ref.[53] Copyright 2021, American Chemical Society.

hydroxyapatite (HAP) (as shown in Figure 3C), opening a new avenue for the design of highly stable supported gold catalysts[50,51]. With the diversification of measurement methodologies and the advancement of characterization techniques, the atomic-level structural evolution of TiO_2 encapsulated layer in a redox-active regime (O_2 + H_2 atmosphere) and the dynamic behavior of particles and interfaces induced by metal-support interaction were systematically revealed via *in situ* transmission microscopy by Frey *et al.*[10]. With the atmosphere switches from O_2 to a redox-active H_2-O_2 mixture, the TiO_2 encapsulation layer was completely retracted from all the particles (as shown in Figure 3D), and the particles exhibited dynamic behavior on the support interface and ceased as soon as H_2 was completely removed from the reactor cell (as shown in Figure 3E), whereby the overlayer is also reformed around the NPs. This phenomenon indicates that the encapsulation layer induced by the O-SMSI and SMSI strategy is vulnerable to the external

environment (e.g., humid atmosphere), resulting in encapsulation failure, metal agglomeration, and a dramatic decrease in stability. To optimize the stability of the TiO_2 overlayers, Liu *et al.* reported that Au/TiO_2 catalysts modified with melamine and annealed at 600 °C in N_2 atmosphere and further treatment at 600 °C in air atmosphere to form an amorphous and permeable TiO_x encapsulation layer on Pt NPs, which is extremely stabilized against re-oxidize in air, in stark contrast to the retreat of the TiO_x encapsulation layer by later oxidation treatment in previous SMSI (as shown in Figure 3F)[52]. Subsequently, they expanded this strategy to TiO_2-supported Pd and Rh NPs, a promising way for designing supported platinum group metal-based catalysts with high activity and stability[53].

Adsorbate-mediated SMSI (A-SMSI)

Notably, the aforementioned examples of SMSI and O-SMSI typically rely on high-temperature thermal treatment (≥ 500 °C) while inevitably decreasing the catalytic performance due to blockage of metal active sites. Matsubu *et al.* reported an adsorbate-mediated SMSI (A-SMSI) encapsulated strategy that forms with the treatment of TiO_2- and Nb_2O_5-supported Rh NPs in $20CO_2$:$2H_2$ atmosphere at a relatively low temperature (150-300 °C)[54]. *In situ* spectroscopy and microscopy demonstrated that the thickness of the A-SMSI overlayer is almost twice that of the SMSI overlayer, thanks to the adsorbates HCO_x species strongly bounded on the support to induct the formation of oxygen-vacancy, prompting the migration of HCO_x-functionalized support onto the metal to form an extremely stabilized encapsulated state against re-oxidation by the air atmosphere (As shown in Figure 4A, line a-b-c). Later, the A-SMSI strategy was labeled as "low-temperature induction" and "encapsulation stability" with its extended application to Cu/CeO_2[55] and Ru/MoO_3[56]. Nowadays, the induction of A-SMSI overlayer is not restricted to CO_2-H_2 atmospheres only. For example, Li *et al.* successfully constructed A-SMSI on a commercial $Cu/ZnO/Al_2O_3$ catalyst under $H_2/H_2O/CH_3OH/N_2$ mixture atmosphere at 300 °C (as shown in Figure 4B) and found that the ZnO_x species migrated onto the surface of metallic Cu^0 NPs to constitute a stable encapsulated structure, and the proper degree of encapsulation could be achieved by adjusting the exposure time[57]. Combined with DFT calculations, the improved methanol steam reforming reaction activity of $Cu/ZnO/Al_2O_3$ catalysts was attributed to the increased number of the ZnO_x-Cu interfacial sites (as shown in Figure 4C).

Wet-chemistry SMSI (wcSMSI)

Besides the A-SMSI strategy enables encapsulation at relatively low temperatures, the wcSMSI method is another effective strategy for achieving SMSI in an aqueous solution at room temperature, which not only avoids the conventional high-temperature redox condition causing pre-sintered metal NPs but also effectively stabilizes the metal NPs against re-oxidation. As an example, an Au/TiO_2-wcSMSI catalyst synthesis was reported by Zhang *et al.* that the average diameter of the TiO_2 overlay was 2 nm, and the supported Au NPs were completely encapsulated[58]. In addition, they provide a proof-of-concept design to reveal the mechanisms of enhancing the catalytic activity of Au_{55} cluster on inert SiO_2 support covered by TiO_x overlayers (Au_{55}@Ti/SiO_2) through DFT calculations (as shown in Figure 4D), thereby extending the wet-chemistry method to inert oxide supported field. Recently, Hao *et al.* synthesized a $Pt@TiO_x/TiO_2$ catalyst via the wcSMSI strategy, which consists of Pt NPs decorated by amorphous TiO_x overlayers and exhibits extremely active and stable in C_3H_8 and C_3H_6 combustion compared with the conventional supported Pt/TiO_2 catalyst owing to the electronic interaction between Pt and TiO_x ($Pt^{x+}/Pt^0 \leftrightarrow Ti^{3+}/Ti^{4+}$)[59]. Since the wcSMSI process protects the severe sintering of the NPs from the high temperature, the stability of catalysts is also substantially ensured.

Reaction-induced SMSI (R-SMSI)

In particular, the abovementioned types of SMSI constructions predominantly rely on the redox oxide supports, such as TiO_2, ZnO, Nb_2O_5, *etc*. However, the relatively redox-inert supports (e.g., Mg- and Al-based oxide supports) are unsuitable for the construction of SMSI as their surface activation is challenging.

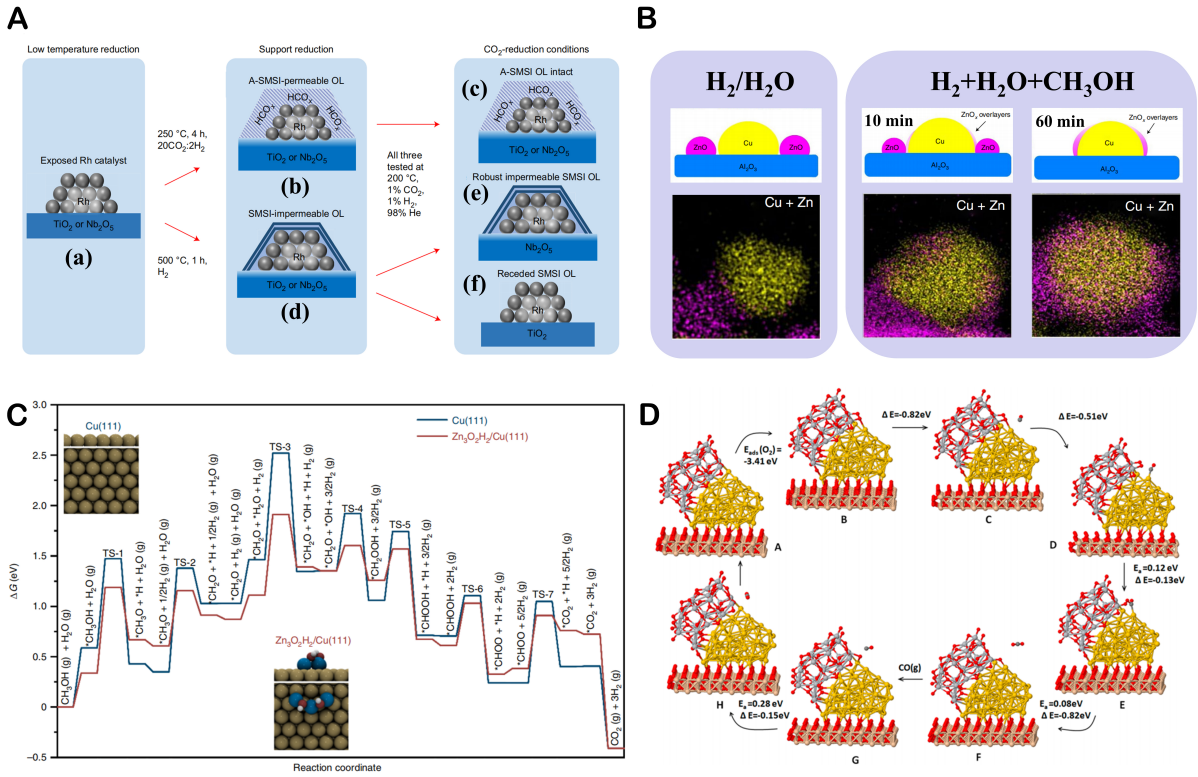

Figure 4. (A) A-SMSI and Classical SMSI overlayer structure and behavior. Reproduced with the permission of Ref.[54]. Copyright 2017, Springer Nature. (B) Structural change of $Cu/ZnO/Al_2O_3$ catalyst after different pretreatments and the corresponding elemental distribution from transmission electron spectroscopy images. The DFT simulations over (C) $Cu/ZnO/Al_2O_3$. Reproduced with the permission of Ref.[57]. Copyright 2022, Springer Nature. (D) Au_{55}@Ti/SiO_2 model with two TiO_x atomic layers. Reproduced with the permission of Ref.[58]. Copyright 2019, American Chemical Society.

Reaction-induced SMSI (R-SMSI) strategy is an effective method to induce the activation, migration, and encapsulation of redox-inert support via its phase transition. For example, Wang *et al.* successfully achieved R-SMSI between Au NPs and Mg-Al layered double oxides (LDO) vis a high-temperature treatment in nitrogen atmosphere[60]. The hydroxide-to-oxide support transformation is the prerequisite for the construction of R-SMSI, and if Au NPs were loaded directly onto the LDO surface, the R-SMSI structure was not obtainable under the same conditions (as shown in Figure 5A). Then, Dong *et al.* reported that the cyclic change (MoC_x-to-MoO_3) in the support of Au/MoC_x catalyst under a 20 vol% CH_4/He atmosphere can realize R-SMSI[61]. Later, they demonstrated that R-SMSI can also be achieved in the Ni/BN catalysts under the same conditions due to the BN-to-BO_x interfacial change[62]. In other studies, the support phase change between $BaCO_3$-to-BaO of Co/BaO and Mn_3O_4-to-Mn_2O_3 of Pt/Mn_2O_3 catalysts were both formed R-SMSI and exhibited excellent catalytic activity and stability[15,63]. Recently, a reversible reaction of $MgO+CO_2 \leftrightarrow MgCO_3$ was employed to induce the R-SMSI of Au/MgO catalysts in a flowing CO_2 atmosphere (as shown in Figure 5B)[64]. CO_2 was applied to react with MgO support, and the $MgCO_3$ was subsequently decomposed into a regenerated MgO overlayer to encapsulate the Au NPs. Intriguingly, the direct application of $MgCO_3$ as a support is also able to realize the $MgCO_3$-to-MgO phase transition and to construct a MgO overlayer on Au NPs. These studies demonstrate that the SMSI effect can also be constructed on relatively redox-inert supports, and the mobility of the support after the phase change is significantly higher than that of the original support, which also implies that the encapsulation rate of metals by the R-SMSI strategy seems to be faster than that of classic SMSI.

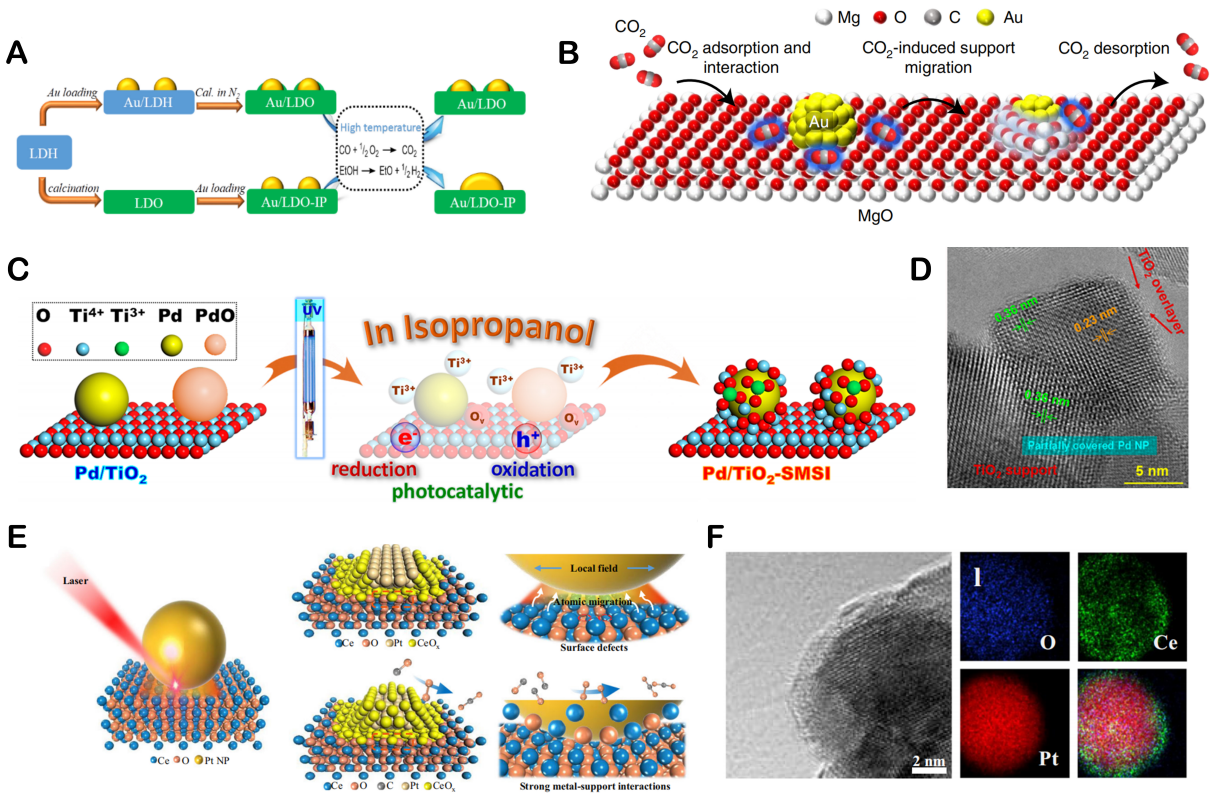

Figure 5. Schematic illustrations of the formation process of (A) R-SMSI in Au/LDO. Reproduced with the permission of Ref.[60] Copyright 2017, American Chemical Society, (B) R-SMSI in Au/MgO. Reproduced with the permission of Ref.[64] Copyright 2021, Springer Nature, (C) L-SMSI in Pd/TiO_2. (D) TEM images of Pd/TiO_2. Reproduced with the permission of Ref.[65] Copyright 2021, American Chemical Society. (E) Schematic illustrations of the formation process of L-SMSI in Pt/CeO_2. (F) TEM images of Pt/CeO_2. Reproduced with the permission of Ref.[66] Copyright 2021, Springer Nature.

Laser-induced SMSI (L-SMSI)

Similar to the wcSMSI, L-SMSI also enables the migration of metastable supports to facilitate SMSI formation without specific gaseous atmospheres and thermal treatment. Recently, Chen *et al.* successfully constructed L-SMSI on a Pd/TiO_2 catalyst by a photochemistry-driven methodology[65]. Specifically, when excitation energy supplied by ultraviolet (UV) irradiation was greater than the band gap of titanium dioxide (3.1 eV), the separated photoinduced reductive electrons (e^-) and oxidative hole (H^+) were generated to trigger the formation of Ti^{3+} species/oxygen vacancies (O_v) and then interfacial Pd-O_v-Ti^{3+} sites, finally constructing the L-SMSI structures (as shown in Figure 5C and D). Subsequently, this as-constructed L-SMSI layer is reversible between retraction on thermal O_2 treatment and re-encapsulation on UV irradiation. Similarly, the L-SMSI strategy has been extended to CeO_2-supported Pt system catalysts and even to non-reducible oxide supports such as Al_2O_3 and MgO. Zhang *et al.* applied an ultrafast laser to a Pt/CeO_2 catalyst to boost the formation of surface defects and the migration of metastable CeO_x, and succeeded in creating porous overlayers of CeO_x on Pt NPs (as shown in Figure 5E and F), which exhibit superior catalytic activity and stability[66].

In summary, we briefly reviewed some typical strategies for constructing SMSI on various atmospheric conditions, annealing temperatures, and oxide and non-oxide supports (as shown in Table 1). These new types displayed similar properties to classical SMSI, including the electron and mass transfer between metal NPs and substrates, the encapsulation of metal species by the migrating substrate, and the suppression of the adsorption behavior of small molecules. Furthermore, they also exhibited remarkable strengths over

Table 1. Comparison between SMSI and novel construction strategies

	SMSI	O-SMSI	A-SMSI	wcSMSI	R-SMSI	L-SMSI
Metal	VIII group metals	VIII/IB group metals	VIII/IB group metals	VIII/IB group metals	VIII/IB group metals	VIII group metals
Support	Reducible metal oxide	Hydroxyapatite, phosphate, and ZnO	Reducible metal oxide	TiO_2	LDO, MoO_3, MgO, BaO, Mn_2O_3	TiO_2, CeO_2
Condition	H_2	O_2	CO_2-H_2, H_2/H_2O /CH_3OH/N_2	Ti^{3+} treatment	N_2, CO_2, CH_4/He	Laser treatment
temperature	High-temperature	High-temperature	> 200 °C	Room-temperature	High-temperature	Room-temperature
Electronic transfer	Support to metal	Metal to support	Support to metal	Support to metal	Support to metal	Support to metal
Suppression of small molecule adsorption	Yes	Yes	Yes	Yes	Yes	Yes

classical SMSI, such as a wide scope of supports, various construction atmospheres, low heating temperatures, and excellent stability under harsh reaction conditions.

APPLICATION OF STRONG METAL-SUPPORT INTERACTIONS IN ORR

In general, the requirement for an ideal ORR catalyst includes both high activity and stability. A series of classical SMSI systems, including SMSI, O-SMSI, and A-SMSI catalysis, precisely satisfy the high stability requirement for ORR due to their inherent encapsulation effect. In addition, the electron and mass transfer between metal and support makes the modulation of the catalyst activity more feasible and efficient. For some new types of SMSI, i.e., L-SMSI, wcSMSI, and R-SMSI, their low or room temperature construction strategy and independent encapsulation phenomena can effectively disperse the metal and prevent its detachment and agglomeration, greatly improving the stability of the catalyst.

Oxide-based materials

TMOs are an ideal alternative to carbonaceous materials as supports for Pt NPs not only because of their robust corrosion resistance but also the strong interaction with the Pt NPs inducing the SMSI effect for enhanced ORR activity and stability enhancement[67]. The SMSI effect mainly arises from an interfacial interaction of Pt-Metal Oxide (Pt-MO), which leads to a modification of the Pt electronic structure and provides several advantages for ORR, including (1) facilitating the O_2 adsorption and O-O bond cleavage on the Pt surface; (2) decreasing the OH coverage on the Pt surface; and (3) preventing the detachment and further aggregation of Pt NPs. Based on this, a variety of TMOs have been applied to support Pt-based catalysts toward ORR, such as titanium oxide, cerium oxide, and tungsten oxide.

Titanium oxide (TiO_2)

Among the various metal oxide supports reported so far, titanium oxide-based materials have been considered as a promising support for nanosized catalysts in the ORR owing to their low cost, nontoxicity, high defect contents, *etc.*[68-70]. The robust corrosion resistance ensures TiO_2 is an intrinsically stable electrode material under harsh operation conditions, especially in acid medium and high-temperature environments. Most importantly, the synergetic effect of SMSI between Pt NPs and TiO_2 can exquisitely enhance the electrocatalytic performance of Pt NPs and the durability of the catalysts. However, as a support, TiO_2 has several drawbacks, such as low electrical conductivity (10^{-8} Scm^{-1}) and poor reactivity, limiting the electron interactions between Pt and Ti atoms[71]. Therefore, the issue of insufficient conductivity of TiO_2 should be primarily resolved before the application of TiO_2 to improve the performance and stability of Pt-based catalysts for ORR.

Coupling TiO_2 NPs with superior conductive carbon-based support materials has been reported as one of the most effective solutions to enhance their low electrical conductivity. Wang *et al.* presented a photochemical deposition method for loading Pt NPs onto a composite TiO_2-C support (Pt/TiO_2-C) and then heated it at 300 °C under H_2/N_2 atmosphere for 2 h to induce the SMSI effect[72]. Such a structure enhances not only the overall conductivity of the catalyst system but also the TiO_2-induced SMSI effect that strongly encapsulates the Pt NPs to facilitate the electron transfer and prevent the migration and aggregation. As a result, the resulting catalysts exhibit excellent ORR activity and durability in high-temperature environment. Additionally, embedding TiO_2 films onto carbon matrix is another fabrication strategy. Shi *et al.* reported a sonochemical reaction method to synthesize a continuous ultrathin (~1.5 nm) TiO_2-coated carbon nanotube (CNT) as the support of Pt NPs[73]. Their investigations revealed that the improved ORR activity of Pt/TiO_2/C catalysts is attributed to the SMSI effect between Pt NPs and TiO_2-coating and the bifunctional mechanism of TiO_2. Notably, either TiO_2 NPs or a layer in these composites serves as a channel that allows electron transfer between Pt NPs and carbon-based support. Therefore, the TiO_2 NPs or coating should not be too big or thick (< 5 nm) to facilitate electrical conductivity. In addition, the TiO_2 NPs or coating should also be conformally continuous over the entire carbon surface to prohibit direct contact between the carbon support and the Pt NPs. Therefore, effective tuning of TiO_2 particle size or film layers thickness in these composites and selective deposition of Pt NPs in composites are key to improving the SMSI effect and thus increasing the ORR activity and durability of the catalyst.

Recently, an attractive method to enhance the electrical conductivity of titanium dioxide is the introduction of structural defects such as oxygen vacancies (V_o) on the surface of TiO_2[74], which can construct the Pt-V_o-Ti interaction and induce the SMSI effect to optimize the ORR catalytic activity by reducing the desorption free energy of Pt-OH, Pt-O, or O_2. In addition, the SMSI effect reduces the binding energy between the active sites and the adsorbed oxygen species, which is beneficial for the ORR process[75]. One common method to introduce V_o in TiO_2 is by doping the metal oxides with other metals, such as W[76-78], Nb[78-84], Cr[85,86], Mo[87,88], Ta[89,90], V[91], and more. In general, similar electron donations from the substrate to metals and induced SMSI effect between them can be observed in various doping systems. Synoptically, a screening strategy was proposed by Tsai *et al.* to quickly find out potential supports and dopants ($Ti_{1-x}M_xO_y$ supports, where M = Nb, W, Mo, Ru, *etc.*) in which based on a method of high-throughput DFT calculations[92]. To predict properties by M dopants, a systematic guide map has been produced for $TiMO_2$ substrate that contains data of metal-induced electronic states (MIES, as shown in Figure 6A), the formation energy of oxygen vacancies (E_{Ovac}), the adsorption energy of single Pt atoms (E_{1Pt}), and charge states of deposited Pt ($\Delta\delta_{Pt}$).

Another effective strategy to enhance ORR performance is to construct nanostructured TiO_2 support, such as microspheres, nanofibers, nanotubes, nanosheet assembly, and nanorods. For example, Murphin Kumar *et al.* presented a Pt NPs decorated one-dimensional (1D) TiO_2 nanorod (Pt/TiO_2 NRs) with remarkably enhanced electronic conductivity and excellent strong coupling of Pt NPs with the TiO_2 NRs support compared to the Pt/TiO_2(Comm) catalyst (as shown in Figure 6B)[93]. The results verified that the as-prepared Pt/TiO_2 NRs composite nanostructures exhibited excellent ORR performance and stability, which are mainly attributed to the unique 1D morphology of the TiO_2 NRs providing a greater surface area and the SMSI effect enhancing electron transfer rate at their functional interface.

Cerium oxides (CeO_2)

Recently, CeO_2 has attracted plenty of attention as ORR catalytic support because of its lower price and corrosion resistance in acidic media. What is more, CeO_2 support could switch between Ce^{3+} and Ce^{4+} oxidation states due to its abundant oxygen vacancies, which is beneficial to the storage and release of lattice

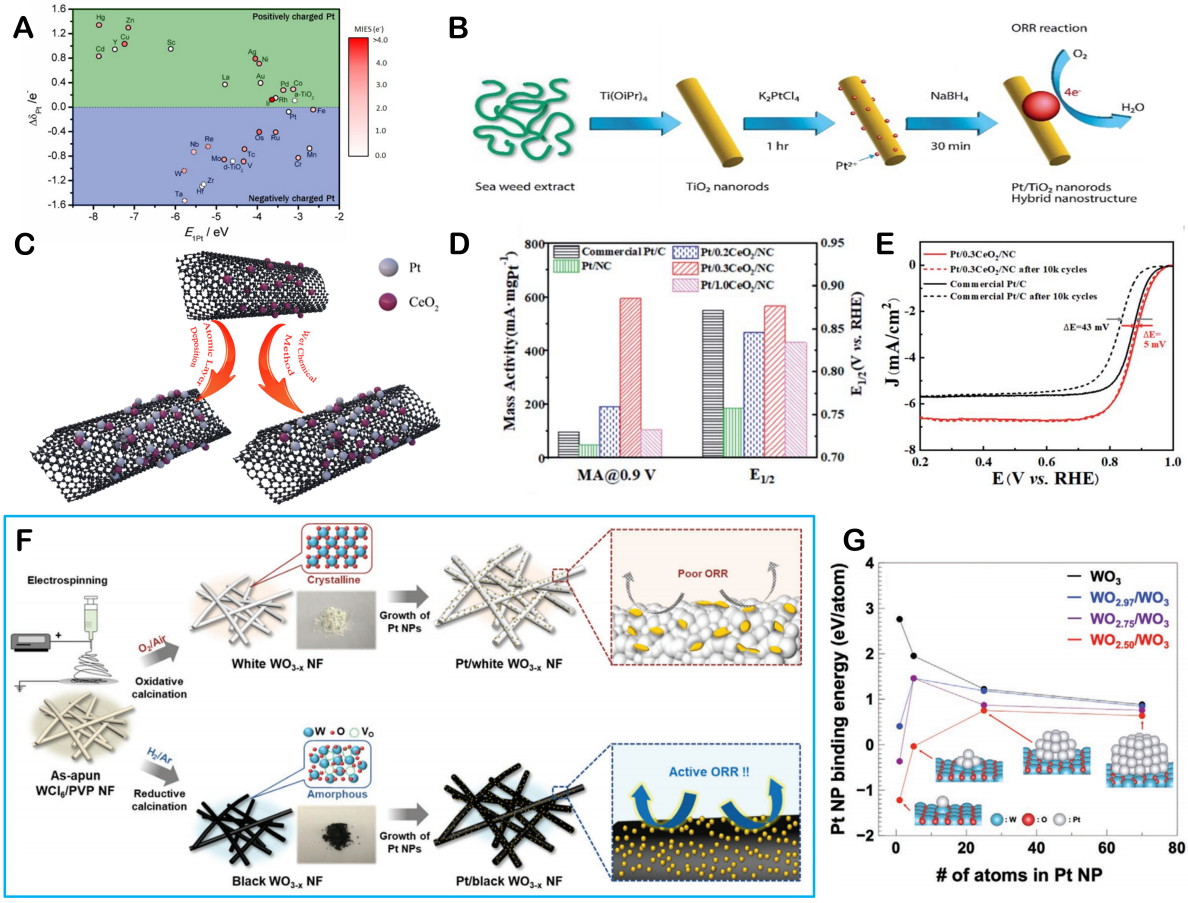

Figure 6. (A) A guide map containing four descriptors, MIES, E_{Ovas}, E_{1Pt}, and $\Delta\delta_{Pt}$ of $TiMO_2$ as the support for Pt catalysts in fuel cells. Reproduced with the permission of Ref.[92] Copyright 2017, Royal Social of Chemistry. (B) Schematic illustrations of the synthesis of Pt/TiO_2 NRs catalyst. Reproduced with the permission of Ref.[93] Copyright 2018, Royal Social of Chemistry. (C) Schematic illustrations of the synthesis of Pt/CeO_2/CNT junction interface catalyst. Reproduced with the permission of Ref.[95] Copyright 2020, Elsevier. (D) The mass activity (at 0.9V *vs.* RHE) and half-wave potential of commercial Pt/C, Pt/NC, and Pt/xCeO_2/NC, (E) LSV curves of Pt/0.3CeO_2/NC and commercial Pt/C before and after 10,000 cycles. Reproduced with the permission of Ref.[99] Copyright 2022, Royal Social of Chemistry. (F) Schematic illustrations of the synthesis of Pt/white WO_{3-x} NF and Pt/black WO_{3-x} NF catalysts, (G) Binding energies of Pt NPs of different sizes supported on WO_{3-x} NFs. Reproduced with the permission of Ref.[100] Copyright 2021, John Wiley and Sons.

oxygen, delivering active oxygen species via a spillover process[94]. When the active oxygen species migrate to the surface of Pt NPs, the Pt-CeO_2 interfaces will form and accelerate the ORR kinetics. Meanwhile, the oxidation state of Ce^{3+} can also stabilize the Pt NPs and enhance the durability of Pt/CeO_2 catalysts. Most importantly, the SMSI effect between Pt NPs and CeO_2 support can facilitate the dispersion of Pt NPs and prevent its detachment and aggregation during long-term potential cycling. However, the inferior electronic conductivity of CeO_2 has been an obstacle to the widespread use of Pt/CeO_2 catalysts in ORR. Similar to TiO_2, the introduction of carbon into Pt/CeO_2 materials to construct Pt/CeO_2/C triple junction interface catalysts has been reported to raise the electronic conductivity without affecting the SMSI between Pt-CeO_2 interface (as shown in Figure 6C)[95-97]. With the unique ternary nanostructure, abundant oxygen vacancies, and SMSI effect advantages, the Pt/CeO_2/C catalysts exhibit higher ORR performance and durability than commercial Pt/C[98]. Lu *et al.* reported that CeO_2/N-C synthesized through a polyol method with an extremely low Pt content (5%) catalyst (Pt/CeO_2/N-C) possessed a higher mass activity of 593.6 mA mg_{pt}^{-1} when compared with the commercial Pt/C (97.0 mA mg_{pt}^{-1}) (as shown in Figure 6D)[99]. Meanwhile, the $E_{1/2}$

of Pt/CeO_2/N-C only negatively shifted by 5 mV after a durability test for 10,000 cycles, while it is 43 mV for Pt/C (as shown in Figure 6E). The enhanced ORR activity and durability of Pt/CeO_2/N-C can be attributed to the abundance of oxygen vacancies present on the CeO_2 surface, leading to a strong interaction between the Pt-CeO_2 interface.

Tungsten oxides (WO_3)

Tungsten oxide is another metal oxide with superior inherent properties and durability in acidic media. Tungsten trioxide (WO_3), as the most stable oxidation state, has been proposed as a promising support for Pt-based electrocatalysts in the ORR due to its series of advantages, which include: (1) the W possesses strong electronegativity, which can modify the electronic structure of Pt and tune the Pt-Pt distance, thereby facilitating the ORR kinetic; (2) WO_3 can introduce hydrogen spillover effect on Pt via the formation of hydrogen tungsten bronze (H_xWO_3), which speeds up the protonation of the O_2 molecule and the rate of oxygen reduction on Pt NPs; (3) the unusual structural defects and unique surface features of WO_3 can promote the high dispersion of the Pt NPs and narrow size distribution; (4) the synergistic effect and SMSI effect between Pt and WO_3 enable Pt/WO_3 catalyst to achieve higher ORR activity and stability. Kim *et al.* synthesized a Pt/black WO_{3-x} nanofiber (NF) catalyst with controlled oxygen deficiency and high electrical conductivity (as shown in Figure 6F)[100]. Their investigations revealed that the as-prepared Pt/black WO_{3-x} NFs exhibited better ORR activity and durability in acidic media as compared to Pt/white WO_{3-x} NFs and Pt/C catalysts. Combined with DFT calculations suggested that the high ORR performance was attributed to plentiful ORR active sites facilitated by numerous oxygen vacancies on the black WO_{3-x} surface and the excellent surface charge properties of the Pt NPs, and the enhanced stability is attributed to the SMSI effect between Pt and oxygen-deficient WO_{3-x} (as shown in Figure 6G). In addition, Pt/WO_3-C system catalysts have been reported to have high ORR activity and stability because of the combination of the excellent electrical conductivity of carbon nanomaterials and the strong interaction at the Pt-W interface[101,102]. Interestingly, besides as a support for Pt NPs or a modified part of the carbon substrate, the WO_3 has also been applied to modify the catalyst surface. For example, Mo *et al.* prepared a WO_x-surface modified PtNi alloy nanowires (WO_x-PtNi NWs) catalyst with a high aspect ratio by a one-step solvothermal method, which showed a superior mass activity of 0.85 A mg_{pt}^{-1} at 0.9V than PtNi NWs (0.33 A mg_{pt}^{-1}) and Pt/C (0.14 A mg_{pt}^{-1})[103]. Meanwhile, the mass activity of WO_x-PtNi NWs only dropped 23.89% after the 30 k cycles durability test, whereas it is 45.94% and 57.9% for PtNi NWs and Pt/C, respectively[104].

Besides TiO_2, CeO_2, and WO_3, other reducible oxide supports, such as NbO_2[67] and Ta_2O_5[105,106], have also been demonstrated to be capable of enhancing the ORR performance through the SMSI effect with Pt NPs. Some newly published literature for Pt/TMO catalysts with the performance of ORR is given in Table 2. However, in a three-electrode system, a high-speed rotating disc electrode can eliminate the influence of mass transfer and conductivity on the performance of oxide-supported Pt-based catalysts due to the limited conductivity and low specific surface area of oxide supports, however, in practical applications, thicker catalyst layers will require higher mass transfer and conduction capabilities of the catalyst. As a result, there are few reports of Pt-based catalysts supported by oxide carriers for hydrogen fuel cells or metal-air batteries.

Nitrides-based materials

TMNs, especially titanium nitride (TiN), niobium nitride (NbN), *etc.*, are used as electrocatalysts because of their excellent electronic conductivity, electrochemical and thermal stability, and corrosion resistance compared with TMOs. In addition, TMNs inherit the characteristics of TMOs in terms of wide source and low price since their synthesis is mainly using TMOs as precursors and roasted under ammonia atmosphere. The excellent corrosion resistance and SMSI facilitate the high catalytic stability and a prolonged lifetime of TMNs-supported catalysts. More importantly, the high electronic conductivity of

Table 2. ORR performance and stability of Oxide-based supported Pt catalysts

Catalyst	Pt (wt.%)	Size of Pt (nm)	Support electrical conductivity (S cm^{-1})	ECSA ($m^2 g^{-1}_{pt}$)	Mass activity (A mg_{pt}^{-1})	Specific activity (mA cm_{pt}^{-2})	Stability	Ref.
TiO_2-based catalysts								
Pt/TiO_2	12	30	/	7.23	0.083	1.134	5.9% loss of ECSA after 5,000 cycles	[68]
Pd/TiO_2/C	/	7.8	/	54.2	2.6	4.8	13% mass activity loss after 10,000 cycles	[69]
PtAu/TiO_2 NWs	/	3.62	/	85.8	0.381	0.441	20% loss of ECSA after 5,000 cycles	[70]
Pt/TiO_2-C	3.5	3.5	/	82	0.205	/	0.8% loss of ECSA after 10,000 cycles	[72]
Pt/TiO_2/C	4.4	2.3	/	50.2	0.442	0.881	2.3% loss of ECSA after 10,000 cycles	[73]
Pt/$TiWN_xO_y$	20	9	2.3	/	0.1	/	22.9% mass activity loss after 5,000 cycles	[78]
Pt/$TiNbO_2$ NTs	6	4	/	110.3	0.314	/	19% loss of ECSA after 2,000 cycles	[84]
Pt/$TiCrO_2$	/	3-5	/	18	/	0.46	/	[86]
Pt/$TiMoO_2$	20	3-4	2.8×10^{-4}	72.5	/	/	8% loss of ECSA after 5,000 cycles	[87]
Pt/$TiTaO_2$	20		0.2		0.06	/	35% loss of ECSA after 10,000 cycles	[89]
Pt/$TiVO_2$	6	2.0	/	115.4	0.356	/	24% mass activity loss after 4,000 cycles	[91]
Pt/TiO_{2-x} NSs	/	3	2.66×10^{-3}	65	0.006	13.27	32% loss of ECSA after 10,000 cycles	[93]
CeO_2-based catalysts								
Pt/CeO_2/CNT	10	2.5/3.7		74.1	~0.38	/	13.4% mass activity loss after 5,000 cycles	[95]
Pt/CeO_2/C	/	2-3	/	50.1	0.05	/	80% loss of ECSA after 10,000 cycles	[97]
Pt/CeO_2N-C	5.6	5.7	/	/	0.238	5.88	/	[98]
Pt/CeO_2-NC	5	2.3	/	/	0.6	6.72	5 mV $E_{1/2}$ loss after 10,000 cycles	[99]
WO_3-based catalysts								
Pt/black WO_{3-x}	/	5	/	/	/	/	13% loss of ECSA after 5,000 cycles	[100]
Pt/WO_3	20	2-3	7.8×10^{-3}	75	0.325	0.769	5.5% loss of ECSA after 5,000 cycles	[101]
$WO_{x-(0.25)}$-PtNi NWs/C	/	2-3	/	77.5	0.45	0.58	15.72% loss of ECSA after 30,000 cycles	[103]
Other oxygen-based catalysts								
Pt/NbO_2/C	/	5.3	/	66	0.56	0.85	15% loss of ECSA after 5,000 cycles	[67]
Pt/N-ALDTa_2O_5/C	/	3.3	85.7	70.3	0.28	/	14.9% mass activity loss after 10,000 cycles	[105]
Pt-Ta_2O_5/CNT	9.06	3	5.8×10^{-5}	78.4	0.23	0.293	3.5% loss of ECSA after 10,000 cycles	[106]

TMNs eliminates the disadvantage of the inherent poor conductivity in TMOs-supported catalysts. Furthermore, recent studies have demonstrated the TMN itself possesses considerable ORR catalytic activity under acidic conditions. Therefore, TMNs-supported Pt-based catalysts display not only excellent ORR

activity and stability but also hold significant potential for use in fuel cell and metal-air battery devices.

Titanium nitride (TiN)

TiN as a high conducting material (119 Scm^{-1} as opposed to 5 Scm^{-1} for carbon black) has been recently reported as a promising alternative candidate to the carbon-based support for Pt NPs due to its good thermal stability, high corrosion- and structure-resistance, and electrochemically stable in fuel cell operating conditions[107]. Also, the SMSI effect between TiN support and Pt NPs has been confirmed to be capable of supplying a strong adhesion to Pt NPs and accelerating electron transfer. Since Ni doping may boost the ability of Ti atoms to transfer electrons to the adsorbed oxygen molecules and simultaneously reduce the Ti-O strength to an appropriate level, thereby resulting in high ORR activity[33,108]. As an example, a marriage of the high activity of the Pt shell and the low cost and superb stability of core TiN NPs was obtained by Tian *et al.* via depositing several atomic layers of thick Pt shell on a binary titanium nickel nitride nanocrystal (as shown in Figure 7A)[109]. The TiNiN@Pt catalyst exhibited extremely high activity and excellent durability for the ORR in the acidic solution owing to the synergetic effects of SMSI between the ultrathin Pt skin and the ultrastable TiNiN support. However, a series of inter-particle grain boundaries may act as electron reservoirs and traps during the electron transfer between TiN support and Pt NPs, resulting in the size of TiN particles decreasing and thereby losing their intrinsic high electrical conductivity. To solve this problem, Shin *et al.* designed a grain-boundary-free scaffold-like porous TiN nanotube (NT) with high electrical conductivity (ca. 30-fold higher than TiN NPs) as a support for Pt NPs (as shown in Figure 7B)[110]. The result showed that the Pt/TiN NT exhibited a higher ORR activity and stability compared with Pt/TiN NPs catalyst because of the unique hollow and porous, scaffold-like, cylindrical structure of TiN NT, which allows for facilitated carrier diffusion in TiN materials, resulting in improved electrical conduction. To date, a series of TiN modifications through nanostructure formation of nanotubes[111-115], nanoflakes[116,117], nanorods[118], nanosphere[119] (as shown in Figure 7C-F, respectively.) and through doping by Nb[120], Mo[121], Cu[122], Co[113,118], Cr[114,123], and Ni[124] were reported to modify the metal-support interface structure, modulate the activation energy of molecular adsorption, and enhance interfacial electron transfer and mass transfer, thereby improving the ORR activity and stability of catalysts.

Vanadium nitride (VN)

Vanadium nitride (VN), a kind of transition metal nitride, has received much attention in the field of supercapacitors and lithium-ion batteries but less attention in ORR since most of the synthesis methods of VN involve high-temperature calcination, which inevitably leads to agglomeration of particles, resulting in lower specific areas. Therefore, it is necessary to seek a breakthrough from the synthesis of VN materials to achieve the expected level of ORR activity of catalysts for Pt/VN systems. Yin *et al.* successfully synthesized a VN/graphitic carbon (GC) nanocomposite for the first time, which acts as an enhanced support of Pt NPs toward ORR[125]. After loading 10% Pt NPs, the resulting Pt-VN/GC catalyst demonstrates higher ORR activity than 20% Pt/C. More importantly, the electrochemically active surface area (ECSA) of 10% Pt-VN/GC catalyst maintains 99% after 2,000 cycles, whereas Pt/C is just 75%. The excellent stability is attributed to the synergistic and SMSI effects between VN and Pt and the stability of the GC. Recently, a high electrical conductivity VN NFs support Pt NPs catalyst (Pt/VN) was prepared by Kim *et al.* (as shown in Figure 7G)[126]. The Pt/VN catalysts exhibited higher ORR activity and durability in acid electrolytes compared to Pt/C. DFT calculations provided further evidence of the SMSI effect between Pt and VN, which contributed to the excellent stability of the catalyst (as shown in Figure 7H).

Chromium nitride (CrN)

Chromium nitride (CrN) is also a viable support material and possesses several desirable properties, including high electrical conductivity, outstanding thermal and electrochemical stability, exceptional

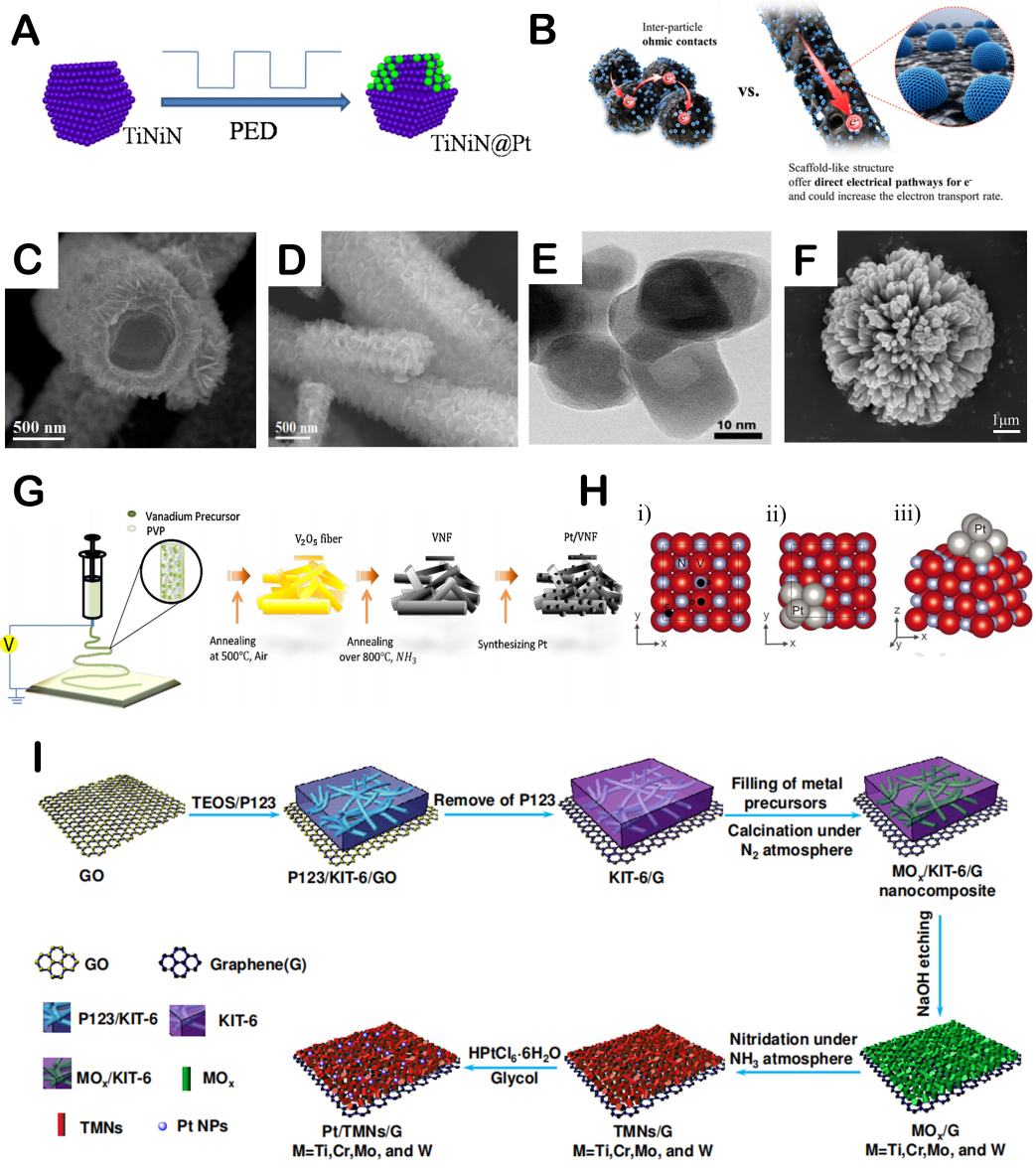

Figure 7. (A) Schematic illustrations of the synthesis of TiNiN@Pt catalyst. Reproduced with the permission of Ref.[109] Copyright 2016, American Chemical Society. (B) Schematic illustrations of Pt/spherical TiN NPs and Pt/scaffold-like TiN NTs catalysts, Reproduced with the permission of Ref.[110] Copyright 2016, American Chemical Society. SEM images of (C) $Ti_{0.9}Ni_{0.1}N$ nanotubes. Reproduced with the permission of Ref.[124]. Copyright 2018, Royal Social of Chemistry, (D) $Ti_{0.9}Cu_{0.1}N$ nanoflakes. Reproduced with the permission of Ref.[116] Copyright 2018, Elsevier, (E) TiN nanorods. Reproduced with the permission of Ref.[110]. Copyright 2016, American Chemical Society, (F) TiN nanosphere. Reproduced with the permission of Ref.[119] Copyright 2022, Elsevier. (G) Schematic illustrations of the synthesis of Pt/VN catalyst. (H) (i) Adsorption sites of Pt_1 or Pt_6 on the VN surface (ii and iii) top view and side view of the Pt_6-VN system, respectively. Reproduced with the permission of Ref.[126] Copyright 2017, Elsevier. (I) Schematic illustrations of the synthesis of 2D layered mesoporous Pt/TMNs/G catalysts. Reproduced with the permission of Ref.[130]. Copyright 2016, American Chemical Society.

hardness and corrosion resistance, and good catalyst-support interaction[127]. Yang *et al.* reported mesoporous CrN-supported Pt NPs (Pt/CrN) catalysts and found that, as compared with the commercial Pt/C catalysts, the obtained Pt/CrN catalysts exhibited both higher ORR activity and stability due to the smaller pore size and higher surface area of the CrN support and the SMSI effect between Pt and CrN[128,129]. Subsequently, Liu *et al.* constructed a series of 2D layered mesoporous TMNs/graphene including mono-

TiN/G, CrN/G, WN/G, MoN/G, and binary-TiCrN/G, TiWN/G and TiMoN/G nanocomposites with a large surface, high porosity, and excellent electrical conductivity (as shown in Figure 7I)[130]. After loading Pt NPs, the binary Pt/$Ti_{0.5}Cr_{0.5}N$/G catalysts exhibit the best ORR activity and stability due to the enhanced exposure of active sites, the large accessible active sites, and the improved specific surface area and porosity, resulting in strengthened electron transfer between Pt, $Ti_{0.5}Cr_{0.5}N$, and graphene.

From the above results, it is clear that the use of TMNs as support is an effective method to enhance the ORR activity and stability of Pt-based catalysts. Firstly, the overall structural stability of the catalyst can be enhanced by the SMSI between TMN and Pt. In addition, the inherent ORR performance and excellent electrical conductivity of TMNs can further promote the catalytic activity in TMNs-supported Pt catalyst systems. Moreover, the ORR catalytic activity can be further enhanced by doping TMN supports with other elements due to the modulated structure and composition of the supported Pt nanomaterials. The detailed ORR performance of Pt/TMN catalysts is presented in Table 3.

Carbides-based materials

Apart from TMO and TMN, TMC also possesses the potential as the ORR catalyst support because of their chemical stability and high electrical conductivity. First, the similar electronic structure and catalytic properties of TMC and Pt-group metals can reduce the overall loading of precious metals. Second, Pt-based metals tend to bind firmly to metal-terminated TMC surfaces and facilitate the electron transfer with its support to improve ORR stability and intrinsic activity[131-133].

Titanium carbide (TiC)

Titanium carbide (TiC) possesses similar structural and physicochemical properties as TiN. This results in a strong interaction between the TiC support and the Pt nanoclusters, which leads to an increase in the adsorption strength of the oxygen molecules on the Pt surface and improves the ORR activity of the Pt/TiC catalyst. According to the DFT calculations, the TiC support can strongly anchor Pt NPs and prevent their exfoliation or agglomeration due to the formation of Pt-C-Ti bonds (as shown in Figure 8A)[134]. Moreover, Pt-C-Ti bonds were also demonstrated to possess stronger electronic interaction as compared to Pt-N-Ti and Pt-O-Ti bonds, which leads to higher accessibility of active Pt sites in Pt/TiC and presents a better ORR activity and stability than Pt/TiN and Pt/TiO_2 catalysts[71]. Lee *et al.* synthesized a high conductive two-dimensional Ti_3C_2 (MXene)-supported Pt NPs catalyst (Pt/Ti_3C_2) and precisely tuned the number of layered Ti_3C_2 to provide more electron transfer for Pt NPs[135]. DFT calculation showed that electron-rich Pt had fewer *d*-band vacancies, weakening the binding of oxygen species to the Pt surface and increasing the rate of *OH desorption. Furthermore, the electron transfer between Pt and Ti_3C_2 triggers the SMSI effect, inducing encapsulation phenomena of metal support and ensuring the stability of the Pt/Ti_3C_2 catalysts. Subsequently, Xie *et al.* presented a Pt/ $Ti_3C_2X_2$ (X = OH, F) catalyst and found that the -OH and -F groups can also prevent Pt NPs from agglomeration, Ostwald ripening, and dissolution, as does SMSI effect[136]. Nevertheless, the TiC substrate is not electrochemically stable and will undergo irreversible electrochemical oxidation. To solve this problem, a Pt_3Pd/TiC@TiO_2 core-shell composite catalyst has been reported to possess better ORR stability than that of Pt/TiC and Pt_3Pd/TiC catalysts by Ignaszak *et al.* due to the TiO_2 shell can act as a protective layer over the TiC core[137]. Besides the core-shell protection strategies, electrochemical modification is another effective method to obtain oxygen-rich species on catalyst surfaces. A surface aluminum-leached Ti_3AlC_2-supported Pt NPs catalyst (Pt/e-TAC) with much-improved ORR activity and stability compared to Pt/C has been synthesized by Xie *et al.* (as shown in Figure 8B)[138]. DFT calculations indicated that the enhancement mechanism of Pt/e-TAC is attributed to the stronger interaction that exists between Pt_{13} clusters and Ti_3C_2 with respect to C. The partial density of states (PDOS) confirmed that the SMSI effect between Pt and Ti_3C_2 results in a considerable overlap between the Pt-d and Ti-d states near the Fermi energy level.

Table 3. ORR performance and stability of Nitrides-based Pt catalysts

Catalyst	Pt (wt.%)	Size of Pt (nm)	Support electrical conductivity (S cm^{-1})	ECSA ($m^2 g^{-1}_{pt}$)	Mass activity (A mg_{pt}^{-1})	Specific activity (mA cm_{pt}^{-2})	Stability	Ref
TiN-based catalysts								
TiNiN@Pt	4.98	2-3	/	97	0.83	0.49	21% loss of ECSA after 10,000 cycles	[109]
Pt/TiN NTs	20	3.65	118	61.3	0.21	3.37	No degradation ECSA after 10,000 cycles	[110]
Pt/TiN NTs	20	3.75	85	45.8	0.4	0.87	23% loss of ECSA after 12,000 cycles	[111]
$Pt/Ti_{0.95}Co_{0.05}N$	20	3.34	/	51.5	0.84	/	14% loss of ECSA after 10,000 cycles	[113]
Pt_3Cu/TiN NTs	20	28	184	45.7	2.43	5.32	16.1% mass activity loss after 10,000 cycles	[115]
$Pt/Ti_{0.9}Cu_{0.1}N$ NFs	20	2.3	/	57.5	1.56	2.64	13% loss of ECSA after 10,000 cycles	[116]
Pt/TiN NPs	20	3.0	679	/	0.65	1.06	12% loss of ECSA after 15,000 cycles	[117]
TiN@Pt	12	2-3	/	66	0.44	0.33	10% loss of ECSA after 3,000 cycles	[119]
$Pt/Ti_{0.8}Mo_{0.2}N$	20	3.4	/	54.9	0.62	1.07	47% loss of ECSA after 9,000 cycles	[121]
$Fe_3Pt/Ti_{0.5}Cr_{0.5}N$	10.5	1-2	/	52.8	0.68	1.28	21.8% mass activity loss after 5,000 cycles	[123]
$Pt/Ti_{0.9}Ni_{0.1}N$ NTs	20	3.1	/	59.7	0.78	1.3	9% mass activity loss after 15,000 cycles	[124]
VN-based catalysts								
Pt-VN/GC	10	3.8	/	12.6	0.137	/	1% loss of ECSA after 2,000 cycles	[125]
Pt/VN	15	2-8	/	/	/	/	/	[126]
CrN-based catalysts								
$Pt/Ti_{0.95}Cr_{0.05}N$ NTs	20	3.0	/	52	0.62	/	29% loss of ECSA after 1,800 cycles	[114]
Pt/CrN	20	3.9	69	75.3	0.009	0.012	30% mass activity loss after 10,000 cycles	[128]
$Pt/Ti_{0.5}Cr_{0.5}N_2/G$	15.6	4	/	76.2	0.79	1.04	9.3% loss in the acidic medium after 1,800 cycles	[130]

Molybdenum carbide (Mo_2C)

Molybdenum carbide (Mo_2C) is another carbide material that has received a lot of interest as a support for Pt-based catalysts[139-142]. Elbaz *et al.* synthesized a Pt/Mo_2C catalyst with unique platinum rafts consisting of 6 atoms or less on the Mo_2C surface, which showed a higher mass activity of 0.29 A mg_{pt}^{-1} at 0.9 V than Pt/XC-72 (0.19 A mg_{pt}^{-1}). Meanwhile, the Pt/Mo_2C lost only 10% of its initial ECSA, whereas the Pt/XC-72 lost approximately 80% after 5,000 cycles of accelerated durability testing[143]. Subsequently, they investigated the formation of Pt nanorafts and its ORR catalytic activity on Mo_2C using first-principles calculations and found that the O-O repulsion between the O atoms on the Mo_2C and the O adsorbate enhances the ORR activity by weakening the O adsorption energy. Moreover, the SMSI effect and strong binding energy between Pt and Mo_2C are prone to show better electrocatalytic activity towards ORR when compared to Pt/XC-72 (as shown in Figure 8C)[144]. More recently, Mo_2C has been demonstrated as a promising support material for anchored Pt single atoms, as the Mo atoms can provide SMSI with Pt species. Significantly, it is able to anchor Pt single atoms over a broad range of concentrations, thereby

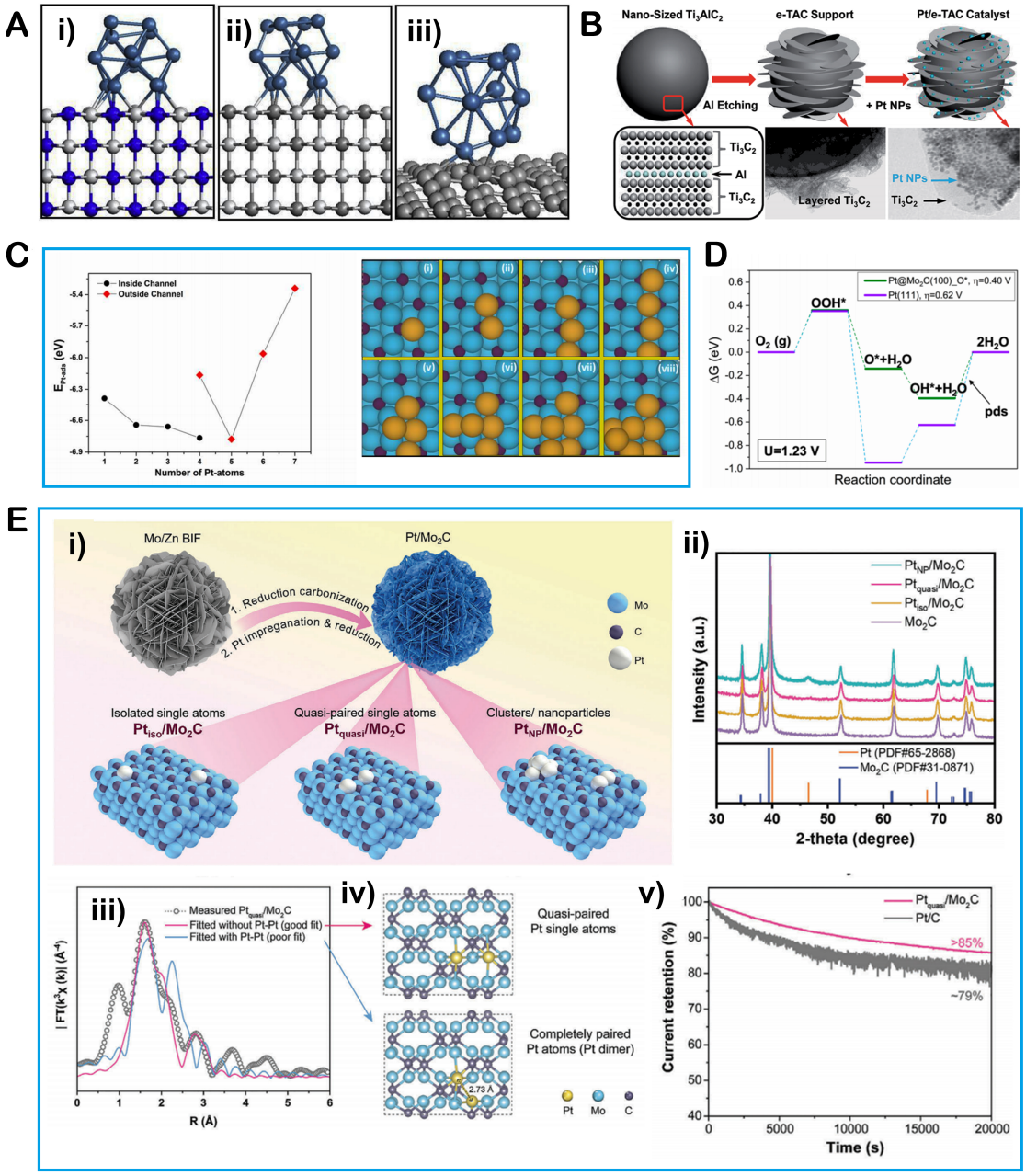

Figure 8. (A) Stable structure models of Pt_{13} clusters on (i) TiN, (ii) TiC, and (iii) graphene. Reproduced with the permission of Ref.[134] Copyright 2019, Elsevier. (B) Schematic of Pt/e-TAC catalyst formation. Reproduced with the permission of Ref.[138]. Copyright 2014, Royal Society of Chemistry. (C) Binding energies of Pt atoms on the ordered Mo_2C surface and the formation of Pt nanorafts on the Mo_2C surface (i) to (iv) Pt deposited growing in a channel, (v) to (viii) Pt atoms deposited outside the channel with an increase in Pt-loading. Purple, blue, and yellow spheres represent C, Mo, and Pt atoms, respectively. Reproduced with the permission of Ref.[144] Copyright 2018, American Chemical Society. (D) Free energy diagrams of ORR on Pt@Mo_2C(100)_O* and Pt(111). Reproduced with the permission of Ref.[148]. Copyright 2021, American Chemical Society. (E) Schematic diagram, phase characterization, and performance. (i) Schematic illustrations of the synthesis of various Pt/Mo_2C samples, (ii) XRD patterns of various Pt/Mo_2C samples, (iii) Fitted EXAFS results of Pt_{quasi}/Mo_2C, without and with Pt-Pt coordination, (iv) Structural models of the cases for quasi-paired Pt single atoms and completely paired Pt atoms, (v) Stability of Pt_{quasi}/Mo_2C determined by chronoamperometry test conducted at a potential of 0.85 V. Reproduced with the permission of Ref.[149] Copyright 2021, John Wiley and Sons.

allowing the modeling of potential synergistic interactions among the densely populated Pt single atoms without affecting the dispersion and durability[145-147]. Huang *et al.* successfully dispersed a series of TM

atoms, including Pt, Pd, Ir, *etc.* atoms, over Mo_2C by bonding with its surface Mo atoms to obtain thermodynamically stable single-atom catalysts (SACs) and investigated their corresponding ORR activity and selectivity based on DFT calculations[148]. It is found that only Pt@Mo_2C exhibits extraordinary $4e^-$ ORR activity with an overpotential of only 0.33 V, exceeding the state-of-the-art Pt (111) catalyst (as shown in Figure 8D). Zhang *et al.* reported a β-Mo_2C support quasi-paired Pt single atoms catalyst (Pt_{quasi}/Mo_2C), that is, two closely neighboring and yet non-contiguous Pt sites exhibit synergistic interactions while remaining "single" (as shown in Figure 8E (i))[149]. Similar to the isolated Pt single atoms, there is no crystalline Pt phase in the X-ray diffraction (XRD) pattern, and no Pt-Pt bond is present (as shown in Figure 8E (ii-iv)). The Pt_{quasi}/Mo_2C catalyst showed higher stability as compared to Pt/C, with a current density retention of more than 85% after 20,000s (as shown in Figure 8E (v)), which was attributed to the synergistic interaction from the two quasi-paired Pt atom sites in modulating the binding mode of reaction intermediates as well as the SMSI between Pt and Mo_2C. Nowadays, Mo_2C-supported Pt single-atom catalysts are at the forefront of research and promising for practical applications in PEMFCs.

Besides TiC and Mo_2C, a series of carbides (TaC[150], WC[151,152], NbC[153,154], ZrC[13,155], *etc.*)-supported Pt-based catalysts have also been reported to exhibit excellent ORR performance due to SMSI effect. Some recently published literature on the ORR performance of Pt/TMCs is summarized in Table 4. In addition, similar to TMNs, it is possible that these carbides may act as catalytic centers themselves. This outcome would be desirable because the parent metals of most TMC are orders of magnitude more abundant in the earth's crust and less expensive than Pt-based metals[156]. However, the carbide particle structure itself and the surface area make the system even more complex. In addition, the nucleation and growth mechanism of catalyst particles on the carbide surfaces is not fully understood at present, and the effects of surface functional groups, surface defects, and relative catalyst particle distribution still need further investigation. Moreover, carbon corrosion has been a drawback for the commercial application of Pt-based catalysts supported by TMCs. Future work should pay more attention to the durability of the TMCs-supported catalysts, especially in a realistic PEMFC cathode environment under working conditions, and elucidate the corrosion mechanisms and durability behavior.

Other non-carbon supporting materials

Transition metal sulfide

Presently, 2D layered transition metal chalcogenides (TMS), especially MoS_2, have been used as potential supports for Pt-based catalysts because of their unique layer structures, abundant defects, and edge locations[157,158]. Bothra *et al.* have systematically explored the ORR activity of different size $(Pt)_n$ clusters (n = 1-12) supported MoS_2 by first-principles density functional theory. This scaling relationship gives rise to a model volcano curve (as shown in Figure 9A), indicating that Pt_7/MoS_2 is the best electrocatalyst for ORR with a minimum overpotential value of 0.33 V, which is highly dependent on the binding strength of the oxygenated species and can be correlated with electron transfer between Pt and MoS_2[159]. Therefore, the restacking behavior of the MoS_2 layer reduces the anchoring sites for Pt deposition and does not provide high catalytic activity for PEMFC applications. To solve this issue, Anwar *et al.* introduced MoS_2 into a graphene with a mesh shape and electronic conductivity to prepare a hybrid support material (MoS_2-rGO) for a Pt-based catalyst. The results show that the abundantly exposed edges of the MoS_2 NPs constitute a homogeneous dispersion of Pt NPs, the mesh structure of graphene prevents the leaching of the Pt NPs, and the outstanding electronic conductivity of the r-GO cooperatively leads to the higher electrochemical performance[160]. Subsequently, a flowerlike MoS_2/N-doped reduced graphene oxide supported ultrafine Pt NPs catalyst (Pt@MoS_2/NrGO) was successfully synthesized by Logeshwaran *et al.*[158]. The purpose of incorporating N atoms into r-GO is to enhance its conductivity and catalytic activity owing to the high-electron transport kinetics and the capability to inhibit Pt NPs from agglomerating on the support.

Table 4. ORR performance and stability of Carbide-based Pt catalysts

Catalyst	Pt (wt.%)	Size of Pt (nm)	Support electrical conductivity (S cm^{-1})	ECSA ($m^2 g^{-1}_{pt}$)	Mass activity (A mg_{pt}^{-1})	Specific activity (mA cm_{pt}^{-2})	Stability	Ref
TiC-based catalysts								
$Pt/Ti_3C_2X_2$	20	3-7	1.2×10^{-5}	54.88	/	/	15.66% loss of ECSA after 10,000 cycles	[136]
Pt_3Pd-TiC-TiO_2	/	3.15	0.12	37.6	0.33	0.883	20% loss of ECSA after 2,000 cycles	[137]
Pt/Ti_3AlC_2	14.8	2	4.3×10^{-2}	44.81	0.18	0.399	No degradation ECSA after 1,500 cycles	[138]
M_2C-based catalysts								
Pt-Mo_2C/CNTs	16	3-6	/	/	/	/	/	[139]
Pt/Mo_2C-F	/	3.25	/	58.5	0.149	0.024	35% loss of ECSA after 5,000 cycles	[142]
Pt/M_2C	5	1	/	/	0.29	/	10% loss of ECSA after 5,000 cycles	[143]
Pt_{quasi}/Mo_2C	2.36	/	/	/	0.224	/	over 85% retention of current density after 20,000 s	[149]
Other carbide-based catalysts								
ALD-Pt-ZrC	19	2-4	/	/	0.12	0.23	17% loss of ECSA after 4,000 cycles	[13]
Pt-Ta_2O_5-TaC	4.95	2.4	/	70	0.297	0.424	5.7% loss of ECSA after 10,000 cycles	[150]
Pt-Ni/WC	9.425	4	/	178.4	2.198	1.232	9.19% loss of ECSA after 3,000 cycles	[152]
Pt/NbC/C	30	3.1	10	52	0.087	/	31% loss of ECSA after 10,000 cycles	[153]

Moreover, the attachment of MoS_2 between NrGO and Pt NPs also generates a synergistic effect and SMSI effect, resulting in Pt@MoS_2/NrGO catalysts exhibiting superior ORR activity and stability, with a half-wave potential at 0.895 V and only 1.7% loss after 30 k ADT in 0.1 M $HClO_4$ solution, which is greater than that of commercial Pt/C by a factor of 0.876 V and 3% loss, respectively. Currently, Pt-based/TMS catalysts are extensively employed in hydrogen evolution reaction (HER), while the catalyst activity in oxygen evolution reaction (OER) and ORR has been limited, mainly because the TMS supports offer poor reactivity, slow electronic conductivity, and fast reunion rate of electrons and holes[161].

Transition metal phosphide and boride

Transition metal phosphide and boride (TMP and TMB) themselves as excellent catalysts have been investigated extensively for HER, OER, and ORR. However, there is still a lack of relevant work and understanding to design the TMP- and TMB-supported Pt-based catalyst[162,163]. Zirconium phosphates (ZrP)-supported Pt NPs catalysts have recently been reported that ORR benefited from the phosphate groups in ZrP has acidic functionality, and thus the close contact with Pt NPs can facilitate the active interface (as shown in Figure 9B). The Pt/ZrP catalyst shows strong evidence of charge transfer from the ZrP support to Pt NPs, contributing to SMSI effect, and in turn directly affecting the adsorption strength of the oxygen and oxygen intermediates[164]. Titanium diboride (TiB_2), as an electrically conducting ceramic material, is a promising support medium for PEMFC catalysts thanks to their low resistance and considerable chemical stability. In previous work, Yin *et al.* successfully prepared Pt/TiB_2 catalyst via a colloidal route and revealed that the durability of

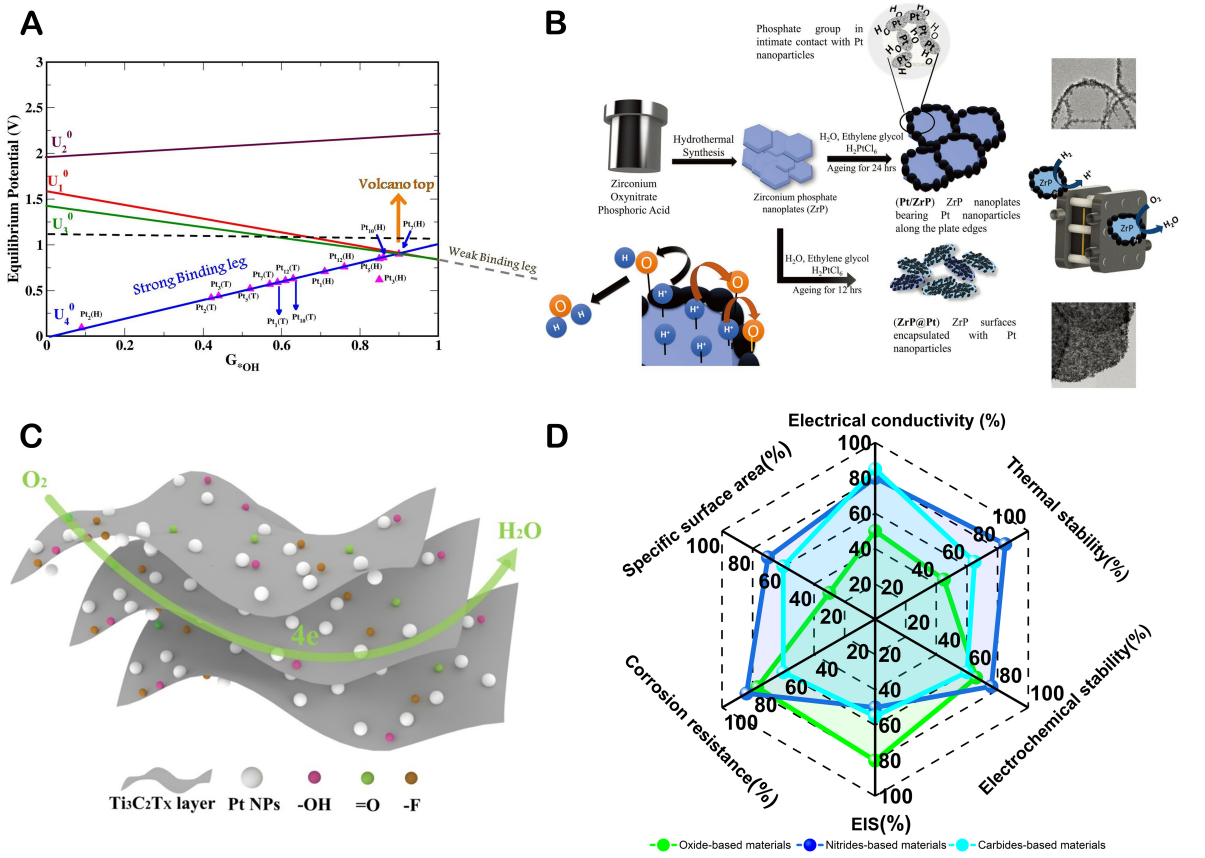

Figure 9. (A) Thermodynamic volcano relation for ORR activity as a function of Gibbs adsorption energy of *OH. Reproduced with the permission of Ref.[159] Copyright 2016, Royal Society of Chemistry. (B) Schematic illustrations of the synthesis of the Pt/ZrP catalysts. Reproduced with the permission of Ref.[164] Copyright 2023 John Wiley and Sons. (C) Schematic diagram of Pt NPs anchored on $Ti_3C_2T_x$ layer Reproduced with the permission of Ref.[168] Copyright 2020, Elsevier. (D) The radar chart of the performance of TMO, TMN, and TMC supports.

Pt/TiB_2 was approximately four times better than that of the commercial Pt/C catalyst[165]. However, the large particle size (1~8 μm) and the low BET surface area of the raw TiB_2 support severely hinder the deposition of Pt NPs. Subsequently, they employed perfluorosulphonic acid as both a proton-conducting polymer and a stabilizer to strengthen the SMSI between the Pt NPs and the TiB_2 support, enabling the Pt NPs to be strongly anchored and effectively dispersed on the inert ceramic support[166]. In the other proposal, Huang *et al.* made defects on the surface of TiB_2 support by H_2O_2 etching to create abundant active sites or functional groups to help the deposition of Pt[167]. The results showed that the mass activity of Pt/H_2O_2-TiB_2 was 80.3 mA mg^{-1}, which was significantly higher than that of Pt/TiB_2 at 2.9 mA mg^{-1}.

Although TMP- and TMB-supported Pt-based catalysts have been demonstrated as promising ORR catalysts, their characteristics of limited conductivity and easy agglomeration cause them to still have a long way for practical application. Therefore, anchoring them to a conducting substrate may be an effective strategy to overcome these shortcomings in the future.

MXenes

MXenes are novel two-dimensional (2D) graphene-like transition metal carbides and/or nitrides that have been developed as competitive candidates for electrocatalyst support for PEMFC applications due to their

unique layer structures, excellent electronic properties (approximately 15,100 S/cm), and high corrosion resistance, which facilitate various electrochemical reactions[168-170]. Among the MXene families, $Ti_3C_2T_x$ support is the most commonly used and expected to supply a strong adhesion for Pt NPs, benefiting from their same elemental composition as TiC[171]. Zhang *et al.* reported the presence of abundant -OH and -F surface termination groups on $Ti_3C_2T_x$, which makes it easier to create Pt deposition sites (as shown in Figure 9C). Thanks to the SMSI effect between Pt NPs and $Ti_3C_2T_x$ nanosheets, the migration and agglomeration of Pt NPs is effectively prevented, leading to Pt/$Ti_3C_2T_x$ catalysts that exhibit superior ORR activity and stability over commercial Pt/C in both acidic and alkaline environments[168]. However, the charge-transfer performance of the $Ti_3C_2T_x$ surface with the functional groups may be limited by the inherent restacking phenomenon of 2D materials. Hybridization of $Ti_3C_2T_x$ with carbon nanotube (CNT) is an effective strategy to prevent the agglomeration of the $Ti_3C_2T_x$ support caused by strong van der Waals forces and enhance electron transport between Pt-$Ti_3C_2T_x$-C. Xu *et al.* demonstrated that the hybridized Pt/CNT-$Ti_3C_2T_x$ shows excellent ORR activity (the mass activity is 3.4-fold over Pt/C) and durability (a great ECSA retention of 94% with respect to that in Pt/C of 73% after 2,000 cycles accelerated stress test (AST))[172]. Furthermore, the Pt/CNT-$Ti_3C_2T_x$ exhibited the peak power density (181 mW cm^{-2}) in the single-cell MEA test compared to Pt/CNT, Pt/$Ti_3C_2T_x$, and Pt/C, attributed to the better mass transport on this cathode material[172]. In addition to $Ti_3C_2T_x$, Yang *et al.* revealed that V_2C MXene displays excellent charge transfer kinetics and conductance[173]. The SMSI effect enables highly dispersed Pt atoms and thin Pt films to form on the V_2C, dramatically improving the stability of Pt/V_2C MXene towards the ORR[173,174]. Li *et al.* have identified Nb_2CT_x as capable of providing a good catalytic support interaction for Pt through an efficient method of generating reactive metal-support interactions on Pt/Nb_2CT_x catalysts at moderate temperature[175]. Although the use of MXene as Pt-based catalyst support has pointed out the direction to ORR, the AST is still unsatisfactory, possibly due to the oxidative environment of the fuel cell cathodes, which exposes MXene to oxidation over an extended period of time. Future designs could consider incorporating nanomaterials such as carbon nanostructures into MXene to improve its oxidative stability.

Finally, while several PGM catalysts have shown impressive ORR activity in half-cell tests, few of them have demonstrated both good activity and durability in PEMFC. This is most likely related to the intrinsic nature of the catalyst supports. A number of novel carbon materials, including 1D carbon nanotubes, 2D graphene, 3D carbon nanocomposites, *etc*., have recently been investigated for PEMFC due to their promising progress in various aspects such as corrosion resistance and porosity of the material[176-180]. However, the small number of nucleation sites, low charge transfer for the deposition of metal NPs with carbon supports, and the mass transfer between metal and support have been major challenges for device performance. A series of noncarbon-based support based on their inherent properties (as shown in Figure 9D) are able to generate SMSI effect with Pt NPs, which greatly helps to suppress the agglomeration/separation of the metal and promote high performance and durability for PEMFC. Despite progress, there are still gaps and challenges between the properties and practical application of Pt-based catalysts supported by TMOs, primarily due to the poor conductivity of the TMOs supported. TMNs and TMCs, in particular TiN, TiC, and Mo_xC, stand out from other materials as Pt NPs support in terms of the ORR activity and stability in half-cell tests and the performance and durability in fuel cells with reported values well above those of carbon-supported Pt-based catalysts.

PERSPECTIVE AND OUTLOOK

The development of high-stability carbon-free Pt-based catalysts is scientifically and technically essential to facilitate their practical application in fuel cells. As discussed in this review, a series of TMOs-, TMNs-, and TMCs-supported Pt-based catalysts provide an excellent opportunity to substitute the use of carbon at the cathode for PEMFCs. Innovative and effective construct strategies of SMSI are essential to improve the

catalytic activity and stability with regards to improving the electron conduction, suppressing the chemisorption of small molecules, and increasing the interaction between metal and support. However, a series of significant challenges remain for the application of TM-supported Pt-based catalysts in PEMFCs.

Firstly, metal-oxide systems and metal-carbide systems suffer from several drawbacks, such as low electronic conductivity and limited surface area, which can be efficiently optimized by doping strategies (introducing V_o) and coupling superior conductive materials. The SMSI effect between metal and supports can also further be enhanced by doping strategies to change the electronic structure of the support. Metal-nitride systems can effectively avoid these drawbacks due to their high conductivity, while the specific areas of TMNs are generally extremely low due to the fact that the high-temperature annealing process is always needed to synthesize TMNs. In addition, the specific preparation method of the catalysts and the size of the metal NPs can significantly affect the charge transfer between the metal and the support, while the charge transfer between the support and the noble metal particle sizes has rarely been reported. Furthermore, the study of the surface/interface structure and dynamic evolution of TM-supported Pt catalysts in the reaction environment at the atomic scale is important for the rational design of catalysts and revealing the reaction mechanism, whereas the key issues such as the interfacial structure performance relationship in the TM-supported Pt catalytic reaction have not been fully elucidated. Finally, although some typical catalysts with SMSI show considerable activity and durability for ORR in the rotating ring disk electrode level, while few electrocatalysts have not yet been practically promoted and applied to the membrane electrode assembly, thus the practical potential of these catalysts cannot be verified. All in all, although many challenges are still in the way, the SMSI provides great potential to improve the performance of the catalysts for ORR and beyond, shedding light on the practical application of these novel materials with high activity and durability.

DECLARATION

Authors' contributions

Conceived and designed the manuscript: Chen M, Miao Z, Tian X
Drafted and revised the manuscript: Chen M, Rao P, Miao Z, Luo J, Li J, Deng P, Huang W, Tian X

Availability of data and materials

Not applicable.

Financial support and sponsorship

This study was supported by the Hainan Provincial Natural Science Foundation of China (522QN281, 521RC495), the National Natural Science Foundation of China (22109034, 22109035, 52164028, 62105083), the Foundation of State Key Laboratory of Marine Resource Utilization in South China Sea (Hainan University, Grant No. MRUKF2021029), the Start-up Research Foundation of Hainan University (KYQD(ZR)-20008, 21170), and the specific research fund of The Innovation Platform for Academicians of Hainan Province.

Conflicts of interest

All authors declared that there are no conflicts of interest.

Ethical approval

Not applicable.

Consent to participate

Not applicable.

REFERENCES

1. Li C, Tan H, Lin J, et al. Emerging Pt-based electrocatalysts with highly open nanoarchitectures for boosting oxygen reduction reaction. *Nano Today* 2018;21:91-105. DOI
2. Chalgin A, Song C, Tao P, Shang W, Deng T, Wu J. Effect of supporting materials on the electrocatalytic activity, stability and selectivity of noble metal-based catalysts for oxygen reduction and hydrogen evolution reactions. *Prog Nat Sci Mater* 2020;30:289-97. DOI
3. Wu G, More KL, Johnston CM, Zelenay P. High-performance electrocatalysts for oxygen reduction derived from polyaniline, iron, and cobalt. *Science* 2011;332:443-7. DOI PubMed
4. Kodama K, Nagai T, Kuwaki A, Jinnouchi R, Morimoto Y. Challenges in applying highly active Pt-based nanostructured catalysts for oxygen reduction reactions to fuel cell vehicles. *Nat Nanotechnol* 2021;16:140-7. DOI PubMed
5. Liu M, Zhao Z, Duan X, Huang Y. Nanoscale structure design for high-performance Pt-based ORR catalysts. *Adv Mater* 2019;31:e1802234. DOI PubMed
6. Miao Z, Wang X, Zhao Z, et al. Improving the stability of non-noble-metal M-N-C catalysts for proton-exchange-membrane fuel cells through M-N bond length and coordination regulation. *Adv Mater* 2021;33:e2006613. DOI
7. Li S, Hao X, Abudula A, Guan G. Nanostructured Co-based bifunctional electrocatalysts for energy conversion and storage: current status and perspectives. *J Mater Chem A* 2019;7:18674-707. DOI
8. He Y, Liu S, Priest C, Shi Q, Wu G. Atomically dispersed metal-nitrogen-carbon catalysts for fuel cells: advances in catalyst design, electrode performance, and durability improvement. *Chem Soc Rev* 2020;49:3484-524. DOI
9. Wu Z, Zhang H, Chen C, Li G, Han Y. Applications of in situ electron microscopy in oxygen electrocatalysis. *Microstructures* 2022;2:2022002. DOI
10. Frey H, Beck A, Huang X, van Bokhoven JA, Willinger MG. Dynamic interplay between metal nanoparticles and oxide support under redox conditions. *Science* 2022;376:982-7. DOI PubMed
11. Zhang W, Chang J, Wang G, et al. Surface oxygenation induced strong interaction between Pd catalyst and functional support for zinc-air batteries. *Energy Environ Sci* 2022;15:1573-84. DOI
12. Miao Z, Li S, Priest C, Wang T, Wu G, Li Q. Effective approaches for designing stable M-N_x/C oxygen-reduction catalysts for proton-exchange-membrane fuel cells. *Adv Mater* 2022;34:e2200595. DOI
13. Cheng N, Norouzi Banis M, Liu J, et al. Atomic scale enhancement of metal-support interactions between Pt and ZrC for highly stable electrocatalysts. *Energy Environ Sci* 2015;8:1450-5. DOI
14. Yang Y, Wu D, Li R, et al. Engineering the strong metal support interaction of titanium nitride and ruthenium nanorods for effective hydrogen evolution reaction. *Appl Catal B Environ* 2022;317:121796. DOI
15. Yan D, Chen J, Jia H. Temperature-induced structure reconstruction to prepare a thermally stable single-atom platinum catalyst. *Angew Chem Int Ed* 2020;59:13562-7. DOI
16. Yang H, Lu N, Zhang J, et al. Ultra-low single-atom Pt on g-C_3N_4 for electrochemical hydrogen peroxide production. *Carbon Energy* 2023;2:1-12. DOI
17. Ling L, Liu W, Chen S, Hu X, Jiang H. MOF templated nitrogen doped carbon stabilized Pt-Co bimetallic nanoparticles: low Pt content and robust activity toward electrocatalytic oxygen reduction reaction. *ACS Appl Nano Mater* 2018;1:3331-8. DOI
18. Zhou M, Liu M, Miao Q, Shui H, Xu Q. Synergetic Pt atoms and nanoparticles anchored in standing carbon-derived from covalent organic frameworks for catalyzing ORR. *Adv Mater Interfaces* 2022;9:2201263. DOI
19. Zhai L, Yang S, Yang X, et al. Conjugated covalent organic frameworks as platinum nanoparticle supports for catalyzing the oxygen reduction reaction. *Chem Mater* 2020;32:9747-52. DOI
20. Yu X, Guo J, Li B, et al. Sub-nanometer Pt clusters on defective NiFe LDH nanosheets as trifunctional electrocatalysts for water splitting and rechargeable hybrid sodium-air batteries. *ACS Appl Mater Interfaces* 2021;13:26891-903. DOI
21. Rao P, Deng Y, Fan W, et al. Movable type printing method to synthesize high-entropy single-atom catalysts. *Nat Commun* 2022;13:5071. DOI PubMed PMC
22. Chang F, Xiao M, Miao R, et al. Copper-Based catalysts for electrochemical carbon dioxide reduction to multicarbon products. *Electrochem Energy Rev* 2022;5:139-74. DOI
23. Wu D, Baaziz W, Gu B, et al. Surface molecular imprinting over supported metal catalysts for size-dependent selective hydrogenation reactions. *Nat Catal* 2021;4:595-606. DOI
24. Deelen TW, Hernández Mejía C, de Jong KP. Control of metal-support interactions in heterogeneous catalysts to enhance activity and selectivity. *Nat Catal* 2019;2:955-70. DOI
25. Wang H, Wang L, Xiao F. New routes for the construction of strong metal-support interactions. *Sci China Chem* 2022;65:2051-7. DOI
26. Luo Z, Zhao G, Pan H, Sun W. Strong metal-support interaction in heterogeneous catalysts. *Adv Energy Mater* 2022;12:2201395. DOI
27. Pu T, Zhang W, Zhu M. Engineering heterogeneous catalysis with strong metal-support interactions: characterization, theory and

manipulation. *Angew Chem Int Ed* 2023;62:e202212278. DOI

28. Li Y, Zhang Y, Qian K, Huang W. Metal-support interactions in metal/oxide catalysts and oxide-metal interactions in oxide/metal inverse catalysts. *ACS Catal* 2022;12:1268-87. DOI
29. Wu B, Meng H, Morales DM, et al. Nitrogen-rich carbonaceous materials for advanced oxygen electrocatalysis: synthesis, characterization, and activity of nitrogen sites. *Adv Funct Mater* 2022;32:2204137. DOI
30. Bai J, Yang L, Jin Z, Ge J, Xing W. Advanced Pt-based intermetallic nanocrystals for the oxygen reduction reaction. *Chinese J Catal* 2022;43:1444-58. DOI
31. Wang J, Kong H, Zhang J, Hao Y, Shao Z, Ciucci F. Carbon-based electrocatalysts for sustainable energy applications. *Prog Mater Sci* 2021;116:100717. DOI
32. Yang X, Priest C, Hou Y, Wu G. Atomically dispersed dual-metal-site PGM-free electrocatalysts for oxygen reduction reaction: opportunities and challenges. *SusMat* 2022;2:569-90. DOI
33. Tian X, Lu XF, Xia BY, Lou XW. Advanced electrocatalysts for the oxygen reduction reaction in energy conversion technologies. *Joule* 2020;4:45-68. DOI
34. Nørskov JK, Rossmeisl J, Logadottir A, et al. Origin of the overpotential for oxygen reduction at a fuel-cell cathode. *J Phys Chem B* 2004;108:17886-92. DOI
35. Tian X, Zhao X, Su YQ, et al. Engineering bunched Pt-Ni alloy nanocages for efficient oxygen reduction in practical fuel cells. *Science* 2019;366:850-6. DOI
36. Ando F, Gunji T, Tanabe T, et al. Enhancement of the oxygen reduction reaction activity of Pt by tuning its *d*-band center via transition metal oxide support interactions. *ACS Catal* 2021;11:9317-32. DOI
37. Tauster SJ, Fung SC, Garten RL. ChemInform abstract: strong metal-support interactions. group 8 noble metals supported on Titanium dioxide. *Chemischer Informationsdienst* 1978;9:170-5. DOI
38. Tauster S. Strong metal-support interactions: occurrence among the binary oxides of groups IIA-VB. *J Catal* 1978;55:29-35. DOI
39. Beck A, Huang X, Artiglia L, et al. The dynamics of overlayer formation on catalyst nanoparticles and strong metal-support interaction. *Nat Commun* 2020;11:3220. DOI PubMed PMC
40. Wang X, Beck A, van Bokhoven JA, Palagin D. Thermodynamic insights into strong metal-support interaction of transition metal nanoparticles on titania: simple descriptors for complex chemistry. *J Mater Chem A* 2021;9:4044-54. DOI
41. Zhao W, Zhou D, Han S, et al. Metal-support interaction in Pt/TiO_2: formation of surface Pt-Ti alloy. *J Phys Chem C* 2021;125:10386-96. DOI
42. Du X, Tang H, Qiao B. Oxidative strong metal-support interactions. *Catalysts* 2021;11:896. DOI
43. Macino M, Barnes AJ, Althahban SM, et al. Tuning of catalytic sites in Pt/TiO_2 catalysts for the chemoselective hydrogenation of 3-nitrostyrene. *Nat Catal* 2019;2:873-81. DOI
44. Kennedy RM, Crosby LA, Ding K, et al. Replication of SMSI via ALD: TiO_2 overcoats increase Pt-catalyzed acrolein hydrogenation selectivity. *Catal Lett* 2018;148:2223-32. DOI
45. Komanoya T, Kinemura T, Kita Y, Kamata K, Hara M. Electronic effect of ruthenium nanoparticles on efficient reductive amination of carbonyl compounds. *J Am Chem Soc* 2017;139:11493-9. DOI PubMed
46. Zhang L, Persaud R, Theodore EM. Ultrathin metal films on a metal oxide surface: growth of Au on TiO_2 (110). *Phys Rev B* 1997;56:10549-57. DOI
47. Gubó R, Yim CM, Allan M, Pang CL, Berkó A, Thornton G. Variation of SMSI with the Au:Pd ratio of bimetallic nanoparticles on TiO_2 (110). *Top Catal* 2018;61:308-17. DOI PubMed PMC
48. Fu Q, Wagner T, Olliges S, Carstanjen HD. Metal-oxide interfacial reactions: encapsulation of Pd on TiO_2 (110). *J Phys Chem B* 2005;109:944-51. DOI PubMed
49. Liu X, Liu MH, Luo YC, et al. Strong metal-support interactions between gold nanoparticles and ZnO nanorods in CO oxidation. *J Am Chem Soc* 2012;134:10251-8. DOI
50. Tang H, Wei J, Liu F, et al. Strong metal-support interactions between gold nanoparticles and nonoxides. *J Am Chem Soc* 2016;138:56-9. DOI
51. Tang H, Su Y, Guo Y, et al. Oxidative strong metal-support interactions (OMSI) of supported platinum-group metal catalysts. *Chem Sci* 2018;9:6679-84. DOI PubMed PMC
52. Liu S, Xu W, Niu Y, et al. Ultrastable Au nanoparticles on titania through an encapsulation strategy under oxidative atmosphere. *Nat Commun* 2019;10:5790. DOI PubMed PMC
53. Liu S, Qi H, Zhou J, et al. Encapsulation of platinum by titania under an oxidative atmosphere: contrary to classical strong metal-support interactions. *ACS Catal* 2021;11:6081-90. DOI
54. Matsubu JC, Zhang S, DeRita L, et al. Adsorbate-mediated strong metal-support interactions in oxide-supported Rh catalysts. *Nat Chem* 2017;9:120-7. DOI
55. Wang X, Liu Y, Peng X, Lin B, Cao Y, Jiang L. Sacrificial adsorbate strategy achieved strong metal-support interaction of stable Cu nanocatalysts. *ACS Appl Energy Mater* 2018;1:1408-14. DOI
56. Xin H, Lin L, Li R, et al. Overturning CO_2 hydrogenation selectivity with high activity via reaction-induced strong metal-support interactions. *J Am Chem Soc* 2022;144:4874-82. DOI
57. Li D, Xu F, Tang X, et al. Induced activation of the commercial Cu/ZnO/Al_2O_3 catalyst for the steam reforming of methanol. *Nat Catal* 2022;5:99-108. DOI

58. Zhang J, Wang H, Wang L, et al. Wet-chemistry strong metal-support interactions in Titania-supported Au catalysts. *J Am Chem Soc* 2019;141:2975-83. DOI
59. Hao H, Jin B, Liu W, Wu X, Yin F, Liu S. Robust Pt@TiO_x/TiO_2 catalysts for hydrocarbon combustion: effects of Pt-TiO_x interaction and sulfates. *ACS Catal* 2020;10:13543-8. DOI
60. Wang L, Zhang J, Zhu Y, et al. Strong metal-support interactions achieved by hydroxide-to-oxide support transformation for preparation of sinter-resistant gold nanoparticle catalysts. *ACS Catal* 2017;7:7461-5. DOI
61. Dong J, Fu Q, Jiang Z, Mei B, Bao X. Carbide-supported Au catalysts for water-gas shift reactions: a new territory for the strong metal-support interaction effect. *J Am Chem Soc* 2018;140:13808-16. DOI PubMed
62. Dong J, Fu Q, Li H, et al. Reaction-induced strong metal-support interactions between metals and inert boron nitride nanosheets. *J Am Chem Soc* 2020;142:17167-74. DOI
63. Sato K, Miyahara S, Tsujimaru K, et al. Barium oxide encapsulating cobalt nanoparticles supported on magnesium oxide: active non-noble metal catalysts for ammonia synthesis under mild reaction conditions. *ACS Catal* 2021;11:13050-61. DOI
64. Wang H, Wang L, Lin D, et al. Strong metal-support interactions on gold nanoparticle catalysts achieved through Le Chatelier's principle. *Nat Catal* 2021;4:418-24. DOI
65. Chen H, Yang Z, Wang X, et al. Photoinduced strong metal-support interaction for enhanced catalysis. *J Am Chem Soc* 2021;143:8521-6. DOI
66. Zhang J, Zhu D, Yan J, Wang CA. Strong metal-support interactions induced by an ultrafast laser. *Nat Commun* 2021;12:6665. DOI PubMed PMC
67. Ma Z, Li S, Wu L, et al. NbOx nano-nail with a Pt head embedded in carbon as a highly active and durable oxygen reduction catalyst. *Nano Energy* 2020;69:104455. DOI
68. Mirshekari G, Rice C. Effects of support particle size and Pt content on catalytic activity and durability of Pt/TiO_2 catalyst for oxygen reduction reaction in proton exchange membrane fuel cells environment. *J Power Sources* 2018;396:606-14. DOI
69. Shi W, Park A, Xu S, Yoo PJ, Kwon Y. Continuous and conformal thin TiO_2-coating on carbon support makes Pd nanoparticles highly efficient and durable electrocatalyst. *Appl Catal B Environ* 2021;284:119715. DOI
70. Deng X, Yin S, Wu X, Sun M, Xie Z, Huang Q. Synthesis of PtAu/TiO_2 nanowires with carbon skin as highly active and highly stable electrocatalyst for oxygen reduction reaction. *Electrochim Acta* 2018;283:987-96. DOI
71. Mirshekari G, Shirvanian A. A comparative study on catalytic activity and stability of TiO_2, TiN, and TiC supported Pt electrocatalysts for oxygen reduction reaction in proton exchange membrane fuel cells environment. *J Electroanal Chem* 2019;840:391-9. DOI
72. Wang J, Xu M, Zhao J, et al. Anchoring ultrafine Pt electrocatalysts on TiO_2-C via photochemical strategy to enhance the stability and efficiency for oxygen reduction reaction. *Appl Catal B Environ* 2018;237:228-36. DOI
73. Shi W, Park A, Li Z, et al. Sub-nanometer thin TiO_2-coating on carbon support for boosting oxygen reduction activity and durability of Pt nanoparticles. *Electrochim Acta* 2021;394:139127. DOI
74. Li J, Zhou H, Zhuo H, et al. Oxygen vacancies on TiO_2 promoted the activity and stability of supported Pd nanoparticles for the oxygen reduction reaction. *J Mater Chem A* 2018;6:2264-72. DOI
75. Chen Y, Chen J, Zhang J, Xue Y, Wang G, Wang R. Anchoring highly dispersed Pt electrocatalysts on TiO_x with strong metal-support interactions via an oxygen vacancy-assisted strategy as durable catalysts for the oxygen reduction reaction. *Inorg Chem* 2022;61:5148-56. DOI
76. Huynh TT, Pham HQ, Nguyen AV, Nguyen ST, Bach LG, Ho VTT. High conductivity and surface area of mesoporous $Ti_{0.7}W_{0.3}O_2$ materials as promising catalyst support for Pt in proton-exchange membrane fuel cells. *J Nanosci Nanotechnol* 2019;19:877-81. DOI
77. Subban CV, Zhou Q, Hu A, Moylan TE, Wagner FT, DiSalvo FJ. Sol-Gel synthesis, electrochemical characterization, and stability testing of $Ti_{0.7}W_{0.3}O_2$ nanoparticles for catalyst support applications in proton-exchange membrane fuel cells. *J Am Chem Soc* 2010;132:17531-6. DOI
78. Hsieh B, Tsai M, Pan C, et al. Platinum loaded on dual-doped TiO_2 as an active and durable oxygen reduction reaction catalyst. *NPG Asia Mater* 2017;9:e403-e403. DOI
79. Shahgaldi S, Hamelin J. The effect of low platinum loading on the efficiency of PEMFC's electrocatalysts supported on TiO_2-Nb, and SnO_2-Nb: an experimental comparison between active and stable conditions. *Energy Convers Manag* 2015;103:681-90. DOI
80. Wang Y, Wilkinson DP, Guest A, et al. Synthesis of Pd and Nb-doped TiO_2 composite supports and their corresponding Pt-Pd alloy catalysts by a two-step procedure for the oxygen reduction reaction. *J Power Sources* 2013;221:232-41. DOI
81. Senevirathne K, Neburchilov V, Alzate V, et al. Nb-doped TiO_2/carbon composite supports synthesized by ultrasonic spray pyrolysis for proton exchange membrane (PEM) fuel cell catalysts. *J Power Sources* 2012;220:1-9. DOI
82. Bing Y, Neburchilov V, Song C, et al. Effects of synthesis condition on formation of desired crystal structures of doped-TiO_2/carbon composite supports for ORR electrocatalysts. *Electrochim Acta* 2012;77:225-31. DOI
83. Huang S, Ganesan P, Popov BN. Electrocatalytic activity and stability of niobium-doped titanium oxide supported platinum catalyst for polymer electrolyte membrane fuel cells. *Appl Catal B Environ* 2010;96:224-31. DOI
84. Noh K, Nam I, Han JW. Nb-TiO_2 nanotubes as catalyst supports with high activity and durability for oxygen reduction. *Appl Surf Sci* 2020;521:146330. DOI
85. Kim J, Kwon G, Lim H, Zhu C, You H, Kim Y. Effects of transition metal doping in Pt/M-TiO_2 (M = V, Cr, and Nb) on oxygen reduction reaction activity. *J Power Sources* 2016;320:188-95. DOI

86. Kim J, Chang S, Kim Y. Compressive strain as the main origin of enhanced oxygen reduction reaction activity for Pt electrocatalysts on chromium-doped titania support. *Appl Catal B Environ* 2014;158-159:112-8. DOI
87. Ho VT, Pan CJ, Rick J, Su WN, Hwang BJ. Nanostructured $Ti_{0.7}Mo_{0.3}O_2$ support enhances electron transfer to Pt: high-performance catalyst for oxygen reduction reaction. *J Am Chem Soc* 2011;133:11716-24. DOI
88. Tsai M, Nguyen T, Akalework NG, et al. Interplay between molybdenum dopant and oxygen vacancies in a TiO_2 support enhances the oxygen reduction reaction. *ACS Catal* 2016;6:6551-9. DOI
89. Kumar A, Ramani V. Strong metal-support interactions enhance the activity and durability of platinum supported on tantalum-modified titanium dioxide electrocatalysts. *ACS Catal* 2014;4:1516-25. DOI
90. Stassi A, Gatto I, Baglio V, Passalacqua E, Aricò AS. Oxide-supported PtCo alloy catalyst for intermediate temperature polymer electrolyte fuel cells. *Appl Catal B Environ* 2013;142-143:15-24. DOI
91. Noh K, Im H, Lim C, Jang MG, Nam I, Han JW. Tunable nano-distribution of Pt on TiO_2 nanotubes by atomic compression control for high-efficient oxygen reduction reaction. *Chem Eng J* 2022;427:131568. DOI
92. Tsai M, Rick J, Su W, Hwang B. Design of transition-metal-doped TiO_2 as a multipurpose support for fuel cell applications: using a computational high-throughput material screening approach. *Mol Syst Des Eng* 2017;2:449-56. DOI
93. Murphin Kumar PS, Ponnusamy VK, Deepthi KR, et al. Controlled synthesis of Pt nanoparticle supported TiO_2 nanorods as efficient and stable electrocatalysts for the oxygen reduction reaction. *J Mater Chem A* 2018;6:23435-44. DOI
94. Masuda T, Fukumitsu H, Fugane K, et al. Role of cerium oxide in the enhancement of activity for the oxygen reduction reaction at Pt-CeO_x nanocomposite electrocatalyst - an in situ electrochemical X-ray absorption fine structure study. *J Phys Chem C* 2012;116:10098-102. DOI
95. Chen J, Li Z, Chen Y, et al. An enhanced activity of Pt/CeO_2/CNT triple junction interface catalyst prepared by atomic layer deposition for oxygen reduction reaction. *Chem Phys Lett* 2020;755:137793. DOI
96. Du C, Gao X, Cheng C, Zhuang Z, Li X, Chen W. Metal organic framework for the fabrication of mutually interacted Pt CeO_2C ternary nanostructure: advanced electrocatalyst for oxygen reduction reaction. *Electrochim Acta* 2018;266:348-56. DOI
97. Xu F, Wang D, Sa B, Yu Y, Mu S. One-pot synthesis of Pt/CeO_2/C catalyst for improving the ORR activity and durability of PEMFC. *Int J Hydrog Energy* 2017;42:13011-9. DOI
98. Tan N, Lei Y, Huo D, et al. Fabricating Pt/CeO_2/N-C ternary ORR electrocatalysts with extremely low platinum content and excellent performance. *J Mater Sci* 2022;57:538-52. DOI
99. Lu Q, Wang Z, Tang Y, et al. Well-controlled Pt-CeO_2-nitrogen doped carbon triple-junction catalysts with enhanced activity and durability for the oxygen reduction reaction. *Sustain Energy Fuels* 2022;6:2989-95. DOI
100. Kim GY, Yoon KR, Shin K, Jung JW, Henkelman G, Ryu WH. Black tungsten oxide nanofiber as a robust support for metal catalysts: high catalyst loading for electrochemical oxygen reduction. *Small* 2021;17:e2103755. DOI
101. Kumar S, Bhange SN, Soni R, Kurungot S. WO_3 nanorods bearing interconnected Pt nanoparticle units as an activity-modulated and corrosion-resistant carbon-free system for polymer electrolyte membrane fuel cells. *ACS Appl Energy Mater* 2020;3:1908-21. DOI
102. Jin Y. WO_3 modified graphene supported Pt electrocatalysts with enhanced performance for oxygen reduction reaction. *Int J Electrochem Sci* 2017;12:6535-44. DOI
103. Mo Y, Feng S, Yu T, et al. Surface unsaturated WO_x activating PtNi alloy nanowires for oxygen reduction reaction. *J Colloid Interface Sci* 2022;607:1928-35. DOI
104. Lee J, Yim D, Park JH, et al. Tuning *d*-band centers by coupling PdO nanoclusters to WO_3 nanosheets to promote the oxygen reduction reaction. *J Mater Chem A* 2020;8:13490-500. DOI
105. Song Z, Banis MN, Zhang L, et al. Origin of achieving the enhanced activity and stability of Pt electrocatalysts with strong metal-support interactions via atomic layer deposition. *Nano Energy* 2018;53:716-25. DOI
106. Gao W, Zhang Z, Dou M, Wang F. Highly dispersed and crystalline Ta_2O_5 anchored Pt electrocatalyst with improved activity and durability toward oxygen reduction: promotion by atomic-scale Pt-Ta_2O_5 interactions. *ACS Catal* 2019;9:3278-88. DOI
107. Hung Y, Liu W, Chen Y, Wang K, Perng T. On the mesoporous TiN catalyst support for proton exchange membrane fuel cell. *Int J Hydrog Energy* 2020;45:14083-92. DOI
108. Tian X, Luo J, Nan H, Fu Z, Zeng J, Liao S. Binary transition metal nitrides with enhanced activity and durability for the oxygen reduction reaction. *J Mater Chem A* 2015;3:16801-9. DOI
109. Tian X, Luo J, Nan H, et al. Transition metal nitride coated with atomic layers of Pt as a low-cost, highly stable electrocatalyst for the oxygen reduction reaction. *J Am Chem Soc* 2016;138:1575-83. DOI
110. Shin H, Kim H, Chung DY, et al. Scaffold-like titanium nitride nanotubes with a highly conductive porous architecture as a nanoparticle catalyst support for oxygen reduction. *ACS Catal* 2016;6:3914-20. DOI
111. Pan Z, Xiao Y, Fu Z, et al. Hollow and porous titanium nitride nanotubes as high-performance catalyst supports for oxygen reduction reaction. *J Mater Chem A* 2014;2:13966. DOI
112. Xiao Y, Zhan G, Fu Z, et al. Robust non-carbon titanium nitride nanotubes supported Pt catalyst with enhanced catalytic activity and durability for methanol oxidation reaction. *Electrochim Acta* 2014;141:279-85. DOI
113. Chen X, Li W, Pan Z, et al. Non-carbon titanium cobalt nitride nanotubes supported platinum catalyst with high activity and durability for methanol oxidation reaction. *Appl Surf Sci* 2018;440:193-201. DOI
114. Chen X, Pan Z, Zhou Q, et al. Pt nanoparticles supported on non-carbon titanium chromium nitride nanotubes with high activity and durability for methanol oxidation reaction. *J Solid State Electrochem* 2019;23:315-24. DOI

115. Wu Z, Dang D, Tian X. Designing robust support for Pt alloy nanoframes with durable oxygen reduction reaction activity. *ACS Appl Mater Interfaces* 2019;11:9117-24. DOI PubMed
116. Yu F, Xie Y, Tang H, et al. Platinum decorated hierarchical porous structures composed of ultrathin titanium nitride nanoflakes for efficient methanol oxidation reaction. *Electrochim Acta* 2018;264:216-24. DOI
117. Zheng Y, Zhang J, Zhan H, Sun D, Dang D, Tian XL. Porous and three dimensional titanium nitride supported platinum as an electrocatalyst for oxygen reduction reaction. *Electrochem Commun* 2018;91:31-5. DOI
118. Feng G, Pan Z, Xu Y, et al. Platinum decorated mesoporous titanium cobalt nitride nanorods catalyst with promising activity and CO-tolerance for methanol oxidation reaction. *Int J Hydrog Energy* 2018;43:17064-8. DOI
119. Yuan Z, Cao Y, Zhang Z, et al. Dandelion-like titanium nitride supported platinum as an efficient oxygen reduction catalyst in acidic media. *Int J Hydrog Energy* 2022;47:15035-43. DOI
120. Yang M, Van Wassen AR, Guarecuco R, Abruña HD, DiSalvo FJ. Nano-structured ternary niobium titanium nitrides as durable non-carbon supports for oxygen reduction reaction. *Chem Commun* 2013;49:10853-5. DOI PubMed
121. Xiao Y, Fu Z, Zhan G, et al. Increasing Pt methanol oxidation reaction activity and durability with a titanium molybdenum nitride catalyst support. *J Power Sources* 2015;273:33-40. DOI
122. Tian X, Tang H, Luo J, Nan H, Shu T. High-performance core-shell catalyst with nitride nanoparticles as a core: well-defined titanium copper nitride coated with an atomic Pt layer for the oxygen reduction reaction. *ACS Catal* 2017;7:3810-7. DOI
123. Liu Q, Du L, Fu G, et al. Structurally ordered Fe_3Pt nanoparticles on robust nitride support as a high performance catalyst for the oxygen reduction reaction. *Adv Energy Mater* 2019;9:1803040. DOI
124. Nan H, Dang D, Tian XL. Structural engineering of robust titanium nitride as effective platinum support for the oxygen reduction reaction. *J Mater Chem A* 2018;6:6065-73. DOI
125. Yin J, Wang L, Tian C, et al. Low-Pt loaded on a vanadium nitride/graphitic carbon composite as an efficient electrocatalyst for the oxygen reduction reaction. *Chemistry* 2013;19:13979-86. DOI
126. Kim NY, Lee JH, Kwon JA, et al. Vanadium nitride nanofiber membrane as a highly stable support for Pt-catalyzed oxygen reduction reaction. *J Ind Eng Chem* 2017;46:298-303. DOI
127. Zheng J, Zhang W, Zhang J, et al. Recent advances in nanostructured transition metal nitrides for fuel cells. *J Mater Chem A* 2020;8:20803-18. DOI
128. Yang M, Cui Z, DiSalvo FJ. Mesoporous chromium nitride as a high performance non-carbon support for the oxygen reduction reaction. *Phys Chem Chem Phys* 2013;15:7041-4. DOI PubMed
129. Yang M, Guarecuco R, Disalvo FJ. Mesoporous chromium nitride as high performance catalyst support for methanol electrooxidation. *Chem Mater* 2013;25:1783-7. DOI
130. Liu B, Huo L, Si R, Liu J, Zhang J. A general method for constructing two-dimensional layered mesoporous mono- and binary-transition-metal nitride/graphene as an ultra-efficient support to enhance its catalytic activity and durability for electrocatalytic application. *ACS Appl Mater Interfaces* 2016;8:18770-87. DOI
131. Chemler SR, Bovino MT. Catalytic aminohalogenation of alkenes and alkynes. *ACS Catal* 2013;3:1076-91. DOI
132. He C, Tao J. Transition metal carbides coupled with nitrogen-doped carbon as efficient and stable Bi-functional catalysts for oxygen reduction reaction and hydrogen evolution reaction. *Int J Hydrog Energy* 2022;47:13240-50. DOI
133. Hunt ST, Milina M, Alba-Rubio AC, et al. Self-assembly of noble metal monolayers on transition metal carbide nanoparticle catalysts. *Science* 2016;352:974-8. DOI
134. Yue R, Xia M, Wang M, et al. TiN and TiC as stable and promising supports for oxygen reduction reaction: theoretical and experimental study. *Appl Surf Sci* 2019;495:143620. DOI
135. Lee Y, Ahn JH, Park H, et al. Support structure-catalyst electroactivity relation for oxygen reduction reaction on platinum supported by two-dimensional titanium carbide. *Nano Energy* 2021;79:105363. DOI
136. Xie X, Chen S, Ding W, Nie Y, Wei Z. An extraordinarily stable catalyst: Pt NPs supported on two-dimensional $Ti_3C_2X_2$ (X = OH, F) nanosheets for oxygen reduction reaction. *Chem Commun* 2013;49:10112-4. DOI
137. Ignaszak A, Song C, Zhu W, et al. Titanium carbide and its core-shelled derivative TiC@TiO_2 as catalyst supports for proton exchange membrane fuel cells. *Electrochim Acta* 2012;69:397-405. DOI
138. Xie X, Xue Y, Li L, et al. Surface Al leached Ti_3AlC_2 as a substitute for carbon for use as a catalyst support in a harsh corrosive electrochemical system. *Nanoscale* 2014;6:11035-40. DOI
139. Min P, Li C, Ding L, Jian Z, Liang C. Microwave-assisted preparation of Mo_2C/CNTs nanocomposites as efficient electrocatalyst supports for oxygen reduction reaction. *Ind Eng Chem Res* 2010;175:275-8. DOI
140. Cheng C, Zhang X, Fu Z, Yang Z. Strong metal-support interactions impart activity in the oxygen reduction reaction: Au monolayer on Mo_2C (MXene). *J Phys Condens Matter* 2018;30:475201. DOI
141. Saha S, Cabrera Rodas JA, Tan S, Li D. Performance evaluation of platinum-molybdenum carbide nanocatalysts with ultralow platinum loading on anode and cathode catalyst layers of proton exchange membrane fuel cells. *J Power Sources* 2018;378:742-9. DOI
142. Hamo ER, Rosen BA. Improved durability and activity in Pt/Mo_2C fuel cell cathodes by magnetron sputtering of tantalum. *ChemElectroChem* 2021;8:3123-34. DOI
143. Elbaz L, Phillips J, Artyushkova K, More K, Brosha EL. Evidence of high electrocatalytic activity of molybdenum carbide supported platinum nanorafts. *J Electrochem Soc* 2015;162:H681-5. DOI

144. Krishnamurthy CB, Lori O, Elbaz L, Grinberg I. First-principles investigation of the formation of Pt nanorafts on a Mo_2C support and their catalytic activity for oxygen reduction reaction. *J Phys Chem Lett* 2018;9:2229-34. DOI PubMed
145. Schweitzer NM, Schaidle JA, Ezekoye OK, Pan X, Linic S, Thompson LT. High activity carbide supported catalysts for water gas shift. *J Am Chem Soc* 2011;133:2378-81. DOI PubMed
146. Zhang K, Yang W, Ma C, et al. A highly active, stable and synergistic Pt nanoparticles/Mo_2C nanotube catalyst for methanol electro-oxidation. *NPG Asia Mater* 2015;7:e153-e153. DOI
147. Li Q, Ma Z, Sa R, et al. Computation-predicted, stable, and inexpensive single-atom nanocatalyst Pt@Mo_2C-an important advanced material for H_2 production. *J Mater Chem A* 2017;5:14658-72. DOI
148. Huang X, Wang J, Gao J, Zhang Z, Gan LY, Xu H. Structural evolution and underlying mechanism of single-atom centers on Mo_2C (100) support during oxygen reduction reaction. *ACS Appl Mater Interfaces* 2021;13:17075-84. DOI PubMed
149. Zhang L, Yang T, Zang W, et al. Quasi-paired Pt atomic sites on Mo_2C promoting selective four-electron oxygen reduction. *Adv Sci* 2021;8:e2101344. DOI PubMed PMC
150. Gao W, Liu T, Zhang Z, Dou M, Wang F. Stabilization of Pt nanoparticles at the Ta_2O_5-TaC binary junction: an effective strategy to achieve high durability for oxygen reduction. *J Mater Chem A* 2020;8:5525-34. DOI
151. Begum M, Yurukcu M, Yurtsever F, et al. Pt-Ni/WC alloy nanorods arrays as ORR catalyst for PEM fuel cells. *ECS Trans* 2017;80:919-25. DOI
152. Yurtsever FM, Yurukcu M, Begum M, Watanabe F, Karabacak T. Stacked and core-shell Pt:Ni/WC nanorod array electrocatalyst for enhanced oxygen reduction reaction in polymer electrolyte membrane fuel cells. *ACS Appl Energy Mater* 2018;1:6115-22. DOI
153. Nabil Y, Cavaliere S, Harkness I, Sharman J, Jones D, Rozière J. Novel niobium carbide/carbon porous nanotube electrocatalyst supports for proton exchange membrane fuel cell cathodes. *J Power Sources* 2017;363:20-6. DOI
154. Stamatin SN, Skou EM. Pt/NbC-N electrocatalyst for use in proton exchange membrane fuel cells. *ECS Trans* 2013;58:1267-76. DOI
155. Justin P, Charan PHK, Rao GR. Activated zirconium carbide promoted Pt/C electrocatalyst for oxygen reduction. *Appl Catal B Environ* 2014;144:767-74. DOI
156. Hamo ER, Rosen BA. Transition metal carbides as cathode supports for PEM fuel cells. *Nano Res* 2022;15:10218-33. DOI
157. Wang Y, Wang M, Lu Z, Ma D, Jia Y. Enabling multifunctional electrocatalysts by modifying the basal plane of unifunctional 1T'-MoS_2 with anchored transition metal single atoms. *Nanoscale* 2021;13:13390-400. DOI
158. Logeshwaran N, Panneerselvam IR, Ramakrishnan S, et al. Quasihexagonal platinum nanodendrites decorated over CoS_2-N-doped reduced graphene oxide for electro-oxidation of C1-, C2-, and C3-type alcohols. *Adv Sci* 2022;9:e2105344. DOI PubMed PMC
159. Bothra P, Pandey M, Pati SK. Size-selective electrocatalytic activity of $(Pt)_n/MoS_2$ for oxygen reduction reaction. *Catal Sci Technol* 2016;6:6389-95. DOI
160. Anwar MT, Yan X, Asghar MR, et al. MoS_2-rGO hybrid architecture as durable support for cathode catalyst in proton exchange membrane fuel cells. *Chinese J Catal* 2019;40:1160-7. DOI
161. Wei L, Ang EH, Yang Y, et al. Recent advances of transition metal based bifunctional electrocatalysts for rechargeable zinc-air batteries. *J Power Sources* 2020;477:228696. DOI
162. Wang D, Song Y, Zhang H, Yan X, Guo J. Recent advances in transition metal borides for electrocatalytic oxygen evolution reaction. *J Electroanal Chem* 2020;861:113953. DOI
163. Cao S, Sun T, Li J, Li Q, Hou C, Sun Q. The cathode catalysts of hydrogen fuel cell: from laboratory toward practical application. *Nano Res* 2023;16:4365-80. DOI
164. Kumar S, Yoyakki A, Pandikassala A, Soni R, Kurungot S. Pt-anchored-zirconium phosphate nanoplates as high-durable carbon-free oxygen reduction reaction electrocatalyst for PEM fuel cell applications. *Adv Sustain Syst* 2023;7:2200330. DOI
165. Yin S, Mu S, Lv H, Cheng N, Pan M, Fu Z. A highly stable catalyst for PEM fuel cell based on durable titanium diboride support and polymer stabilization. *Appl Catal B Environ* 2010;93:233-40. DOI
166. Yin S, Mu S, Pan M, Fu Z. A highly stable TiB_2-supported Pt catalyst for polymer electrolyte membrane fuel cells. *J Power Sources* 2011;196:7931-6. DOI
167. Huang Z, Lin R, Fan R, Fan Q, Ma J. Effect of TiB_2 pretreatment on Pt/TiB_2 catalyst performance. *Electrochim Acta* 2014;139:48-53. DOI
168. Zhang C, Ma B, Zhou Y, Wang C. Highly active and durable Pt/MXene nanocatalysts for ORR in both alkaline and acidic conditions. *J Electroanal Chem* 2020;865:114142. DOI
169. Ponnada S, Kiai MS, Gorle DB, et al. Recent status and challenges in multifunctional electrocatalysis based on 2D MXenes. *Catal Sci Technol* 2022;12:4413-41. DOI
170. Peera SG, Liu C, Sahu AK, et al. Recent advances on MXene-based electrocatalysts toward oxygen reduction reaction: a focused review. *Adv Mater Interfaces* 2021;8:2100975. DOI
171. Huang X, Song M, Zhang J, et al. Investigation of MXenes as oxygen reduction electrocatalyst for selective H_2O_2 generation. *Nano Res* 2022;15:3927-32. DOI
172. Xu C, Fan C, Zhang X, et al. MXene ($Ti_3C_2T_x$) and carbon nanotube hybrid-supported platinum catalysts for the high-performance oxygen reduction reaction in PEMFC. *ACS Appl Mater Interfaces* 2020;12:19539-46. DOI
173. Yang X, Zhang Y, Fu Z, et al. Tailoring the electronic structure of transition metals by the V_2C MXene support: excellent oxygen reduction performance triggered by metal-support interactions. *ACS Appl Mater Interfaces* 2020;12:28206-16. DOI

174. Wei B, Fu Z, Legut D, et al. Rational design of highly stable and active MXene-based bifunctional ORR/OER double-atom catalysts. *Adv Mater* 2021;33:e2102595. DOI
175. Li Z, Cui Y, Wu Z, et al. Reactive metal-support interactions at moderate temperature in two-dimensional niobium-carbide-supported platinum catalysts. *Nat Catal* 2018;1:349-55. DOI
176. Du L, Shao Y, Sun J, Yin G, Liu J, Wang Y. Advanced catalyst supports for PEM fuel cell cathodes. *Nano Energy* 2016;29:314-22. DOI
177. Samad S, Loh KS, Wong WY, et al. Carbon and non-carbon support materials for platinum-based catalysts in fuel cells. *Int J Hydrog Energy* 2018;43:7823-54. DOI
178. Gao Y, Kong D, Liang J, et al. Inside-out dual-doping effects on tubular catalysts: structural and chemical variation for advanced oxygen reduction performance. *Nano Res* 2022;15:361-7. DOI
179. Liu X, Zhao Z, Liang J, et al. Inducing covalent atomic interaction in intermetallic Pt alloy nanocatalysts for high-performance fuel cells materials. *Angew Chem Int Ed* 2023;62:e202302134. DOI
180. Xiao F, Wang Y, Xu GL, et al. Fe-N-C boosts the stability of supported platinum nanoparticles for fuel cells. *J Am Chem Soc* 2022;144:20372-84. DOI

Ge *et al. Microstructures* 2023;3:2023026
DOI: 10.20517/microstructures.2023.13

Microstructures

Research Article

Open Access

Check for updates

180° head-to-head flat domain walls in single crystal $BiFeO_3$

Wanbing Ge[1], Richard Beanland[1], Marin Alexe[1], Quentin Ramasse[2], Ana M. Sanchez[1]

[1]Department of Physics, University of Warwick, Coventry CV4 7AL, UK.
[2]SuperSTEM Laboratory, SciTech Daresbury, Keckwick Lane, Warrington WA4 4AD, UK.

Correspondence to: Prof. Richard Beanland, Department of Physics, University of Warwick, Coventry CV4 7AL, UK. E-mail: R.Beanland@warwick.ac.uk

How to cite this article: Ge W, Beanland R, Alexe M, Ramasse Q, Sanchez AM. 180° head-to-head flat domain walls in single crystal $BiFeO_3$. *Microstructures* 2023;3:2023026. https://dx.doi.org/10.20517/microstructures.2023.13

Received: 20 Mar 2023 **First Decision:** 12 Apr 2023 **Revised:** 28 Apr 2023 **Accepted:** 12 May 2023 **Published:** 12 Jun 2023

Academic Editor: Shujun Zhang **Copy Editor:** Fangling Lan **Production Editor:** Fangling Lan

Abstract

We investigate flux-grown $BiFeO_3$ crystals using transmission electron microscopy (TEM). This material has an intriguing ferroelectric structure of domain walls with a period of approximately 100 nm, alternating between flat and sawtooth morphologies. We show that all domain walls are of 180° type and that the flat walls, lying on (112) planes, are reconstructed with an excess of Fe and a deficiency of Bi. This reconstruction is similar to that observed in several previous studies of deposited layers of $BiFeO_3$. The negative charge of the reconstructed layer induces head-to-head polarisation in the surrounding material and a rigid-body shift of one domain relative to the other. These characteristics pin the flat 180° domain walls and determine the domain structure of the material. Sawtooth 180° domain walls provide the necessary reversal of polarisation between flat walls. The high density of immobile domain walls suppresses the ferroelectric properties of the material, highlighting the need for careful control of growth conditions.

Keywords: Bismuth ferrite, ferroelectric domains, 180° domain walls, reconstructed domain walls

INTRODUCTION

$BiFeO_3$ is arguably the most investigated multiferroic material[1-3], simultaneously showing ferroelectric, antiferromagnetic, and ferroelastic order at room temperature[4]. The coupling of ferroelectric and ferromagnetic properties makes it ideal for the promising application of mutual control of electrical and

magnetic order in multiferroic devices[5,6].

$BiFeO_3$ has a rhombohedral structure (space group *R3c*) below its Curie temperature T_c = 1,100 K[4], with a pseudocubic lattice parameter of 3.965 Å and rhombohedral angle 89.4° (pseudocubic indexing is used throughout this paper). Its spontaneous ferroelectric polarisation ($\mathbf{P}_s$) has a magnitude P_s approximately 100 μC cm^{-2} along [111] and mostly arises from the displacement of Bi ions relative to their surrounding FeO_6 cages[7]. Oxygen octahedra are tilted antiphase around the three-fold [111] axis by 10°-14° ($a^-a^-a^-$ in Glazer notation[8]). The formation of domains in $BiFeO_3$, similar to other ferroelectric materials, occurs to minimise the total energy, comprised of electrostatic, depolarisation, and elastic components[9]. Depending on the angle ϕ between $\mathbf{P}_s$ of adjacent domains, the meeting of these domains at domain walls can result in either purely ferroelectric (ϕ = 180°) or ferroelectric-ferroelastic (ϕ = 71° or 109°). The orientation or habit plane of domain walls has been of great interest as it provides insight into the competing energy components[10-13] and determines functional properties[14,15].

The batch of flux-grown single-crystals of $BiFeO_3$ investigated in this study have been subject to several previous investigations[16,17], all of which have revealed a dense array of parallel domain walls seen in piezoresponse force microscopy (PFM) and conventional transmission electron microscopy (TEM) as alternating sawtooth and flat bands of contrast [Figure 1]. The complex microdomain structure in these crystals is extremely stable, exhibiting no change upon observation, even in the thinnest specimens. Furthermore, no observable switching (or rapid back-switching into the pristine domain pattern) was found, even with 200 V applied to the surface with an AFM tip. The inability to access the functional properties of these high-quality single crystals is concerning and may have implications for the exploitation of $BiFeO_3$ in practical applications. Therefore, it is important to understand the nature and origin of this domain structure.

The first study of these crystals[16] showed the domain walls to be either 180°- or 109°-type and due to the high predicted energy of 180°-type domain walls, it was proposed that they were probably 109°-type. A second study[17] of the same batch of crystals using negative C_s high-resolution TEM imaging found a variety of domain wall types, including 71°-, 109°-, and 180°-type. Another recent study of similar material[18] confirms the sawtooth walls to be 180°-type but proposes that flat domain walls are 109°-type. In this article, along with its companion publication[19], we revisit the domain structure in this same batch of crystals using a combination of PFM, conventional TEM, convergent beam electron diffraction (CBED), atomic resolution scanning TEM (STEM), and electron energy loss spectroscopy (EELS). The high stability of the domains ensured there was no influence of specimen preparation on the structure. We find that there are only 180° domains in the crystal, i.e., all domain walls are 180°-type. The difficulties experienced in previous work may potentially be attributed to projection effects when the three-dimensional domain structure is observed in an electron-transparent foil. To overcome this, we use a focused ion beam (FIB) technique to prepare multiple sections with different orientations from the same region of the crystal. We describe the sawtooth domains in a companion article[19]; the focus of this article is on the flat 180° domain walls.

MATERIALS AND METHODS

$BiFeO_3$ single crystals were obtained from the same batch used in the studies of Berger *et al.*[16] and Jia *et al.*[17], who described growth conditions in detail. In brief, crystals were precipitated from a $Fe_2O_3/Bi_2O_3/B_2O_3$ flux cooled very slowly from 1,170 K to 875 K. Much of the growth took place below the paraelectric-ferroelectric phase transition at 1,098 K. The crystals were compact and had sizes of half to a few millimetres, with a top surface of four (*hhl*) facets, only a few degrees away from (001). For this study, several well-formed single crystals that had no contact with the crucible sidewalls were selected.

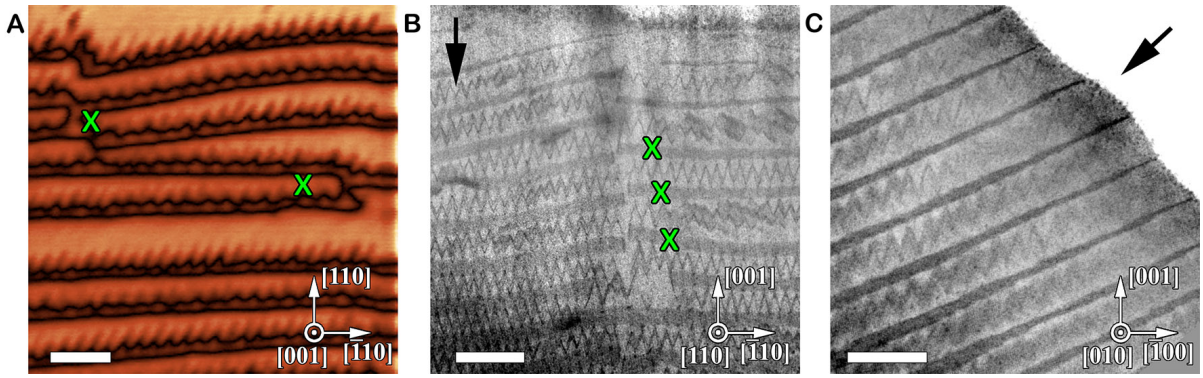

Figure 1. (A) PFM out-of-plane amplitude image of the sectioned and polished (001) surface of the $BiFeO_3$ crystal. (B) Low magnification BF-STEM image of a (110) FIB-prepared lamella. (C) Low magnification BF-STEM image of a (010) FIB-prepared lamella. Arrows in (B and C) point towards increasing thickness. Examples of continuity of domain walls, where a sawtooth wall changes direction and becomes a flat wall, are marked by x in (A and B). Scale bars are 100 nm.

For PFM measurements, a crystal was ground and polished to (001) using diamond lapping film of decreasing sizes to 0.1 μm, finishing with a dilute 0.04 μm colloidal silica solution. PFM measurements were conducted on a Bruker Dimension Icon AFM at a scan rate of 0.5 Hz using a Bruker OSCM-PT-R3 tip with Pt coating, along with a drive frequency of 254 kHz and a drive voltage of 2 V.

Specimens for TEM were prepared by lift-out on a Tescan Amber Ga^+ FIB-SEM from a second crystal in its as-grown state, with (110), (010), and ($\bar{1}$10) orientations. Cutting and thinning were performed using an ion beam energy of 30 kV, with a final low-energy polish at 2 kV. The specimens were taken from a compact region on the crystal, and their orientations were verified by their relative position, selected area electron diffraction (SAED) patterns, and atomic resolution images. To obtain the thinnest possible specimens for very high-resolution imaging, wedge-shaped lamellae were produced.

STEM images were taken with a double-corrected JEOL ARM 200F TEM/STEM operating at 200 kV, with a beam convergence semi-angle of 22 mrad. The annular bright field (ABF) and annular dark field (ADF) detectors covered 11.5-24 and approximately 45-180 mrad, respectively[11]. In atomic resolution STEM images, atom positions are determined by fitting two-dimensional Gaussian peaks[11,20].

EELS data and ADF images were acquired at the UK SuperSTEM Laboratory using a Nion UltraSTEM 100 MC operated at 60 kV, with a beam convergence semi-angle of 32 mrad. The acceptance semi-angles of EELS and ADF were 44 mrad and 79-185 mrad, respectively.

RESULTS AND DISCUSSION

Domains on the polished (001) surface imaged by PFM follow a regular stripe pattern running along [$\bar{1}$10] with reversal of both in-plane and out-of-plane phase and alternating sawtooth and straight domain walls, as shown in Figure 1A and Supplementary Figure 1A. No relation between domain structure and surface topography was present (see Supplementary Figure 1B). The spacing between stripes varies between 60 and 120 nm. Occasionally, domains can be found to terminate where sawtooth and straight domain walls meet (e.g., at x in Figure 1), indicating that these two types of walls separate the sample into only two different domains. Bright-field (BF) STEM images of (110) and (010) FIB lift-out lamellae are shown in Figure 1B and C (see Supplementary Figure 2A). In both (110) and (010) orientations, the domain walls appear as alternating sawtooth and planar bands of contrast. In these BF-STEM images, the crystal is

aligned to the zone axis, and local conditions, such as strain, composition, or a small change in crystal orientation across a boundary, can strongly affect the transmission of the electron probe. As a result, domain boundaries appear slightly darker. Their orientation varies depending on the direction of view. In the (110) section [Figure 1B], straight bands are parallel to the (001) surface, while in the (010) section [Figure 1C], they are inclined at an angle of approximately 25°, running along [$\bar{2}$01]. Sawtooth walls present different V-shapes when observed from different directions, and their structure is considered in detail elsewhere[19]. The domain appearance and PFM measurements agree with the observations of Berger *et al.*[16]. However, they interpreted the flat bands of contrast seen in Figure 1B and C as domains with a width of approximately 10 nm. The varying thickness of the lamellae in Figure 1 shows this to be incorrect. In Figure 1C, the lamella decreases to a thickness of just a few nm at the edge of the specimen on the top-right of the image. The width of the bands decreases as the specimen thickness decreases, indicating that they correspond to planes in the material that are inclined to the direction of view. The same effect can also be seen in Figure 1B, where the specimen thickness increases towards the bottom of the image. Therefore, the darker bands are not slabs of material that form domains, different to the adjacent lighter material. They are the projection of a plane that is inclined to the point of view.

The proposal that the flat bands of contrast in Figure 1B and C are planes rather than slabs of finite thickness is confirmed by the ($\bar{1}$10) section shown in Figure 2A. In this projection, their width does not depend on specimen thickness. Here, they are seen edge-on and appear as sharp, straight lines at an angle of 35° to (001) surface, i.e., lying on (112) planes. The sawtooth domain pattern can be recognised in the thinnest part of the specimen but becomes indistinct where the lamella is thicker due to overlapping projections. Higher magnification images [Supplementary Figure 2B] show that the average habit plane is slightly away from (112); the flat domain walls have a terraced structure, with (112) facets seen edge-on, separated by steps 1-2 nm in height.

High-resolution ($\bar{1}$10) STEM images of one of these domain walls, seen edge-on in the thinnest part of the specimen, are shown in Figure 2C and D. In any {110} section of $BiFeO_3$, the [111] polar axis can either lie within the plane of the section or at 35° to it, (i.e. with an out-of-plane component). The $a^-a^-a^-$ antiphase tilting of oxygen octahedra in the *R3c* structure gives different projections for the two cases. When the polar axis is in the image plane, the antiphase tilting of octahedra is not visible, and oxygen columns appear as a dumbbell at the same location in every unit cell[21]. Conversely, when it has an out-of-plane component, O-Fe-O-Fe-O chains form an arc with a curvature indicating the direction of $\mathbf{P}_s$[17] [Supplementary Figure 3]. In Figure 2C, the polar axis is in the image plane for both domains, consistent with a [$\bar{1}$10] $BiFeO_3$ projection [Figure 2B]. On a unit-cell level, polarisation $\mathbf{P}_s$ is often taken to be proportional to the negative displacement of Fe relative to the centre of the rectangle defined by its four Bi neighbours, namely $-\boldsymbol{\delta}_{FB}$[22,23]. Since the polar axis lies in the image plane, we observe a full projection of the displacement (in comparison, one can only observe approximately 57% or 81% of the displacement in [110] or [100] projections, respectively[23]). The quiver map of $-\boldsymbol{\delta}_{FB}$ vectors overlaid on the ADF-STEM image of Figure 2D shows that polarisation changes by 180°, pointing towards the wall on both sides. (N.B. at the domain wall itself, $\boldsymbol{\delta}_{FB}$ is not calculated because it is unclear how to define the unit cell.) Away from the domain wall, the magnitude of $\boldsymbol{\delta}_{FB}$ is generally around 40 pm, in good agreement with the theoretical value of 41 pm for P_s of approximately 100 μC cm^{-2}[7,23,24]. As a final observation in Figure 2D, Bi atom columns in the domain wall are not as bright as equivalent atom columns in the surrounding material, indicating a lower occupancy of Bi at the domain wall.

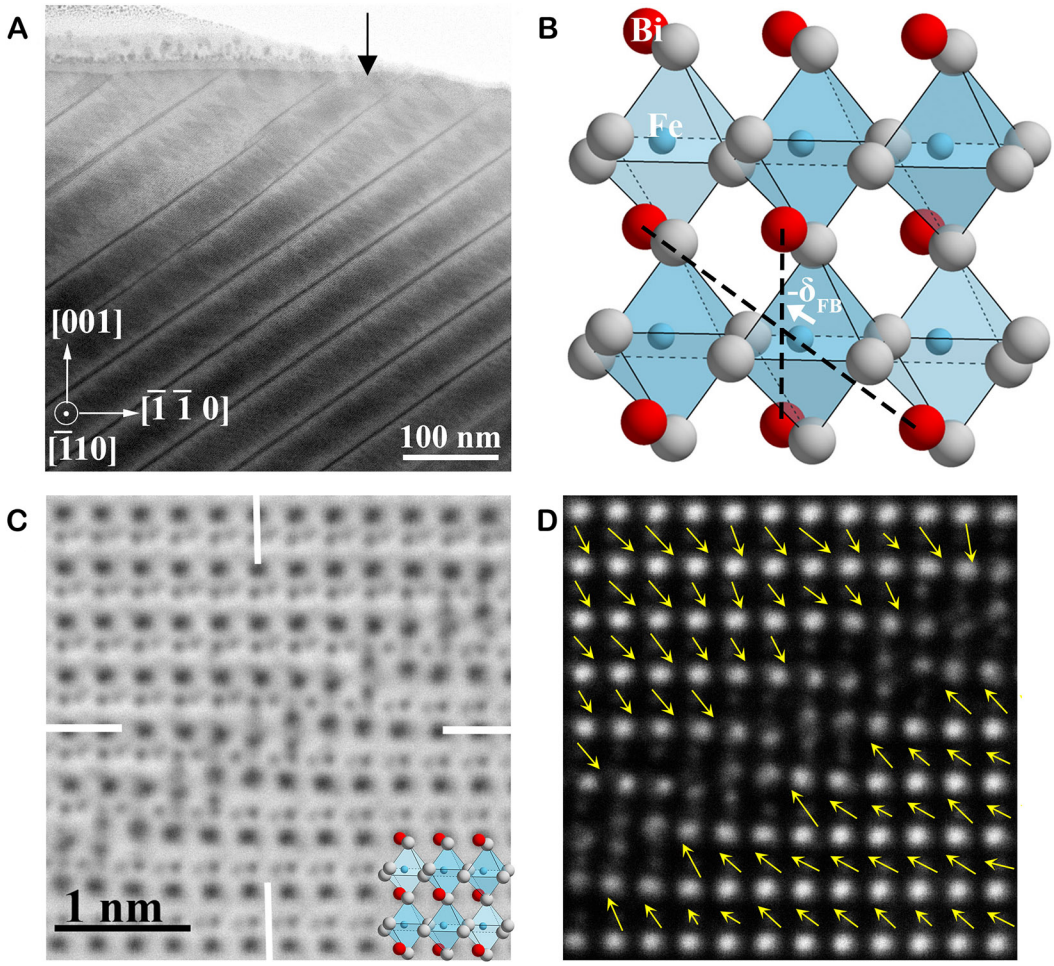

Figure 2. (A) Low magnification BF-STEM image of a ($\bar{1}$10) FIB-prepared lamella. The dark arrow at the thin edge of the lamella points towards increasing thickness. The width of the straight dark lines is independent of specimen thickness, showing that they correspond to planes seen edge-on. The crystal orientation applies to all images in this figure. (B) Ideal ($\bar{1}$10) projection of $BiFeO_3$, where Bi atoms are presented in red, Fe blue, and O grey. The direction of the $-\boldsymbol{\delta}_{FB}$ vector is also shown. (C) A high-resolution ABF-STEM image of a flat wall. White lines are aligned horizontally and vertically, allowing the rigid-body displacement of the domains along [110] and [001] to be seen. (D) An ADF-STEM image taken simultaneously with C). Arrows in (D) show local $-\boldsymbol{\delta}_{FB}$ vectors, indicating the magnitude and direction of polarisation in each unit cell.

It is apparent from Figure 2C and D that these 180° head-to-head domain walls are reconstructed; the local structure is different from the bulk crystal, and the associated distortions are quantified in Figure 3. Examining the horizontal (001) planes of bright Bi atom columns in Figure 2D, downwards displacements (i.e., along [00$\bar{1}$]) are seen on the left, starting approximately 0.5 nm away from the domain wall, while upwards displacements along [001] are seen on the right. These displacements are shown as blue points and lines in Figure 3A and reach a value of approximately 0.1 nm at the domain wall itself. Far from the domain wall, these displacements tend to zero, showing that the (001) planes are aligned, as can be directly seen from the horizontal white lines in Figure 2C. The orange line in Figure 3A shows a similar measurement for the vertical (110) planes. Here, there is greater scatter as the displacements vary from place to place along the domain wall. Interestingly, there is a slight increase in displacements immediately adjacent to the domain wall. Additionally, a long-range misalignment of about 0.1 nm is observed, corresponding to a lateral shift of ½[110]. This rigid-body displacement can be directly observed in Figure 2C by comparison of the vertical white lines with the position of atom columns. The average value of P_s changes its sign abruptly

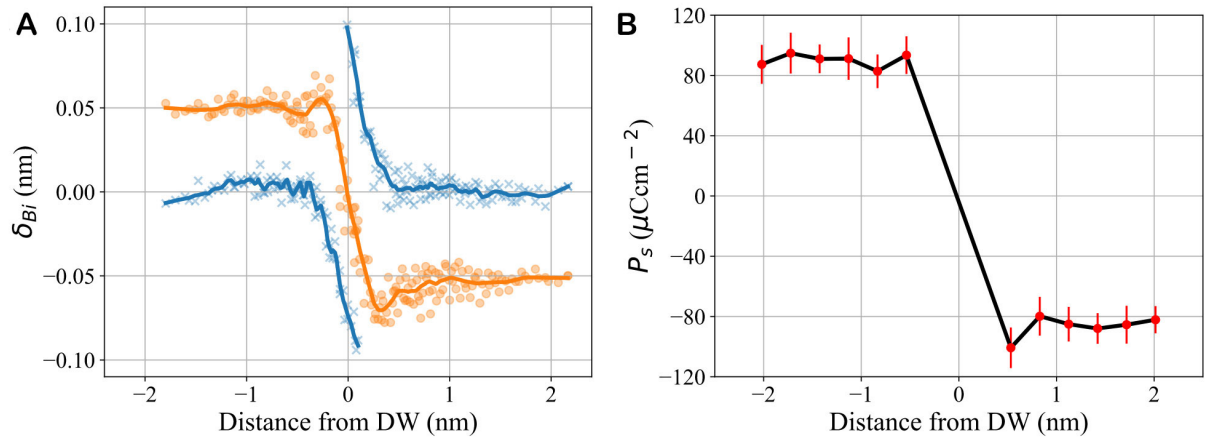

Figure 3. (A) Distortion of unit cells in the vicinity of the domain wall shown in Figure 2D, measured by the displacement of Bi atom columns away from (110) planes (orange) or (001) planes (blue). Points correspond to individual measurements, and the line is an average value. (B) Average polarisation P_s obtained from -$\boldsymbol{\delta}_{FB}$ vectors, measured in bands parallel to the domain wall.

(over approximately 1 nm) at the wall [Figure 3B], which is significantly different from the previously reported thicker (> 2 nm) widths for charged domain walls in $BiFeO_3$ without any local reconstruction[23,25-27]. The narrow domain wall width indicates the presence of a strong electrical field related to the local change in structure at the domain wall.

More information on the reconstruction at these domain walls can be obtained from a second point of view, obtained from a (010) section shown in Figure 4. Although the domain wall is probably inclined to the electron beam direction, this image is taken at the thinnest part of the lamella, and the high electron beam convergence angle gives a reduced depth of field[28]. Consequently, the domain wall is sharply delineated in ADF-STEM images. (The effect of reduced depth of field is shown in Supplementary Figure 4). At the domain wall [Figure 4A], the reconstruction appears as alternating bright and dark clusters of atoms, forming either 2 × 1 or 2 × 2 atom blocks, while -$\boldsymbol{\delta}_{FB}$ vectors demonstrate the 180° head-to-head nature [Figure 4B]. There is no obvious change in the magnitude of P_s immediately adjacent to the reconstructed domain wall, which is approximately 1.5 unit cells in width and runs along $[\bar{2}01]$ in this projection. Just as in the $[\bar{1}10]$ images of Figure 2, (001) planes are fully aligned (horizontal white lines), while a ½[100] displacement is visible (vertical white lines). Since the component along the beam direction is not visible, this is in full agreement with the ½[110] rigid body shift observed in Figure 2. Bending of the (001) Bi planes can also be found at the domain wall (see Supplementary Figure 5). Figures 4E-G show core-loss EELS elemental maps of the domain wall, together with a simultaneously recorded ADF image in Figure 4D. The brightest atom columns in the ADF image are shown to be Bi in a separate EELS acquisition [Supplementary Figure 6]. Dark regions in the ADF image at the domain wall lack Bi and consist of Fe+O. These findings, along with the results presented in Figures 2 and 4, show that the flat domain wall has a structure and stoichiometry different from bulk $BiFeO_3$. They are consistent with each other both in the observed rigid-body shift, lower Bi content, bending of (001) Bi planes, and $\mathbf{P}_s$ distribution around them.

The nonstoichiometry of the reconstruction in the flat 180° head-to-head walls is an indication that they form during crystal growth, while the periodic domain structure indicates a degree of self-organisation. Synthesis of crystalline $BiFeO_3$ is only possible within a narrow range of conditions, both in the deposition of thin epitaxial layers[22,29-32] and as ceramics or single crystals[31,33-35]. In bulk crystal growth, the secondary Bi-rich sillenite $Bi_{25}FeO_{39}$ and/or Fe-rich mullite $Bi_2Fe_4O_9$ phases readily form to accommodate deviations

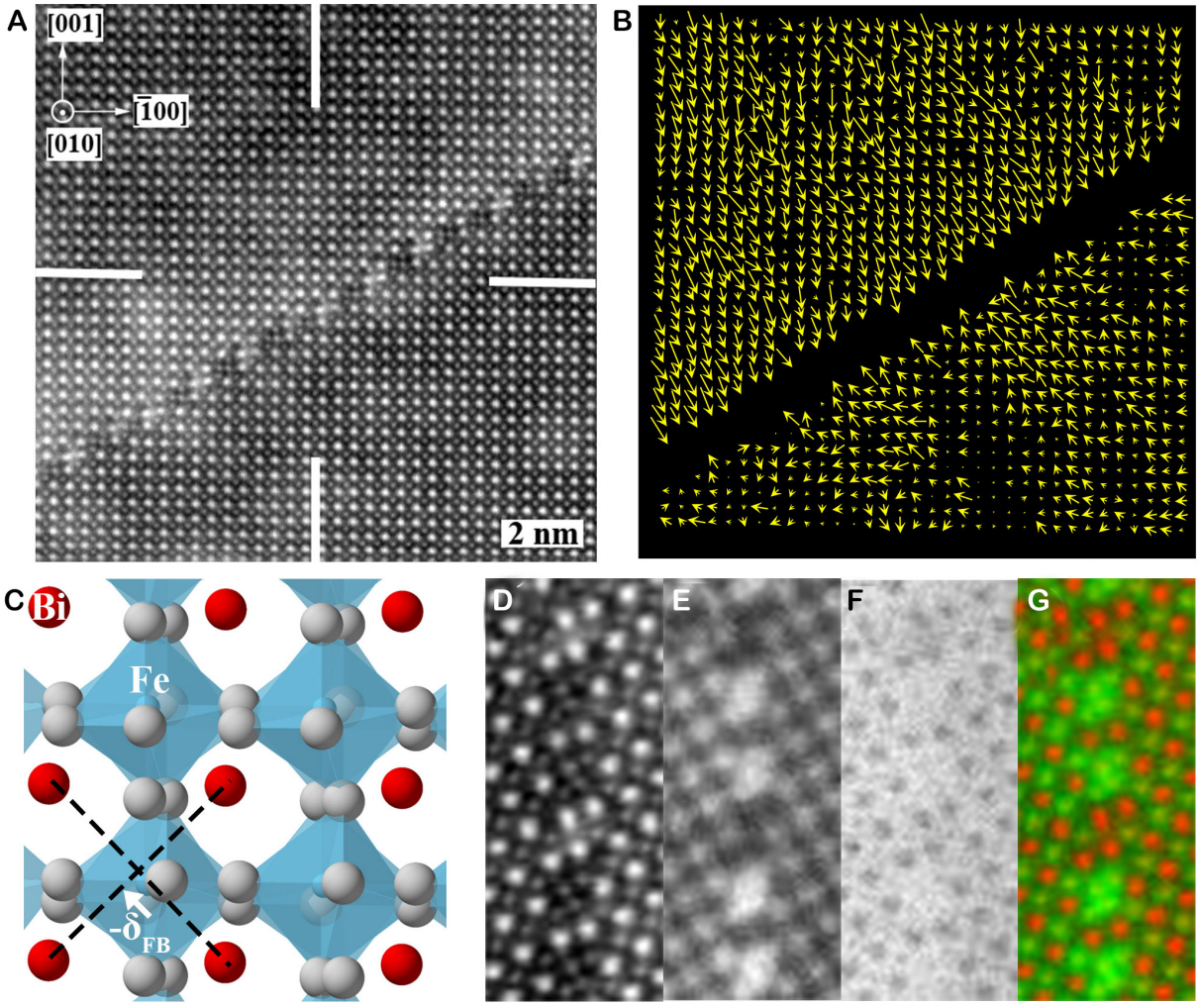

Figure 4. (A) An ADF-STEM image of a head-to-head 180° domain wall in a (010) FIB-prepared lamella. Large and bright atoms columns are Bi, and smaller ones are Fe. O atoms are not visible. (B) Quiver plot of local $-\boldsymbol{\delta}_{FB}$ vectors, indicating the magnitude and direction of polarisation in each unit cell. (C) Ideal (010) projection of $BiFeO_3$; Bi atoms are red, Fe blue, and O grey. The direction of the $-\boldsymbol{\delta}_{FB}$ vector is also shown. (D-G) core-loss EELS data: image size is 1.32 × 3.13 nm. (D) HAADF-STEM; (E) an element map of Fe; (F) an element map of O; (G) a composite of ADF (red) and Fe (green).

from perfect stoichiometry, e.g., due to the relative volatility of Bi_2O_3[33,35]. In epitaxial thin film growth, locally nonstoichiometric planar defects that strongly resemble those shown in Figure 4 are often seen[22,29,30,32,36,37]. Maclaren *et al.* found iron-rich regions consisting of edge-sharing FeO_6 octahedra, resembling the structure of γ-Fe_2O_3, (and, indeed, mullite)[30,36,37]. Li *et al.* showed that they can be induced by a slight increase in substrate temperature during MBE deposition, which makes the surface Fe-rich[22,29,32]. Similar to the observed reconstruction in this study, these previously observed planar defects also have a half-unit-cell rigid body shift across them caused by the switch from corner-sharing to edge-sharing oxygen octahedra. The deviation from stoichiometry gives a local excess of oxygen anions, giving a negative charge density estimated to be between -68 μC cm^{-2} and -110 μC cm^{-2}[22,36,37]. The effect of these negatively charged planar defects in the surrounding $BiFeO_3$ matrix is to induce an increased local polarisation towards them, producing charged head-to-head domain walls[32]. The intrinsic negative charge density accommodates the majority of the -190 μC cm^{-2} polar discontinuity expected at the flat domain walls in our crystal, explaining the relatively narrow region of adjacent material that has a different polarisation to the bulk material.

Therefore, in our material, we may explain the origin of the domain microstructure as follows. Since the temperature during crystal growth is below T_c, ferroelectric domains are to be expected, and ideally, they would assume a form to minimise the competing ferroelectric/ferroelastic/electrostatic energy components of the system. In thin film growth, it is well established that domain microstructures may evolve during film deposition[38] and, in turn, can influence growth morphology[39]. Therefore, in our case of single-crystal $BiFeO_3$ growth, we may expect regions with positive and negative surface charges that have an effect on domain structure and subsequent growth. Importantly, Li[29] showed that nonstoichiometric monolayers may form on polarisation-up, negatively charged $BiFeO_3$ growth surfaces. They found that as growth progresses, a region with polarisation pointing towards the growth surface may, therefore, reach a critical negative charge, causing the incorporation of FeO_6 octahedra at the crystal surface and producing nonstoichiometric monolayers of the defective material. They also showed that the negative charge induces and pins head-to-head polarisation[32]. It seems plausible that a similar mechanism is responsible for the head-to-head domain walls that we observe. On a (*hhl*) growth surface, the FeO_6 octahedra would form edge-sharing chains along $[1\bar{1}0]$, partly defining the orientation of the wall. These negatively-charged defects stabilise the 180° domain walls and perpetuate incorporation of FeO_6 octahedra in the next monolayer of crystal growth. It is not clear if the (112) plane makes the best match of their structure to the adjacent *R3c* BFO or whether this habit plane is a result of the asymmetrical surface charge where the domain wall intersects the surface, which may vary with, for example, the growth rate. An array of such structures can only exist with a further reversal of polarisation between them, and tail-to-tail 180° domain walls are the most efficient way of achieving this. The presence of the sawtooth walls is thus topologically necessary. It has been shown that unpinned 180° domain walls are expected to develop a crenellated structure to balance polarisation and electrostatic energy[40,41]. The crenellated structure of these walls indicates that they are not pinned in the same way as the flat walls, and a very recent study of these tail-to-tail walls indicates that they are, to some extent, mobile when an electric field is applied, while head-to-head flat walls are immobile[18]. This is in good agreement with our measurements of P_s hysteresis, which gave essentially no signal, indicating that the flat walls are completely pinned. It is commonly observed that measurements of P_s in bulk $BiFeO_3$ crystals are usually an order of magnitude smaller than in thin films, even though our measured $\boldsymbol{\delta}_{FB}$ vectors at the atomic scale are similar, equivalent to P_s approximately 100 μC cm^{-2}. While this batch of material now dominates high-resolution structural studies of bulk $BiFeO_3$[16,17], there is nothing in the proposed origin of the domain structure that would indicate it to be specific to these particular crystals. On a macroscopic scale, the deviation from perfect stoichiometry is miniscule; approximating the defects as sheets of Bi with 50% occupancy, a spacing of 100 nm gives a Fe excess of only approximately 0.2 at.%, meaning that they are unlikely to be avoided by changes in starting composition.

CONCLUSIONS

Periodic domain structures in single crystal $BiFeO_3$ have been re-investigated. Our results show that all domain walls are of 180°-type, alternating between flat head-to-head and sawtooth tail-to-tail walls. We focus on the flat walls here, finding that they have an orientation close to (112) and a polarisation reversal that occurs over only approximately 1 nm, significantly less than seen in other charged domain walls in $BiFeO_3$. They are locally nonstoichiometric, with an atomic reconstruction of roughly a unit cell in thickness, similar to that seen in planar defects in thin film $BiFeO_3$ and related materials. The reconstructed region contains edge-sharing FeO_6 octahedra that produce a rigid-body shift of half a unit cell and a negative charge density that induces head-to-head polarisation. We propose that the periodic domain structure forms during crystal growth in regions where negative surface charges exceed a critical value, causing the incorporation of FeO_6 octahedra that is perpetuated and becomes self-organised as growth proceeds. The reconstruction and local charge strongly pin head-to-head 180° domain walls, explaining the poor response of these $BiFeO_3$ single crystals in measurements of polarisation. Avoiding their formation is,

therefore, a necessary prerequisite for high-performance $BiFeO_3$ crystals and ceramics.

DECLARATIONS

Authors' contributions

Performed data acquisition, data analysis, and interpretation and wrote the first draft of the article: Ge W, Sanchez AM
Performed data acquisition (STEM+EELS maps) at SuperSTEM: Ramasse Q
Provided material, conception and design of the study and interpretation: Alexe M
Performed data analysis and interpretation and contributed to the development of the article: Beanland R, Sanchez AM

AVAILABILITY OF DATA AND MATERIALS

The data that support the findings of this study are openly available in WRAP at http://wrap.warwick.ac.uk/173964.

Financial support and sponsorship

Ge W. acknowledges support from the EPSRC International Doctoral Scholars grant, number EP/R513374/1.

Conflicts of interest

All authors declare that there are no conflicts of interest.

Ethical approval and consent to participate

Not applicable.

Consent for publication

Not applicable.

REFERENCES

1. Neaton JB, Ederer C, Waghmare UV, Spaldin N, Rabe K. First-principles study of spontaneous polarization in multiferroic $BiFeO_3$. *Phys Rev B* 2005;71:014113. DOI
2. Ramesh R, Spaldin NA. Multiferroics: progress and prospects in thin films. *Nat Mater* 2007;6:21-9. DOI PubMed
3. Wang J, Neaton JB, Zheng H, et al. Epitaxial $BiFeO_3$ multiferroic thin film heterostructures. *Science* 2003;299:1719-22. DOI
4. Catalan G, Scott JF. Physics and applications of bismuth ferrite. *Adv Mater* 2009;21:2463-85. DOI
5. Eerenstein W, Mathur ND, Scott JF. Multiferroic and magnetoelectric materials. *Nature* 2006;442:759-65. DOI PubMed
6. Scott JF. Data storage. Multiferroic memories. *Nat Mater* 2007;6:256-7. DOI
7. Kubel F, Schmid H. Structure of a ferroelectric and ferroelastic monodomain crystal of the perovskite $BiFeO_3$. *Acta Crystallogr B Struct Sci* 1990;46:698-702. DOI
8. Glazer AM. The classification of tilted octahedra in perovskites. *Acta Crystallogr B Struct Crystallogr Cryst Chem* 1972;28:3384-92. DOI
9. Catalan G, Seidel J, Ramesh R, Scott JF. Domain wall nanoelectronics. *Rev Mod Phys* 2012;84:119-56. DOI
10. Yadav AK, Nelson CT, Hsu SL, et al. Observation of polar vortices in oxide superlattices. *Nature* 2016;530:198-201. DOI
11. Peters JJP, Apachitei G, Beanland R, Alexe M, Sanchez AM. Polarization curling and flux closures in multiferroic tunnel junctions. *Nat Commun* 2016;7:13484. DOI PubMed PMC
12. Rusu D, Peters JJP, Hase TPA, et al. Ferroelectric incommensurate spin crystals. *Nature* 2022;602:240-4. DOI
13. Meyer B, Vanderbilt D. *Ab* initio study of ferroelectric domain walls in $PbTiO_3$. *Phys Rev B* 2002;65:104111. DOI
14. Bhatnagar A, Roy Chaudhuri A, Heon Kim Y, Hesse D, Alexe M. Role of domain walls in the abnormal photovoltaic effect in $BiFeO_3$. *Nat Commun* 2013;4:3835. DOI PMC

15. Seidel J, Martin LW, He Q, et al. Conduction at domain walls in oxide multiferroics. *Nat Mater* 2009;8:229-34. DOI
16. Berger A, Hesse D, Hähnel A, Arredondo M, Alexe M. Regular nanodomain vertex arrays in $BiFeO_3$ single crystals. *Phys Rev B* 2012;85:064104. DOI
17. Jia C, Jin L, Wang D, et al. Nanodomains and nanometer-scale disorder in multiferroic bismuth ferrite single crystals. *Acta Mater* 2015;82:356-68. DOI
18. Condurache O, Dražić G, Rojac T, et al. Atomic-level response of the domain walls in bismuth ferrite in a subcoercive-field regime. *Nano Lett* 2023;23:750-6. DOI PubMed PMC
19. Ge W, Beanland R, Alexe M, Sanchez AM. 3D reconstruction of sawtooth 180° tail-to-tail domain walls in single crystal $BiFeO_3$. *Adv Funct Mater* 2023:2301171. DOI
20. Peters JJP, Bristowe NC, Rusu D, et al. Polarization screening mechanisms at $La_{0.7}Sr_{0.3}MnO_3$-$PbTiO_3$ interfaces. *ACS Appl Mater Interfaces* 2020;12:10657-63. DOI
21. Woodward DI, Reaney IM. Electron diffraction of tilted perovskites. *Acta Crystallogr B* 2005;61:387-99. DOI PubMed
22. Li L, Zhang Y, Xie L, et al. Atomic-scale mechanisms of defect-induced retention failure in ferroelectrics. *Nano Lett* 2017;17:3556-62. DOI
23. Nelson CT, Winchester B, Zhang Y, et al. Spontaneous vortex nanodomain arrays at ferroelectric heterointerfaces. *Nano Lett* 2011;11:828-34. DOI
24. Lebeugle D, Colson D, Forget A, Viret M. Very large spontaneous electric polarization in $BiFeO_3$ single crystals at room temperature and its evolution under cycling fields. *Appl Phys Lett* 2007;91:022907. DOI
25. Condurache O, Dražić G, Sakamoto N, Rojac T, Benčan A. Atomically resolved structure of step-like uncharged and charged domain walls in polycrystalline $BiFeO_3$. *J Appl Phys* 2021;129:054102. DOI
26. Bednyakov PS, Sturman BI, Sluka T, Tagantsev AK, Yudin PV. Physics and applications of charged domain walls. *NPJ Comput Mater* 2018;4:65. DOI
27. Li L, Gao P, Nelson CT, et al. Atomic scale structure changes induced by charged domain walls in ferroelectric materials. *Nano Lett* 2013;13:5218-23. DOI
28. Nellist PD, Pennycook SJ. The principles and interpretation of annular dark-field Z-contrast imaging. *Adv Electron Electron Phys* 2000;113:147-203. DOI
29. Li L, Jokisaari JR, Zhang Y, et al. Control of domain structures in multiferroic thin films through defect engineering. *Adv Mater* 2018;30:e1802737. DOI
30. MacLaren I, Sala B, Andersson SM, et al. Strain localization in thin films of $Bi(Fe,Mn)O_3$ due to the formation of stepped Mn^{4+}-rich antiphase boundaries. *Nanoscale Res Lett* 2015;10:407. DOI PubMed PMC
31. Deniz H, Bhatnagar A, Pippel E, et al. Nanoscale Bi_2FeO_{6-x} precipitates in $BiFeO_3$ thin films: a metastable Aurivillius phase. *J Mater Sci* 2014;49:6952-60. DOI
32. Li L, Cheng X, Jokisaari JR, et al. Defect-induced hedgehog polarization states in multiferroics. *Phys Rev Lett* 2018;120:137602. DOI
33. Rojac T, Bencan A, Malic B, et al. $BiFeO_3$ ceramics: processing, electrical, and electromechanical properties. *J Am Ceram Soc* 2014;97:1993-2011. DOI
34. Wu J, Fan Z, Xiao D, Zhu J, Wang J. Multiferroic bismuth ferrite-based materials for multifunctional applications: Ceramic bulks, thin films and nanostructures. *Prog Mater Sci* 2016;84:335-402. DOI
35. Lu J, Qiao L, Fu P, Wu Y. Phase equilibrium of Bi_2O_3-Fe_2O_3 pseudo-binary system and growth of $BiFeO_3$ single crystal. *J Cryst Growth* 2011;318:936-41. DOI
36. Maclaren I, Wang L, Craven AJ, et al. The atomic structure and chemistry of Fe-rich steps on antiphase boundaries in Ti-doped $Bi_{0.9}Nd_{0.15}FeO_3$. *APL Mater* 2014;2:066106. DOI
37. Maclaren I, Wang L, Morris O, et al. Local stabilisation of polar order at charged antiphase boundaries in antiferroelectric $(Bi_{0.85}Nd_{0.15})(Ti_{0.1}Fe_{0.9})O_3$. *APL Mater* 2013;1:021102. DOI
38. Luca G, Strkalj N, Manz S, Bouillet C, Fiebig M, Trassin M. Nanoscale design of polarization in ultrathin ferroelectric heterostructures. *Nat Commun* 2017;8:1419. DOI PubMed PMC
39. Wang H, Wu H, Chi X, et al. Large-scale epitaxial growth of ultralong stripe $BiFeO_3$ films and anisotropic optical properties. *ACS Appl Mater Interfaces* 2022;14:8557-64. DOI
40. Zhang J, Wang Y, Liu J, et al. Origin of sawtooth domain walls in ferroelectrics. *Phys Rev B* 2020;101:060103. DOI
41. Marton P, Gonçalves MAP, Paściak M, et al. Zigzag charged domain walls in ferroelectric $PbTiO_3$. *Phys Rev B* 2023;107:094102. DOI

AUTHOR INSTRUCTIONS

1. Submission Overview

Before you decide to publish with *Microstructures*, please read the following items carefully and make sure that you are well aware of Editorial Policies and the following requirements.

1.1 Topic Suitability

The topic of the manuscript must fit the scope of the journal. Please refer to Aims and Scope for more information.

1.2 Open Access and Copyright

The journal adopts Gold Open Access publishing model and distributes content under the Creative Commons Attribution 4.0 International License. Copyright is retained by authors. Please make sure that you are well aware of these policies.

1.3 Publication Fees

Microstructures is an open access journal. When a paper is accepted for publication, authors are required to pay Article Processing Charges (APCs) to cover its editorial and production costs. The APC for each submission is $600. There are no additional charges based on color, length, figures, or other elements. For more details, please refer to OAE Publication Fees.

1.4 Language Editing

All submissions are required to be presented clearly and cohesively in good English. Authors whose first language is not English are advised to have their manuscripts checked or edited by a native English speaker before submission to ensure the high quality of expression. A well-organized manuscript in good English would make the peer review even the whole editorial handling more smoothly and efficiently.

If needed, authors are recommended to consider the language editing services provided by Charlesworth to ensure that the manuscript is written in correct scientific English before submission. Authors who publish with OAE journals enjoy a special discount for the services of Charlesworth via the following two ways.

Submit your manuscripts directly at http://www.charlesworthauthorservices.com/~OAE;

Open the link http://www.charlesworthauthorservices.com/, and enter Promotion Code “OAE” when you submit.

1.5 Work Funded by the National Institutes of Health

If an accepted manuscript was funded by National Institutes of Health (NIH), the author may inform editors of the NIH funding number. The editors are able to deposit the paper to the NIH Manuscript Submission System on behalf of the author.

2. Submission Preparation

2.1 Cover Letter

A cover letter is required to be submitted accompanying each manuscript. It should be concise and explain why the study is significant, why it fits the scope of the journal, and why it would be attractive to readers, etc.

Here is a guideline of a cover letter for authors’ consideration:

In the first paragraph: include the title and type (e.g., Research Article, Review Article, etc.) of the manuscript, a brief on the background of the study, the question the author sought out to answer and why;

In the second paragraph: concisely explain what was done, the main findings and why they are significant;

In the third paragraph: indicate why the manuscript fits the Aims and Scope of the journal, and why it would be attractive to readers;

In the fourth paragraph: confirm that the manuscript has not been published elsewhere and not under consideration of any other journal. All authors have approved the manuscript and agreed on its submission to the journal. Journal’s specific requirements have been met if any.

If the manuscript is contributed to a special issue, please also mention it in the cover letter.

If the manuscript was presented partly or entirely in a conference, the author should clearly state the background information of the event, including the conference name, time and place in the cover letter.

2.2 Types of Manuscripts

There is no restriction on the length of manuscripts, number of figures, tables and references, provided that the manuscript is concise and comprehensive. The journal publishes Research Article, Review Article, Editorial, Perspective etc. For more details about paper type, please refer to the following table.

Manuscript Type	Definition	Abstract	Keywords	Main Text Structure
Research Article	A Research Article describes detailed results from novel research. All findings are extensively discussed.	Structured abstract including Aim, Methods, Results and Conclusion. No more than 250 words.	3-8 keywords	The main content should include four sections: Introduction, Materials and Methods, Results and Discussion.
Review Article	A Review Article summarizes the literature on previous studies. It usually does not present any new information on a subject.	Unstructured abstract. No more than 250 words.	3-8 keywords	The main text may consist of several sections with unfixed section titles. We suggest that the author include an "Introduction" section at the beginning, several sections with unfixed titles in the middle part, and a "Conclusion" section in the end.
Meta-Analysis	A Meta-Analysis is a statistical analysis combining the results of multiple scientific studies. It is often an overview of clinical trials.	Structured abstract including Aim, Methods, Results and Conclusion. No more than 250 words.	3-8 keywords	The main content should include four sections: Introduction, Methods, Results and Discussion.
Technical Note	A Technical Note is a short article giving a brief description of a specific development, technique or procedure, or it may describe a modification of an existing technique, procedure or device applied in research.	Unstructured abstract. No more than 250 words.	3-8 keywords	/
Commentary	A Commentary is to provide comments on a newly published article or an alternative viewpoint on a certain topic.	Unstructured abstract. No more than 250 words.	3-8 keywords	/
Editorial	An Editorial is a short article describing news about the journal or opinions of senior editors or the publisher.	None required.	None required.	/
Letter to Editor	A Letter to Editor is usually an open post-publication review of a paper from its readers, often critical of some aspect of a published paper. Controversial papers often attract numerous Letters to Editor.	Unstructured abstract (optional). No more than 250 words.	3-8 keywords (optional)	/
Opinion	An Opinion usually presents personal thoughts, beliefs, or feelings on a topic.	Unstructured abstract (optional). No more than 250 words.	3-8 keywords	/
Perspective	A Perspective provides personal points of view on the state-of-the-art of a specific area of knowledge and its future prospects. Links to areas of intense current research focus can also be made. The emphasis should be on a personal assessment rather than a comprehensive, critical review. However, comments should be put into the context of existing literature. Perspectives are usually invited by the Editors.	Unstructured abstract. No more than 150 words.	3-8 keywords	/

2.3 Manuscript Structure

2.3.1 Front Matter

2.3.1.1 Title

The title of the manuscript should be concise, specific and relevant, with no more than 16 words if possible. When gene or protein names are included, the abbreviated name rather than full name should be used.

2.3.1.2 Authors and Affiliations

Authors' full names should be listed. The initials of middle names can be provided. Institutional addresses and email addresses for all authors should be listed. At least one author should be designated as corresponding author. In addition, corresponding authors are suggested to provide their Open Researcher and Contributor ID upon submission. Please note that any change to authorship is not allowed after manuscript acceptance.

2.3.1.3 Highlights

Highlights are mandatory because they can help increase the discoverability of your article through search engines. They consist of a short collection of bullet points that capture the novel results of your research as well as new methods that were used during the study (if any). They should be submitted in a separate editable file in the online submission system. Please use 'Highlights' in the file name and include 3 to 5 bullet points (maximum 85 characters per bullet point, including spaces).

2.3.1.4 Abstract

The abstract should be a single paragraph with word limitation and specific structure requirements (for more details please refer to Types of Manuscripts). It usually describes the main objective(s) of the study, explains how the study was done, including any model organisms used, without methodological detail, and summarizes the most important results and their significance. The abstract must be an objective representation of the study: it is not allowed to contain results which are not presented and substantiated in the manuscript, or exaggerate the main conclusions. Citations should not be included in the abstract.

2.3.1.5 Graphical Abstract

The graphical abstract is essential as this can catch first view of your publication by readers. We recommend you to submit an eye-catching figure. It should summarize the content of the article in a concise graphical form. It is recommended to use it because this can make online articles get more attention. The graphic abstract should be submitted as a separate document in the online submission system. Please provide an image with a minimum of 730 × 1,228 pixels (h × w) or proportionally more. The image should be readable at a size of 7 × 12 cm using a regular screen resolution of 96 dpi. Preferred file types: TIFF, PSD, AI, JPG, JPEG, EPS, PNG, ZIP and PDF files.

2.3.1.6 Keywords

Three to eight keywords should be provided, which are specific to the article, yet reasonably common within the subject discipline.

2.3.2 Main Text

Manuscripts of different types are structured with different sections of content. Please refer to Types of Manuscripts to make sure which sections should be included in the manuscripts.

2.3.2.1 Introduction

The introduction should contain background that puts the manuscript into context, allow readers to understand why the study is important, include a brief review of key literature, and conclude with a brief statement of the overall aim of the work and a comment about whether that aim was achieved. Relevant controversies or disagreements in the field should be introduced as well.

2.3.2.2 Materials and Methods

Materials and Methods should contain sufficient details to allow others to fully replicate the study. New methods and protocols should be described in detail while well-established methods can be briefly described or appropriately cited. Experimental participants selected, the drugs and chemicals used, the statistical methods taken, and the computer software used should be identified precisely. Statistical terms, abbreviations, and all symbols used should be defined clearly. Protocol documents for clinical trials, observational studies, and other non-laboratory investigations may be uploaded as supplementary materials.

2.3.2.3 Results and Discussion

This section should contain the findings of the study and discuss the implications of the findings in context of existing research and highlight limitations of the study. Future research directions may also be mentioned. Results of statistical analysis should also be included either as text or as tables or figures if appropriate. Authors should emphasize and summarize

only the most important observations. Data on all primary and secondary outcomes identified in the section Methods should also be provided. Extra or supplementary materials and technical details can be placed in supplementary documents.

2.3.2.4 Conclusions

It should state clearly the main conclusions and include the explanation of their relevance or importance to the field.

2.3.3 Back Matter

2.3.3.1 Acknowledgments

Anyone who contributed towards the article but does not meet the criteria for authorship, including those who provided professional writing services or materials, should be acknowledged. Authors should obtain permission to acknowledge from all those mentioned in the Acknowledgments section. This section is not added if the author does not have anyone to acknowledge.

2.3.3.2 Authors' Contributions

Each author is expected to have made substantial contributions to the conception or design of the work, or the acquisition, analysis, or interpretation of data, or the creation of new software used in the work, or have drafted the work or substantively revised it.

Please use Surname and Initial of Forename to refer to an author's contribution. For example: made substantial contributions to conception and design of the study and performed data analysis and interpretation: Salas H, Castaneda WV; performed data acquisition, as well as provided administrative, technical, and material support: Castillo N, Young V.

If an article is single-authored, please include "The author contributed solely to the article." in this section.

2.3.3.3 Availability of Data and Materials

In order to maintain the integrity, transparency and reproducibility of research records, authors should include this section in their manuscripts, detailing where the data supporting their findings can be found. Data can be deposited into data repositories or published as supplementary information in the journal. Authors who cannot share their data should state that the data will not be shared and explain it. If a manuscript does not involve such issue, please state "Not applicable." in this section.

2.3.3.4 Financial Support and Sponsorship

All sources of funding for the study reported should be declared. The role of the funding body in the experiment design, collection, analysis and interpretation of data, and writing of the manuscript should be declared. Any relevant grant numbers and the link of funder's website should be provided if any. If the study is not involved with this issue, state "None." in this section.

2.3.3.5 Conflicts of Interest

Authors must declare any potential conflicts of interest that may be perceived as inappropriately influencing the representation or interpretation of reported research results. If there are no conflicts of interest, please state "All authors declared that there are no conflicts of interest." in this section. Some authors may be bound by confidentiality agreements. In such cases, in place of itemized disclosures, we will require authors to state "All authors declare that they are bound by confidentiality agreements that prevent them from disclosing their conflicts of interest in this work.". If authors are unsure whether conflicts of interest exist, please refer to the "Conflicts of Interest" of *Microstructures* Editorial Policies for a full explanation.

2.3.3.6 Copyright

Authors retain copyright of their works through a Creative Commons Attribution 4.0 International License that clearly states how readers can copy, distribute, and use their attributed research, free of charge. A declaration "© The Author(s) 2023." will be added to each article. Authors are required to sign License to Publish before formal publication.

2.3.3.7 References

References should be numbered in order of appearance at the end of manuscripts. In the text, reference numbers should be placed in square brackets and the corresponding references are cited thereafter. If the number of authors is less than or equal to six, we require to list all authors' names. If the number of authors is more than six, only the first three authors' names are required to be listed in the references, other authors' names should be omitted and replaced with "et al.". Abbreviations of the journals should be provided on the basis of Index Medicus. Information from manuscripts accepted but not published should be cited in the text as "Unpublished material" with written permission from the source.

References should be described as follows, depending on the types of works:

Types	Examples
Journal articles by individual authors	Weaver DL, Ashikaga T, Krag DN, et al. Effect of occult metastases on survival in node-negative breast cancer. *N Engl J Med* 2011;364:412-21. [DOI: 10.1056/NEJMoa1008108]

Organization as author	Diabetes Prevention Program Research Group. Hypertension, insulin, and proinsulin in participants with impaired glucose tolerance. *Hypertension* 2002;40:679-86. [DOI: 10.1161/01.hyp.0000035706.28494.09]
Both personal authors and organization as author	Vallancien G, Emberton M, Harving N, van Moorselaar RJ; Alf-One Study Group. Sexual dysfunction in 1,274 European men suffering from lower urinary tract symptoms. *J Urol* 2003;169:2257-61. [DOI: 10.1097/01.ju.0000067940.76090.73]
Journal articles not in English	Zhang X, Xiong H, Ji TY, Zhang YH, Wang Y. Case report of anti-N-methyl-D-aspartate receptor encephalitis in child. *J Appl Clin Pediatr* 2012;27:1903-7. (in Chinese)
Journal articles ahead of print	Odibo AO. Falling stillbirth and neonatal mortality rates in twin gestation: not a reason for complacency. *BJOG* 2018; Epub ahead of print [DOI: 10.1111/1471-0528.15541]
Books	Sherlock S, Dooley J. Diseases of the liver and billiary system. 9th ed. Oxford: Blackwell Sci Pub; 1993. pp. 258-96.
Book chapters	Meltzer PS, Kallioniemi A, Trent JM. Chromosome alterations in human solid tumors. In: Vogelstein B, Kinzler KW, editors. The genetic basis of human cancer. New York: McGraw-Hill; 2002. pp. 93-113.
Online resource	FDA News Release. FDA approval brings first gene therapy to the United States. Available from: https://www.fda.gov/NewsEvents/Newsroom/PressAnnouncements/ucm574058.htm. [Last accessed on 30 Oct 2017]
Conference proceedings	Harnden P, Joffe JK, Jones WG, editors. Germ cell tumours V. Proceedings of the 5th Germ Cell Tumour Conference; 2001 Sep 13-15; Leeds, UK. New York: Springer; 2002..
Conference paper	Christensen S, Oppacher F. An analysis of Koza's computational effort statistic for genetic programming. In: Foster JA, Lutton E, Miller J, Ryan C, Tettamanzi AG, Editors. Genetic programming. EuroGP 2002: Proceedings of the 5th European Conference on Genetic Programming; 2002 Apr 3-5; Kinsdale, Ireland. Berlin: Springer; 2002. pp. 182-91.
Unpublished material	Tian D, Araki H, Stahl E, Bergelson J, Kreitman M. Signature of balancing selection in Arabidopsis. *Proc Natl Acad Sci U S A*. Forthcoming 2002.

For other types of references, please refer to U.S. National Library of Medicine.

The journal also recommends that authors prepare references with a bibliography software package, such as EndNote to avoid typing mistakes and duplicated references.

2.3.3.8 Supplementary Materials

Additional data and information can be uploaded as Supplementary Materials to accompany the manuscripts. The supplementary materials will also be available to the referees as part of the peer-review process. Any file format is acceptable, such as data sheet (word, excel, csv, cdx, fasta, pdf or zip files), presentation (powerpoint, pdf or zip files), image (cdx, eps, jpeg, pdf, png or tiff), table (word, excel, csv or pdf), audio (mp3, wav or wma) or video (avi, divx, flv, mov, mp4, mpeg, mpg or wmv). All information should be clearly presented. Supplementary materials should be cited in the main text in numeric order (e.g., Supplementary Figure 1, Supplementary Figure 2, Supplementary Table 1, Supplementary Table 2, etc.). The style of supplementary figures or tables complies with the same requirements on figures or tables in main text. Videos and audios should be prepared in English, and limited to a size of 500 MB.

2.4 Manuscript Format

2.4.1 File Format

Manuscript files can be in DOC and DOCX formats and should not be locked or protected.

2.4.2 Length

There are no restrictions on paper length, number of figures, or number of supporting documents. Authors are encouraged to present and discuss their findings concisely.

2.4.3 Language

Manuscripts must be written in English.

2.4.4 Multimedia Files

The journal supports manuscripts with multimedia files. The requirements are listed as follows:

Video or audio files are only acceptable in English. The presentation and introduction should be easy to understand. The frames should be clear, and the speech speed should be moderate.

A brief overview of the video or audio files should be given in the manuscript text.

The video or audio files should be limited to a size of up to 500 MB.

Please use professional software to produce high-quality video files, to facilitate acceptance and publication along with the submitted article. Upload the videos in mp4, wmv, or rm format (preferably mp4) and audio files in mp3 or wav format.

2.4.5 Figures

Figures should be cited in numeric order (e.g., Figure 1, Figure 2) and placed after the paragraph where it is first cited;
Figures can be submitted in format of TIFF, PSD, AI, EPS or JPEG, with resolution of 300-600 dpi;
Figure caption is placed under the Figure;
Diagrams with describing words (including, flow chart, coordinate diagram, bar chart, line chart, and scatter diagram, etc.) should be editable in word, excel or powerpoint format. Non-English information should be avoided;
Labels, numbers, letters, arrows, and symbols in figure should be clear, of uniform size, and contrast with the background;
Symbols, arrows, numbers, or letters used to identify parts of the illustrations must be identified and explained in the legend;
Internal scale (magnification) should be explained and the staining method in photomicrographs should be identified;
All non-standard abbreviations should be explained in the legend;
Permission for use of copyrighted materials from other sources, including re-published, adapted, modified, or partial figures and images from the internet, must be obtained. It is authors' responsibility to acquire the licenses, to follow any citation instruction requested by third-party rights holders, and cover any supplementary charges.

2.4.6 Tables

Tables should be cited in numeric order and placed after the paragraph where it is first cited;
The table caption should be placed above the table and labeled sequentially (e.g., Table 1, Table 2);
Tables should be provided in editable form like DOC or DOCX format (picture is not allowed);
Abbreviations and symbols used in table should be explained in footnote;
Explanatory matter should also be placed in footnotes;
Permission for use of copyrighted materials from other sources, including re-published, adapted, modified, or partial tables from the internet, must be obtained. It is authors' responsibility to acquire the licenses, to follow any citation instruction requested by third-party rights holders, and cover any supplementary charges.

2.4.7 Abbreviations

Abbreviations should be defined upon first appearance in the abstract, main text, and in figure or table captions and used consistently thereafter. Non-standard abbreviations are not allowed unless they appear at least three times in the text. Commonly-used abbreviations, such as DNA, RNA, ATP, etc., can be used directly without definition. Abbreviations in titles and keywords should be avoided, except for the ones which are widely used.

2.4.8 Italics

General italic words like vs., et al., etc., in vivo, in vitro; t test, F test, U test; related coefficient as r, sample number as n, and probability as P; names of genes; names of bacteria and biology species in Latin.

2.4.9 Units

SI Units should be used. Imperial, US customary and other units should be converted to SI units whenever possible. There is a space between the number and the unit (i.e., 23 mL). Hour, minute, second should be written as h, min, s.

2.4.10 Numbers

Numbers appearing at the beginning of sentences should be expressed in English. When there are two or more numbers in a paragraph, they should be expressed as Arabic numerals; when there is only one number in a paragraph, number < 10 should be expressed in English and number > 10 should be expressed as Arabic numerals. 12345678 should be written as 12,345,678.

2.4.11 Equations

Equations should be editable and not appear in a picture format. Authors are advised to use either the Microsoft Equation Editor or the MathType for display and inline equations.

2.5 Submission Link

Submit an article via https://oaemesas.com/login?JournalId=microstructures.

Microstructures

Los Angeles Office
245 E Main Street ste122, Alhambra,
CA 91801, USA
Tel: +1 323 9987086
E-mail: editorialoffice@microstructj.com
Website: https://www.oaepublish.com/microstructures